ARISTOTLE UNIVERSITY OF THESSALONIKI
FACULTY OF SCIENCE
SCHOOL OF GEOLOGY
DEPARTMENT OF GEOPHYSICS

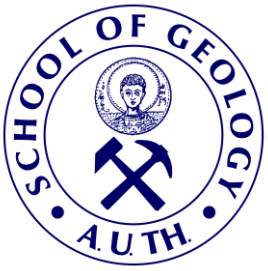

IOANNIS GRENDAS
M.Sc. Geologist

Contribution to the study of the parameters that control the seismic motion on surface geological formations: Experimental and theoretical approach based on ARGONET, Greek and French earthquake records

DOCTORAL THESIS

This Doctoral Thesis was carried out under the scholarship of IKY funded by the program: "Human resources support through doctoral research implementation", financial resources of the operational Program "Human Resources Development, Education and Lifelong learning", 2014–2020.

THESSALONIKI, 2022

ΑΡΙΣΤΟΤΕΛΕΙΟ ΠΑΝΕΠΙΣΤΗΜΙΟ ΘΕΣΣΑΛΟΝΙΚΗΣ
ΣΧΟΛΗ ΘΕΤΙΚΩΝ ΕΠΙΣΤΗΜΩΝ
ΤΜΗΜΑ ΓΕΩΛΟΓΙΑΣ
ΤΟΜΕΑΣ ΓΕΩΦΥΣΙΚΗΣ

ΙΩΑΝΝΗΣ ΓΡΕΝΔΑΣ
M.Sc. ΓΕΩΛΟΓΟΣ

Συμβολή στη μελέτη παραμέτρων που διαμορφώνουν τη σεισμική κίνηση σε επιφανειακούς γεωλογικούς σχηματισμούς: Πειραματική και θεωρητική προσέγγιση με έμφαση στο πεδίο δοκιμών ARGONET στην Κεφαλονιά καθώς και με τη χρήση άλλων δεδομένων του Ελληνικού και Γαλλικού δικτύου

ΔΙΔΑΚΤΟΡΙΚΗ ΔΙΑΤΡΙΒΗ

Η διδακτορική διατριβή υλοποιήθηκε με υποτροφία του ΙΚΥ η οποία χρηματοδοτήθηκε από την Πράξη «ΕΝΙΣΧΥΣΗ ΤΟΥ ΑΝΘΡΩΠΙΝΟΥ ΕΡΕΥΝΗΤΙΚΟΥ ΔΥΝΑΜΙΚΟΥ ΜΕΣΩ ΤΗΣ ΥΛΟΠΟΙΗΣΗΣ ΔΙΔΑΚΤΟΡΙΚΗΣ ΕΡΕΥΝΑΣ» από πόρους του ΕΠ «Ανάπτυξη Ανθρώπινου Δυναμικού, Εκπαίδευση και Δια Βίου Μάθηση», 2014-2020.

ΘΕΣΣΑΛΟΝΙΚΗ, 2022

GRENDAS IOANNIS
M.Sc. Geologist

Contribution to the study of the parameters that control the seismic motion on surface geological formations: Experimental and theoretical approach based on ARGONET, Greek and French earthquake records

DOCTORAL THESIS

Examining Committee:

Prof. Hatzidimitriou Panagiotis, Faculty of Science, School of Geology, AUTH, Greece, supervisor
Dr. Theodoulidis Nikolaos, Seismologist, Research director, ITSAK, Greece, co-supervisor
Dr. Hollender Fabrice, Geophysicist, CEA and ISTerre, France, co-supervisor
Prof. Kiratzi Anastasia, Faculty of Science, School of Geology, AUTH, Greece
Prof. Papazachos Constantinos, Faculty of Science, School of Geology, AUTH, Greece
Assist. Prof. Roumelioti Zafeiria., Faculty of Science, Department of Geology, UP, Greece
Prof. Sokos Efthimios, Faculty of Science, Department of Geology, UP, Greece

THESSALONIKI, 2022

ΣΥΜΒΟΛΗ ΣΤΗ ΜΕΛΕΤΗ ΤΩΝ ΠΑΡΑΜΕΤΡΩΝ ΠΟΥ ΔΙΑΜΟΡΦΩΝΟΥΝ ΤΗ ΣΕΙΣΜΙΚΗ ΚΙΝΗΣΗ ΣΕ ΕΠΙΦΑΝΕΙΑΚΟΥΣ ΓΕΩΛΟΓΙΚΟΥΣ ΣΧΗΜΑΤΙΣΜΟΥΣ: ΠΕΙΡΑΜΑΤΙΚΗ ΚΑΙ ΘΕΩΡΗΤΙΚΗ ΠΡΟΣΕΓΓΙΣΗ ΜΕ ΕΜΦΑΣΗ ΣΤΟ ΠΕΔΙΟ ΔΟΚΙΜΩΝ ARGONET ΣΤΗΝ ΚΕΦΑΛΟΝΙΑ ΚΑΘΩΣ ΚΑΙ ΜΕ ΤΗ ΧΡΗΣΗ ΑΛΛΩΝ ΔΕΔΟΜΕΝΩΝ ΤΟΥ ΕΛΛΗΝΙΚΟΥ ΚΑΙ ΓΑΛΛΙΚΟΥ ΔΙΚΤΥΟΥ ΕΠΙΤΑΧΥΝΣΙΟΓΡΑΦΩΝ. – *Διδακτορική Διατριβή*

CONTRIBUTION TO THE STUDY OF THE PARAMETERS THAT CONTROL THE SEISMIC MOTION ON SURFACE GEOLOGICAL FORMATIONS: EXPERIMENTAL AND THEORETICAL APPROACH BASED ON ARGONET, GREEK AND FRENCH EARTQUAKE RECORDS. – *Ph.D. Thesis*

Citation:
Γρένδας, Ι., 2022. – Συμβολή στη μελέτη παραμέτρων που διαμορφώνουν τη σεισμική κίνηση σε επιφανειακούς γεωλογικούς σχηματισμούς: Πειραματική και θεωρητική προσέγγιση με έμφαση στο πεδίο δοκιμών ARGONET στην Κεφαλονιά καθώς και με τη χρήση άλλων δεδομένων του Ελληνικού και Γαλλικού δικτύου επιταχυνσιογράφων. Διδακτορική Διατριβή, Τμήμα Γεωλογίας Α.Π.Θ., Αριθμός Παραρτήματος Επιστημονικής Επετηρίδας Τμ. Γεωλογίας Νο 227, 217 σελ.
Grendas, I., 2022. – Contribution to the study of the parameters that control the seismic motion on surface geological formations: Experimental and theoretical approach based on ARGONET, Greek and French earthquake records. Ph.D. Thesis, School of Geology, Aristotle University of Thessaloniki, Annex Number of Scientific Annals of the School of Geology No 227, 217 pp.

Dedicated to my parents
and to my brother

TABLE OFCONTENTS

PREFACE

The present Doctoral thesis has been carried out under the postgraduate studies program of Aristotle University of Thessaloniki, through the school of Geology (department of Geophysics and Seismology). The objective of this thesis mainly focuses on issues of engineering seismology, attempting to investigate and determine parameters related to the seismic source, to the wave attenuation due to propagation path, as well as to the effect of site surface geological conditions on seismic motion. Two algorithms referring to the Generalized Inversion Technique (GIT) and Spectral Factorization of Coda waves (SFC) have been developed for the sake of this study. This thesis was carried out under a three-year scholarship provided by the State Scholarships Foundation of Greece (IKY) for the period between May 2018 – April 2021 and was partially supported by the Institute of Engineering Seismology and Earthquake Engineering (ITSAK) through the project: "*Site Response empirical Estimation using Advanced Techniques-SIREAT*" funded by the French Alternative Energies and Atomic Energy Commission (CEA), for the period between May 2021-December 2021.

At this point, I would like to express my gratitude to all those who supported my efforts and contributed to the completion of this study. Firstly, I would like to thank Prof. Panagiotis Hatzidimitriou for entrusting me and taking over the supervision of this thesis and also for his advices and remarks during its preparation. A "thousand thanks" may not be enough to express my gratitude to the Research Director of ITSAK, Dr. Nikolaos Theodoulidis, who besides his acceptance to co-supervising this thesis, was also my mentor all these four years, offering me continuous guidance, support and encouragement, as well as helping me to complete the research and the writing part of this Thesis. I would also like to deeply thank my co-supervisor and geophysicist in CEA and ISTerre, France, Dr. Fabrice Hollender, who supported me these four years and substantially helped me through his advices and knowledge. Also, I would like to thank him for the opportunity he gave me to visit him in France and to work together, as well as for the friendly "environment" who has created with his team in CEA.

Here, I would like to thank Prof. Kiratzi Anastasia and Prof. Papazachos Constantinos of Aristotle University of Thessaloniki as well as the Assistant Prof. Roumelioti Zafeiria and Prof. Sokos Efthimios of University of Patras, for accepting to be members of the examining committee of this PhD Thesis, as well as for their valuable comments and review to the manuscript, substantially contributing to the improvement of its quality.

Besides my advisors and the members of the examining committee, I would like to express my gratitude to Prof. Pierre-Yves Bard, senior scientist in ISTerre, Univ. Grenoble-Alps, for his time, for the priceless scientific help and for the hospitality offered me during my few weeks visit in ISTerre, but also for his contribution to the research paper of this study regarding the SFC application. I also thank my Professors in Seismology and Geophysics, Papazachos Constantinos and Tsourlos Panagiotis for the constructive courses in "Inversion" during my MSc studies in School of Geology of AUTH, which helped me to understand and to "build" a part of this study related to the GIT algorithm. Moreover, I would like to thank the Professor of Disaster Prevention at Kyoto University, Hiroshi Kawase, as well as Dr. Ian Main and Dr. Christophe Martin, reviewers

of Sigma-2 project, for their valuable comments and suggestions towards improving the quality of two scientific papers corresponding to the two main subjects of this thesis.

During my visit in France, I was lucky that I met researchers and collaborated with them helping me to carry out several parts of this work. Special thanks to Dr. Vincent Perron for his substantial help to understand several parts of the SFC method, as well as for his contribution to the research paper corresponding to the SFC application, to Dr. Paola Traversa for providing me data used in this thesis and for her time and the helpful advices in all the meetings that we had, to Dr. Olivier Sebe for the valuable discussion that we had for the issues of the SFC method, to Dr. Stephane Drouet for the discussion we had about ideas regarding the improvement of his GIT algorithm, as well as to Pungy Suroyo for providing some part of her programming scripts regarding the coda attenuation. I also thank Dr. Mathieu Causse, Dr. Areti Panou and Prof. Sokos Efthimios, for providing me data of specific earthquakes, used in this study. At this point, I would like to thank ITSAK for providing me the majority of the data used in the present study, but also its personnel for creating a constructive and friendly working environment during these four years. Special thanks to Kiriaki Konstantinidou, responsible of the department of Informatics of ITSAK, for her help where needed all these years, as well as to research director of ITSAK, Dr. Basil Margaris for the discussions and advices during this period. Many thanks to all the researchers and friends in ITSAK, CEA, ISTerre and of course in Aristotle University of Thessaloniki and the Seismological Station of AUTH, Nikos Chatzis, Dimitris Sotiriadis, Husshein Shible, Costas Trevlopoulos and Eleni Koufoudi, for the constructive discussions we had at several issues in seismology and for their help at several aspects of this work.

Finally, I would like to specially thank my parents Mpoula and Sakis, as well as my brother Nikolas, for the priceless and inexhaustible support in several aspects of my life and of course I will not forget to warmly thank my friends, who helped me all this time by their own way.

Regarding the structure of this thesis, the 1st chapter constitutes an Introduction to the topics of this study, as well as to the factors which are investigated, and the methodologies applied.

The 2nd chapter refers to the data used in the examined methodologies and offers information about their selection and processing.

The 3rd chapter refers to the Generalized Inversion Technique (GIT) and includes the analyses of the methodology applied to the new developed GIT algorithm. Moreover, this chapter includes the results coming from the application of this algorithm to synthetic and real data, aiming at validating the algorithm and retrieving new results for the examined region of western Greece.

The 4th chapter refers to the Spectral Factorization method of Coda waves (SFC), as well as to the Site Amplification Factor (SAF) estimation technique introduced in this study based on the SFC method. More specifically, this chapter includes the strategy followed for the SAF estimation in 10 steps, 9 of which refers to the SFC method and the modifications applied in this thesis. Moreover, the results of the application of the SAF estimation technique in data corresponding to western Greece and southeastern France, are also presented. Finally, in this chapter, the SFC method is applied to four low-to-large magnitude earthquakes so that to further investigate the

computed by SFC, Source Time Function, with respect to the already computed one by independent methodologies.

The Conclusions, as well a Discussion and perspectives of this Thesis, are included in the chapter 5.

In Appendices all the supplementary material of this study, with several matrices and Figures, is presented.

Concluding, it's worth noting that all the digital maps presented in the present manuscript were created by the use of the free software: Generic Mapping Tools (http://gmt.soest.hawaii.edu/, ***Wessel and Smith, 1998***) and that all the procedures applied for the production of the results have been carried out based on the interactive mathematical program of MATLAB software (***MATLAB, 2017***). The scripts of the GIT and the SFC algorithms developed in this study, are publicly available upon request to the author.

Parts of the 3rd and of the 4th chapter, have been published as results of this PhD thesis in scientific papers, in Journals, by Grendas et al., (2021b) and Grendas et al., (2022), respectively and as scientific papers and extended abstracts in scientific conferences, by Grendas et al., (2019), Grendas et al., (2021a) and Γρένδας et al., (2019).

ABSTRACT (in English)

Ground motion simulation and consequently seismic hazard assessment are fundamentally based on the knowledge of the following three factors; the seismic source, the wave attenuation due to the loss of energy radiated away from the source (geometrical spreading and anelastic attenuation), as well as the Site Amplification Factor (SAF), due to the local surface geological conditions (the so-called site effects). Further understanding of these three fundamental factors which control seismic ground motion at surface geological formations, constitutes one of the main challenges in engineering seismology. Especially, the SAF estimation is an important topic that can significantly contribute to even more realistic seismic hazard assessment. The Generalized Inversion Technique (GIT) of an adequate number of earthquake recordings, corresponding to a specific examined region, is a useful tool to retrieve these three factors, in frequency domain. The simultaneous computation property of GIT is desirable, since it satisfies the best solution of the three fundamental factors, so as to "match" between each other, satisfying at the same time the real data.

In this study a parametric GIT algorithm (in MATLAB), based on the one proposed by ***Drouet et al., (2008a)***, has been developed, by introducing distance and regional dependent attenuation parameters, regarding the geometrical spreading and anelastic attenuation terms, respectively. This step aims at a more detailed investigation of the attenuation path, anticipating to improve estimation of all three fundamental factors controlling seismic ground motion. The algorithm is based on a Gauss-Newton iterative inversion method, using initial realistic model parameters. Source term is parametrically investigated for seismic moment and corner frequency, which can be simultaneously controlled with respect to stress drop. A synthetic dataset, approximating a simplified real dataset, was inverted by the proposed GIT algorithm verifying its computational validity. Four tests were implemented, with or without reference conditions, providing encouraging results.

The applicability of the algorithm is supported by the inversion of a real dataset which was also examined by ***Grendas et al., (2018)*** by using a previously developed algorithm investigating a uniform attenuation model. Almost 9% reduction of the misfit between real and corresponding to the computed model, data, is achieved, showing the effectiveness of the proposed algorithm. Moreover, this GIT algorithm was applied to a real dataset of S-wave records corresponding to western Greece earthquakes, estimating parameters that control the seismic motion in this region. The regional dependent quality factor, Q_s was found to vary between 23 – 91 for one standard deviation range, with a geometric mean value equal to 45, while a distance dependent geometrical spreading attenuation factor gamma, γ, was found to be smoothly decreased from 12 km to 200 km, with values from 0.98 to 0.77. The SAF for both horizontal and vertical components in 24 sites located in the study area were also determined. Moment Magnitudes, M_w and corner frequencies, f_c, were computed for the 180 earthquakes examined, indicating an increasing trend of stress drop, $\Delta\sigma$ from 6 to 55 bars for the M_w range between 2.5 to 5.2, respectively. The estimated values of these parameters, which are in good agreement with the corresponding ones based on other methodologies, indicate the reliability of the GIT algorithm, encouraging its further development

and wider application. This is also essentially supported by the quite low total average logarithmic misfit (~0.17) between the observed and synthetic FAS. The latter ensures that the attenuation and site factors computed from GIT can assure, among other things, improvement of seismic hazard assessment, when considering input parameters to the stochastic S-wave simulations.

In contrast to GIT which requires an adequate set of records corresponding to several earthquakes and stations, there are other methodologies attempting to estimate SAF or/and Source Time Function (STF) of an earthquake at a specific site, either by using numerical simulation tools or empirical approaches, without requiring a set of seismic records. For instance, a widely used empirical method for SAF estimation is the "Standard Spectral Ratio" (SSR) technique ***(Borcherdt, 1970***) based on the Fourier Amplitude Spectra (FAS) ratio of seismic records at a target site to the corresponding ones at a nearby amplification-free "rock" site (reference site). The main limitation of this method lies in the availability of a reference site relatively close to the target one. In this study, a SAF estimation technique at a target site in relation to a distant reference site is also presented and evaluated, through a new developed algorithm. This algorithm is based on the retrieval of the minimum phase Source Time Function (mpSTF) at a pair of examined sites (target-reference), based on the Spectral Factorization analysis of Coda waves (SFC) proposed by ***Sèbe et al., (2005, 2018)***. The so-derived mpSTF is considered as a convolution of the actual source function with the SAF of the site, so that the FAS ratio between the mpSTF, derived at one site (target) and at a distant reference site, should be an estimate of the target SAF. The latter is confirmed in this study. Under the conditions of a common STF at the examined sites and of similar coda waves excitation factor, the ratio of the FAS of the mpSTFs (target over reference site) can safely approach the actual SAF, at least when target-reference distance is up to ~60 km and provides satisfactory results at longer distances. This technique was applied to 24 sites in western Greece, used also in the GIT application and to 18 in southeastern France, in relation to 4 and 3 reference sites, respectively, located at varying distances from the target ones (from 0.4 km to 110 km). More than 700 STFs were calculated for 89 earthquakes ($3.9 \leq M \leq 5.2$) in western Greece, while 144 STFs were computed for 58 earthquakes in southeastern France ($3.2 \leq M \leq 5.2$). Finally, the average SAFs were computed and compared with those determined by GIT applications, as well as with those computed by SSR, where possible, demonstrating the reliability of the proposed technique in estimating site effects (SAF).

ABSTRACT (in Greek)

Η προσομοίωση της εδαφικής κίνησης και κατά συνέπεια η εκτίμηση της σεισμικής επικινδυνότητας βασίζονται ουσιαστικά στη γνώση των ακόλουθων παραμέτρων: της σεισμικής πηγής, της απόσβεσης των κυμάτων εξ αιτίας της απομείωσης της διαδιδόμενης ενέργειας σε θέσεις απομακρυσμένες από την πηγή (γεωμετρική εξάπλωση κύματος και ανελαστική απόσβεση), καθώς επίσης του παράγοντα της τοπικής εδαφικής ενίσχυσης της θέσης μελέτης εξαιτίας των τοπικών επιφανειακών γεωλογικών συνθηκών (γνωστού ως site effects). Η περαιτέρω κατανόηση των τριών αυτών παραγόντων οι οποίοι διαμορφώνουν την εδαφική σεισμική κίνηση σε επιφανειακούς γεωλογικούς σχηματισμούς αποτελεί μία από τις βασικές «προκλήσεις» στην τεχνική σεισμολογία. Ειδικότερα, η εκτίμηση του παράγοντα "site effects" αποτελεί ένα σημαντικό πεδίο μελέτης το οποίο μπορεί να συνεισφέρει σημαντικά προς την κατεύθυνση της πιο ρεαλιστικής εκτίμησης της σεισμικής επικινδυνότητας. Η Τεχνική της Γενικευμένης Αντιστροφής (Generalized Inversion Technique: GIT) ενός επαρκούς αριθμού σεισμικών καταγραφών, οι οποίες αντιστοιχούν σε μία συγκεκριμένη περιοχή μελέτης, είναι ένα χρήσιμο εργαλείο για τον υπολογισμό των τριών παραγόντων της σεισμικής κίνησης, στο πεδίο των συχνοτήτων. Ο ταυτόχρονος υπολογισμός των παραπάνω τριών παραγόντων στη GIT επιδιώκεται, στοχεύοντας στον καλύτερο προσδιορισμό αυτών, έτσι ώστε να αλληλοεπιδρούν μεταξύ τους «ικανοποιώντας» στο μέγιστο βαθμό τα πραγματικά δεδομένα.

Στη μελέτη αυτή αναπτύχθηκε ένας παραμετρικός αλγόριθμος GIT, βασισμένος σε εκείνον που προτάθηκε από τους ***Drouet et al., (2008a)***, εισάγοντας παραμέτρους απόσβεσης εξαρτώμενες από την απόσταση και την εξεταζόμενη περιοχή, που αφορούν αντίστοιχα στη γεωμετρική εξάπλωση και στην ανελαστική απόσβεση των σεισμικών κυμάτων. Αυτό το βήμα στοχεύει σε μία πιο λεπτομερή διερεύνηση των ιδιοτήτων της απόσβεσης του δρόμου διάδοσης, προσδοκώντας στη βελτίωση εκτίμησης των τριών παραγόντων που διαμορφώνουν τη σεισμική κίνηση. Ο αλγόριθμος αυτός είναι βασισμένος στη μέθοδο της επαναληπτικής αντιστροφής Gauss-Newton, χρησιμοποιώντας αρχικές τιμές για τις παραμέτρους που εξετάζονται. Η συνάρτηση της σεισμικής πηγής εξετάζεται παραμετρικά για τη σεισμική ροπή και τη γωνιακή συχνότητα, οι οποίες μπορούν να αλληλοεπιδρούν ανάλογα με την πτώση τάσης. Ένα συνθετικό δείγμα δεδομένων το οποίο προσεγγίζει ένα αντίστοιχο πραγματικό, αντιστράφηκε με βάση τον προτεινόμενο αλγόριθμο GIT, επαληθεύοντας την αξιοπιστία και υπολογιστική του δυνατότητα. Εκτελέστηκαν τέσσερις δοκιμές, με ή χωρίς συνθήκη αναφοράς, που οδήγησαν σε ενθαρρυντικά αποτελέσματα.

Η τεκμηρίωση και αξιοπιστία του νέου αλγορίθμου βασίσθηκε επιπλέον στην αντιστροφή ενός δείγματος πραγματικών δεδομένων, το οποίο είχε μελετηθεί από τους ***Grendas et al., (2018)***, χρησιμοποιώντας ένα προηγούμενο αλγόριθμο GIT, υποθέτοντας ωστόσο ένα ενιαίο μοντέλο απόσβεσης στην περιοχή μελέτης. Με την εφαρμογή του νέου αλγορίθμου σε σχέση με του προηγούμενου, επιτεύχθηκε μείωση ~9% της μέσης διαφοράς μεταξύ των πραγματικών δεδομένων και εκείνων που αντιστοιχούν στις παραμέτρους που διερευνώνται (αποκαλούμενη ως misfit), επιβεβαιώνοντας την αποτελεσματικότητα του προτεινόμενου αλγορίθμου. Ακόμη, ο αλγόριθμος αυτός εφαρμόστηκε σε ένα δείγμα πραγματικών δεδομένων από σεισμικές

καταγραφές διατμητικών (S) κυμάτων στη Δυτική Ελλάδα, εκτιμώντας τις παραμέτρους που διαμορφώνουν τη σεισμική κίνηση σε αυτή την περιοχή. Ο χωρικά εξαρτώμενος παράγοντας ποιότητας, Q_s υπολογίστηκε μεταξύ 23-91 για εύρος μία τυπικής απόκλισης, με γεωμετρική μέση τιμή 45, ενώ ο εξαρτώμενος από την απόσταση παράγοντας της γεωμετρικής εξάπλωσης, γ, βρέθηκε να μειώνεται σταδιακά από τα 12 km στα 200 km, με τιμές από 0.98 μέχρι 0.77. Επιπλέον υπολογίστηκαν οι παράγοντες ενίσχυσης (Spectral Amplification Factors: SAF) των οριζόντιων και των κατακόρυφων συνιστωσών σε 24 θέσεις σταθμών επιταχυνσιογράφων στην περιοχή μελέτης καθώς και τα μεγέθη σεισμικής ροπής, M_w και οι γωνιακές συχνότητες, f_c των 180 εξεταζόμενων σεισμών, υποδεικνύοντας μία αύξηση της πτώσης τάσης, $\Delta\sigma$, από 6 bar σε 55 bars για εύρος μεγεθών M_w 2.5 - 5.2. Οι τιμές αυτών των παραμέτρων βρίσκονται σε καλή συμφωνία με τις αντίστοιχες από άλλες μεθοδολογίες, και υποδεικνύουν την αξιοπιστία του νέου αλγορίθμου GIT, ενθαρρύνοντας την περαιτέρω ανάπτυξή του και την ευρεία εφαρμογή του. Τα παραπάνω υποστηρίζονται επί της ουσίας από την αρκετά χαμηλή τιμή της λογαριθμικής τιμής του μέτρου προσδιορισμού της διαφοράς (misfit, ~0.17), μεταξύ των παρατηρούμενων και των συνθετικών φασμάτων Fourier. Η τελευταία παρατήρηση διασφαλίζει τη ρεαλιστική εκτίμηση των παραγόντων απόσβεσης και της τοπικής εδαφικής ενίσχυσης που προέκυψαν από την αντιστροφή, με συνέπεια η χρήση τους ως δεδομένων εισόδου σε στοχαστικές προσομοιώσεις, να οδηγήσει σε βελτίωση εκτίμησης της σεισμικής επικινδυνότητας.

Σε αντίθεση με τη μεθοδολογία της Γενικευμένης αντιστροφής (GIT), η οποία απαιτεί ένα επαρκές δείγμα σεισμικών καταγραφών σε διάφορους σεισμούς και σταθμούς, υπάρχουν μεθοδολογίες που επιδιώκουν την εκτίμηση του παράγοντα SAF ή/και της Χρονικής Συνάρτησης της Σεισμικής Πηγής (Source Time Function: STF), ενός σεισμού σε μία θέση, είτε μέσω αριθμητικών εργαλείων προσομοιώσεων ή εμπειρικών τεχνικών, χωρίς τη χρήση μεγάλου δείγματος καταγραφών. Για παράδειγμα, μία ευρέως χρησιμοποιούμενη εμπειρική μέθοδος της εκτίμησης του παράγοντα SAF, είναι η τεχνική του φασματικού λόγου (Standard Spectral Ratio: SSR) ***(Borcherdt, 1970***), βασισμένη στο λόγο των φασματικών πλατών Fourier σεισμικών καταγραφών σε μία θέση μελέτης (target site) και σε μια γειτονική θέση "βράχου", χωρίς ενίσχυση (reference rock site). Ο κύριος περιορισμός αυτής της μεθοδολογίας είναι η διαθεσιμότητα ενός σταθμού αναφοράς σχετικά κοντά στη θέση μελέτης. Στην Διατριβή αυτή παρουσιάζεται και αξιολογείται μία τεχνική εκτίμησης του παράγοντα SAF σε μία θέση μελέτης, σε σχέση με έναν απομακρυσμένο σταθμό αναφοράς, μέσω της ανάπτυξης ενός νέου αλγορίθμου. Ο αλγόριθμος αυτός βασίζεται στον υπολογισμό της ελάχιστης φάσης της Χρονικής Συνάρτησης της Σεισμικής πηγής (minimum phase Source Time Function: mpSTF), σε δύο θέσεις (θέση μελέτης και αναφοράς), χρησιμοποιώντας τη μέθοδο φασματικής παραγοντοποίησης των κυμάτων ουράς μίας σεισμικής καταγραφής (Spectral Factorization of Coda waves: SFC), η οποία προτάθηκε από τους ***Sèbe et al., (2005, 2018)***. Η υπολογισμένη mpSTF θεωρείται ως η συνέλιξη μεταξύ της STF του σεισμού και του SAF στη θέση μελέτης, και κατά συνέπεια ο λόγος μεταξύ των mpSTFs που υπολογίζονται σε μία θέση μελέτης και σε έναν απομακρυσμένο σταθμό αναφοράς θα πρέπει να οδηγεί στην εκτίμηση του SAF στην εκάστοτε θέση μελέτης. Αυτή η εκτίμηση επιβεβαιώνεται στην παρούσα εργασία. Υπό την προϋπόθεση της κοινής STF μεταξύ των εξεταζόμενων θέσεων,

αλλά και του κοινού παράγοντα διασποράς των κυμάτων ουράς, ο λόγος μεταξύ των FAS των mpSTFs στις θέσεις μελέτης και αναφοράς, μπορεί να προσεγγίσει ικανοποιητικά τον παράγοντα SAF, τουλάχιστον όταν η απόσταση μεταξύ των δύο σταθμών είναι ~60 km, ενώ παρέχει ικανοποιητικά αποτελέσματα για μεγαλύτερες αποστάσεις. Η τεχνική αυτή εφαρμόστηκε σε 24 θέσεις σταθμών στη Δυτική Ελλάδα, οι οποίοι χρησιμοποιήθηκαν και στην εφαρμογή του νέου αλγορίθμου GIT, καθώς και σε 18 θέσεις σταθμών στη Νοτιοανατολική Γαλλία, σε σχέση με 4 και 3 σταθμούς αναφοράς αντίστοιχα, οι οποίοι βρίσκονται σε αποστάσεις από τις θέσεις μελέτης, που κυμαίνονται από 0.4 km μέχρι 110 km. Περισσότερες από 700 STFs υπολογίστηκαν για 89 σεισμούς ($3.9 \leq M \leq 5.1$) στη Δυτική Ελλάδα, ενώ 144 STFs υπολογίστηκαν για 58 σεισμούς στη Νοτιοανατολική Γαλλία ($3.2 \leq M \leq 5.2$). Τελικά, οι μέσες τιμές των SAFs, υπολογίστηκαν και συγκρίθηκαν με εκείνες που προσδιορίστηκαν από την εφαρμογή τόσο του GIT, όσο και της τεχνικής SSR, όπου αυτό ήταν δυνατόν, υποδεικνύοντας την αξιοπιστία του προτεινόμενου αλγορίθμου στον υπολογισμό της επίδρασης των τοπικών εδαφικών συνθηκών(SAF) στη σεισμική κίνηση.

1 GENERAL INTRODUCTION

Earth is usually called as a "living" planet, not only because of the organic processes directly related to life but also due to those ones related to its geologically active "character" and expressed by plethora of natural phenomena. Large earthquakes is one of them caused by Earth's crust activity and their impacts have been related, many times, to what is generally called natural disasters. It's worth noting that between 1998-2017, nearly 750 thousand human losses were globally recorded (https://www.who.int/health-topics/earthquakes) and more than 125 million people were affected by earthquake consequences. Structural damages which are directly related to the earthquakes, and the indirect effects of the large events (e.g. landslides, tsunamis, soil liquefactions, or even other secondary effects like fires and floods), constitute the main reasons of human losses and costly damages. Reduction of devastating earthquake impacts constitutes a challenge that has to be achieved in parallel to the prevailing daily needs of human living. Towards this direction, understanding of seismic hazard in a region of interest, in combination with the vulnerability of structures, may provide realistic seismic risk assessment, leading to the rationale decisions towards earthquake impact mitigation.

In seismic hazard analysis, quantification of ground motion intensity measure at a specific site can be expressed either in a probabilistic and/or deterministic way. The first one is expressed by the quantification of the probability that a specified level of ground motion intensity will be exceeded at least once at the site during a specified exposure time, while the latter is controlled by ground motion simulation analysis at the specific site, based on several scenarios (among others; ***Kijko, 2011***). Regarding the deterministic seismic hazard assessment, ground motion simulation analysis is directly expressed as a function of three basic factors, i.e. the seismic source, wave attenuation due to the propagation path properties and site specific amplification due to the particular surface geological conditions (the so-called site effects) (e.g. **Figure 1**).

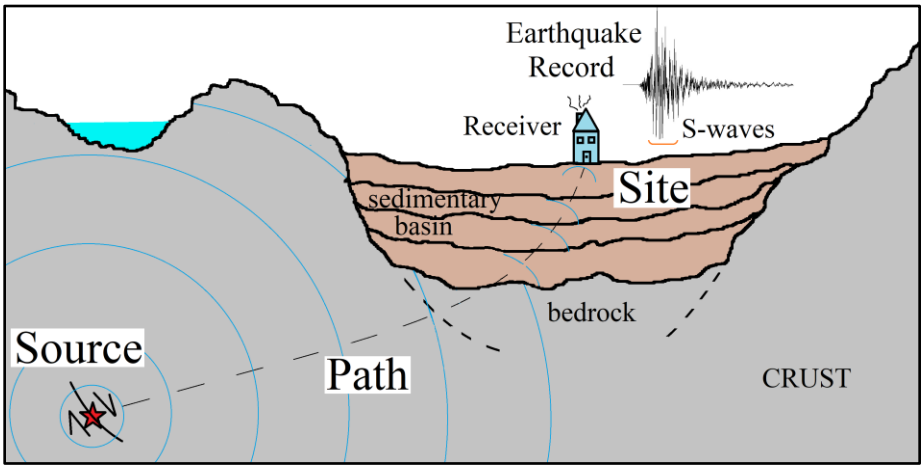

Figure 1. An unscaled sketch of the generation process of an earthquake, with seismic waves coming from the source (fault), attenuated by the propagation path (geometrical spreading and intrinsic-anelastic properties of the crust) and affected (e.g. amplified) by the surface site-specific geological conditions (e.g. a sedimentary basin).

The main object of this study focuses on further understanding of these three factors that control the seismic motion, as well as on their interpretation. The main goal of this thesis is the modification and the improvement in analysis of two methodologies which use specific parts of earthquake records as data, aiming at detailed investigation of these three fundamental factors. This goal is pursued to be achieved through the development of two algorithms, corresponding to the two methodologies. By the application of these algorithms to real datasets, validation of their implementation as well of their reliability is pursued. The two methodologies refer to the Generalized Inversion of the S-wave seismic motion (the most energetic part of an earthquake record), in frequency domain, and to the Spectral Factorization analysis of coda waves (the waves that arrive late in time, after the S and surface waves) both in frequency and time domain.

During the last years, an important effort towards the direction of deeper comprehension of the three fundamental factors (seismic source, attenuation path, site effects) affecting seismic ground motion is emerging. The properties and characteristics of these factors are theoretically and experimentally investigated. A better understanding of them can directly or indirectly contribute to many topics of seismology, improving ground motion models and reducing epistemic uncertainties. In order to estimate these factors, several methods have been developed. Some of these methods independently investigate each factor, while others simultaneously, taking into account the existing trade-off between them. For example, two widely studied and used techniques to estimate site predominant frequencies which present intense spectral amplification and at some cases are capable of estimating even the absolute site spectral amplification are: (i) the Horizontal-to-Vertical Spectral Ratio (HVSR) based either on ambient noise (***Nakamura, 1989***) or on body S-waves (***Lermo and Chavez-Garcia, 1993***) and (ii) the Standard Spectral Ratio (SSR) applied also on body S-waves (***Borcherdt, 1970***) or/and indirectly on ambient noise (among others: ***Kagami et al., 1982; Milana et al., 1996; Perron et al., 2018a***). Other methods investigate mainly the seismic Source Time Function (STF) using P or S body waves, based on deconvolution of empirical Green's functions (e.g. ***Hartzell, 1978; Mueller, 1985; Hough et al., 1991***), controlled by a deterministic attenuation path model. The above methods are some examples where the factors affecting seismic motion are individually studied.

In contrast to these methods, in recent years, the Generalized Inversion Technique (GIT), constitutes a tool in seismology aiming at a simultaneous, full, or partial computation of the seismic source, the S-wave attenuation due to anelastic properties and geometry of the path and the Site Amplification Factor (*SAF(f)*). GIT introduced and firstly applied by ***Andrews, (1986)***, ***Iwata and Irikura, (1988)*** and ***Castro et al., (1990)***, is based on the idea of spectral decomposition of the Fourier Amplitude Spectra (FAS) retrieved from several earthquake records, into the three above fundamental factors. In fact, GIT aims at solving a system of equations, to retrieve these three factors, by inverting the FAS of earthquake records (the data), having as a precondition the existence of common seismic sources, recording sites and ray path area of the recordings used. However, the solution of a system of equations like this, is not simple since it is considered as a non-linear system, where the equations which are to be solved, cannot be directly written as a linear combination of the unknown variables, expressed by matrices. For this reason, the two

following approaches of GIT applications, the non-parametric and the parametric one, as well as a semi-parametric approach, have been introduced, aiming at the solution of this system of equations.

The three GIT approaches, mentioned above, study the *SAF(f)* for each distinct examined frequency, in a non-parametric form, since *SAF(f)* is not controlled by a certain function, but affected by various factors (e.g. S-wave velocity, medium density distribution, geometry of surface geological formations, etc.). The non-parametric GIT approach aims at inverting for the source and attenuation path factor, without adopting any specific theoretical or empirical function. This strategy is based on reference conditions regarding the shortest epicentral distance of the earthquake records used, or/and the reference considered station(s). Several GIT algorithms based on this strategy have been developed and widely used during the past years (among others: ***Edwards et al., 2008; Oth et al., 2009; Bindi et al., 2009***; ***Klin et al., 2018***; ***Ortiz-Alemán et al., 2017***; ***Davatgari et al., 2021***, for the United Kingdom, Romania, central Italy, northeast Italy, central Mexico and northern Iran, respectively). Semi-parametric GIT algorithm has been applied by ***Nakano et al., (2015)*** for Japan, and is similar to the non-parametric one with the exception that the attenuation path factor is parametrically studied based on a specific function. On the contrary, parametric GIT is initially controlled by theoretical functions for the seismic source and attenuation path factors without the use of reference conditions, since initial reasonable empirical values for the investigated parameters, are used. In this approach, inversion is implemented in one step, based on non-linear least squares iterative inversion algorithms (e.g. *Levenberg-Marquard*, *Gauss-Newton* method, among others: ***Mandal and Dutta, 2011***; ***Drouet et al., 2008a***, respectively).

Parametric GIT, which is the one GIT approach used in this study, is based on the appropriate mathematical process of ***Gauss-Newton*** iterative inversion algorithm, analytically described in ***Tarantola, (2004)***. This inversion technique uses an initial parameter model and its *a priori* covariance values in order to converge to a reasonable solution of the non-linear system of equations. This solution satisfies at the same time the lowest misfit between real and computed by the inverted model, data, and between the initial and the inverted model parameters, taking into account their *a priori* covariance values. ***Drouet et al., (2008a)***, first developed and applied a parametric GIT algorithm based on a ***Gauss-Newton*** inversion method, in order to estimate *SAF(f)* factors for the French accelerometric network stations. At the same time, they determined an average attenuation model (geometric and intrinsic-anelastic terms) for the examined area, as well as the moment magnitudes and corner frequencies of the earthquakes used. Following this study, a series of applications of the parametric GIT, have taken place during recent years, for various datasets at several regions worldwide. ***Drouet et al., (2008b)*** for the Lefkas island (Greece), ***Drouet et al., (2010)*** for three different areas in the broader France area (Rhine Graben, Alps and Pyrenees), ***Drouet et al., (2011)*** for local earthquakes recorded at French West Indies and ***Drouet and Assumpção, (2013)***, for records selected from stations located in eastern Brazil, are four representative studies where parametric GIT algorithm was successfully applied. ***Grendas et al., (2018)*** applied this method for a large dataset of seismic recordings in Greece, with moderate to

large magnitude earthquakes, obtaining results in satisfactory agreement with the corresponding ones based on different methods. The above studies confirm that this method constitutes an effective seismological "tool" in order to estimate the main factors controlling earthquake ground motion. However, the improvement of the GIT, towards reduction of uncertainties and of "extreme" computed parameters diverging from reasonable ones, still remains an issue to be solved and is examined and discussed in the present thesis.

For this reason and based on the GIT algorithm introduced by ***Drouet et al., (2008a)***, the study of a more detailed attenuation model was considered in this thesis as a reasonable step, toward improving this algorithm. This improvement is going to be defended by the reduction of the misfit between real and computed from the inverted model data, as well as by better estimating the three factors that control the seismic motion. A new GIT algorithm was developed for the sake of this thesis, referring to a more detailed attenuation model based on two different approaches. The first one corresponds to the inversion of data for a distance dependent geometrical spreading factor at specific pre-defined distance-ranges, instead of a single one for the entire region. The second one refers to the simultaneous inversion of a regional dependent quality factor, *Q(f)*, following the concept of a pseudo 2-D tomography, based on the division of the examined region in subareas ("cells") and on their investigation, pursuing to detect the lateral variabilities of *Q(f)*. The achievement of the computation of a desirable lower possible misfit between the real and synthetic from the inversion data in a case study, encourages the more reliable "generation" of S-wave FAS of a potential higher magnitude future earthquake, at the examined sites, in forward stochastic modeling, based on the computed path and site parameters. In other words, the better understanding of the factors affecting the seismic motion in an examined region, can lead to an essential contribution to ground motion simulation and consequently to deterministic Seismic Hazard assessment.

Regarding the site effect (*SAF(f)*) assessment, which is considered as a main factor that can significantly affect the expected seismic motion at a site, several efforts have been made towards this direction. Some of them imply theoretical studies (e.g. ***Kennett and Kerry, 1979***; ***Bard and Gariel, 1986***), which however require site specific information about the geological structure (e.g. 1D, 2D, or 3D shear wave velocity structure, geometry of the examined basin, density distribution, etc.). Alternatively, various empirical techniques have been developed to estimate the SAF based on actual earthquake records.

One of the most commonly used *SAF(f)* estimation techniques is the so-called Standard Spectral Ratio (SSR) ***(Borcherdt, 1970***). This technique provides the *SAF(f)* of a target site by dividing the Fourier Amplitude Spectrum of an earthquake S-wave record of this site by the corresponding one at a nearby rock site. The latter is the so-called "reference" and is considered as an amplification "free" site. The valid implementation of this technique is based on the following three fundamental conditions.

The first one is related to the assumption of a "free" of amplification surface reference (rock) site. This assumption is used when the nearby surface rock site exhibits Vs_{30} higher than ~760 m/s, so as to consider that its physical properties (e.g. shear wave velocity, density, etc) and

consequently its seismic behavior remains similar to the one in bedrock (below the target site), which is more likely to be considered as absolute "free" of amplification (Vs_{30} > ~3000 m/s). However, although this assumption has been widely used in recent years at several SSR application studies, ***Steidl et al., (1996)*** trying to define "*what is a reference site*", have outlined the potentially non absolute reference behavior of the surface rock sites. This behavior seems to be related to the near-surface weathering and fractured nature of the outcrop bedrock that causes decrease of shear-wave velocity. This is presented as spectral amplification of its response by a factor of 2-4, mainly for frequencies above 2 to 5 Hz, diverging from their expected flat response behavior. The same observation has been obtained by ***Cadet et al., (2012)*** by examining the SSR technique between borehole bedrock and surface outcrop sites, at several locations in Japan, after taking into account the up and down-going waves, affecting the borehole site. ***Cadet et al., (2012)*** proposed a simple SAF correction for the surface rock site, with respect to the pure bedrock site, which however requires, among others, the S-wave velocity profile, down to the depth of the bedrock. Based on the above and taking into account that it is not always feasible to use a station installed on the absolute reference bedrock site, for the SSR application, or to know the bedrock depth and the S-wave velocity profile, the surface bedrock outcrop site, should be cautiously used as reference one.

The second condition of the valid SSR application refers to the use of two recordings at the examined sites, corresponding to the same earthquake, so as to satisfy the common seismic source factor, allowing thus its elimination at the Spectral Ratio computation. The third one refers to the reasonable assumption of the common propagation path of the seismic waves, which arrive at the target and the reference site, from the same source, allowing its elimination as well. The proper application of the SSR technique depends on the aforementioned conditions and constraints.

Except for the GIT progress, the second goal of this study is to assess the performance of a new SAF estimation technique, following the SSR application rationale (***Borcherdt, 1970***) which is based on the three conditions mentioned above, but allowing the use of a distant reference station. By this way the adjacent stations requirement of the SSR technique can be overcome. This technique requires a more sophisticated processing, based on the spectral factorization method of coda waves (SFC), proposed by ***Sèbe et al., (2018)***, to recover the Source Time Function (STF) of the examined earthquake. The coda waves are the late in arrival time, low-energy part of a seismic record which are also affected by site effects. The STF recovered at a given site based on the SFC method is theoretically the "apparent STF" resulting from the convolution of the real STF and the SAF, in time domain. The latter is investigated for its validity in this study. The comparison of the Fourier Amplitude Spectra (FAS) computed from the "apparent STF" of the same earthquake retrieved at two different sites could thus theoretically reveal their relative amplification. In case that one of the two sites, is a reference one, as in SSR technique, then the SAF of the other, "target" site could be estimated from the ratios of the FAS of the "apparent STF".

The STF estimation methodology developed by ***Sèbe et al., (2018)***, can be implemented as a single-record analysis, which is a significant advantage of its application and also for the application of the SAF estimation technique proposed here, in contrast to the GIT idea which requires an adequate amount of data. Briefly, the SFC analysis is applied on the coda signal for

which the frequency dependent attenuation factor can be determined as firstly introduced by ***Aki, (1969)***. This factor configures the exponential decrease of the energy arriving late in time at a site from the seismic source, after seismic waves undergo propagation reflections-refractions-diffractions at the crust scatterers (faults, folds, Vs discontinuities, etc), similar to the "echo" phenomenon (e.g. **Figure 2**). Thereafter, this factor may then be removed from the coda wave record in time domain, as proposed by ***Margrave, (1998)*** and ***Margrave et al., (2011)***, leading to a stationary waveform. This waveform is characterized by the two following facts: (a) Although it is corrected for the frequency dependent attenuation factor, it is still scaled by a constant (frequency independent) scaling factor directly controlled by the average shear wave velocity of the propagation path and by the mean free path factor (***Sato, 1978***) which control the coda excitation factor. (b) This stationary waveform theoretically consists of multiple echoes of the same STF wavelet, arriving late in time after the direct S-waves(***Aki, 1969; Aki and Chouet, 1975; Sato, 1977***). Based on these two facts, ***Sèbe et al., (2018)*** utilized the "stationarized" signal of the corrected coda waveform, to retrieve the STF spectrum according to ***Wiener-Khinchin*** theorem and taking its minimum phase wavelet through the spectral factorization method.

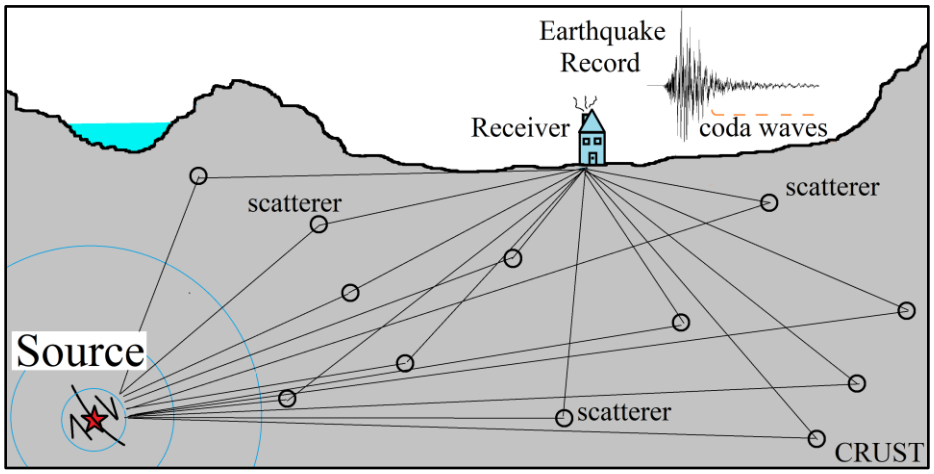

Figure 2. An unscaled sketch of the generation process of the coda waves, based on the single scattering model, as waves arriving at the receiver after reflections-refractions-diffractions in the crust scatterers (following the corresponding sketch of ***Lacombe et al., (2003)***.

The above approach was firstly used by ***Sèbe et al., (2005)***, to retrieve the STF characteristics of the fatal Kursk submarine explosion, occurred in 12/8/2000. That study allowed to recover a rather complex, high-frequency STF, including an initial explosion, a consecutive bubble pulse, and their reflections at the sea surface. Later, ***Sèbe et al., (2018)*** analytically applied the SFC method to a moderate magnitude earthquake, trying to detect the STF characteristics. Moreover, ***Sèbe et al., (2014)*** in their STF estimation experimental study, for three earthquakes in the Eastern France, outlined the possibility to detect the existence of site effect, into the "apparent STF" FAS, obtained separately for each record at each component. This observation comes from the Horizontal to Vertical Spectral Ratio (HVSR) computation of the "apparent STF" FAS.

The SAF estimation technique proposed here is based on the same approach as in ***Sèbe et al., (2018)***, i.e. the comparison of the "apparent STF" wavelets retrieved at two distant sites (target and reference) based on seismic coda wave records. This comparison may lead to the SAF estimation at the target site under the following three fundamental conditions:

(1) Use of the same earthquake records at the pair of examined stations (reference and target site), like in SSR technique (***Borcherdt, 1970***), without the restrictive requirement of a nearby reference station.

(2) An isotropic Source Radiation pattern must be considered, so that the FAS shape of the computed STF, is unique and the proposed spectral comparison is valid. This can be reasonably considered as true for relatively low magnitude earthquakes ($M_L < 5.0$) without prominent rupture directivity, for which the STF can be considered as a simple pulse wavelet. Moreover, scattered waves in the coda, allow to smooth out the azimuthal dependence linked to radiation pattern and focal mechanism.

(3) A similar scaling can be assumed for the stationary coda waveforms at reference and target sites (i.e. similar average shear wave velocity v_s along the propagation path, and similar scattering properties characterized by the mean free path, l, (***Sato, 1978***)). The latter condition must be considered in case where the values of v_s, and l are unknown, so that to be eliminated as common parameters in the spectral ratio. Understanding the validity of this last condition constitutes one the main objective of the present study.

The study area is examined both by the GIT and the SFC methods in order to retrieve information on Site Amplification Factors, at the examined sites, as well as on attenuation and seismic source factors, is western Greece region, including the Ionian islands, Cephalonia, Lefkas, Zakynthos and Ithaca (**Figure 3**). This area and especially the one including the Ionian islands, is one of the most seismically active regions in Europe, characterized by the quite high seismic parameter, $b = 0.9\text{-}1.1$, of the frequency-magnitude relation (***Gutenberg and Richter, 1944***), which has been detected during the past years for the broader area of Greece (among others; ***Hatzidimitriou et al., 1985; Papazachos, 1990; Stavrakakis and Drakopoulos, 1995; Papazachos and Kiratzi, 1996; Papazachos, 1999; Papaioannou and Papazachos, 2000; Vamvakaris et al., 2016a***). Except for the large number of low magnitude earthquakes occurred during the past years, plethora of moderate to large magnitude earthquakes have been also occurred in this region (based on the catalogues of ***Papazachos et al., 2000; Burton et al., 2004*** and ***Makropoulos et al., 2012***). These earthquakes are related to the tectonic processes of the wider active boundary between Africa and Eurasia tectonic plates (***Papazachos et al., 1998; Sachpazi et al., 2000***) (**Figure 3**). The collision of these two major tectonic plates lead to the three following tectonically active regimes which dominate this area: (i) the Cephalonia Transform Fault zone ("CTF") (***Scordilis et al., 1985***) and its northern extension to Lefkas island (***Louvari et al., 1999; Svigkas et al., 2019***), (ii) the reverse fault zone, mainly controlled by horizontal compressional strains (***Hatzfeld et al., 1995; Papazachos et al., 1999; Tselentis et al., 2006***) and which is related to the upper part of the S-W Hellenic Arc ("HA") subduction and to its northern Transition to the continental collision tectonic regime ("CC") (***Papazachos et al., 1999; Pérouse et al., 2017***) and (iii) the normal faults

zone of the Gulf of Patras (among others: ***Melis et al., 1989***), which belong to the wider back-arc extension zone (***Flerit et al., 2004; Papanikolaou and Royden, 2007***) (**Figure 3**).

The seismicity potential of the wider western Greece region is quite high as has been estimated during the past years by plethora of studies (among others ***Makropoulos and Burton, 1985; Papazachos et al., 1993; Papazachos, 1999***) and is characterized by the highest seismic hazard level zone (Zone III, a_g=0.36g) in Greece (***EAK, 2003***). Most recent studies (among others: ***Koutrakis et al., 2002; Burton et al., 2003; Danciu et al., 2007; Tselentis et al., 2010; Vamvakaris et al., 2016b***), confirmed this quite high seismicity potential of western Greece and Ionian islands, through the generation of seismic hazard maps based on probabilistic and deterministic approaches, in terms of Peak Ground Accelerations (PGA), Peak Ground Velocities (PGV), macro-seismic intensities, strong motion duration, energy release, etc. ***Papoulia et al., (2014)***, outlined this high seismicity regime and tectonic activity based on seismotectonic data, on microseismicity and on several large magnitude earthquakes occurred before 2008.

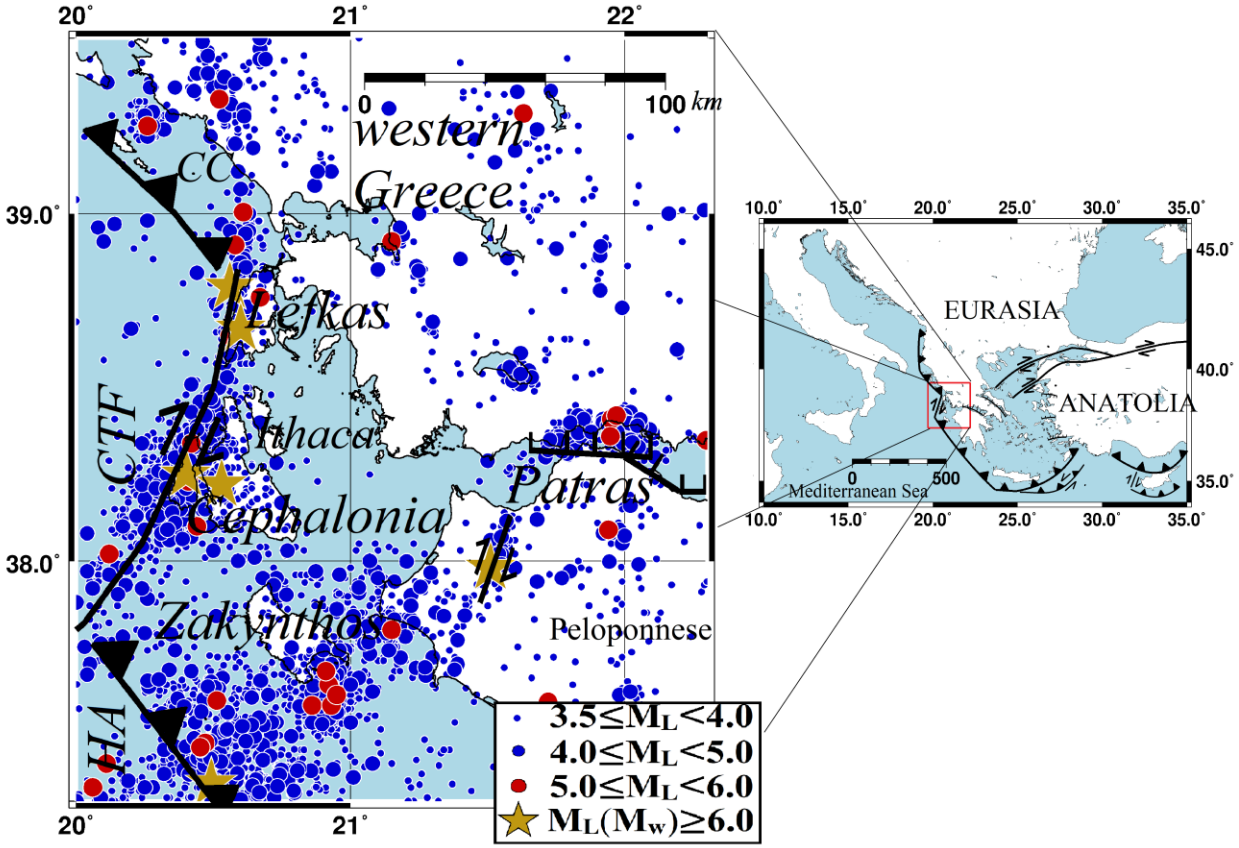

Figure 3. The seismicity (earthquake epicenters) of the western Greece, for the last ~21 years (01/01/2000 - 15/7/2021). Cephalonia Transform Fault zone ("CTF") and part of the Hellenic Arc ("HA") and of the Continental Collision (CC), are also depicted. (The right figure grossly displays the broader tectonic regime of the neighboring region). The borders of the active tectonic regime in both Figures are based on ***Papazachos et al., (1998)*** and on ***Pérouse et al., (2017)***.

Characteristic of the high seismicity potential in this area (~200 x 200 km) is the occurrence of 6 earthquakes with moment magnitudes, $M_w \geq 6.0$ and of their seismic sequences, within a time period of 16 years (2003-2018). Two of these earthquakes ($M_w = 6.0$ and 6.1, of 26/01/2014 and 03/02/2014, respectively) took place in Cephalonia island (***Sokos et al., 2015; Theodoulidis et al., 2016***) and related to the dextral strike-slip activity of the "CTF" zone (**Figure 3**) and two ($M_w = 6.2$ and 6.4, of 14/08/2003 and 17/11/2015, respectively) to its extension in western Lefkas island (***Benetatos et al., 2005; Lekkas et al., 2018; Sokos et al., 2016***). The highest magnitude earthquake of this period ($M_w = 6.8$, of 28/10/2018) occurred near the subducting slab of the N-W Hellenic Arc (HA), 30 km S-W of Zakynthos island (***Sokos et al., 2020***), while an event of $M_w = 6.5$ (08/06/2008) (***Margaris et al., 2010***), occurred in N-W Peloponnese (S-W of Patras), at the Achaia dextral strike-slip Fault zone (***Kiratzi, 2014***), due to the upper-plate slip partitioning related to the end of the Hellenic Arc and to the N-S crustal extension dominated in Gulf of Corinth (***Ganas et al., 2009; Kassaras et al., 2016***). Beside the 6 aforementioned earthquakes with $M_w \geq 6.0$, the most recent, high magnitude earthquake ($M_w = 5.8$, 21/03/2020), occurred in western Greece mainland (N of Lefkas island) due to a thrust fault activity (***Svigkas et al., 2021***). From the aforementioned, it becomes clear, that the broader western Greece area constitutes a natural "laboratory", whose data can be used in appropriately developed methodologies, like the GIT or/and SFC to reveal significant information of source, attenuation and site effects properties. In addition, they can be used to validate new techniques that could be applied accordingly in other areas of lower seismicity.

Except for the western Greece area, earthquake data corresponding to the broader southwestern France area (**Figure 4**) are also examined by the SFC method in this thesis. This area includes the Rhine Graben, the French Alps, as well as the eastern part of Massif Central. Some of the strongest earthquakes in France occurred at the first two regions, which are characterized by low to moderate seismicity (***Duverger et al., 2021***). The largest earthquake of the past 20 years had moment magnitudes lower than 5.0 (**Figure 4**, left), as provided by the Bureau Seismological Center of France, BCSF, https://www.franceseisme.fr/ and the following four earthquakes had moment magnitude greater than 4.0: (i) The Le Teil earthquake occurred in Rhine Graben (November 11, 2019) with $M_w = 4.8$, (ii) the Barcelonette earthquake occurred on the western Alps region close to the France-Italy borders (April, 7, 2014) with $M_w = 4.8$ (iii) the one occurred close to the France-Switzerland borders (September, 8, 2005) with $M_w = 4.7$ and (iv) the one occurred into the sea close to the southeastern France coasts (February, 25, 2001), with $M_w = 4.7$.

However, larger magnitude earthquakes ($M_w > 5.0$), have also occurred in the broader southeastern France, as the 1909 Provence earthquake (**Figure 4**, right, blue circle) occurred on June 11 in Provence with $M_w = 6.2$ (***Baroux et al., 2003***) and which is the largest recorded earthquake in metropolitan France area. Except for this earthquake and albeit this area belongs to the western European intraplate domain, which behaves as a rigid block characterized by low internal deformation rate (***Nocquet and Calais, 2004***), a low, but non negligible number of earthquakes with moment magnitudes greater than 5.8 occurred into or very close to it during the past 500 years. Based on the French seismic catalogue of ***Manchuel et al., (2018)***, four earthquakes

(in 1664-M_w ~ 6.1, in 1831-M_w ~ 5.8, in 1854-M_w ~ 5.9 and in 1887- M_w ~ 6.7) occurred at the southern Alps, close to the France-Italy borders and two (in 1524- M_w ~ 5.9 and in 1584- M_w ~ 5.8) occurred on the northwestern Alps close to France-Switzerland borders (**Figure 4**, right, red circles). The above-mentioned earthquakes indicate the potential seismic activity of this region, albeit it is considered as a low to moderate seismicity region.

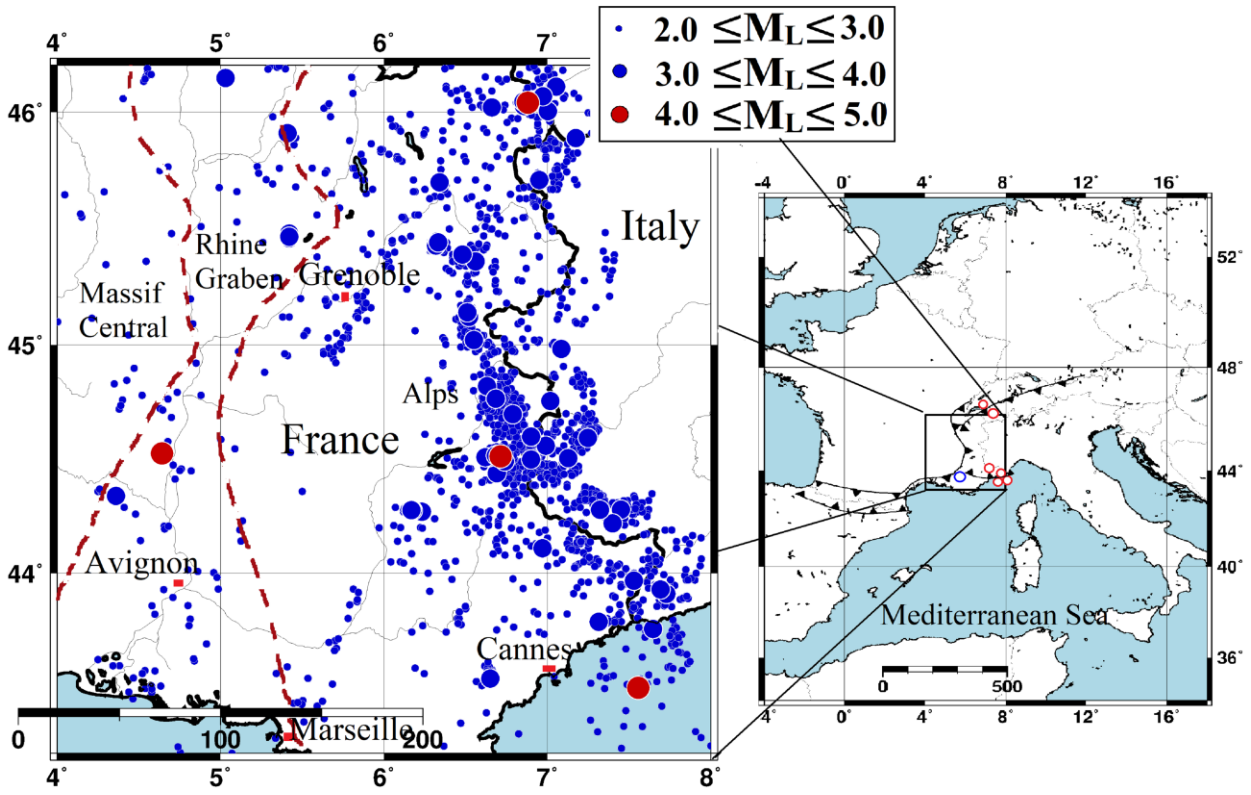

Figure 4. The seismicity (earthquake epicenters) of the southeastern France, for the last ~21 years (01/01/2000 - 31/12/2021) (Bureau Central Sismologique Français, BCSF, https://www.franceseisme.fr/). With red dashed lines at the **left** figure, the borders of the Massif Central, the Rhine Graben and the French Alps regions are depicted. In the **right** figure with red circles, the epicenters of the 6 earthquakes with $M_w \geq 5.8$, are depicted, while in blue circle the 1909 Provence earthquake, $M_w = 6.2$, is shown. The **right** figure grossly displays the broader tectonic regime of the neighboring region based on ***Billi et al., (2011)*** and ***Le Breton et al., (2017)***.

The present study is divided into the two following research parts: (i) the development of the new GIT algorithm and (ii) the introduction of a new SAF estimation technique, based on a new SFC algorithm as well.

The actual data used for the GIT and SFC algorithm applications are presented in *ch. 2*, referring to: (i) the S-waves part, of the earthquake records corresponding to western Greece and used by GIT (ii) the coda wave part, selected from the corresponding earthquake record dataset of western Greece, used by SFC (iii) the coda wave records of earthquake located in southeastern France, used by SFC (iv) the coda wave records of the four low to-to-high magnitude earthquakes, separately examined for their STFs by the SFC algorithm.

Regarding the GIT algorithm, details of its theoretical background are referred in *ch. 3*. Moreover, validation of the algorithm is attempted to be achieved through its application to synthetic data provided in chapter *3* as well, aiming at understanding the operational potential of the algorithm. Its validation is also investigated by examining a real dataset, which has been inverted by an independent study, using a previously developed GIT algorithm, which constitutes the basis of the new one. A comparison between them is carried out, anticipating to observe data misfit reduction, improvement of the model parameters based on other methodologies, "correction" of extreme "outlier" results that cannot be satisfied by the previous GIT algorithm and a more detailed attenuation model. Finally, the GIT algorithm is applied to a new created dataset, corresponding to earthquake records in western Greece, extracting information about the examined seismic sources, for the attenuation factors dominating this region and estimating SAFs of 24 specific accelerometer station sites.

In *ch. 4*, details of the new SAF estimation technique, based on a distant reference station, are provided and the new SFC algorithm which constitutes the tool to achieve this SAF estimation is analytically presented in 9 steps. Thereafter, two applications of the SAF estimation technique to western Greece and southeastern France data, are separately presented, following three successive steps for each case: The first step is the estimation of the "apparent STFs" of several earthquakes recorded at selected sites of the examined area, based on the SFC algorithm. The second step is to determine the SAFs by comparing the FAS of the "apparent STFs" retrieved for each earthquake-site pair, by considering four references "rock" sites located some tens of kilometers away from each other. The stability of the computed SAFs at each target site based on all the examined earthquakes, in relation to each examined reference site, is the main goal in order to support the applicability potential and the reliability of the proposed technique. The third, necessary step is to perform a statistical check, on the agreement between the average SAFs for each target site separately, by using the four different reference sites. Finally, the reliability and the practical applicability of the proposed SAF estimation technique, is investigated by comparing the estimated SAFs with those based on already well-established techniques, i.e. classical SSR method where possible, Generalized Inversion Technique, and HVSR. At the end of *ch. 4*, an application of SFC algorithm is carried out for four low-to-high magnitude earthquakes, for which their STFs are known based on applications of independent methodologies. A comparison between the known STFs and those estimated by the SFC, after removing the SAF, is attempted. Observations about the seismic moment, source duration and source directivity effects estimation, as well as about the validity of the minimum phase scenario used in STF computation, are examined and discussed.

Finally, in *ch. 5*, conclusions of the two main research parts of this Thesis (*ch. 3* and *ch. 4*) are presented and discussed, while the perspectives on several aspects of this research are provided.

2 DATA USED

The data used in this study consist of four groups that are separately used in the four main applications analyzed in this thesis. The first group of data is used in the application of the Generalized Inversion Technique (GIT) (*ch.* 3), while the rest three are used in the Spectral Factorization of Coda waves (SFC) application (*ch.* 4). For this reason, in the following four sections each group of data is described.

2.1 First Group of Data (S-waves, western Greece)

Regarding the Generalized Inversion Technique (GIT), the reliable part of the Fourier Amplitude Spectra (FAS) of the S-waves of several earthquake records is used as input data, and is explained below analytically.

2593 seismic records (three-components), corresponding to 180 earthquakes (M_L = 3.0-5.4), occurred in broader western Greece (including Ionian islands: Cephalonia, Zakynthos, Lefkas, Ithaca, **Figure 5**), during the period: 13/08/2015 – 26/11/2019, (details are given in **Appendix B**, based on the catalogue of the Seismological Station of Aristotle University of Thessaloniki, http://geophysics.geo.auth.gr/ss/), were selected. Here it's worth noting that the study area is considered as a high seismicity one (among others; ***Papazachos and Papazachou, 1997; Burton et al., 2004***).

The 2593 records were obtained from 24 stations (**Figure 5**) installed in western Greece (**Appendix C**). Six of them are broadband accelerometric stations and belong to the **ARGONET** (**ARGO**stoli **NET**work) vertical array (***Theodoulidis et al., 2018***). These stations are equipped with a 24-bit digitizer (Centaurs) and force balance Episensor (Kinemetrics) accelerometers (DC-200 Hz). One of them, CK0, is installed on a surface soft-soil site, while the other four are installed at the same location but inside boreholes of 6 m, 15 m, 40 m and 83 m depth. The 6th station (CKWP) is installed ~400 m away from the 5 borehole stations, on a surface rock site (limestone). The rest 18 stations which belong to ITSAK (Institute of Engineering Seismology and Earthquake Engineering, http://www.itsak.gr/en) accelerometric network, consist of 24-bit digitizers and Guralp-CMG-5TDE broadband accelerometers (0.05-100 Hz) and they have been installed during the period 2012 and 2014.

The data used in GIT, consist of displacement FAS derived from the S-wave windows acceleration FAS of the selected seismic records, after dividing them by ω^2 ($\omega = 2\pi f$, the angular frequency). The horizontal components FAS and the corresponding vertical ones (2593 FAS number at each component) were separately inverted, for the same S-wave window which is determined as follows.

First, the entire accelerogram is band-pass filtered (*Butterworth* filter, 2nd order) in the frequency range: 0.05 Hz to 50 Hz. Thereafter, the direct body S-wave windows of each earthquake record component (E-W, N-S and Vertical), were selected starting from the S-arrival, t_s (manually picked), with duration, T_{S-wave} (in *sec*) given by the following formula (***Kishida et al., 2016***):

$$T_{S-wave} = T_{source} + 0.1 \cdot R_{hyp} \quad [1]$$

R_{hyp} (in *km*) is the hypocentral distance, ($R_{hyp} = [R_{ep}^2 + d^2]^{1/2}$, R_{ep} the epicentral distance and d the depth of the earthquake), while T_{source} is the seismic source duration ($T_{source} = 1/f_c$). The corner frequency, f_c, is estimated based on Brune's formula (***Brune, 1970***):

$$f_c = 0.37 \cdot \beta \cdot \left(\frac{16 \cdot \Delta\sigma \cdot 10^5}{7 \cdot M_o} \right)^{\frac{1}{3}} \quad [2]$$

where, $\Delta\sigma$ (in *bar*), is the stress drop, M_o is the seismic moment and β is the shear wave velocity at the source. We adopted an average stress drop value of $\Delta\sigma$ = 10 bar and an average shear wave velocity close to the seismic source, β = 3500 m/s. The seismic moment, M_o(in $N \cdot m$) is determined by ***Hanks and Kanamori, (1979)*** equation:

$$M_o = 10^{1.5 M_w + 9.1} \quad [3]$$

where, M_w, is the moment magnitude, considering $M_w = M_L$, for the examined local magnitude range, M_L = 3.0-5.4 (***Scordilis et al., 2016***), if also take into account the average $\pm$0.2 standard deviation of M_L.

However, following the technique of Standard Spectral Ratios (SSR) (***Borcherdt, 1970***) as it was implemented by ***Grendas et al., (2021c)***, longer S-wave windows (T_{S-wave} + 4 s), were selected, without overpassing the coda waves arrival time, t_c (here it is considered $t_c = 2 \cdot t_s$), (**Figure 6**), while, in difference case, they were restricted up to t_c time. These windows seem to better represent the maximum energy of the body S-wave phase, affected by site effects, including the significant duration (***Dobry et al., 1978***) of the seismic motion, based on the so-called Arias intensity (***Arias, 1970***). Thereupon, an extra second before and after the already chosen S-wave windows (T_{S-wave} + 4 s), was included and tapered by the half part of a 2 s *Parzen* window (left and right part, respectively) as in the example of **Figure 6**. Finally, a 60 s signal time window was artificially constructed by a zero-padding process to all the S-wave windows, resulting to the same number of discrete points in time.

The FAS_{comp} of the finally used S-wave windows, were separately computed for each component. Then, the smoothed FAS_{comp}, by applying the logarithmic weight function of ***Konno and Ohmachi (1998)*** (with b = 50), were calculated for 37 discrete frequencies, equally distributed in logarithmic scale, between 0.3 Hz and 15.1 Hz. A constraining criterion of the existence of at least 3 signal cycles, corresponding to the selected S-wave windows (T_{S-wave} + 4 s, Eq. [1]) was applied to ensure the reliability of each frequency of the FAS_{comp}, as was proposed by ***Perron et al. (2018)***.

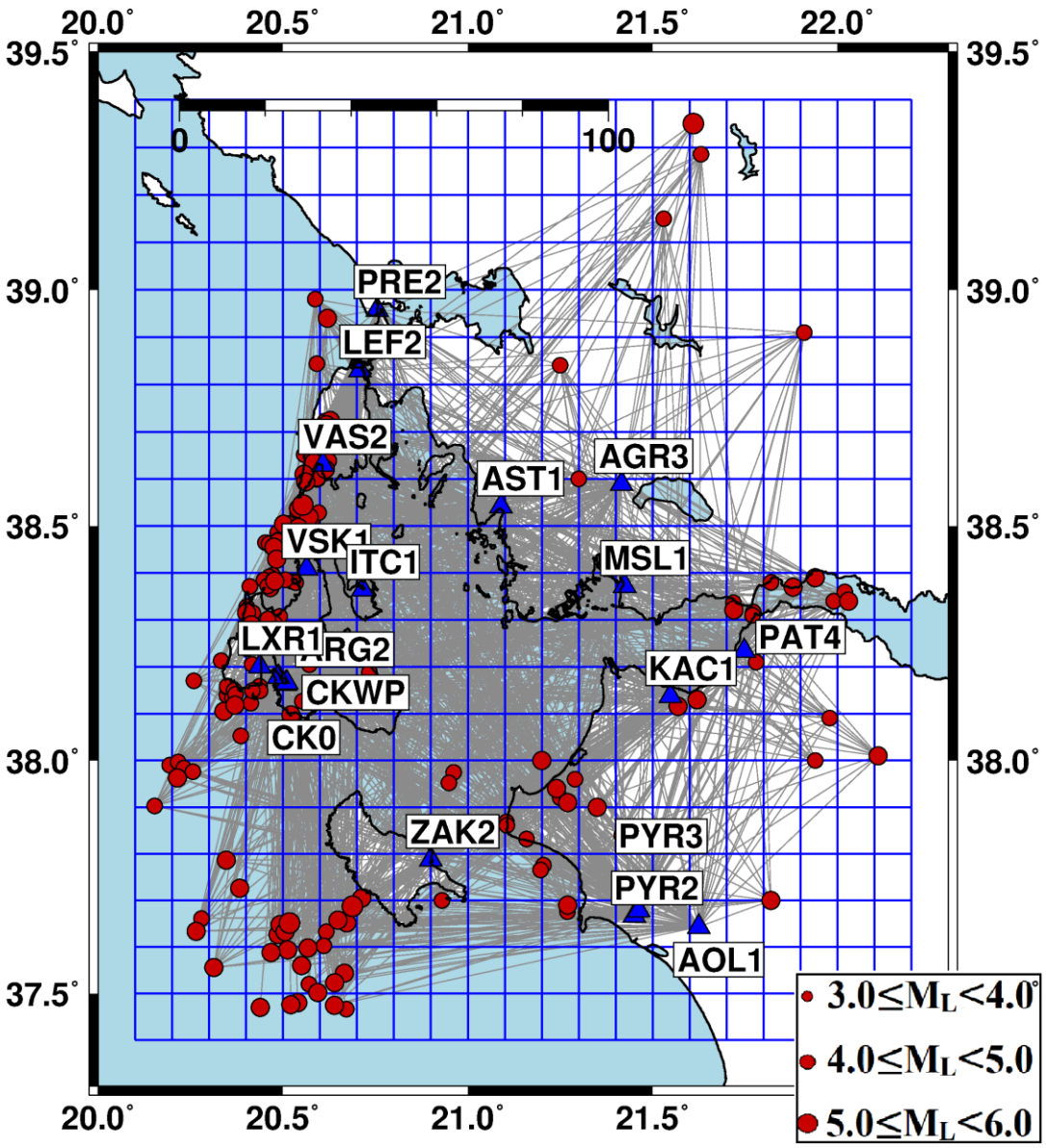

Figure 5. The area of western Greece (same as **Figure 3**). The epicenters (red circles) of the 180 earthquakes, recorded at the 24 stations (blue triangles), are depicted. The ray paths (2593, grey lines) of the seismic records, used in this study and the 406 sub-areas (0.1° x 0.1°, blue cells), for which the quality factors $Q_s(f_k)$, were investigated, are also depicted. The identity number of each sub-area **Appendix K**) counts from the upper left corner to the bottom right.

The aforementioned procedure was also applied for the noise time window (**Figure 6**) of each component, selected exactly before the P-waves arrival. The corresponding smoothed FAS_n was also computed for each component. Finally, a criterion of Signal to Noise Ratio (SNR) greater than 5, was adopted per each frequency, to determine the reliable FAS_{comp} of the S-waves. The "single" horizonal component FAS_{hor} of S-waves was computed based on the reliable part of both horizontal components, FAS_{EW} and FAS_{NS}, following Eq. [4]:

$$FAS_{hor} = \sqrt{FAS_{EW}^2 + FAS_{NS}^2} \quad [4]$$

Here, it's worth noting that the P-waves recorded exactly before the S-wave arrival (**Figure 6**) can be also considered as "noise" for the S-waves. However, at the SNR criterion of the final examined S-wave windows, only the pre-event noise record was taken into account, as the totally independent part on the earthquake motion, following the common applied noise-selection strategy in GIT studies. By this way, those P-waves arriving at the same time to the examined S-waves, were considered as a part of the intense earthquake motion, which is mainly controlled by the S-waves.

The seismic records used for the GIT application in this study, are associated with hypocentral distances between 12-200 km, covering at least one theoretical wavelength, λ ($\lambda = v_S/f_L$) of the lowest reliable frequency limit (f_L = 0.3 Hz), considering an average shear wave velocity of the propagation path, v_S = 3500 m/s. Finally, a total number of 5186 FAS (2593 horizontal and 2593 vertical) were inverted.

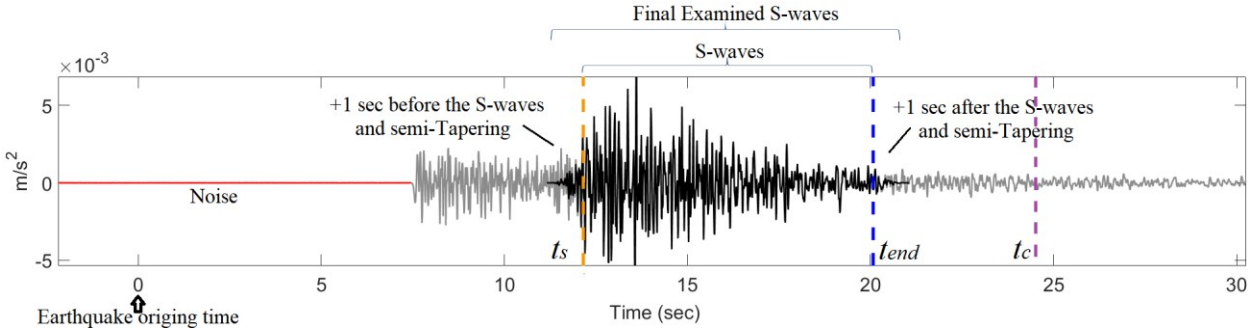

Figure 6. A seismic record (vertical component) of the 2nd event in **Appendix B** (M_L = 3.4), in VSK1 station, at 31 km epicentral distance. With black and red lines, the examined S-wave and Noise records, are respectively depicted. With orange and blue vertical dashed lines, the S-wave arrival, t_s and its ending time, $t_{end} = t_s + T_{S-wave} + 4$ sec (Eq. [1], details into the text), are respectively depicted. The +1 s, semi-tapered signals before t_s and after t_{end}, included into the finally used S-wave window are also shown. The coda wave arrival time, t_c (purple line) is also depicted.

2.2 Second Group of Data (Coda waves, western Greece)

Regarding the **S**pectral **F**actorization method of **C**oda waves (SFC), the reliable part of all three component coda waves records of an earthquake can be used as the input data, as analytically explained below.

The first group of data used for the application and investigation of the SFC method in this thesis, are based on earthquake recordings retrieved from the aforementioned 24 accelerometer stations (**Figure 7a**, and **Appendix C**), used for the GIT application (**Figure 5**). The seismic records (3-components) of the 180 earthquakes used for the GIT data selection (**Figure 5**), were investigated for the SFC application. However, after the process of investigating the reliability of the coda wave selection per component and based on the corresponding part of the SFC algorithm,

mentioned below (see *ch*. 4.2.2), 88 earthquakes with M_L magnitudes, ranging from 3.9 to 5.4 were finally used (**Appendix B**). The seismic records used in SFC method of this dataset, have hypocentral distances $R_{hyp} \leq 180$ km.

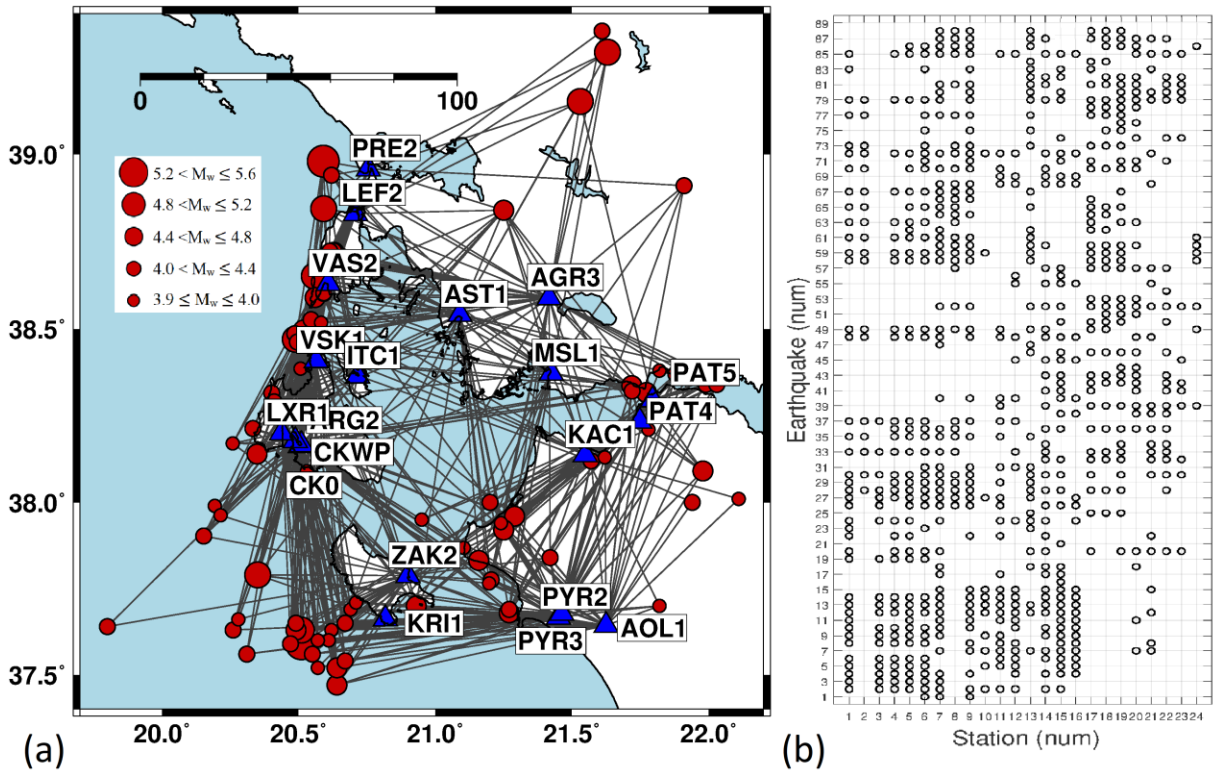

Figure 7. (**a**) The study area (western Greece-Ionian Sea). 739 pairs of earthquakes-station for which coda wave recordings were used in this study. 88 earthquakes (epicenters: red circles) and 24 accelerometer stations (blue triangles), are also depicted. (**b**) The distribution of recordings for each earthquake at each station id according to **Appendix B** and **Appendix C**, respectively.

2.3 Third Group of Data (Coda waves, southeastern France)

This group of data is the second one used for the **S**pectral **F**actorization of **C**oda waves (SFC) method in this study. The data consist of recordings from 58 earthquakes occurred mainly in the Alps region (South-eastern France, North-western Italy) (**Figure 8**), a low to moderate seismicity area and were recorded by three seismological networks located on South-eastern France. The first one consists of 12 surface-installed broadband accelerographs (0.05-200 Hz) of the French seismological network ("RESIF RAP" ***Traversa et al., (2020)***, **Appendix D**). The data corresponding to this group have been appropriately processed as explained by ***Traversa et al., (2020)***. The second and the third networks refer to 4 free-field broadband (0.05-200 Hz) seismometers (velocity records), located at the Cadarache Technological Research and Development Center for Energy (**Appendix D**).

After the process of investigating the reliability of the coda wave selection per component, and based on the corresponding part of the SFC algorithm, mentioned below (see *ch*. 4.2.2), 35

earthquakes which occurred between August, 2000 and November, 2019, with M_L magnitudes ranging from 3.2 to 5.2 were finally used (**Figure 8, Appendix F**). From this dataset, in total 148 seismic records were used in the SFC method, with hypocentral distances between 18 km and 220 km (**Figure 8**).

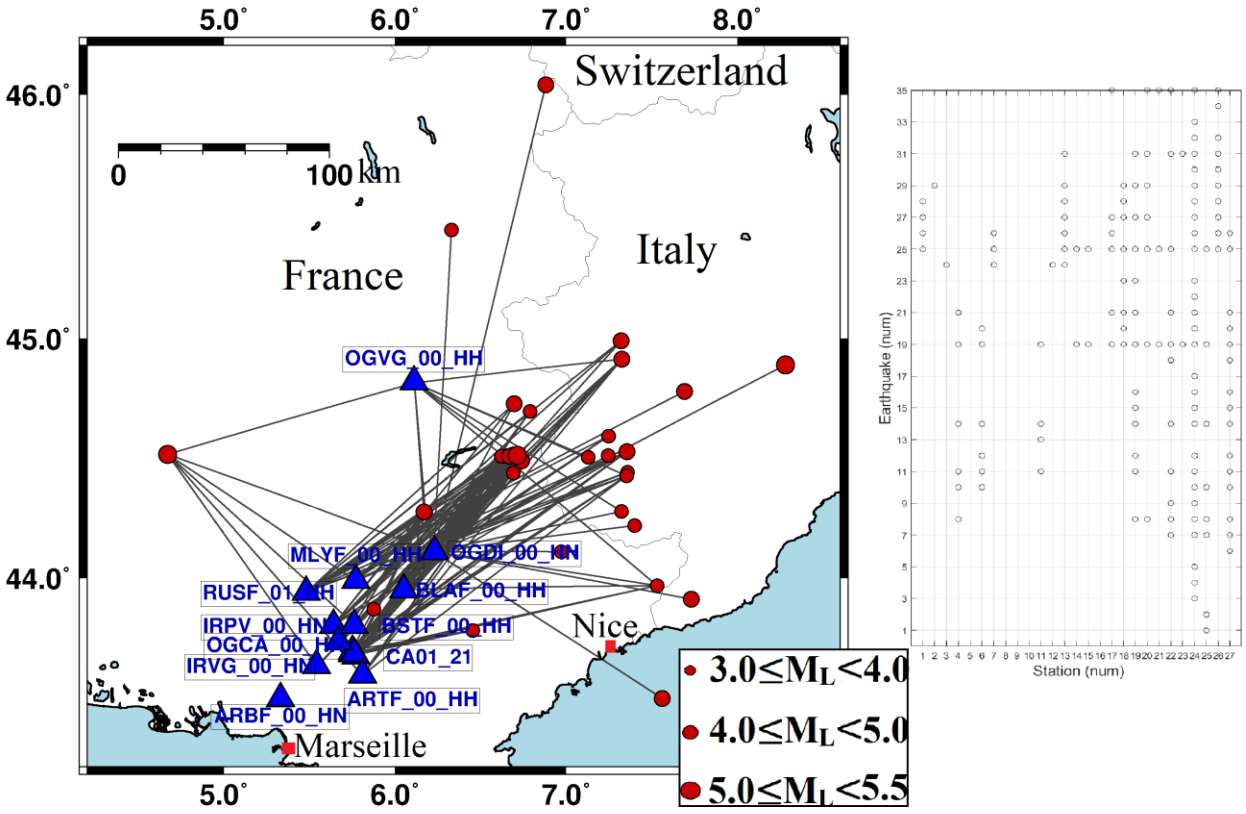

Figure 8. (**left**) The epicenters (red cycles) of the 35 earthquakes (**Appendix F**), used for the 2nd SFC application recorded at 16 stations (blue triangles, **Appendix D**), in Southeastern France. With grey lines the corresponding 148 ray paths, are depicted. (**right**) The distribution of recordings for each earthquake at each station id according to (**Appendix F** and **Appendix D**), respectively.

2.4 Fourth Group of Data (Four low-to-large magnitude earthquakes)

This group of data is the 3rd examined by the Spectral Factorization Method and it refers to four earthquakes of higher magnitudes (M_w close to ~4.0, ~5.0, ~6.0 and ~7.0) than the average magnitude examined in the 2nd and 3rd group of data mentioned above in this chapter. These earthquakes were chosen to be separately examined due to the fact that their STF was available by independent studies and they could be compared to the corresponding ones computed here by the SFC method. These comparisons are provided below, in chapter *4.3.3*, attempting to extract conclusions which express the validity of the minimum phase scenario to higher magnitude earthquake, where the rupture process can vary and the STF can be complicated, as well as to assess the effectiveness of the SFC method in extracting information for the rupture directivity.

More specifically, an earthquake of moment magnitude, M_w= 4.15 (±0.2) (M_L= 4.5) (**Figure 9a**), occurred on 26/02/2012 (at 22:37:56 GMT) close to the France-Italy borders (Latitude: 44.496º, Longitude: 6.664º, Depth: ~7 km, determined by Sismalp network, https://sismalp.osug.fr), has been examined for its minimum phase STF in this study. ***Courboulex et al., (2013)*** indicate that this earthquake comes from a normal fault of 2 km length, with a rupture directivity towards SE as presented in **Figure 9a**. ***Courboulex et al., (2013)*** conclude to this rupture information based on the real earthquake waveforms retrieved by the stations depicted in **Figure 9a** with red color. The earthquake records of the following seven stations of **Appendix D**: CA01_21, BSTF_00_HH, IRPV_00_HN, OGDI_00_HH, OGDI_OO_HN, MYLF_00_HH and RUSF_01_HH (**Figure 9a**), were selected in this study to be examined for the SFC analysis, since they presented available coda wave records, suitable to be studied, based on the criteria mentioned at the SFC algorithm development chapter (see *ch*. 4.2.2), below in this study. Moreover, the earthquake records of the following four broadband (0.05-200 Hz) accelerographs (same to the ones mentioned in **Appendix D**) of the France accelerometric network (RAP): OGMB, OGAG, ISO and SAOF, (**Appendix E**) which were not examined in the 3rd group of data (*ch.* 2.3), were also chosen to be examined for the following four reasons. Firstly, these stations provided coda wave records. The second reason refers to the fact that they were the same stations to the ones examined by ***Courboulex et al., (2013)*** at which the apparent STF have been retrieved. The third reason was that these stations are installed on rock sites with high Vs30 values (>1000 m/s) and not significant site effects are normally expected (mainly below f < ~8 Hz), while the fourth reason was that these stations offer a better azimuthal coverage of the earthquake epicenter, with respect to the obtained coverage (~210º-240º) by the first mentioned seven stations, as it becomes clear in **Figure 9a.**

The second, investigated for its STF, earthquake was the one that occurred on 11/11/2019 (at 10:52:45 GMT, Lat: 44.518°, Long: 4.671°, Depth: 1 km, ***Ritz et al., (2019)***), close to the Le Teil commune, in Southern France. This earthquake, which corresponds to moment magnitude, M_w = 4.85 (±0.2), was "generated" by a reverse fault of ~5 km length, with a direction NE-SW (***Causse et al., 2021***), as presented in **Figure 9b**. After 2000 realization fault kinematic tests, carried out by ***Causse et al., (2021)*** using real earthquake records, the rupture model of this earthquake seems to fit better to a bilateral rupture, depicted in **Figure 9b**.

The third earthquake is the one of M_w = ~6.05 (±0.2) (M_L = 5.8), occurred in western Greece area, on Cephalonia island, on 26/02/2014 (at 13:55:43 GMT, Lat: 38.1522º, Long: 20.3912º, Depth: ~15 km, determined by the Seismological Station of Aristotle University of Thessaloniki, confirmed by the study of ***Sokos et al., (2015)*** (**Figure 10a**). ***Karakostas et al., (2015)*** indicate the fault process of this earthquake as an implication of the Cephalonia Transform Fault zone (***Scordilis et al., (1985)***, **Figure 3**), dominated mainly by a dextral strike slip motion and less by a reverse fault component. ***Sokos et al., (2015)***, carrying out a rupture process study of this earthquake, found that the fault direction lies on NNE-SSW direction, and its plane is steeply dipping to the East. They indicate the fault length up to ~25 km and the source duration close to 9 s, with a rupture directivity towards NE (**Figure 10a**). In the present study, the earthquake

records of the following five stations: PRE2, MSL1, PAT4, KAC1 and ZAK2, used in 2nd group of data (*ch.* 2.2, **Appendix C**), were found suitable to be examined, since they include an appropriate to be analyzed coda wave record, which was not interrupted by the presence of another local earthquake recording.

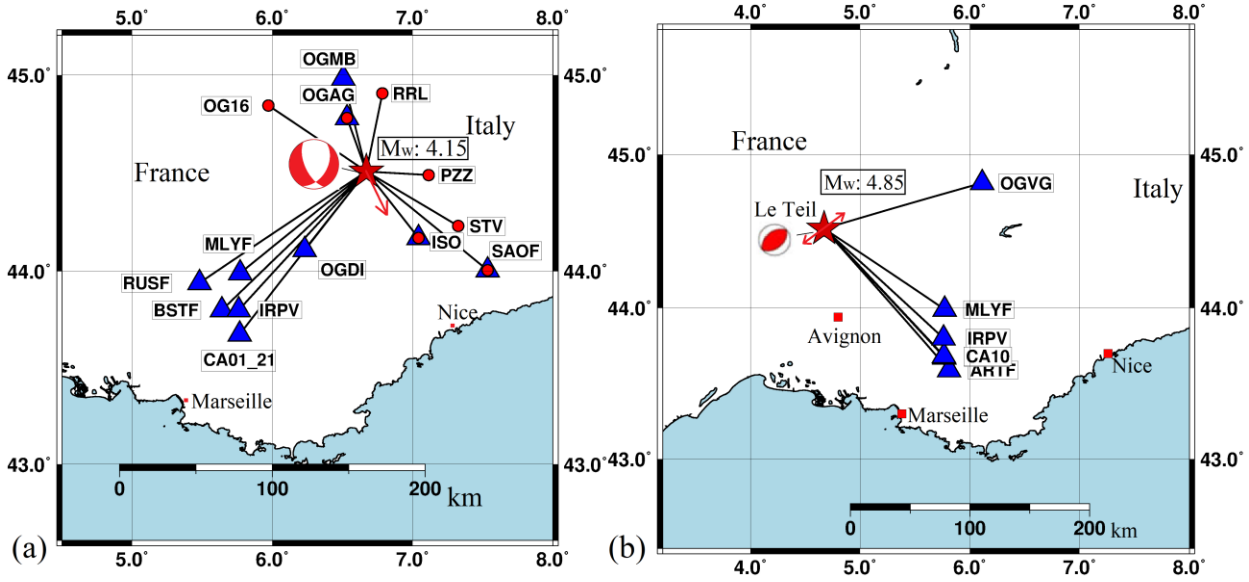

Figure 9. (**a**) The epicenter (red asterisk) of the M_w= 4.15 earthquake (20120226_223756) examined for its STF, its focal mechanism and the rupture directivity (red vector) as provided by ***Courboulex et al., (2013)***. Blue triangles represent the stations used for the SFC analysis in this study, while the red ones the stations used for the STF computations by ***Courboulex et al., (2013)***. (**b**) The corresponding to (**a**) map for the M_w = 4.85 (20191111_15245) earthquake. Focal mechanism and rupture directivity (red vector) are depicted based on ***Causse et al., (2021***).

Finally, the fourth, investigated for its STF in this study, earthquake was the one of M_w = ~7.0 (±0.2) (M_L = 6.7), occurred on the Northern coast of Samos island (in Eastern Greece) on 30/10/2020 (at 11:51:25 GMT, Lat: 37.914º, Long: 26.804º, Depth: 13 km, determined by the Seismological Station of Aristotle University of Thessaloniki and confirmed by the USGS corresponding study, https://earthquake.usgs.gov, as well as by ***Lentas et al., (2021)***). According to ***Lentas et al., (2021)***, a non-uniform bilateral rupture of ~60 km x 20 km normal fault area of E-W direction, is suggested from a kinematic rupture inversion analysis. The main rupture direction has been found towards the West, as depicted in **Figure 10b**. For the STF analysis in this study based on the SFC method, the earthquake records of the following four accelerographs: SGR1, MYT1 SMG1 and NAX1 belonging to the ITSAK network (http://www.itsak.gr/en), were used together with CHOS and APE seismographs, belonging to the Hellenic Unified Seismic Network (http://www.gein.noa.gr/en/networks/husn). The coda wave records at these stations were suitable to be examined under the Signal to Noise ratio criteria analyzed below (see *ch*. 4.2.2) at the SFC algorithm development.

The process applied to the seismic records of the above four earthquakes, for the SFC analysis (see *ch*. 4.2.2), is the same as the one applied at the 2nd and 3rd group of data mentioned above in this chapter.

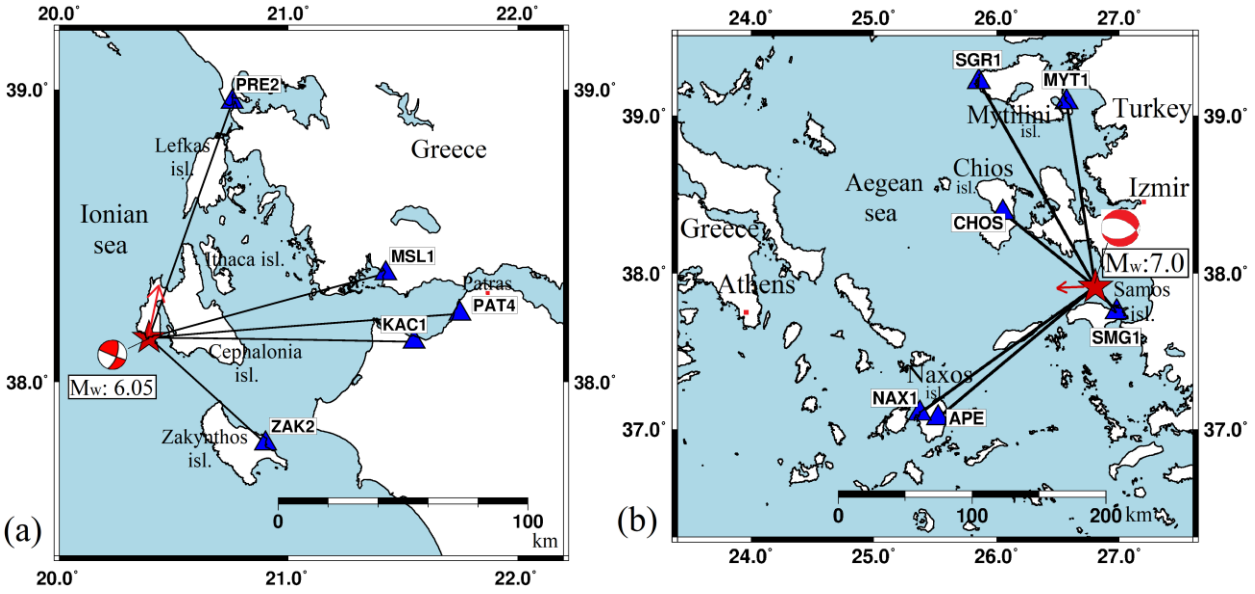

Figure 10. (**a**) The corresponding to **Figure 9a** map for the M_w = 6.05 (20140126_135543) earthquake. Focal mechanism and rupture directivity (red vector) are depicted based on Seismological Station of AUTh (http://geophysics.geo.auth.gr/ss/) and on ***Sokos et al., (2015)*** study, respectively. The five examined stations are also depicted (blue tringles). (**b**) The corresponding to figure (**a**) map for the M_w = 7.0 (20201030_115125) earthquake. Focal mechanism and rupture directivity (red vector) are depicted based on Seismological Station of AUTh (http://geophysics.geo.auth.gr/ss/) and ***Lentas et al., (2021)*** study, respectively. The six examined stations are also depicted (blue tringles).

3 DEVELOPMENT, VALIDATION AND APPLICATION OF A NEW GENERALIZED INVERSION TECHNIQUE (GIT) ALGORITHM

3.1 Introduction

There are mainly four goals attempted to be achieved in this chapter. The first one refers to the presentation of the theoretical background of the newly developed parametric GIT algorithm, in the framework of the present thesis. This algorithm follows the parametric GIT algorithm developed by ***Drouet et al., (2008a)***, but a more detailed attenuation model regarding the geometrical spreading and the anelastic attenuation factor is considered and studied. This new approach is achieved as a reasonable step so as to improve the GIT investigated factors (Seismic Source, Propagation Path and Site Effects), in comparison to the uniform-single attenuation model (e.g. **Figure 11a**), adopted by ***Drouet et al., (2008a)***. This improvement is expected to lead to the reduction of the misfit of the real and the computed from the inverted model data, resulting from the application of both parametric GIT algorithms; that of ***Drouet et al., (2008a)*** and the one developed in this study.

The second goal of this chapter refers to an application of the new GIT algorithm to a suitable synthetic dataset presented below, in order to validate as well as possible, the correct computational operation of the algorithm. The synthetic dataset has been created to be as similar as possible to a simplified actual one.

The third goal of this chapter refers to an effort of practically confirming, to a certain degree, the improvement of the new algorithm with respect to the previous one by ***Drouet et al., (2008)***, regarding the attenuation model of the examined area. Thus, the dataset inverted by ***Grendas et al., (2018)***, for a uniform attenuation model, based on the GIT algorithm of ***Drouet et al., (2008a)***, was also inverted here by the new algorithm. The results of this comparison are presented below in this chapter and by this comparison, the applicability of the new algorithm on real data, as well as its potential improvement are tested and discussed.

Finally, in the framework of this PhD study, the proposed GIT algorithm is implemented, focusing on a more detailed study in the western Greece region (including the Ionian islands of Cephalonia, Lefkas, Zakytnhos and Ithaca), which is the area with the highest seismicity in Greece. This study is based on a new dataset, created in this thesis, including low to moderate magnitude earthquakes (details into *ch. 2.1*), trying to assess Seismic Source, Propagation Path and Site Amplification factors, which are going to be used for the validation of the second investigated methodology in this PhD thesis (*ch. 4*), for the same region of western Greece.

Before the presentation of the four goals of this chapter, mentioned above, the concept that is included in the new GIT algorithm concerning the attenuation model is briefly explained below. A given study area where stations and earthquakes are located (e.g. **Figure 11a**), is divided to *n* subareas (cells) (e.g. **Figure 11b**), so that the anelastic attenuation factor can be separately investigated within each one of them. This division is defined by choosing meridians and parallels for the sake of these *n* cell-areas representation. At the example of **Figure 11b** four meridians and

four parallels divide the area of **Figure 11a** into $n = 9$ sub-areas. The earthquake ray paths are divided into sub-ray paths, for these subareas (cells) and they are used in the inversion process in order to individually investigate anelastic attenuation factors for these cells, as if a pseudo-2D lateral anelastic attenuation tomography is performed. The pre-inversion process required for this ray path deviation is analytically presented in **Appendix A**.

Furthermore, working on the GIT improvement, a distance dependent geometrical spreading attenuation factor was also considered as a reasonable condition of S-waves propagation, supported as well by other GIT applications (e.g. ***Edwards et al., 2008***) focusing to the inversion misfit reduction and to the improvement of the investigated factors. Finally, a relation that controls the inverted seismic moments, M_o and corner frequencies, f_c in accordance with the Brune's (***Brune, 1970***) stress drop parameter, is also introduced in this algorithm as an extra "tool" helping the inversion to converge and/or restrict the solution in case where stress drop is provided.

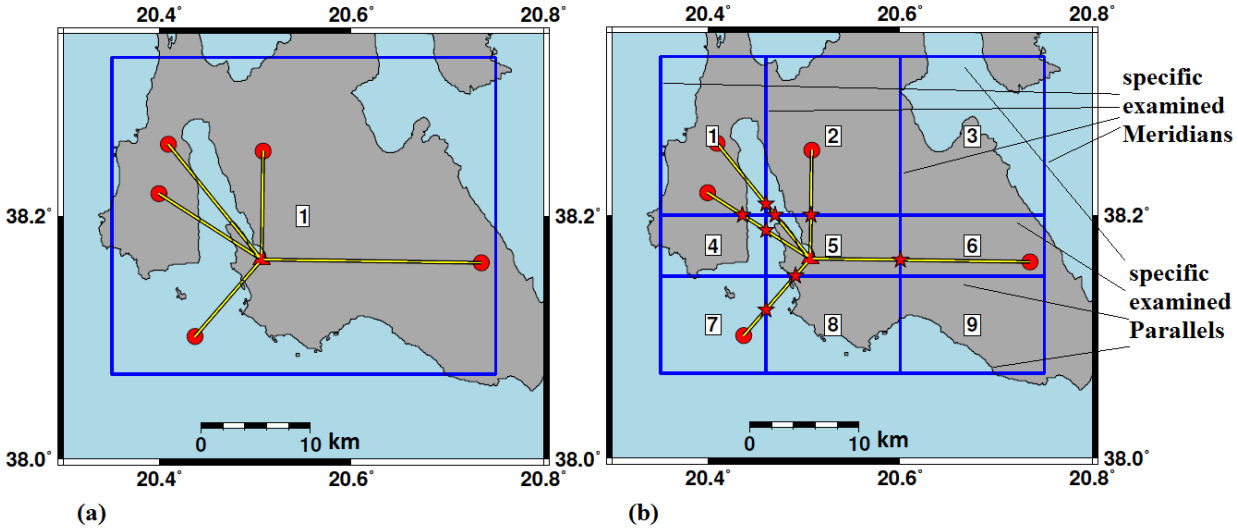

Figure 11. An example (Cephalonia island, Greece) of the separation of a uniform attenuation model area (into the blue rectangle) (**Figure 11a**), to nine attenuation model areas (**Figure 11b**). With red circles and triangle are some random located earthquakes and a station, respectively, while with red asterisks are the intersection points of the ray paths (yellow lines) with parallels and/or meridians that define the model areas being studied. Intersection points are calculated by the formulas analytically described in **Appendix A** and used for the ray paths division in the new inversion algorithm.

3.2 Methodology

The Generalized Inversion Techniques (GIT) are based on the theoretical spectral decomposition of the Fourier Amplitude Spectra (FAS) of S-wave displacement records, $A_{ij}(f_k)$, from i earthquake and j station, to the Seismic Source, $\Omega_i(f)$, attenuation path, $D_{ij}(f)$ and site effect $S_j(f)$ factors, according to the following equation:

$$A_{ij}(f_k) = \Omega_i(f_k) \cdot D_{ij}(f_k) \cdot S_j(f_k) \qquad [5]$$

for the discrete frequencies, f_k. Based on the diffuse field theory (***Weaver 1982***; ***Sánchez-Sesma et al., 2008***), Eq. [5] can use as data, $A_{ij}(f_k)$, both the horizonal, FAS_{hor} and vertical, FAS_{ver} S-wave records. Regarding the latter, it is considered that a part of the body S-waves which are propagated through the high shear wave velocity bedrock, below the target site, is converted to P-waves at the interface of bedrock-soil and they are recorded at the vertical surface component. For this reason, it must be noted that the site effect factor $S_{jH}(f)$ which corresponds to the horizontal motion, is directly expressed by the so-called Site Amplification Factor (SAF_{hor}), while the vertical one, $S_{jV}(f)$, is controlled by the following formula (***Kawase et al., 2011***):

$$S_{jV}(f_k) = SAF_{ver} \cdot \sqrt{\beta_s/\alpha_s} \qquad [6]$$

where α_s and β_s, are the P and S-waves velocities of the bedrock below the target site, respectively. The $\sqrt{\beta_s/\alpha_s}$ coefficient controls the conversion of the horizontal S-wave amplitudes to the vertical P-wave ones, as is analytically shown by ***Kawase et al., (2011)***. Thus, regarding the vertical component, the inversion applied in this study, investigates directly the $S_{jV}(f_k)$ factor, including the unknown $\sqrt{\beta_s/\alpha_s}$ coefficient for each site, and does not directly provide the SAF_{ver} factors (Eq. [6]).

The parametric GIT algorithm used in this study, constitutes a modification of the one developed by ***Drouet et al., (2008)***, applying the ***Gauss-Newton*** non-linear inversion iterative algorithm (Tarantola, 2005). The "keystone" of this new GIT algorithm is the following equation which is a more analytical form of Eq. [5]:

$$A_{ij}(f_k) = \left(\frac{M_{o_i} \cdot \frac{F_s \cdot R_{\theta\varphi}}{4\pi\rho\beta^3}}{\left[1 + (f_k/f_{c_i})^2\right]} \right) \cdot \left(\frac{1}{r_{ij}^{\gamma_h(r_{ij})}} \right) \cdot \left(\prod_{n=1}^{N} e^{\left(-\frac{\pi r_{ijn} f_k}{Q_{s_n} f_k^{a_n} v_{s_n}} \right)} \right) \cdot S_j(f_k) \qquad [7]$$

where the first analytical term of the product refers to the $\Omega_i(f_k)$ factor of Eq. [5], while the second and the third terms refer to the $D_{ij}(f_k)$ factor, corresponding to the geometrical spreading and anelastic attenuation, respectively. $\Omega_i(f_k)$ factor is based on the Brune's source model (***Brune, 1970***), controlled by the seismic moment, M_o (in $N{\cdot}m$) and corner frequency, f_c, parameters. This factor is also corrected by the source scaling factor including the radiation pattern coefficient $R_{\theta\varphi}$ = 0.55 (***Boore and Boatwright, 1984***), the average shear wave velocity, β = 3500 m/s (same as Eq. [2]) and density, ρ = 2800 kg/m^3 of the medium at the source. Moreover, the constant, free surface site amplification factor, F_s = 2, for the normally incident *SH* waves and a good approximation for *SV* waves, (***Aki and Richards, 2002***), is also included. The latter factor should normally be combined with the site factor, $S_j(f_k)$, but it is conventionally included in the scaling factor of the source, since it is a constant one. $S_j(f_k)$ is a non-parametric factor, studied in discrete values for each frequency, f_k at each station, j. Finally, the $D_{ij}(f_k)$ factor, the investigation of which consists the keystone of this new GIT algorithm, is controlled by the two following

parameters: (i) a hypocentral distance dependent, gamma, $\gamma_h(r_{ij})$ parameter ($\gamma = 1$ and $\gamma = 0.5$, for spherical and cylindrical spreading, respectively and h is an index characterizing the different studied gamma values) and (ii) a regional (sub-area, n) dependent anelastic attenuation factor (N is the total number of sub-areas that do not overlap between each other). The latter is a function of frequency dependent S-wave quality factor $Q_s(f_k)_n = Q_{s_n} f_k^{a_n}$, of each sub-area, n (e.g. **Figure 11b**), of the corresponding mean shear wave velocity, (v_{sn} = 3500 m/s), as well as of the part of hypocentral distances, r_{ijn}, crossing the certain sub-area.

This GIT algorithm is considered as a parametric one, since the source, $\Omega_i(f_k)$ and path attenuation, $D_{ij}(f_k)$, factors (Eq. [5]) are studied for the specific unknown parameters M_{o_i}, f_{c_i} and $\gamma_h(r_{ij})$, Q_{s_n}, a_n (Eq. [7]), respectively, while the $S_j(f_k)$ (Eq. [5] and [7]) factor is studied in a non-parametric form.

Taking the decimal logarithm of each part of Eq. [7], to convert this equation from a product to a sum of factors, the following equation is produced:

$$Z_{ijk} = m_{0_i} - log_{10}\left[1 + \left(\frac{f_k}{f_{c_i}}\right)^2\right] - \gamma_h(r_{ij}) \cdot log_{10}(r_{ij}) - \\ - \sum_{1}^{n}\left(\frac{\pi\, r_{ijn} f_k}{ln(10)\, Q_{s_n} f_k^{a_n} v_{s_n}}\right) + s_{jk} \qquad [8]$$

where $Z_{ijk} = log_{10}(A_{ijk})$, $m_{0_i} = \log_{10}\left(M_{o_i} \times \frac{2R_{\theta\varphi}}{4\pi\rho\beta^3}\right)$ and $s_{jk} = log_{10}\left(S_{jk}(f_k)\right)$. Based on Eq. [8], a system of equations is built from recordings corresponding to, i earthquakes and, j stations. The goal of this inversion technique is to invert an adequately large dataset of $Z_{D_{real}} = Z_{ijk}$ (D x 1, D, the total number of Data) (Eq. [9]), for specific k number of frequencies (f_k), in order to solve for a model matrix m_M (M x 1, M, the number of Model parameters) (Eq. [9]), composed by 6 groups of the following parameters: m_{0_i}, f_{c_i}, $\gamma_h(r_{ij})$, Q_{s_n}, a_n and s_{jk}.

$$Z_{D_{real}} = \begin{bmatrix} Z_{111} \\ \vdots \\ Z_{11k} \\ \vdots \\ Z_{1j1} \\ \vdots \\ Z_{1jk} \\ \vdots \end{bmatrix}, \quad \begin{bmatrix} \vdots \\ Z_{i11} \\ \vdots \\ Z_{i1k} \\ \vdots \\ Z_{ij1} \\ \vdots \\ Z_{ijk} \end{bmatrix}, \quad m_M = \begin{bmatrix} m_{0_1} \\ \vdots \\ m_{0_i} \\ f_{c_1} \\ \vdots \\ f_{c_i} \\ \gamma_1 \\ \vdots \\ \gamma_h \\ Q_{s_1} \\ \vdots \end{bmatrix}, \quad \begin{bmatrix} \vdots \\ Q_{s_n} \\ a_1 \\ \vdots \\ a_n \\ s_{11} \\ \vdots \\ s_{1k} \\ \vdots \\ s_{j1} \\ \vdots \\ s_{jk} \end{bmatrix} \qquad [9]$$

The unknown-desirable matrix m_M, must directly produce data $Z(m_M)_D$, as close as possible to the real data $Z_{D_{real}}$ (ideally the real data), following a linear relation between m_M and $Z(m_M)_D$ matrices (i.e. $B \times m_M = Z(m_M)_D$, where B is an unknown appropriately created matrix of

D x Mdata). However, the solution of such a system of equations is a non-linear problem. For this reason, the operation of the GIT algorithm is based on the iterative ***Gauss-Newton*** non-linear inversion algorithm, that uses an initial, *a priori* model parameter matrix m_M^{init} which is composed by appropriate reasonable-realistic parameter values (similar form to the m_M, Eq. [9]) such that to reduce, as much as possible, the following misfit-function, $F(m)$:

$$F(m) = \frac{1}{2}\left[\sum\nolimits_D W_D \cdot \left(Z(m_M)_D - Z_{D_{real}}\right)^2 + \sum\nolimits_M W_M \cdot \left(m_M - m_M^{init}\right)^2\right] \quad [10]$$

where W_D and W_M are the "weight" matrices (diagonal matrices of D x D and M x M data respectively, similar form with the $Z_{D_{real}}$ and m_M in Eq. [9]), characterizing the model parameters and the data, respectively. Each weight function can be expressed by the product of two partial weight functions as follows:

$$W_D = W_D^{init} \cdot C_D^{-1}, \quad W_M = W_M^{init} \cdot C_M^{-1} \quad [11]$$

where $C_D = \sigma_D^2$ and $C_M = \sigma_M^2$ are the *a priori* covariance matrices of data (D x D) and model parameters (M x M), respectively (σ_D and σ_M the corresponding initially considered standard deviations), while $W_D^{init}$and W_M^{init} control the initial (pre-inversion applied) considered weight of each data and model parameter, respectively. Equal weights are considered for all data (W_D^{init} = 1), while for the initial values of the studied parameters (m_M^{init}), a reasonable distribution of the weights was considered, independently of the initially provided standard deviations, σ_M of the examined parameters. This distribution was applied since the number of the parameters corresponding to seismic source, to attenuation path and to site effect, is not equal. Thus, the W_M^{init} (Eq. [11]) was *a priori*, appropriately determined being equally "shared" between the following 5 investigated group of parameters of Eq. [8]: m_{0_i}, f_{c_i}, $\gamma_h(r_{ij})$, $Q_s(f_k)_n$ and $s_j(f_k)$ (1/5 to each group of parameters). However, because, the seismic moment parameters, m_{0_i} (including the M_{o_i}), are the only ones for which the initial values are not totally unknown, with respect to the other parameters, the weights were finally considered to be distributed as follows: 2/6 for the m_{0_i} parameters and 1/6 for the rest four group parameters. Moreover, since in this study, two sites with no amplification have been initially considered (reference sites, with $S_j(f_k)$ = 1), it was chosen to be expressed by the 50% of the total weights of the examined parameters. In this way all the other examined parameters which were mentioned above, share the rest 50% of the weights (i.e. 2/12 for the m_{0_i} parameters, 1/12 for the rest four group of parameters mentioned above and 6/12 the $S_j(f_k)$ of the reference sites).

The misfit, $F(m)$ reduction is attempted to be achieved at each iteration of the ***Gauss-Newton*** non-linear inversion algorithm (***Tarantola, 2005***) (included in the GIT algorithm developed here) by recomputing the new m_M^{x+1} model parameter matrix at each new iteration, x, based each time on the already computed, m_M^xd, of the previous iteration (for $x = 0$, it is $m_M^x = m_M^{init}$), applying the following formula:

$$m_M^{x+1} = m_M^x - \mu_x (G_x^T\, C_D^{-1} G_x + C_M^{-1})^{-1} \{ G_x^T\, C_D^{-1} [Z(m_M^x)_D - Z_{real}] + C_M^{-1} (m_M^x - m_M^{init}) \} \quad [12]$$

This inversion algorithm is based on the use of the partial derivatives matrix, G_x of the Z_{ijk} (Eq. [8] and [10]), for each parameter of the model, m_M^x (Eq. [9]), recalculated at each iteration x based on the following equation:

$$G_x = \frac{\partial Z(m_M)_D}{\partial m_M} \quad [13]$$

The partial derivatives of Eq. [13] of the 6 groups of parameters, included in the $\mathrm{m_M}$ matrix (m_{0_i}, f_{c_i}, $\gamma(r_{ij})$, Q_{s_n}, a_n and $s_j(f_k)$), have been computed and presented by ***Drouet et al., (2008a)***. The G_x matrix (D x M dimensions) is composed as follows:

$$G_x = \begin{bmatrix} \frac{\partial Z_{111}}{\partial m_{0_1}} & \cdots & \frac{\partial Z_{111}}{\partial m_{0_i}} & \frac{\partial Z_{111}}{\partial f_{c_1}} & \cdots & \frac{\partial Z_{111}}{\partial f_{c_i}} & \frac{\partial Z_{111}}{\partial \gamma_1} & \cdots & \frac{\partial Z_{111}}{\partial \gamma_h} & \frac{\partial Z_{111}}{\partial Q_{s_1}} & \cdots & \frac{\partial Z_{111}}{\partial Q_{s_n}} & \frac{\partial Z_{111}}{\partial s_{11}} & \cdots & \frac{\partial Z_{111}}{\partial s_{jk}} \\ \vdots & \cdots & \vdots & \vdots & \cdots & \vdots & \vdots & \cdots & \vdots & \vdots & \cdots & \vdots & \vdots & \cdots & \vdots \\ \frac{\partial Z_{ijk}}{\partial m_{0_1}} & \cdots & \frac{\partial Z_{ijk}}{\partial m_{0_i}} & \frac{\partial Z_{ijk}}{\partial f_{c_1}} & \cdots & \frac{\partial Z_{ijk}}{\partial f_{c_i}} & \frac{\partial Z_{ijk}}{\partial \gamma_1} & \cdots & \frac{\partial Z_{ijk}}{\partial \gamma_h} & \frac{\partial Z_{ijk}}{\partial Q_{s_1}} & \cdots & \frac{\partial Z_{ijk}}{\partial Q_{s_n}} & \frac{\partial Z_{ijk}}{\partial s_{11}} & \cdots & \frac{\partial Z_{ijk}}{\partial s_{jk}} \end{bmatrix} \quad [14]$$

following in horizontal axis the row of the m_M parameters and in vertical axis the row of the $Z_{D_{real}}$, data, presented in Eq. [9].

The inversion algorithm (Eq. [12]), is also controlled by the μ_x ($\mu_x > 0$) coefficient, which is an *ad hoc* real constant, defining the length of the "jump" at each iteration (small enough to avoid divergence of the algorithm and large enough to allow the algorithm to advance). Usually, it is considered, $\mu_x = 1$ (Tarantola, 2005). However, in some cases, by using $\mu_x = 1$, the inversion algorithm cannot steadily approach the minimum value at a local minimum of the misfit function, "moving" between more than one specific solutions at each new inversion iteration (Eq. [12]). For these cases the reduction of μ_x (e.g. ~ 0.8 or lower, $\mu_x > 0$) during the inversion iterations can help the algorithm to converge at one substantially stable solution of the desirable m_M model parameter matrix.

In the GIT algorithm developed here, an extra condition is considered into the system of equations created by Eq. [8] and the data and unknown parameters of which are expressed by the $Z_{D_{real}}$and m_M matrices (Eq. [9]). More specifically, a number of i extra equations corresponding to the i earthquakes, are also added at the system of equations and control the relation between seismic moment M_{o_i} and corner frequency f_{c_i} for each earthquake, i, by the Brune's stress drop ($\Delta\sigma$) formula, in bar units (1 bar = 10^5 Pa) (***Brune, 1970***) (same as Eq. [2]):

$$\Delta\sigma_i = \frac{7}{16} M_{o_i} \left(\frac{f_{c_i}}{0.37\,\beta} \right)^3 10^{-5} \qquad [15]$$

where β is the shear wave velocity (same as in Eq. [2]). In fact, these stress drop values, $\Delta\sigma_i$ are considered as data in the system of equations. In case that they are initially unknown, their values should be reasonable (usually in the range of 1-100 bar, e.g $\Delta\sigma_i$ = 10 bar) and their *a priori* C_D covariance values (Eq. [11]) should be large enough (quite high standard deviations, σ_D, e.g. σ_D = 1000), so as their initial weight being quite low and these initial values do not affect the inversion process as well as the solution of the model parameter.

Thus, the new system of equations, which is attempted to be solved by the inversion algorithm, will have as data, $Z_{D_{real}}$, the matrix finally expressed by Eq. [16], while the unknown model parameters matrix, m_M will remain the same, since M_{o_i} (actually m_{0_i}, Eq. [8]) and f_{c_i} are already included in it.

$$Z_{D_{real}} = \begin{bmatrix} Z_{111} \\ \vdots \\ Z_{11k} \\ \vdots \\ Z_{1j1} \\ \vdots \\ Z_{1jk} \\ \vdots \end{bmatrix}, \quad \begin{bmatrix} \vdots \\ Z_{i11} \\ \vdots \\ Z_{i1k} \\ \vdots \\ Z_{ij1} \\ \vdots \\ Z_{ijk} \\ \vdots \end{bmatrix}, \quad \begin{bmatrix} \vdots \\ \Delta\sigma_1 \\ \vdots \\ \Delta\sigma_i \end{bmatrix} \qquad [16]$$

For the extra considered equations (Eq. [15]), in Eq. [16], with respect to, the corresponding partial derivative functions (Eq. [13]), required in the inversion algorithm (Eq. [12]), were defined and presented below:

$$\frac{\partial \Delta\sigma_i}{\partial m_{o_i}} = \frac{7}{16} \cdot M_{o_i} \cdot \left(\frac{f_{c_i}}{0.37\,\beta} \right)^3 \cdot ln(10) \cdot 10^{-5},$$

$$\frac{\partial \Delta\sigma_i}{\partial f_{c_i}} = \frac{7}{16} \cdot M_{o_i} \cdot 3\, \frac{{f_{c_i}}^2}{(0.37 \cdot \beta)^3} \cdot 10^{-5}, \qquad [17]$$

$$\frac{\partial \Delta\sigma_i}{\partial \gamma_h} = \frac{\partial \Delta\sigma_i}{\partial Q_{s_n}} = \frac{\partial \Delta\sigma_i}{\partial \alpha_n} = \frac{\partial \Delta\sigma_i}{\partial s_{jk}} = 0$$

and they are added at the end of the G_x matrix in Eq. [14], as the new equations (Eq. [15]) which have been added at the end of the $Z_{D_{real}}$, in Eq. [9], leading thus to Eq. [16].

At this point, it is useful to mention that the study of $log_{10}(f_{c_i})$, $log_{10}(Q_{s_n})$ and $log_{10}(a_n)$ parameters instead of f_{c_i}, Q_{s_n} and a_n at the parameter model, m_M (Eq. [9]), is a more convenient choice, avoiding the negative values for these parameters and studying them with a logarithmic "weight" which seems to better represent them. This choice is reasonable if we think that the visual

selection of the corner frequency on the Fourier spectrum of a Source Time Function, is accomplished based on a *log-log* dimension space (figure), in contrast to a *log-lin*, or a *lin-lin* one, where the higher frequencies exhibit disproportionately higher weights than the lower ones. The same disproportionate weights in frequencies are also applied to the quality factor, Q_s (Eq. [7]), which is frequency, f_k dependent. Finally, based on the above, the partial derivatives G_x, required in Eq. [12], must also be adjusted on these logarithmic parameters. It's worth noting that based on the logarithmic expressions of the above three group of parameters, the inversion tests, applied in this study using synthetic data, (details are given below), but also the GIT application on real data, converged easier to the final solutions of m_M, avoiding "diversions" and failures in computations. Finally, the results of the investigated logarithmic parameters were subsequently converted to linear values so that they are easier comparable to the synthetic ones.

3.3 Results

3.3.1 GIT Algorithm Application-Validation to Synthetic Data

3.3.1.1 Synthetic Data

In order to test the correctness and the computational validity of the developed in this thesis inversion algorithm, as well as possible limitations and potentials, a synthetic dataset consisted of 4313 synthetic Fourier spectra was created based on Eq. [7]. This synthetic dataset was created for a parameter model approximating a simplified actual dataset. Synthetic S-wave spectra are computed for 20 equally distributed in logarithmic scale frequencies between 0.5-14 Hz and correspond to epicentral distances between 20-200 km. It is obvious that this is a non-ideal dataset that would cover all possible features of an actual one, but it is used to investigate the reliability computation level of the proposed algorithm and possible limitations and potentials. The synthetic parameters are presented below.

60 stations were considered being non-homogeneously distributed in central and southern Greece (**Figure 12** and **Appendix G**) with locations coincident with the ITSAK permanent accelerometric network stations (http://www.itsak.gr). In addition, 126 shallow earthquakes at zero depth were considered being randomly distributed in the same area (**Figure 12**). Their seismic source spectra follow the scaled Brune's model (first term of the product in Eq. [7]), for seismic moments M_o computed from the moment magnitudes, M_w (Eq. [3]) and from the corner frequencies, f_c given in **Appendix H**. Moment magnitudes, M_w range between 1.0 and 6.0, while corner frequencies, f_c were computed from the synthetic M_w based on Eq. [2] for stress drop $\Delta\sigma$ = 100 bar. Four typical seismic source spectra of M_w = 3, 4, 5, 6 are given in **Figure 13a**. The hypocentral distances, r_{ij} used in the inversion, are in fact epicentral distances, since the depths of the earthquakes were considered to be zero.

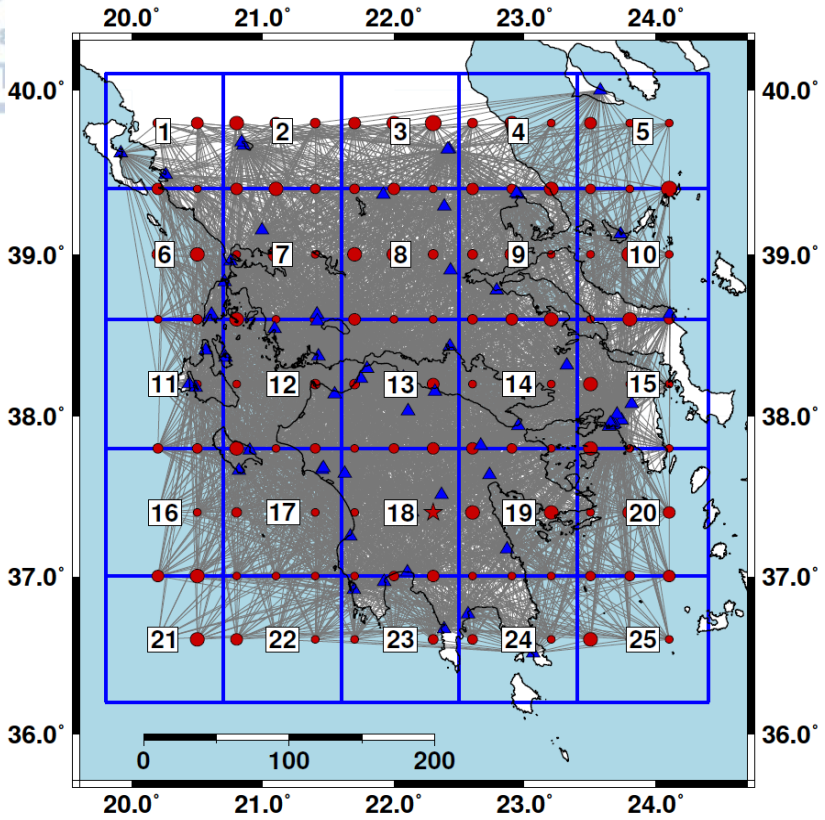

Figure 12. The 4313 theoretical ray paths (grey lines) correspond to the synthetic spectra created by the 126 artificial seismic sources (red circles, **Appendix H**) and one more (red star in rectangular No 18 , M_w = 6.0) theoretically recorded at 60 site-stations (blue triangles), information of which are given in **Appendix G**. The background of this figure (part of Greece) is depicted in order to give a more realistic sense of this experiment and does not express the synthetic data.

The geometric attenuation factor is controlled by three values of gamma (**Table 1**) for the distance ranges 20-100 km, 100-140 km and 140-200 km, while anelastic attenuation was considered to vary for each one of the 25 individual regions (**Figure 12**), with different frequency dependent quality factors (**Table 2**). Considering the site effect factor at each one of the 60 sites, the HVSRs computed by ***Grendas et al., (2018)*** were adopted here as synthetic values. These HVSRs site amplification values are used here for convenience as random values, instead of creating new ones. For the 2nd, 3rd and 4th inversion tests, presented below, the logarithmic values, Z_{ijk} (Eq. [8]), of the synthetic spectra, $A_{ij}(f_k)$, (Eq. [7]), were "contaminated" by computationally inserting "random errors" (noise) at each frequency f_k. The whole number of these errors were normally distributed around zero with standard deviation ± 0.2. This data alteration took place in order to represent even better the Fourier spectra computations as in actual seismic records. In **Figure 13b,c** the synthetic acceleration Fourier spectra, $A_{ij}(f_k)$, corresponding to a single earthquake (number 50, **Appendix H**) at all the sites and to all the earthquakes at a single station, ITE1 (**Appendix G**), with intense amplification evident in all the synthetic spectra, are presented.

Four groups of inversion tests on the synthetic data presented above, using different initial parameter models, were performed and the results of these tests are given below.

Briefly, the first inversion test constitutes a simple but essential computation test of the inversion algorithm confirming the correct inversion process. More specifically, the synthetic parameters are used as the initial model parameters, with relatively large standard deviation, expecting the algorithm to precisely invert for the synthetic ones. The synthetic spectra used (only for this case) were not contaminated with a 0.2 standard error, as in all the other tests, in order to precisely detect possible malfunction of the algorithm.

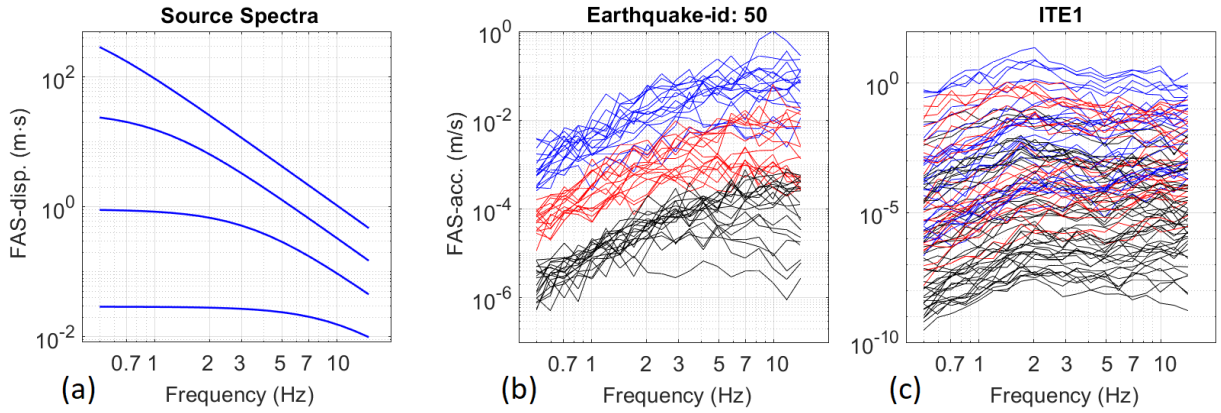

Figure 13. (**a**) Four characteristic seismic source spectra (***Brune, 1970***) for M_w = 3, 4, 5 and 6 computed for stress drop $\Delta\sigma$ = 100 bar (details in the text). (**b,c**) The synthetic acceleration Fourier spectra for a specific case, that of event number "50" (**Appendix H**) for all the 60 stations, and (**c**) of the ITE1 station (**Appendix G**), for all the earthquakes. Blue, red and black colors correspond to 20-100 km, 100-140 km and 140-200 km hypocentral distance ranges, respectively, related to the synthetic values of gamma parameter (**Table 1**).

The 2nd test is a kind of a "blind" inversion test, simulating a real case study, where all the study parameters are initially unknown. However, this test is not totally "blind", since the specific sub-areas 1 to 25 (**Figure 12**) are studied and not random ones. Such a reliability inversion test constitutes a main step to understand, to a certain degree, the computation potential of the algorithm, in order to "move" to a real dataset study investigating this regional 2-D pseudo-tomography of anelastic attenuation factor.

The 3rd and 4th inversion tests are similar to the second one but using each time one or more stable initial parameters. These parameters are the known ones among the synthetic parameters, considering them as "reference" ones. These tests are also simulating a real case study, where some parameters, as the moment magnitudes or site amplifications are *a priori* known from other studies. The 3rd and 4th aforementioned inversion tests aim at improving the reliability of blind inversion results and at a better understanding of their stability under different reference parameters. After all these tests, some constraints and limitations of the developed algorithm are suggested before its application to real dataset.

Table 1. The values of gamma (γ_h) parameter as they were considered in the synthetic model and in the initial model of the inversion tests, as well as the corresponding ones computed in the three inversion tests (2nd, 3rd, 4th).

Range (h) of distances (km)	Gamma (γ_h)				
	Synthetic	Initial (inv.)	Inversion Tests Results		
			2nd	3rd	4th
20-40	1.00	1±0.5	0.951 ± 0.009	0.995 ± 0.006	1.004 ± 0.006
40-60			0.953 ± 0.008	0.995 ± 0.006	1.004 ± 0.006
60-80			0.954 ± 0.008	0.995 ± 0.006	1.004 ± 0.006
80-100			0.953 ± 0.008	0.994 ± 0.006	1.002 ± 0.006
100-120	1.15		1.104 ± 0.008	1.144 ± 0.006	1.152 ± 0.006
120-140			1.104 ± 0.008	1.143 ± 0.006	1.152 ± 0.006
140-160	1.40		1.353 ± 0.008	1.392 ± 0.006	1.401 ± 0.006
160-180			1.354 ± 0.008	1.393 ± 0.006	1.401 ± 0.006
180-200			1.353 ± 0.008	1.393 ± 0.006	1.400 ± 0.006

Table 2. The synthetic frequency dependent quality factors ($Q_s(f_k)_n = Q_{s_n} f_k^{a_n}$) and the computed ones in the three inversion tests (2nd, 3rd, 4th), for the 25 sub-areas (**Figure 12**).

n	Syn Q_{s_n}	Inversion Tests Results, Q_{s_n}			Syn (a_n)	Inversion Tests Results, *alpha* (a_n)		
		2nd	3rd	4th		2nd	3rd	4th
1	853	933±586	1007± 665	956± 626	0.56	0.537±0.281	0.529±0.293	0.571±0.297
2	622	471± 95	508± 109	518± 110	0.69	0.714±0.096	0.701±0.102	0.695±0.096
3	351	323± 37	341± 40	347± 40	0.43	0.431±0.050	0.416±0.052	0.401±0.051
4	513	388± 63	417± 72	422± 73	0.84	0.883±0.085	0.881±0.091	0.885±0.089
5	402	477±163	525± 193	610± 231	0.73	0.570±0.154	0.546±0.165	0.461±0.152
6	76	73.5±1.7	074± 1.7	74.2± 1.6	0.36	0.373±0.010	0.371±0.010	0.370±0.009
7	240	219± 11	225± 12	227± 12	0.45	0.469±0.019	0.462±0.019	0.459±0.019
8	123	116± 03	119± 03	119± 03	0.39	0.410±0.009	0.404±0.009	0.404±0.009
9	184	161± 07	166± 07	166± 07	0.78	0.825±0.016	0.822±0.016	0.825±0.016
10	240	213± 16	221± 17	225± 17	0.73	0.776±0.034	0.771±0.035	0.763±0.033
11	417	332± 40	329± 38	344± 39	0.43	0.472±0.053	0.483±0.051	0.457±0.048
12	49	47.9±0.5	48.2± 0.5	48.3± 0.5	0.69	0.697±0.004	0.696±0.004	0.695±0.004
13	903	662±105	740± 128	761±135	0.94	0.931±0.052	0.930±0.058	0.925±0.059
14	945	602± 89	669± 106	681±110	0.78	0.846±0.050	0.837±0.055	0.837±0.055
15	491	386± 48	415± 055	420±56	0.70	0.760±0.057	0.750±0.060	0.749±0.059
16	489	353± 44	362± 45	366±45	0.10	0.211±0.053	0.204±0.053	0.199±0.051
17	338	291± 20	302± 21	308±021	0.38	0.418±0.026	0.408±0.027	0.398±0.026
18	900	714±123	801±151	817±154	0.59	0.645±0.059	0.619±0.065	0.618±0.065
19	369	328± 25	346± 27	347±27	0.45	0.474±0.028	0.460±0.029	0.460±0.028

20	111	107± 2.6	108± 2.6	109±2.6	0.12	0.134±0.010	0.131±0.010	0.126±0.009
21	781	996±458	1021±474	1058±536	0.22	0.163±0.158	0.163±0.158	0.182±0.176
22	390	222± 26	229±27	244±0	0.83	1.000±0.065	1.003±0.067	0.945±0.054
23	241	221± 14	226±14	230±14	0.15	0.175±0.027	0.167±0.027	0.160±0.026
24	404	358± 55	381±61	390±62	0.86	0.924±0.080	0.924±0.085	0.911±0.076
25	96	99.5±9.1	101±9.3	103±9.4	0.80	0.760±0.048	0.757±0.049	0.745±0.047

3.3.1.2 1st Inversion Test

Firstly, the synthetic dataset (without the contamination of normally distributed input standard errors) was inverted using as initial model the one composed by known synthetic values, but with *a priori* large covariance values. As it was expected the calculated results of this inversion, for all the study parameters, are in absolute agreement with the corresponding synthetic parameters. This test consisted a necessary step in order to confirm the correct computational operation of the algorithm. The results of this test are not presented since they are identical to the synthetic ones.

3.3.1.3 2nd Inversion Test

In the second inversion test a kind of "blind" inversion is attempted, using as initial model a reasonable one, that could represent a real case, while the investigated synthetic model is unknown. This test focuses more on detecting the parameters estimation potential and any possible limitations of the proposed algorithm in relation to the initial model which could be used in a case of "blind" inversion. Before the presentation of the results for this inversion test, the values of the initial parameter model, as well as the *a priori* model and data covariance values, are given below.

Starting from the source parameters, the initial m_0 parameters (Eq. [8]) were defined based on the moment magnitudes, M_w, given in **Appendix H**, which were "contaminated" by input errors normally distributed around zero with standard deviation ±0.3, a bit higher than the typically considered ±0.2, in real cases, so as to test the computational reliability of the inversion algorithm by using initial input M_w values, with even higher deviations from the expected M_w synthetic values. Using these initial M_w values, the corresponding steps which are applied on real datasets GIT, where the initial m_0 are based on the already computed M_w or M_L provided in seismological catalogues, were followed. Since the M_w or M_L are accompanied by their standard deviation (usually around 0.2), it is obvious that their values may deviate from the real ones. For this reason, the initial m_0 parameters in the inversion test, are based on the "contaminated" M_w values, simulating a real case. The *a priori* standard deviation values of M_w used in inversion was considered ±0.2 for all synthetic earthquakes. Initial $log_{10}(f_c)$ values, were calculated from the corner frequencies, f_c, based on Eq. [2] for stress drop, $\Delta\sigma$ = 10 bars, using the aforementioned initial M_w in combination with Eq. [3]. Their *a priori* standard deviation values were considered very large, σ_{f_c} = 1000 Hz, in order to be almost "freely" inverted. For the stress drop parameters, $\Delta\sigma_i$ (Eq. [15]) used as data (Eq. [16]) (i, extra equations at the system of equations), it was taken

$\Delta\sigma$ = 10 bars, having *a priori* an also large standard deviation $\sigma_{\Delta\sigma}$ = ±400 bars, so that the relation between the inverted M_o and f_c (Eq. [15]) is not significantly affected. Strongly constrained initial $\Delta\sigma_i$ can be used in cases where the real stress drop is known.

Regarding the attenuation factor, the geometrical spreading parameter gamma, $\gamma_h(r_{ij})$ was studied for h = 9 different distance ranges as they are presented in **Table 1**, with initial gamma value, $\gamma_h(r_{ij})$ = 1.0±0.5 for all distance ranges. Anelastic attenuation parameters were studied for the 25 sub-areas (**Figure 12**). The initial values of the 25 frequency independent quality factors were: $log_{10}(Q_{s_n})$ = 2 (Q_{s_n} = 100) (Eq. [7]) with standard deviation, $\sigma_{log10(Q_{s_n})}$ = ± 1, so one standard deviation of Q_{s_n} ranges between 10 and 1000 (**Table 2**).The initial values corresponding to the 25 alpha parameters (Eq. [7]) of the frequency dependent quality factor were $log_{10}(a_n)$ = -0.4815 (a_n = 0.33) and their initial standard deviation was, $\sigma_{log10(a_n)}$ = ± 0.4771, so the one standard deviation of a_n ranges between 0.11 and 0.99 (**Table 2**). The site spectra amplification factors, s_{jk} (Eq. [7]), were considered for all the j sites as: $s_{jk} = log_{10}(S_{jk})$ = 0±1, so the one standard deviation of S_{jk} ranges between 0.1 and 10. The above range is reasonable and is usually considered in "blind" inversions where the site effects are unknown. Finally, the *a priori* covariance values of the data were considered to be 0.2.

The results of this inversion test were computed after 20 iterations of the inversion algorithm. From the 5th iteration the inversion quickly converged at a local minimum of the misfit function and the misfit substantially stabilized at the 10th iteration. In **Figure 14a**, the comparison of the computed moment magnitudes M_w with the initial synthetic values of M_w, is presented. It is encouraging that the algorithm computes the correct values of synthetic moment magnitudes, using different initial ones (**Appendix H**) with negligible deviation, up to a maximum of ±0.02 for most of the inverted magnitudes.

In **Figure 14b**, a plot of the computed corner frequencies f_c versus moment magnitudes M_w, is shown and their relation is compared with the Brune's stress drop (dashed lines) computed by Eq. [15]. As it can be seen, for M_w > 3.0, the corner frequencies indicate a stress drop of ~100 bar. Thus, taking into account that the inverted, M_w are comparable with the synthetic ones (**Figure 14a)**, it is deduced that the corresponding inverted corner frequency values are similar to the synthetic ones, since their relation indicates stress drop $\Delta\sigma_i$ = 100 bar which are the synthetic stress drop values. For magnitudes 2.0 - 3.0 the computed corner frequencies tend to approximate the synthetic ones for $\Delta\sigma_i$ = 100 bar, while for M_w < 2.0 a remarkable dispersion of the estimated corner frequencies, is observed. The latter values are also characterized by large standard deviations which is satisfactory for the inversion results, taking into account that synthetic corner frequencies may fall beyond the data frequency range (f_c >14 Hz).

The results of geometrical spreading factor gamma, $\gamma(r_{ij})$, given in **Table 1**, are close to the synthetic ones, but they indicate slightly lower attenuation, probably affected by the lower initial values ($\gamma(r_{ij})$ = 1.0±0.5) for more than half of the synthetic gamma parameters. Frequency dependent quality factors $Q_{s_n}(f_k) = Q_{s_n} f_k^{a_n}$ (**Table 2**) for most of the, n, sub-areas (**Figure 12**) tend to approximate the synthetic ones, while a few of them are not in good agreement. It is

observed that the low synthetic Q_{s_n} (<200) values (high attenuation) are well determined, while some higher computed Q_{s_n} (>400) values (low attenuation) deviate up to 75% for a few of the corresponding synthetic values. The alpha (a_n) parameters of this factor present a satisfactory agreement with the majority of the corresponding synthetic values, but in two sub-areas, 16 and 21, where the deviations is greater than 25% (**Table 2**).

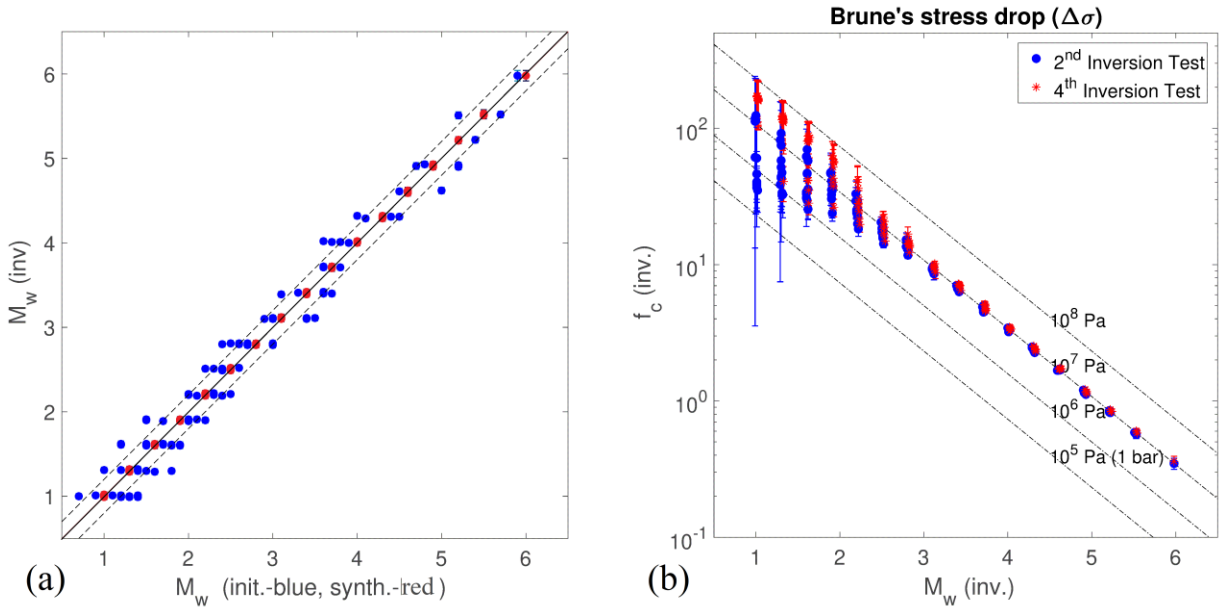

Figure 14. (**a**) Inversion computed moment magnitude M_w (inv.) versus initial M_w (blue points) used in the inversion and versus synthetic M_w (red points). With dashed line the range of ± 0.2 of the bisectrix is depicted. (**b**) Comparisons between the corner frequencies, f_c and moment magnitude, M_w, computed from the 2nd (blue points) and 4th (red points) inversion tests for initial $\Delta\sigma_i$ = 10 and 400 bar respectively. Brune's stress drop (Eq. [15]) values of 1, 10, 100 and 1000 bar are also shown (black dashed lines).

The relatively big differences in some of the higher Q_{s_n}, are apparent because the quality factor Q_s is exponentially related to the anelastic attenuation factor (third term of Eq. [7]) and the final effect of this difference is less than 25% for epicentral distances longer ~100 km. This is visually presented in **Figure 15**, through the ratio between the anelastic attenuation factors computed from the synthetic and inverted Q_s and alpha (a), for frequencies equal to 0.5, 1, 14 Hz, for all 25 sub-areas of **Table 2** (**Figure 12**). The computations are shown for up to 120 km, which is close to the largest hypocentral distance that a ray path can cross through each one of the 25 sub-areas of **Figure 12**. The most extreme difference in this ratio is ~1.27 and corresponds to sub-area, n = 22. Such a difference, less than 27%, corresponds to a logarithmic difference of the spectral values, $A_{ij}(f_k)$ (Eq. [7]) equal to 0.104. This difference is not so significant considering that the initially introduced errors in the $Z_{ijk} = log_{10}(A_{ijk})$ (Eq. [8]) values were ±0.2. As it is presented in **Figure 15**, most of the rest sub-areas have ratio differences lower than ~11%, corresponding to logarithmic spectra differences less than 0.046 (<<0.2). The "extreme" case of the sub-area n = 22 presented in **Figure 15**, is particular, because no complete ray path

(earthquake-station), passes exclusively through it (**Figure 12**). Such a condition may increase the difficulty level of inversion convergence. However, this condition did not affect the reliability in similar cases, as in cells, n = 20 and 25 (**Figure 12**), where there is no complete ray path passing only through them.

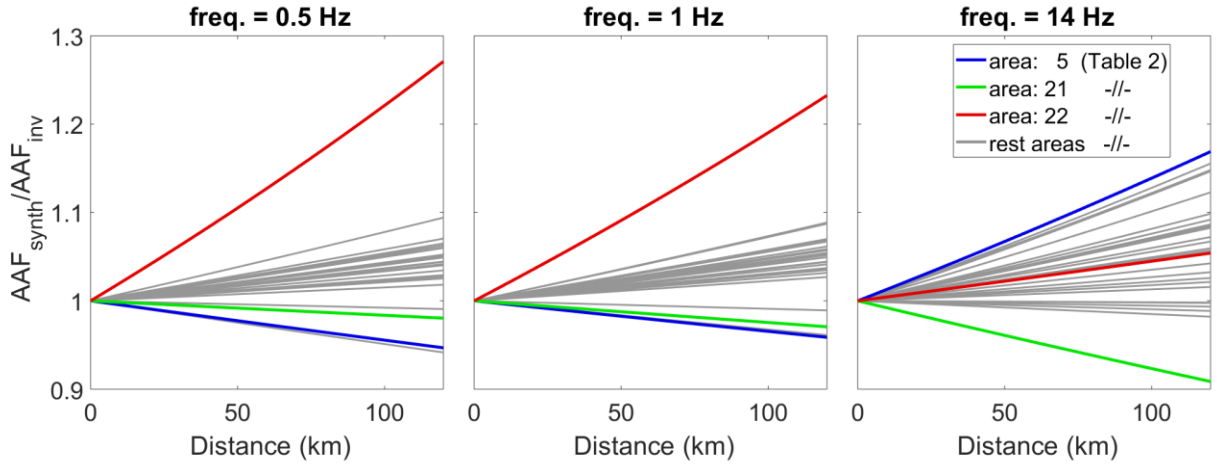

Figure 15. The ratio of Anelastic Attenuation Factor (third term of Eq. [7]), between the synthetic and the inverted values as they are presented in **Table 2** for all 25 sub-areas of **Figure 12**. With blue, red and green, the most extreme differences based on the ratio for the areas 5, 21 and 22, are respectively depicted, for frequencies 0.5 Hz (left), 1.0 Hz (middle) and 14 (right) Hz.

Finally, although the inverted site effect parameters (**Figure 16**) present the same shape with the synthetic site amplification, they have a systematic lower amplification by a factor of 2. In terms of the logarithm of site amplification this de-amplification corresponds to ~0.3, which is comparable with the inserted errors (0-0.2) in logarithmic values. However, the inserted errors in the logarithmic data do not affect the inversion results, since an extra inversion test with the same initial model in logarithmic data without inserted errors was performed and the results have not significantly changed. The observed de-amplification in the site parameter results is probably due to the interaction to the lower computed geometrical spreading, gamma parameters, $\gamma(r_{ij})$, than the expected synthetic set. Also, this de-amplification may be related to the initial values of site effects ($\log_{10}(S_{jk}(f_k))$ = 0±1) which are lower than almost all the synthetic values. The last assumption is confirmed since using higher initial site effect values (e.g. $\log_{10}(S_{jk}(f_k))$ = 0.3±10, or 0.477±10, corresponding to initial $S_{jk}(f_k)$ = 2 and 3, respectively) the results of site effect are higher and they are in agreement with the synthetic values. This trade-off between the initial values and the computed ones is a weak point and a possible limitation of the method that needs further investigation.

Concluding on this inversion test, the average computed misfit between the synthetic Fourier Spectrum, $Z_{D_{synth}}$ ($Z_{D_{real}}$ in Eq. [10]) and the computed, $Z(m_M)_D$ from the inverted model parameters is ~0.2, that is comparable with the initially inserted error of 0.2 used to "contaminate" the synthetic data.

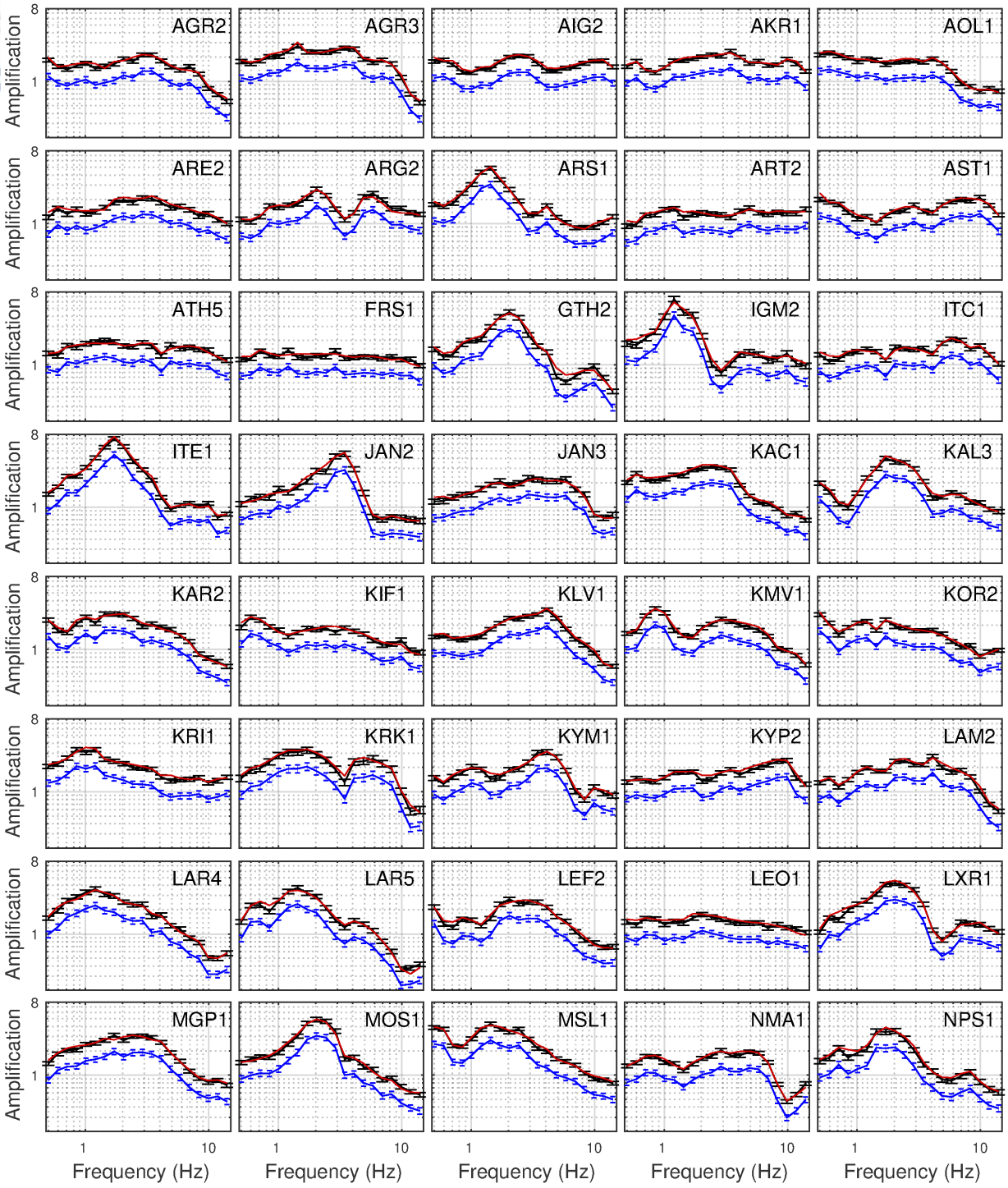

Figure 16. The synthetic site spectral amplification for each one of the 60 sites (red lines) used in this study (**Appendix G**, **Figure 12**) and the computed ones from the "blind" inversion of the 2nd test (blue lines), as well as from the inversion of the 3rd and 4th tests in which a reference site is used (black lines, identical results).

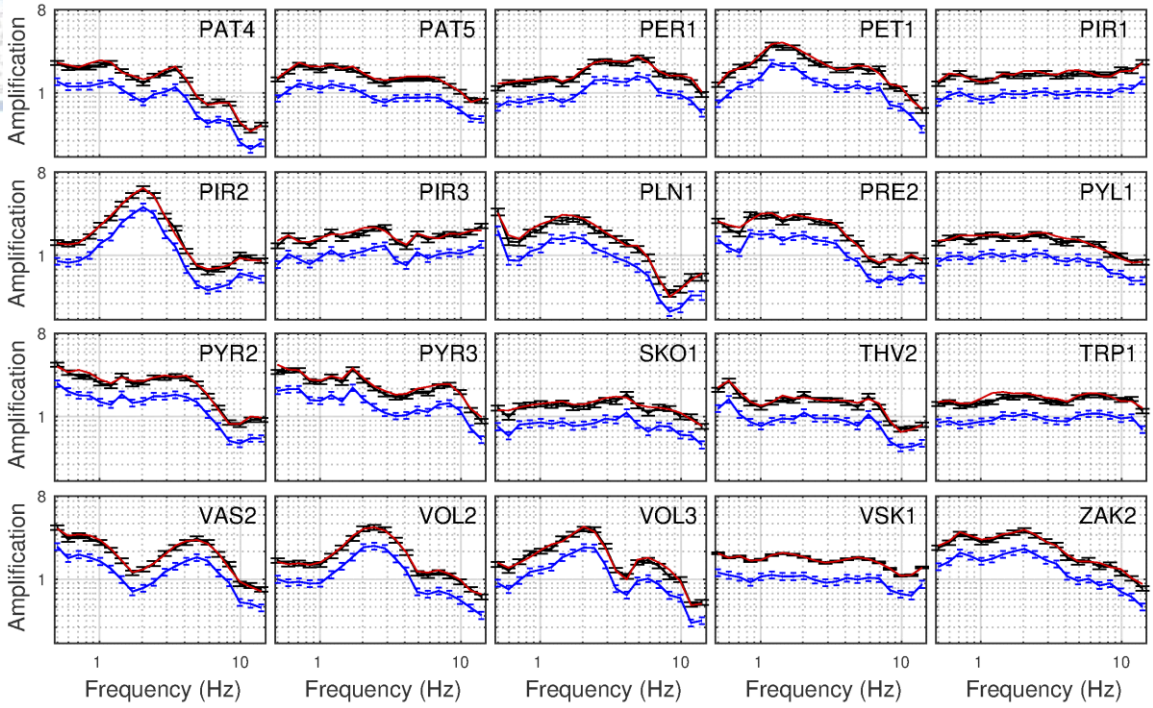

Figure 16. (continued)

3.3.1.4 3rd Inversion Test

This test consists of two inversion cases based on the same initial model as the one used for the 2nd ("blind") inversion test but using two different reference conditions. The first one uses the synthetic values of *VSK1* site factor, $S(f_k)$, that are close to 1 for each frequency, with very low initial standard deviation ($\sigma_{log10(S(f_k)),}$ = 0.001). The second one uses the initial value of $\gamma(r_{ij})$ = 1±0.005 up to 60 km. The results of these two cases are substantially similar to each other and for this reason only the results of the first case, using a reference site amplification, are presented below.

The results show an improvement of the estimation of almost all the study parameters and they are in even better agreement with the synthetic parameters, compared to those of the 2nd inversion test, which represents the "blind" inversion. Moment magnitudes are the same as those determined by the 2nd inversion, showing for some earthquakes a maximum difference of 0.01 between synthetic and inverted data. Corner frequencies are similar with those in the 2nd inversion test with the same $\Delta\sigma_i$ for all earthquakes used. Due to their similarity, M_{w_i} and f_{c_i} results are not presented in **Figure 14a,b**. Gamma values (**Table 1**), controlling the geometrical spreading attenuation, are apparently improved presenting very good agreement with the synthetic values. A similar improvement, though not so striking, is also observed for almost all Q_{s_n} and a_n values (**Table 2**), except for few cases in specific sub-areas (n = 1, 3, 5, 11, 21, 25) where the inverted results slightly diverge from the synthetic values in comparison to the previous inversion test. The inverted Q_{s_n} and a_n parameters are also in agreement with the synthetic ones, except for the n = 1,

5, 11, 16, 21, 22 sub-areas (**Figure 12**, **Figure 17**), where both of parmeters are not precisely determined, either presenting relatively high standard deviation or diverging at some level from the synthetic ones (**Table 2**). It's worth noting that these sub-areas are located at the edges of the entire study area (**Figure 12**) and their anelastic attenuation factors is more difficult to be estimated as mentioned also in the previous inversion test.

Finally, the site amplification results for all stations (**Figure 16**) are apparently improved and they are similar to the synthetic ones. The improvement of the estimated gamma and site parameters in relation to the very good or satisfactory stability of source and anelastic attenuation factors respectively, confirm an obvious trade-off between the geometrical spreading factor and the site amplification level. The average computed misfit between the calculated model parameters and those of the synthetic data is also ~0.2, as in previous inversion tests, indicating the non-linearity of the system of equations, approaching the solution close to the initial model parameters.

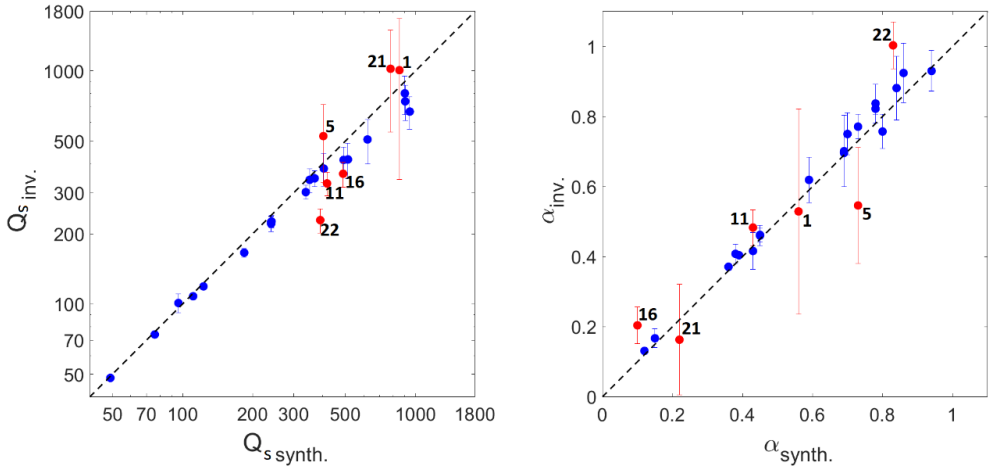

Figure 17. Q_{s_n} (**left**) and a_n (**right**) (Eq. [8]) synthetic values versus Q_{s_n} and a_n values computed from the 3rd inversion test, as they are given in **Table 2**. With red points the values of the specific sub-areas n = 1, 5, 11, 16, 21 and 22 (**Figure 12**) are depicted.

3.3.1.5 4th Inversion Test

This inversion test refers to a group of inversion sub-tests using as initial model the same as in 3rd one, with a reference site, but varying initial stress drop ($\Delta\sigma$) and corner frequency parameters, $\log_{10}(f_c)$, depending on $\Delta\sigma$. More specifically, three inversion applications were implemented using initial stress drop values, $\Delta\sigma$ = 70, 100 and 400 bar, knowing in advance that the synthetic value is 100 bar. In the first two cases (70 and 100 bars) all the results are similar with the ones derived from the 3rd inversion test, where the initial stress drop value was $\Delta\sigma$ = 10 bar, with negligible improvement compared to synthetic data. Consequently, these results are not presented here. In the last case ($\Delta\sigma$ = 400 bar) the M_w results are substantially similar as in 3rd inversion test, showing for some earthquakes slightly higher differences than the synthetic M_w (about 0.04), compared to 0.01 of the 3rd inversion test.

The computed Q_{s_n} and a_n values (**Table 2**) are negligibly improved for most of the cases, except for the areas n = 3, 4, 5, 9, 11, 21, 25, for which only negligible differences are observed with respect to the corresponding results of the 3rd inversion test. The same stability is also observed for the gamma values (**Table 1**), as well as for the site spectra amplifications indicating slight improvement. Consequently, these results are not presented since they are similar to those of the 3rd inversion test. The computed corner frequencies and stress drop, $\Delta\sigma$, values for magnitudes $M_w > 2.5$, (**Figure 14b**), remain in agreement both with the synthetic and with the previous inversion tests results. For lower magnitudes ($M_w < 2.5$), where the synthetic corner frequencies are beyond the data frequency range (> 14 Hz), the results cannot be reliably estimated to approach the synthetic data with stress drop, $\Delta\sigma$ = 100 bar. In fact, large standard deviations are calculated for these f_c values. This failure in determining most of the synthetic f_c values for frequencies higher than 14 Hz, remains the same as in the 2nd and 3rd inversion test. This instability is due to non-well determined f_c related to extreme initial $\Delta\sigma$ values (e.g. 10 and 400 bar) and can be indirectly used to detect those earthquakes with f_c probably out of the data frequency range. Consequently, records of such earthquakes may be removed from the dataset, so that they will not affect the rest of parameters in a new inversion application.

3.3.2 GIT Algorithm Application-Validation to Real Data (broader Aegean sea)

As it was mentioned above, the main goal of the GIT algorithms, is to conclude to a seismic parameter model, achieving as lower as possible misfit between the real and the computed data from inversion model. It is obvious that this misfit reduction indicates an increased reliability of the parameter model. The proposed in this study inversion algorithm aims at improving the previously developed algorithm by ***Drouet et al., (2008a)***, trying to reduce the data misfit and to calculate more representative seismic ground motion parameters. For this reason, a comparison of an application of the original GIT algorithm and the newly developed one, based on the same real data is attempted, in order to detect any improvement in results, expecting misfit reduction, as well as to show the applicability of the new algorithm in a real dataset. Thus, the real dataset inverted by ***Grendas et al., (2018)*** using the original algorithm proposed by ***Drouet et al., (2008a)***, is also inverted here and the comparison of the results are presented and discussed below.

Regarding the real dataset, it is briefly reminded that 4.204 S-wave acceleration Fourier spectra were inverted, corresponding to 136 earthquakes with moment magnitudes $4.2 \leq M_w \leq 6.5$ recorded at 112 accelerometric stations of ITSAK network (http://www.itsak.gr/) (**Figure 18**). These spectra are computed for 20 frequencies equally distributed in logarithmic scale between 0.25 Hz and 15 Hz, with hypocentral distances $20 \leq R_{hyp} \leq 350$ km. Their amplitudes are equal to the geometric convolution of the S-waves Fourier Amplitude spectra computed from both horizontal components (N-S and E-W) (Eq. [4]). The criterion of a Signal to Noise ratio greater than 3 in frequency domain was adopted for both horizontal components. Details of this dataset are analytically provided in ***Grendas et al., (2018)***.

The new inversion application was based on similar initial conditions of the model parameter, as the one used in ***Grendas et al., (2018)***, wherever this was possible. In some cases, higher initial standard deviation of the investigated parameters was adopted in this study, so that all parameters be even more "freely" inverted. Regarding the seismic source factor, the initial m_{0_i} parameters (Eq. [8]) were defined by Eq. [3] from the moment magnitude, M_w as computed by the Seismologic Station of AUTh (http://geophysics.geo.auth.gr/ss/). Their typical standard deviation (± 0.2) was used for the *a priori* covariance matrix, C_M (Eq. [11]). Initial $log_{10}(f_{c_i})$ values, were calculated from the corner frequencies f_{c_i} based on Eq. [2] for stress drop 5 bar, using the aforementioned initial M_w. Their *a priori* standard deviation values were considered large enough, σ_{f_c} = 1500 Hz, in order to be almost "freely" inverted. Concerning the unknown stress drop parameter, $\Delta\sigma_i$ it was considered $\Delta\sigma_i$ = 5 bar for all the seismic sources having an *a priori* high standard deviation σ_{Δ_σ} = ±1500 bar, so that the relation between M_w and f_{c_i} is not significantly affected.

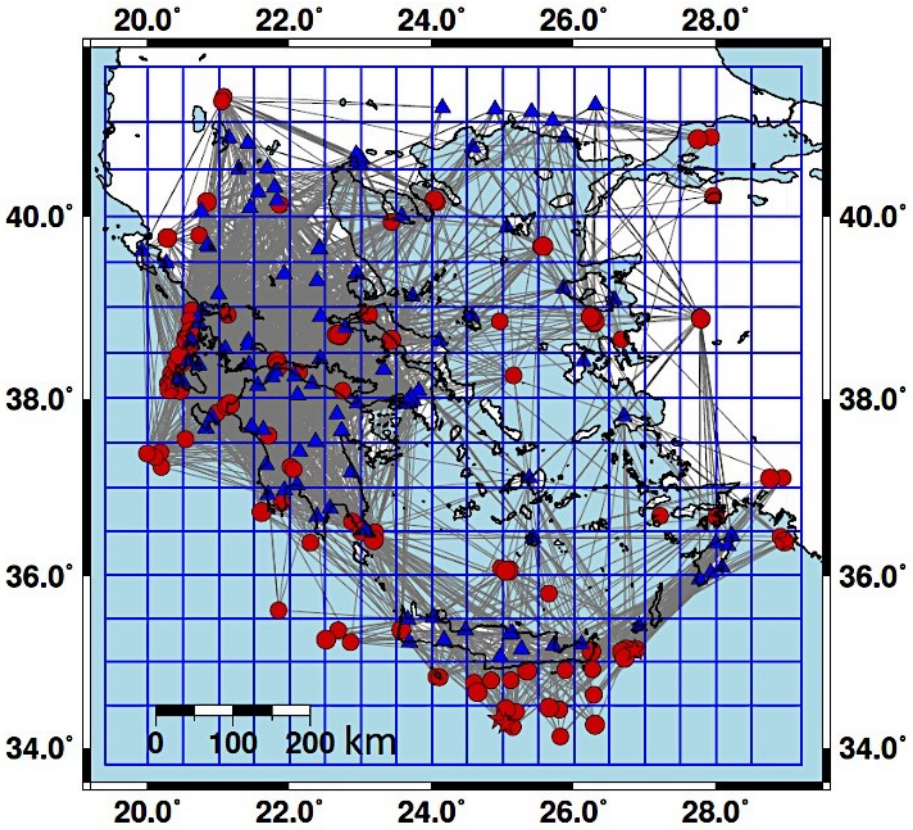

Figure 18. Ray paths (grey lines) of 4.204 actual seismic recordings, used by ***Grendas et al., (2018)*** and re-inverted in this study. Records correspond to 136 earthquakes (red circles) and to 112 accelerometric stations (blue triangles) of the ITSAK network. Blue lines constitute Meridians and Parallels that were chosen to define the 285 sub-areas studied for the anelastic attenuation factor. Details into the text. (Same as Fig. 1 of ***Grendas et al., (2018)***.

Regarding the attenuation factor, the geometrical spreading parameter gamma, $\gamma_h(r_{ij})$ was studied for h = 16 different distance ranges separated by 20 km as they are presented in **Table 3**, with initial gamma value, $\gamma_h(r_{ij})$ = 1.0±0.5 for all the distance ranges. Anelastic attenuation parameters were studied based on the separation of the total area into 285 sub-areas (cells) (**Figure 18**) between the Meridians 20° – 28.5° and the Parallels 34.5° – 41°, for 0.5° step. The borders of the total area were defined by Meridians 19.4° and 29.2° as well as by Parallels 33.8° and 41.6°. As it is obvious there are no ray paths crossing all the sub-areas of **Figure 18** and for this reason from the initial 285 sub-areas only 216 have been finally studied for the anelastic attenuation factors Q_{s_n} and a_n. Their initial values, $\log_{10}(Q_{s_n})$ = 2 (Q_{s_n} = 100) and a_n = 0.5, in combination with their *a priori* quite high standard deviation $\sigma_{\log10(Q_{s_n})}$ = ±0.6 (Q_{s_n} = 25–400, one standard deviation range) and σ_{a_n} = ±0.25, allows the algorithm to invert for these parameters without being significantly affected by their initial value.

The site amplification factors, s_{jk} (Eq. [8]), were considered for all the j sites as $s_{jk} = \log_{10}(S_{jk}(f_k))$ = 0±1, so the one standard deviation of $S_{jk}(f_k)$ ranges between 0.1 and 10. The stations: ATH5, KYP2, NAX1, SEIS, VSK1, were conventionally considered as "reference" stations, since their initial values were: $s_{jk} = \log_{10}(S_{jk}(f_k))$ = 0±0.6, corresponding to one standard deviation ranges of $S_{jk}(f_k)$ ~ 0.25 – 4. It is worth noting that in the past application (***Grendas et al., 2018***) of the algorithm of ***Drouet et al., (2008a)***, the reference condition was considered as the average value of these five site amplification factors, s_{jk}, in the entire frequency range, to be equal to 1. Moreover, as in the previous inversion, a crustal amplification generic rock velocity profile with Vs_{30} = 2000 m/s (***Boore and Joyner, 1997***) was also included to the site amplification factors. Finally, the *a priori* covariance values of the data were considered to be 0.3, based on a typical average to maximum standard deviation of the smoothed Fourier spectra computation with respect to the directly computed FAS by the Fourier Transform.

In this study 50 iterations of the inversion algorithm were implemented, to achieve the final model parameter solution presented below. The computed moment magnitudes (**Appendix I**) are presented in **Figure 19a** in comparison to the corresponding ones as determined from seismic catalogues (details in ***Grendas et al., 2018)***. In **Figure 19a**, the same results computed by ***Grendas et al., (2018)*** for the same data set, are also presented. Corner frequencies, f_{c_i} (**Appendix I**) are shown in **Figure 19b** in comparison to the computed M_w, indicating a geometric mean Brune's stress drop (Eq. [15]) of 26 bar (the one standard deviation range in logarithmic scale is 11 to 59 bar,), lower than the corresponding one computed by ***Grendas et al., (2018)***, (Δσ = 54 bar, with the one standard deviation range between 17 to 166 bar). The $\Delta\sigma_i$ values computed in this study do not present extreme cases (e.g. $\Delta\sigma_i$ > 1000), in comparison to the previous study, even though the initial standard deviation of Δσ was very high (Δσ = ±1500) and the corresponding one of the corner frequencies were significantly higher in this study (±1500) than in the previous one (±5).

Regarding the geometrical spreading factor, the computed gamma, $\gamma_h(r_{ij})$ parameters (**Table 3**) present a negligible increase from 1.10 to 1.12 for hypocentral distances 20-120 km and then a reduction from 1.12 to 1.05 for hypocentral distances 120-350 km. These values are

comparable to the average one (γ = 1.15) computed by ***Grendas et al., (2018)*** for the same dataset, exhibiting lower deviation from the characteristic spherical geometrical spreading (γ = 1).

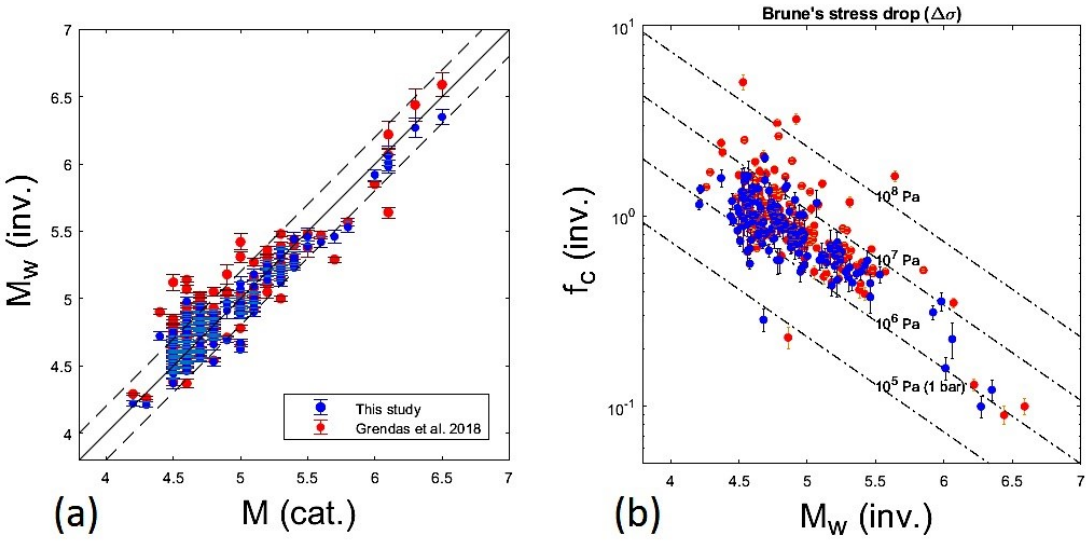

Figure 19. (**a**) The computed from the inversion moment magnitudes, M_w compared to the catalogue ones and (**b**) the computed from the inversion corner frequencies, f_c compared to the corresponding computed M_w. Blue points correspond to this study, while red points to the previous study by ***Grendas et al., (2018)*** using the same dataset.

Table 3. The values of gamma (γ_h) parameter Eq. [7] computed by the new inversion algorithm. Their values at the initial parameter model were γ_h = 1.0 ±0.5 for all the distance ranges.

Range (h) of distances (km)	Gamma (γ_h) (inversion)	Number of Records	Range of distances (km)	Gamma (γ_h) (inversion)	Number of Records
20-40	1.0998±0.0067	123	180-200	1.1078±0.0084	366
40-60	1.0990±0.0066	142	200-220	1.1008±0.0089	355
60-80	1.1134±0.0065	212	220-240	1.0920±0.0094	311
80-100	1.1134±0.0067	284	240-260	1.0850±0.0099	302
100-120	1.1179±0.0069	392	260-280	1.0828±0.0104	218
120-140	1.1130±0.0072	315	280-300	1.0807±0.0110	276
140-160	1.1132±0.0076	318	300-320	1.0693±0.0116	133
160-180	1.1100±0.0080	332	320-350	1.0537±0.0122	125

Anelastic attenuation factors Q_{s_n} and α_n (Eq. [8]) were computed for the 216 sub-areas , of the total 285 in **Figure 18** and they are given in **Appendix J**. Based on the inverted Q_{s_n} and α_n values at each sub-area, the frequency dependent quality factors $Q_{s_n}(f_k) = \mathrm{Q_{s_n} f_k^{a_n}}$ were computed for three characteristic frequencies 0.5 Hz, 1 Hz and 5 Hz and the results are presented in **Figure 20a,d,g**, respectively. For the decimal logarithms of these values ($\log_{10}(Q_{s_n}(f_k)$ the Coefficients of Variation, CV (%) were also computed for frequencies 0.5 Hz, 1 Hz and 5 Hz (**Figure 20b,e,h**, respectively) based on the corresponding logarithmic standard deviation (**Appendix J**), indicating

the reliability of these values. It is obvious that the lower CV (closer to zero, i.e. higher reliability) values are related to the higher density of the ray paths (**Figure 18**). Reasonably, the inverted "$\log_{10}(Q_{s_n}(f_k))$" values with CV > 10%, present relatively high variation and their level of reliability is low. Based on the above, the "smoothed" maps (**Figure 20c,f,i**) of the corresponding maps depicted in **Figure 20a,d,g**, were compiled using the $Q_{s_n}(f_k)$, data of the sub-areas with CV < 10%. The smoothing process was based on a Gauss filter of 0.25° (degrees), so that each cell (0.5° x0.5°) being affected by the "neighboring" cells.

These "smoothed" maps of the $Q_{s_n}(f_k)$ distribution (**Figure 20c,f,i)**, are presented only for visual reasons showing the "trend" of its spatial distribution. Short variations (~70-120) of Q_{s_n} (1 Hz) in comparison to the average 97.6 (***Grendas et al., 2018***) appears on the Greek mainland, while slightly lower values (higher attenuation) are presented towards the back-arc area (~30-70). Low values (~55) at 1 Hz were also observed by ***Polatidis et al., (2003)*** for the back-arc area, studying S-waves records for hypocentral distances 65-515 km.

High attenuation $Q_s(f)$ values (30 -360) of the upper crust of the continental Greece, were also observed by ***Hatzidimitriou et al., (1993)***, using strong motion data. Lower attenuation (Q_s = 400) for the upper 40 km crust of the broader Aegean area was observed by ***Hashida et al., (1988)*** using macroseismic data (> ~1 Hz), while high attenuation (Q_s = 60) was determined for the Northeast Aegean, in satisfactory agreement with the results of the present study. Similar lower attenuation (Q_s = 350±140) was also estimated for the upper 20 km crust of the broader Greek area, by ***Papazachos (1992)*** also based on macroseismic data, while ***Kovachev et al., (1991)*** found Q_s = 200-300 for frequencies around 8 Hz at the sea of Crete, in satisfactory agreement with the corresponding results of this study.

The inverted site Transfer Functions (TF) of this study (**Figure 21**) are in good agreement with the corresponding ones determined by ***Grendas et al., (2018)*** for the same dataset, with a few differences, which indicate improvement of $S_{jk}(f_k)$ factors. This may be due to the following reasons: (i) A better agreement of the well-known, surface rock station SEIS used as a reference one (no amplification). This is quite encouraging taking into account that its standard deviation in the initial parameter inversion model was quite high (one std of amplification range is 0.25 to 4) to restrict it to $S_{jk}(f_k)$ = 1. In addition, the rest 6 stations (ITS1, KLR1, LSM0, PLA1, PRF0, STL1) located close to SEIS in the wider sedimentary basin of Thessaloniki, present amplifications similar to their SSR (**Figure 21**) computed from this dataset using SEIS as reference station. The same is observed for the ATH5 reference station and the other 6 stations (MOS1, PER1, PIR1,2,3, KIF1) located close to it in the wider sedimentary basin of Athens. (ii) A non-negligible indication of improvement of the new $S_{jk}(f_k)$ estimation, is that the majority of the sites present amplifications equal or higher than those corresponding to S-waves Horizontal-to-Vertical Spectral ratio (**Figure 21**) computed from this dataset (***Grendas et al., 2018***). Such an observation is in agreement with a similar one by ***Haghshenas et al., (2008***). However, a few sites present amplification lower than the HVSR. The amplification of these sites remains an issue which is probably related to local peculiarities (e.g. low amplification of vertical component) that couldn't be modeled by the attenuation model of this GIT application.

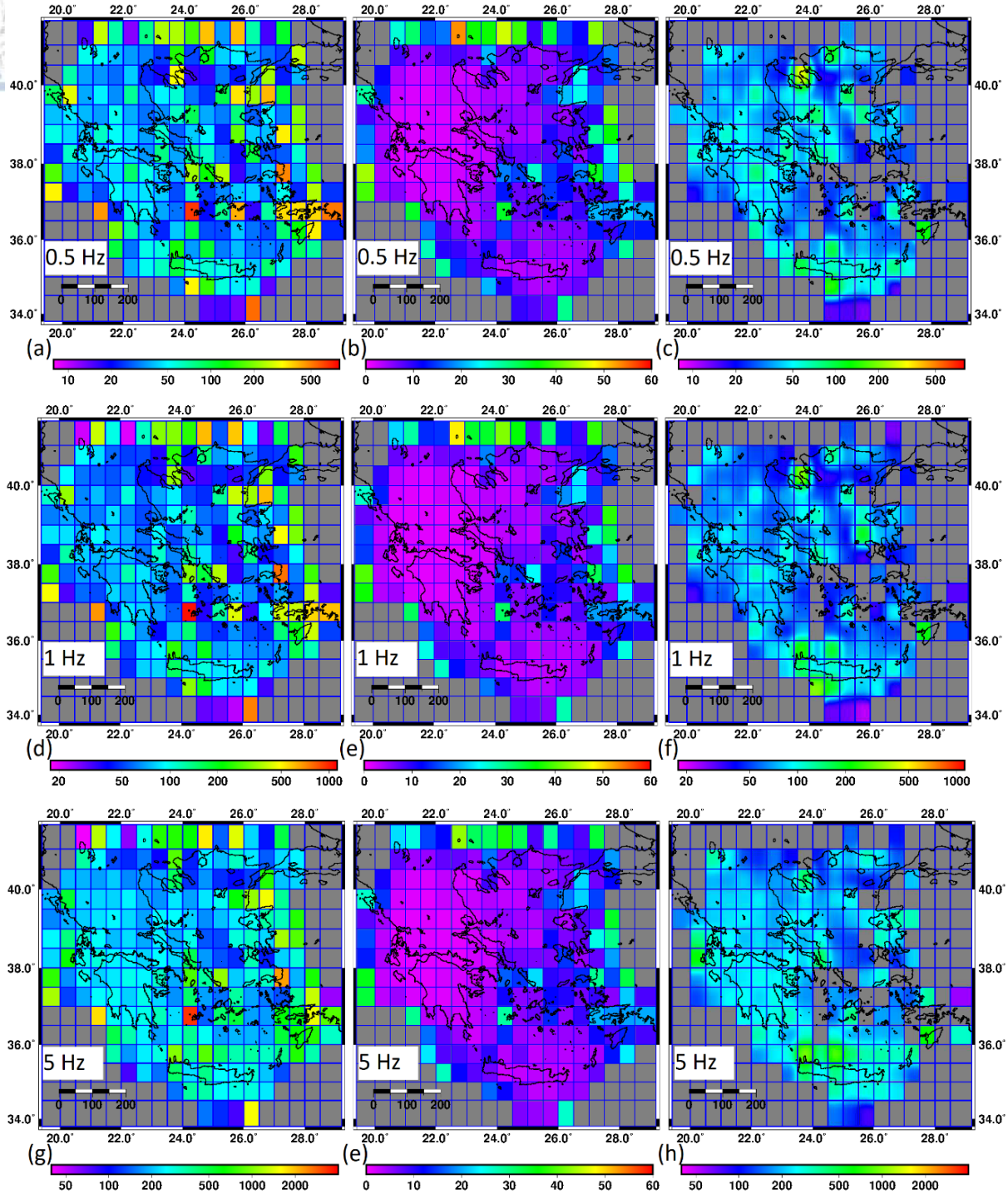

Figure 20. Three groups (in lines) of maps corresponding to the computed $Q_{s_n}(f_k)$ (**Appendix J**, Eq. [7]) for frequencies f_k = 0.5, 1 and 5 Hz, respectively. The 1st column maps (**a,d,g**) show the computed $Q_{s_n}(f_k)$ for the 216 sub-areas. The 2nd column maps (**b,e,h**) show the spatial distribution of the Coefficients of Variation, CV (%)for these $Q_{s_n}(f_k)$, in relation to their computed standard deviation. The 3rd column maps (**c,f,i**) show the smoothed spatial distribution of the $Q_{s_n}(f_k)$, taking into account only the sub-areas with CV < 10%.

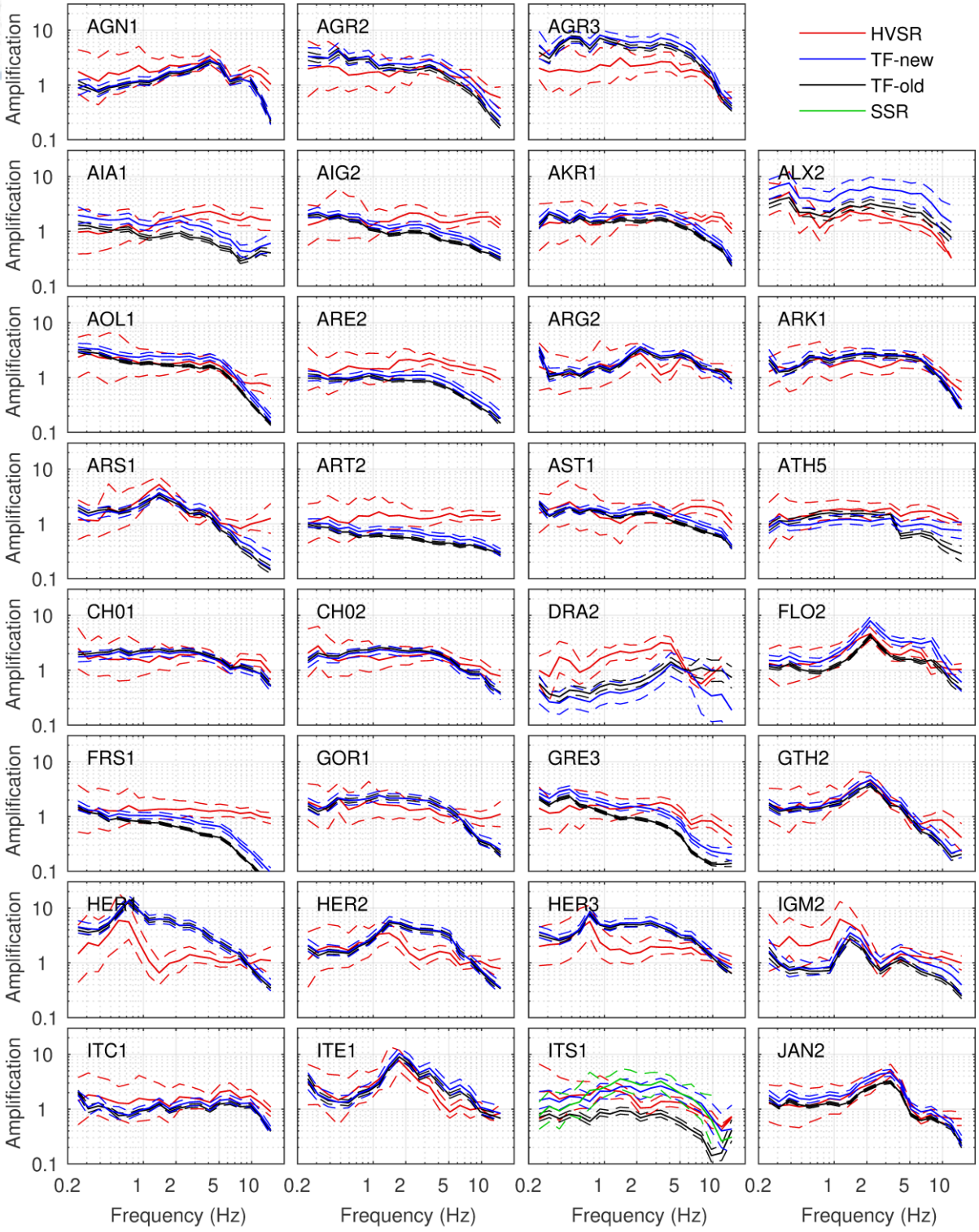

Figure 21. Site Amplification Factors $S_j(f_k)$ computed in this study (blue lines) and in the previous study of ***Grendas et al., (2018)*** (black lines), as well as the S-wave HVSR (red line) of the examined dataset and the SSR function (green line) for 12 sites (details into the text), as has been determined by ***Grendas et al., (2018)***.

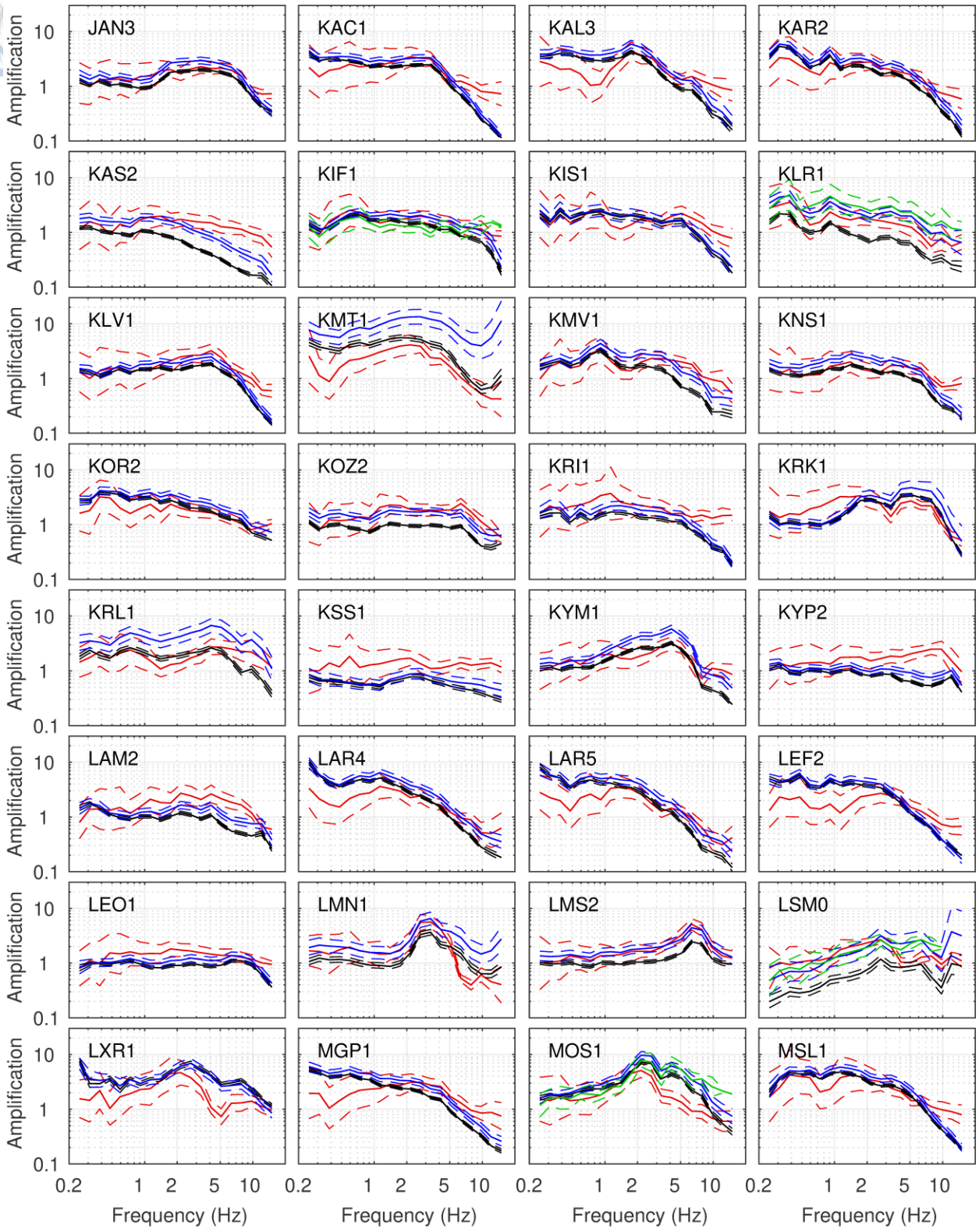

Figure 21. (continued)

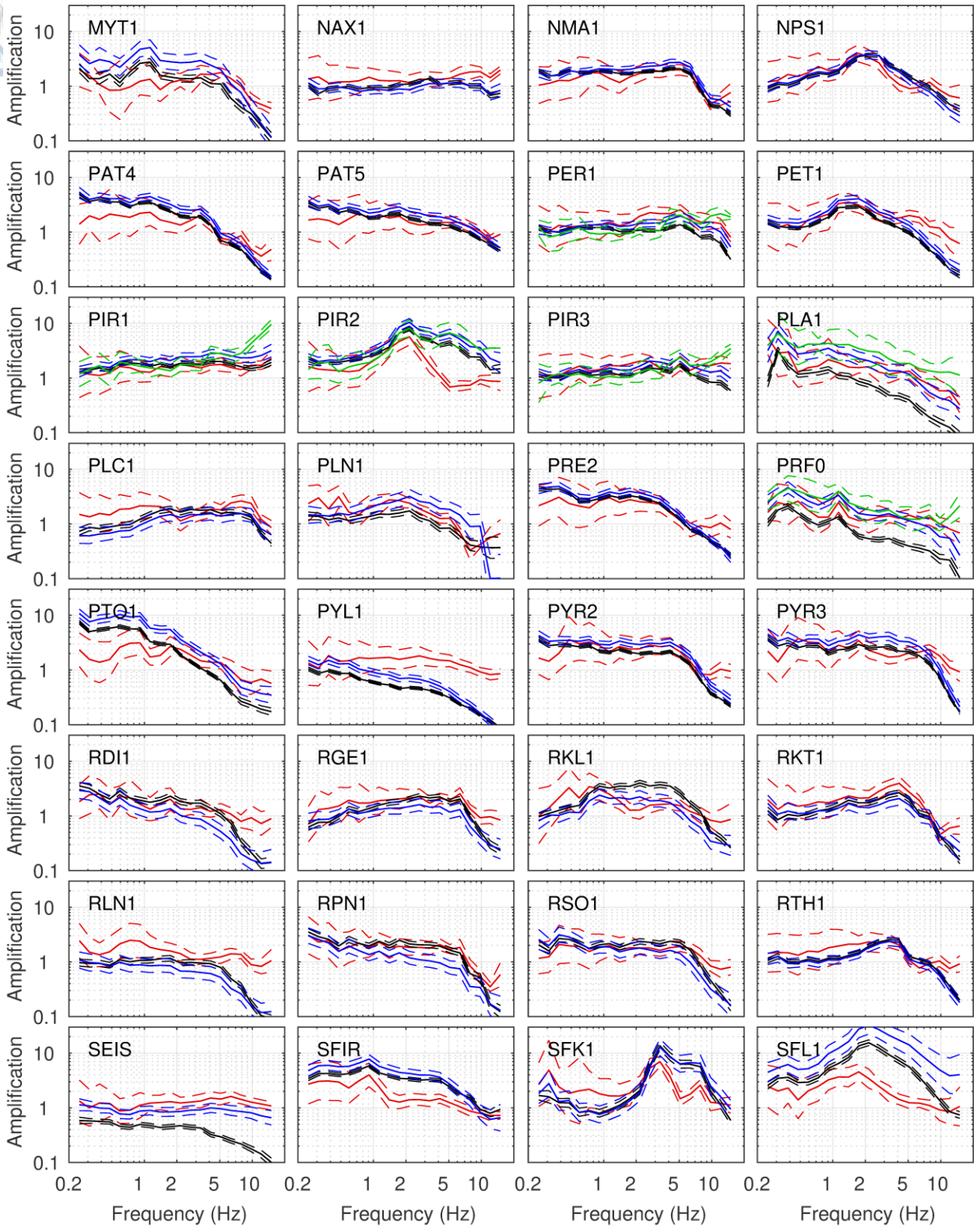

Figure 21. (continued)

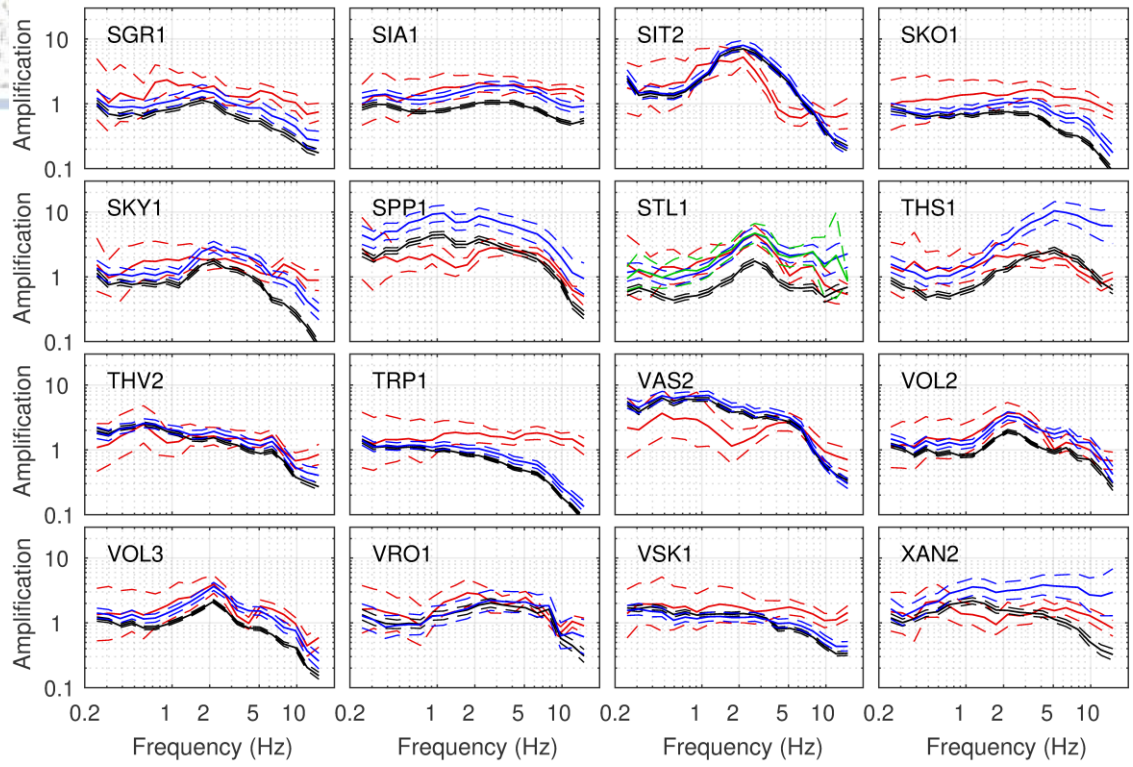

Figure 21. (continued)

The Residuals (**Figure 22a**) between the logarithmic values of the real spectra, $Z_{D_{real}}$ (Eq. [9] and [10]) and the corresponding spectra, $Z(m_M)_D$ as computed by the inverted model parameters, m_M, are normally distributed around zero (**Figure 22b**), with a standard deviation of 0.2275, which is ~9% lower than the corresponding one (0.25) determined by ***Grendas et al., (2018)***.

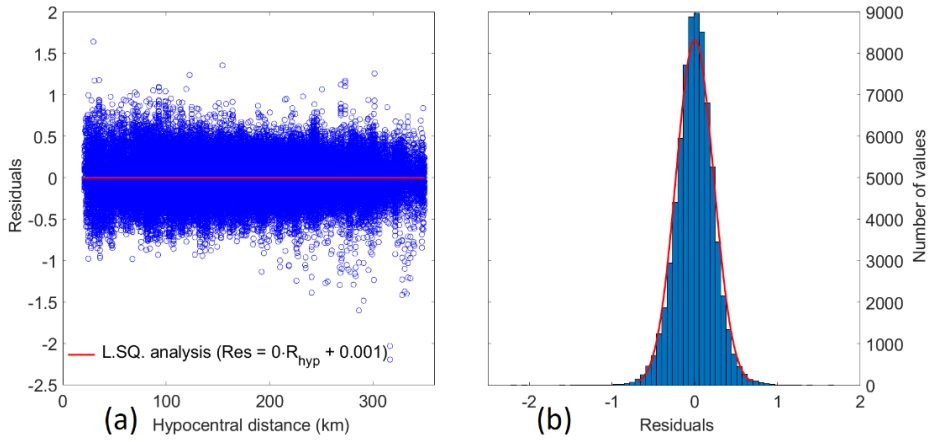

Figure 22. (**a**) Residuals between the logarithmic values of the real spectra, $Z_{D_{real}}$ (Eq. [10]) and the corresponding spectra, $Z(m_M)_D$ (Eq. [10]). (**b**) The distribution of the residuals of **Figure 22a (**normal with standard deviation = 0.2275).

3.3.3 GIT Algorithm Application to Real Data (western Greece)

The new GIT algorithm, which was used for the data corresponding to western Greece, was based on the following initial model parameters, $m_{M_{init}}$. Regarding the initial seismic moment magnitudes, M_w of all the 180 earthquakes used (**Figure 5**), it was considered $M_w = M_L$, where M_L is the local magnitude computed by the Seismological Station of Aristotle University of Thessaloniki (AUTh-SS) (http://geophysics.geo.auth.gr/ss), as given in **Appendix B**. Their initial standard deviations were considered equal to 0.2 given by AUTh-SS. Their corresponding initial corner frequencies values, f_c were determined by Eq. [2] for $\Delta\sigma$ = 1 bar, based on Eq. [3] and on the initial M_w values. Since, f_c values are unknown for all earthquakes, their initial standard deviations were considered quite high (σ_{f_c} = 5000) so that to be almost unweighted (Eq. [11]) and free to be investigated.

Regarding the geometrical spreading factor, 28 distance dependent gamma, $\gamma_h(r_{ij})$ (Eq. [7]) parameters were *a priori* defined with initial values 1 ± 0.5, for the distance ranges given in **Table 4**. For the anelastic attenuation factor the total area was divided into *n* = 420 cells (sub-areas) of 0.1° x 0.1° (**Figure 5**) (Longitude: 20.1°- 22.2° and Latitude: 37.4°-39.4°), for which the $\log_{10}(Q_{s_n})$ and the $\log_{10}(a_n)$ were investigated with initial values $\log_{10}(100) \pm \log_{10}(6)$ (std Q_{s_n} range: 16.6-600) and $\log_{10}(0.3) \pm \log_{10}(3)$ (std a_n range: 0.1-0.9), respectively.

For the unknown site amplification factors, $S_{jk}(f_k)$ of each site (both for vertical and horizontal component), the $\log_{10}[S_j(f_k)]$ parameters were investigated, with initial values 0±3. In other words, no amplification was initially considered for all the sites ($S_j(f_k)$ = 1), with a large range of investigated amplification from 0.001 to 1000 times.

A reference condition was also used to control the scaling of the estimated site and geometrical spreading factors of the inversion, where a trade-off between them is usually expected, as observed by the application of GIT algorithm in synthetic data, mentioned earlier in this chapter. More specifically, the VSK1 and CKWP stations, which are installed on surface rock sites (**Appendix C**), were chosen as reference sites under three considerations mentioned directly below and which are related to their deviation from a real, high shear wave velocity (Vs ~ 3500 m/s for pure hard rock) reference site.

Firstly, since the shear wave velocity of the first 30 m depth at these two stations (VSK1 and CKWP), is Vs_{30} ~ 1180 m/s (***Margaris et al., 2021***) and Vs_{30} = 700-800 m/s ***(Theodoulidis et al., 2018***), respectively, this characterizes them as rock sites with moderate weathering, corresponding to the category "B" according to the U.S. National Earthquake Hazard Reduction Program (NEHRP, https://www.nehrp.gov/) classification. Therefore, they cannot directly be considered as hard rock reference sites (free of amplification). For this reason a so-called crustal amplification for generic rock sites, is normally expected at these bedrock outcrops, as has been introduced by ***Boore and Joyner, (1997)***, based on the seismic impedance phenomenon and considering theoretical shear wave velocity profiles with depth, from the high velocity bedrock to the surface. This average generic amplification initially determined by ***Boore and Joyner, (1997)*** and modified by ***Margaris and Boore, (1998)***, is given in **Table 5**. According to ***Boore and Joyner, (1997)***, in

some cases this generic amplification could exceed a factor of 3.5 at high frequencies. In addition, together with the generic amplification effect, a standard attenuation (damping) effect of the S-waves during their propagation from the bedrock to the outcrop, also takes place, mainly for the higher frequencies, as has been outlined by ***Boore and Joyner, (1997)***. This effect is empirically expressed by the distance independent factor "$\exp(-\pi \cdot \kappa_o \cdot f)$", controlled by the site dependent, κ_o parameter, which corresponds to the zero-distance intercept of the high frequency decay parameter, κ, introduced by ***Anderson and Hough, (1984)***. Moreover, independently of the theoretically expected unattenuated, generic amplification and the simultaneously high frequency attenuation effect, the surface "reference" sites can also have a site response of their own above ~ 2 to 5 Hz because of the near-surface weathering, controlled by a factor of 2 to 4, depending on frequency and site (***Steidl et al., 1996***). Based on the three above considerations, the following strategy was applied so that to use VSK1 and CKWP stations, as "true" reference sites.

Table 4. The 28 different distant dependent gamma, $\gamma_h(r_{ij})$ parameters (Eq. [7]), a priori defined to be studied and computed by the inversion, corresponding to the S-wave records, the hypocentral distance of which lies on the specific distant range, "Range-r_{ij}". Their computed standard error of the average $\gamma_h(r_{ij})$values, σ_{γ_h} and the Number of Records (both vertical and single horizontal Eq. [4]) used at each "Range-r_{ij}", are also given.

h	Range-r_{ij} (km)	NoR	$\gamma_h(r_{ij})$	σ_{γ_h}	h	Range-r_{ij} (km)	NoR	$\gamma_h(r_{ij})$	σ_{γ_h}
1	12-20	298	0.979	0.006	15	85-90	184	0.895	0.008
2	20-25	308	0.977	0.005	16	90-95	112	0.884	0.008
3	25-30	290	0.979	0.006	17	95-100	163	0.873	0.008
4	30-35	192	0.976	0.006	18	100-105	150	0.870	0.009
5	35-40	390	0.971	0.006	19	105-110	155	0.857	0.009
6	40-45	290	0.960	0.006	20	110-115	176	0.849	0.009
7	45-50	170	0.960	0.006	21	115-120	124	0.845	0.009
8	50-55	212	0.947	0.006	22	120-125	112	0.829	0.010
9	55-60	220	0.948	0.006	23	125-130	120	0.819	0.010
10	60-65	318	0.946	0.006	24	130-135	104	0.817	0.010
11	65-70	154	0.937	0.007	25	135-140	106	0.804	0.011
12	70-75	210	0.927	0.007	26	140-160	130	0.791	0.011
13	75-80	266	0.912	0.007	27	160-180	30	0.766	0.013
14	80-85	194	0.902	0.007	28	180-195	8	0.769	0.017

The non-intense but non-negligible generic amplification (**Table 5**) corresponding to "average" soft rock site, was firstly removed from the data, $A_{ij}(f_k)$ (Eq. [7]) corresponding only to the horizontal component records retrieved at the two rock stations (VSK1 and CKWP), before the GIT application. In this way, the reference character (free of amplification) for the horizontal component of these two stations is a more reasonable condition to be considered. However, because this site spectral amplification is not the absolute computed one for these sites, as mentioned above, their site amplification factor, $\log_{10}[S_j(f_k)]$ (Eq. [8]), in the initial model

parameter matrix, $m_{M_{init}}$, (Eq. [9]) was considered as 0±0.5. In other words, these two rock sites were considered as free of amplification ($S_j(f_k)$ = 1), after the generic amplification removal. The deviation range of $S_j(f_k)$ defined by ×/÷3, corresponding to the 0±0.5 of its logarithmic value, is allowed to be investigated, accounting for the uncertainties of the considered generic amplification, as well as for the extra site response related to the near-surface weathering. Moreover, this deviation range is used for the expected high frequency spectral amplitude attenuation, mentioned above, which is unknown for both stations, but is not expected to be intense.

Table 5. The generic amplification factor per each frequency, for the site Class "B" of the NEHRP site classification, as given by ***Margaris and Boore, (1998)*** (modification to the one given by ***Boore and Joyner, (1997)***.

Freq. (Hz)	Ampl.
0.01	1
0.09	1.21
0.16	1.32
0.51	1.59
0.84	1.77
1.25	1.96
2.26	2.25
3.17	2.42
6.05	2.7
16.6	3.25
61.2	4.15

Finally, at this GIT application, the initial standard deviation, σ_D (Eq. [11]), of the logarithmic data ($Z_{D_{real}}$, Eq. [9]), was considered equal to 0.3, due to the smoothing procedure applied on the initial computed Fourier Amplitudes of the S-waves from the Fast Fourier Transform. By this σ_D, the potential deviations of the mathematical functions in Eq. [7] with the actual "models" that control the physical procedures of source, attenuation and site effects, are attempted to be "absorbed", to some level.

In **Figure 23a** the moment magnitudes, M_w, computed based on the computed from the inversion seismic moments, M_o and on Eq. [3], are compared to the corresponding, local magnitudes, M_L, given in **Appendix B**. A satisfactory agreement between each other, with a low trend of M_w underestimation in higher magnitudes (maximum 0.1 difference for M_L = 5.1), is observed. Moreover, a low RMS = 0.18 (**Figure 23a**) comparable to the routinely computed local magnitude standard error σ_{M_L} = 0.2, was determined, with a low enough σ_{M_w} = 0.09. Comparing the M_w computed from the inversion (**Figure 23b**) to those given in catalogues (**Appendix B**) (where available, mainly for earthquakes with M_w > 4), it is clear that a good agreement between them is observed, taking also into account the typical ± 0.2 standard deviation of the latter. This agreement confirms the reliable operation of the algorithm, in computing moment magnitudes.

In **Figure 23c** the M_w and the corner frequencies, f_c computed from the GIT are compared. Taking into account their logarithmic regression analysis (equation within **Figure 23c**) and the theoretical computed values of the f_c for stress drop, $\Delta\sigma$ = 1, 10, 100 and 1000 bar (based on Eq. [2]), a low trend of $\Delta\sigma$ increase, as the M_w is increased, is observed. More specifically a geometric mean $\Delta\sigma$ = ~5.8 bar (std range 2.4-14.3 bar) up to $\Delta\sigma$ = ~54.5 bar (std range 22.2-133.7 bar) is estimated, for the M_w range of 2.5 to 5.2. The average, $\Delta\sigma$ = 15 bar (in logarithmic scale) (**Figure 24a**) of all the indirectly computed $\Delta\sigma$ values (based on Eq. [15], **Appendix B**), with a standard deviation range from 5.8 to 40 bar (the 85% of the earthquakes, **Figure 24c**), represents a relatively low to moderate stress drop regime dominating this region for this range of earthquake magnitudes (M_w = 2.5-5.2). It's worth noting that all $\Delta\sigma$ values lie between ~0.9 bar and ~209 bar, where the 96.6% of the earthquakes lie between ~2.2 and ~104 bar, which is the range of two standard deviations in logarithmic scale.

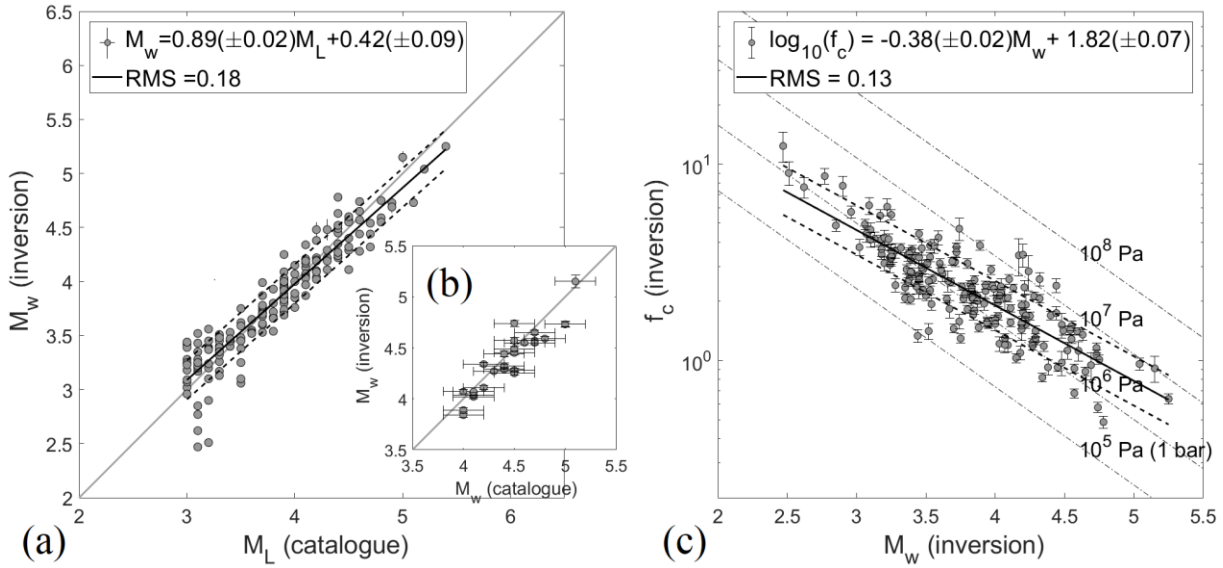

Figure 23. (**a**) The computed from inversion M_w versus the M_L from the catalogue (**Appendix B**). The linear regression equation (black line) and its standard deviation (black dashed line) are also shown. With grey line the bisectrix is shown. (**b**) M_w (inv.) vs M_w (from catalogue, where available, **Appendix B**) (**c**). The computed from inversion M_w versus the corner frequencies, f_c. The logarithmic regression analysis (black line) equation is also given (and its standard deviation, black dashed line). The black parallel dashed lines represent the theoretical corner frequencies with stress drop, $\Delta\sigma$ values equal to 1, 10, 100 and 1000 bar, according to Eq. [2].

These values, even though they present a distribution around the average of 15 bar, may not be related with a standard stress drop regime, that fully dominates the seismotectonic properties of this area. The focal mechanisms of the seismic sources, may control the amount of stress drop, as has been outlined by ***Margaris and Hatzidimitriou, (2002)*** for the broader Aegean area. They found typically moderate, $\Delta\sigma$ values (55 ± 16 bar), for moderate to large magnitude earthquakes, occurred on normal and strike slip faults and higher values (257 ± 49 bar) for reverse faults. Similar average (~ 56 bar), $\Delta\sigma$ value has been determined by ***Margaris and Boore, (1998)*** for

moderate to large magnitude earthquakes for the same area, mainly associated to earthquakes of normal and strike slip faults, with $\Delta\sigma$ values ranging between 48 and 63 bar. The above $\Delta\sigma$ ranges are comparable to the "average" estimated one in this study for the higher computed moment magnitude earthquake, M_w = 5.2 ($\Delta\sigma$ = ~54.5 bar, std range 22.2-133.7 bar, **Figure 23c**). ***Grendas et al., (2018)***, investigating moderate to large magnitude earthquakes (4.2-6.5), concluded to a similar average, $\Delta\sigma$ = 54 bar, value, for the broader Aegean area, with a standard deviation range between 17 to 166 bar, including the variation of the stress drop due to the different focal mechanisms. In the previous section, based on the same dataset of ***Grendas et al., (2018)***, the average stress drop has been re-determined to 26 bar, with a standard deviation range between 11 and 59 bar.

Regarding the attenuation factors, the geometrical spreading coefficient indicate a slightly weaker attenuation, from short (12 km) to longer (~200 km) hypocentral distances, which is shown by the decrease, of the computed by the inversion, gamma, $\gamma_h(r_{ij})$ (Eq. [7]) values (**Table 4**) with distance, as presented in **Figure 25a**. This decrease is defined, on average, from γ = 0.98 to γ = 0.77 for distances 12 km - 200 km, respectively, between the theoretical spherical geometrical spreading, (γ = 1) and the cylindrical one (γ = 0.5). These gamma values present a slightly lower geometrical spreading coefficient than those determined above in this chapter from the GIT application for the broader Aegean region, where $\gamma_h(r_{ij})$ is decreased from 1.1 to 1.05 for hypocentral distances between 12 km and 350 km, respectively.

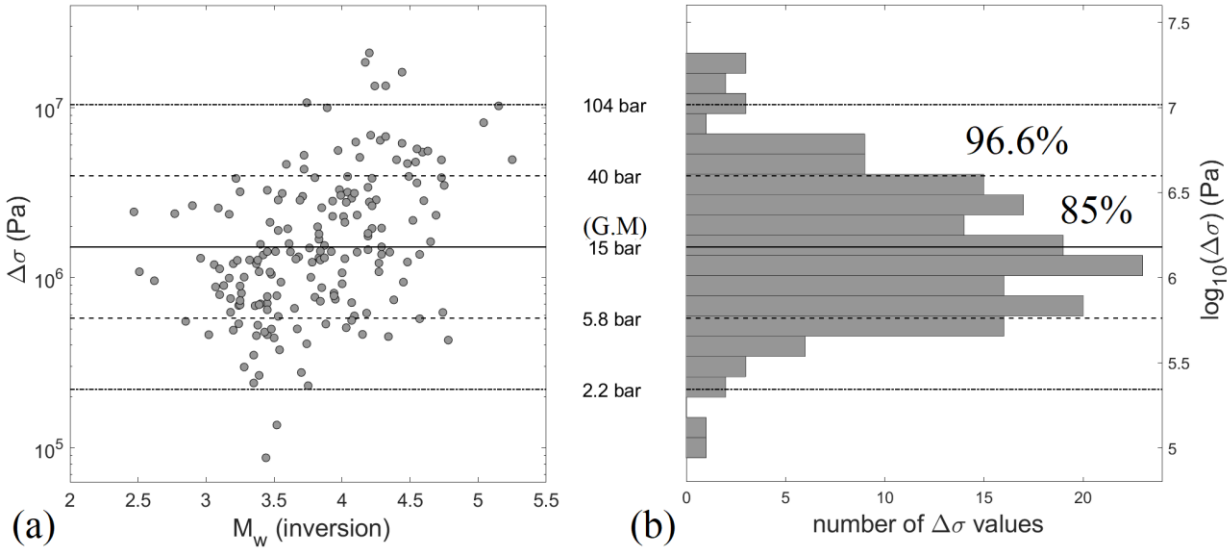

Figure 24. (**a**) The stress drop, $\Delta\sigma$ values computed based on Eq. [15] and on the M_w and f_c computed by the GIT in this study (**Appendix B**). The geometric mean (G.M.) and the corresponding ranges of one and two standard deviations (in logarithmic scale), where the 84.4% and 95.5% of the earthquakes are included, respectively. (**b**) The histogram, corresponding to the $\Delta\sigma$ values of **Figure 24a**.

The anelastic attenuation factors, $\log_{10}(Q_{s_n})$ and $\log_{10}(a_n)$ (Eq. [7]), were computed for 275 cells (**Appendix K, Figure 26**) from the 406, initially defined ones (0.1° x 0.1°) of **Figure 5**, where

ray paths passed through them. In **Figure 27a,d,g** the indirectly computed $Q_{s_n}(f)$, for the frequencies, f = 0.5, 1 and 5 Hz, are presented. Moreover, the coefficient of variation, CV (%) for these $Q_{s_n}(f)$ values, based on the computed from the inversion $\log_{10}(Q_{s_n})$ and $\log_{10}(a_n)$ (Eq. [7]) and on their corresponding standard deviation, were determined (**Figure 27b,e,h**).

In **Figure 27c,f,i**, the smoothed, by a Gaussian filter of 0.2°, $Q_{s_n}(f)$ values are presented, only for cells with CV < 15% (**Figure 27b,e,h**). In **Figure 27e** ($Q_{s_n}(1) = Q_{s_n}$) the quality factor, Q_s varies mainly between 22.5 and 90.5, which is its standard deviation range, representing the 74.6% of the total number of Q_s, for which CV < 15%. The geometric mean of Q_s is 45 (11.2-182, two standard deviations range, including the 94.4% of the data). A few anomalies of strong anelastic attenuation (6.5 < Q_s < 11.2, 4 cells) or weak enough (182 < Q_s < 461, 6 cells) are also observed. The 75% of the Q_s values (22.5-90.5), dominating this region indicate a relevant high anelastic attenuation (< 100) in agreement to the average Q_s ~ 55, computed by ***Polatidis et al., (2003)*** for the Hellenic back-arc area, as well as to the average ~ 98 determined by ***Grendas et al., (2018)***, for the broader Aegean area. Moreover these values (22.5-90.5) agree with an average range (70-120) computed above in this chapter from the new GIT algorithm application (**Figure 20d**, **Appendix J**) with the same dataset of ***Grendas et al., (2018)***. ***Tselentis, (1998)*** studying coda wave records in western Greece, found an average quality factor ~157, corresponding to the intrinsic attenuation. This moderate to high value is expected to be higher than the corresponding S-waves one, as has been found for the coda waves by ***Baskoutas et al., 2000*** and ***Hatzidimitriou et al., 1993***), in northern Greece.

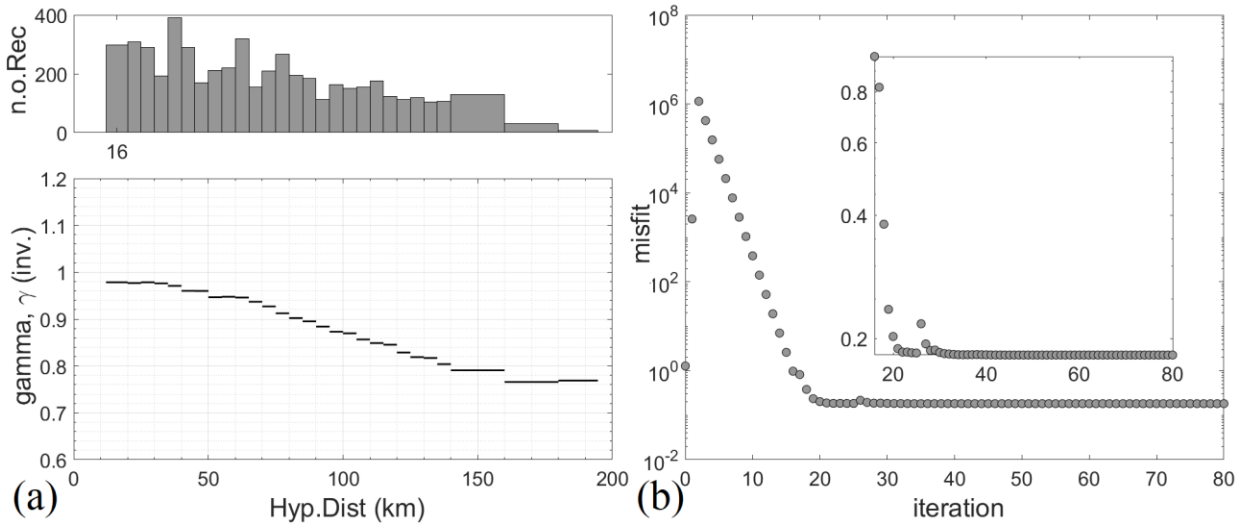

Figure 25. (**a**) The computed from the inversion gamma factors, $\gamma_h(r_{ij})$ (Eq. [7], **Table 4**) versus the corresponding hypocentral distance, r_{ij}, and the histogram presenting the number of records (n.o.Rec) at each distance range. (**b**) The log-data, (Z, Eq. [10]) misfit computed at each one of the 80 inversion iterations ("zooming" of this figure from the 17th iteration and beyond, is also presented).

Regarding the site factors (site effects), computed from the inversion, for each station, *j* and for each component (horizontal and vertical), the average $S_j(f_k)$ (Eq. [7]) and their standard deviation range are presented in **Figure 28**. It's worth noting that the $S_j(f_k)$ of the horizontal components, computed for the "reference" considered sites, VSK1h and CKWPh, ("h" the index for the horizontal component), for which the corresponding data $A_{ij}(f_k)$ (Eq. [7]) were corrected (divided) before the inversion by the corresponding generic amplification factor (**Table 5**), are inversely re-corrected (multiplied) for this factor (**Figure 28**) so that to correspond to the real-uncorrected data. In this way all the presented $S_j(f_k)$ of **Figure 28**, are purely the $S_j(f_k)$ factors that correspond to Eq. [7] and substantially include the corresponding at each site, unknown generic amplification and high frequency attenuation, as explained above in this sub-chapter in the reference station choice strategy. Taking into account that the reference considered sites, VSK1h and CKWPh, were allowed to be inverted ($\log_{10}S_j(f_k)$ = 0±0.5, $S_j(f_k)$ = 1×/÷3), with respect to the generic amplification curve (**Table 5**, **Figure 28**), it seems that the computed $S_j(f_k)$ for these two stations do not significantly diverge from the generic amplification (at rock sites), as it is observed in **Figure 28**. In other words, the generic amplification determined by ***Boore and Joyner, (1997)*** and modified by ***Margaris and Boore, (1998)***, for the surface rock sites of class "B" (**Table 5**) in NEHRP classification, seems to be an appropriate approach of the $S_j(f_k)$ for the horizontal component, assuming that the expected high frequency attenuation is not intense up to the maximum examined frequency (15.1 Hz).

Regarding the $S_j(f_k)$ of the vertical components, it should be reminded that they include the $\sqrt{\beta_s/\alpha_s}$ factor (< 1) (Eq. [6]), which satisfy the obtained de-amplifications at several frequencies (**Figure 28**). The horizontal to vertical spectral ratios (HVSR), computed from the same S-wave record dataset used in the inversion (**Appendix L**), are compared to the $S_j(f_k)$ factors (**Figure 28**). What can be observed is that all the $S_j(f_k)$ curves of the horizontal components are equal or higher than the corresponding HVSR ones, revealing the resonance frequencies, as they are also obtained by the HVSR curves. Moreover, a quality observation for the $S_j(f_k)$ of the vertical components is that they follow a trend of spectral amplification between the fundamental frequency and the 2nd dominant one, presented at HVSR curves (e.g. CK0, CK6, CK15, CK40, ARG2, LXR1, VAS2, LEF2, PYR2, in **Figure 28**). In **Figure 28**, the $S_j(f_k)$ computed in this subchapter, based on the dataset of western Greece are compared to the corresponding ones computed at the previous sub-chapter, based on the GIT application at the dataset of ***Grendas et al., (2018)*** for the broader Aegean area. These two groups of $S_j(f_k)$ results for these two GIT applications are in satisfying agreement in shape, but a slightly higher amplification of the first group, in some cases, is observed. This amplification seems to correct some de-amplification effects in $S_j(f_k)$ of the second group of results, that are probably related to the more "poor" attenuation factor analysis of the second group (**Figure 12**), with respect to the most targeted one for the area of western Greece (**Figure 18**).

The computed from this inversion application, $S_j(f_k)$ factors of the 5 borehole ARGONET stations (CK0, CK6, CK15, CK40 and CK83) and of the ARG2 station located in Argostoli town

in Cephalonia island (close to ARGONET) are compared to the corresponding $S_j(f_k)$ estimated by ***Grendas et al., (2021c)*** (**Figure 28**), applying the Standard Spectral Ratio technique (***Borcherdt, 1970***), with respect to the nearby surface rock site, CKWP. These computed SSRs are "corrected" here by multiplying them with the computed from the inversion, $S_j(f_k)$ of the CKWP station (**Figure 28**), so that the SSRs and the $S_j(f_k)$ of the 6 stations mentioned above, computed from the inversion, to be comparable.

Regarding the reliability of the inverted model parameter matrix, m_M (Eq. [9]) solution, the inversion algorithm converged to stable, m_M, after ~ 43 iterations (**Figure 25b**), with the misfit between real, $Z_{D_{real}}$ and synthetic, $Z(m_M)_D$ data (Eq. [10]), reaching a minimum ~ 0.182, same as the last (80th) inversion iteration (**Figure 25b**). In **Figure 29a**, the residuals of the misfit quantity, $Z_{D_{real}}$ - $Z(m_M)_D$ (Eq. [10]), are presented and a normal distribution around zero is observed (**Figure 29b**). Moreover, it is worth noting that the average value of all the groups of residuals, grouped in hyponentral distances of 2 km range, from 12 km up to 200 km (**Figure 29a**), lie very close to zero, while the 70.3%, 95% and 99.4% of the total number of data lie between ±0.182, ±0.365 and ±0.548, respectively (**Figure 25b**).

Based on the real data $A_{ijk}(f_k)$ (Eq. [7]), as well as on the computed from the inversion non-parametric site factors (**Figure 28**) and attenuation model ($\gamma_h(r_{ij})$, **Table 4**, **Figure 25a** and $Q_{s_n}(f)$ parameters, **Figure 27**, **Appendix K**), the non-parametric source spectrum of each earthquake, was computed, solving Eq. [7], as the results in the example of **Figure 30** (grey lines). The geometric mean values (e.g. **Figure 30**, black lines) and the corresponding standard deviation, were separately computed per each frequency, concluding to an "average" non-parametric source factor (**Appendix M**). The average (in logarithmic scale) Root Mean Square ($\log_{10}$RMS) of these source spectra is 0.158 with std = 0.033, based on the computed $\log_{10}$RMS of each earthquake (**Appendix B**). Finally, based on these average, non-parametric source spectra (**Appendix M**) and on the already computed from the GIT site and attenuation factors, new synthetic data, $Z(m_M)_D$ were computed according to Eq. [7], resulting to a new average data misfit (Eq. [10]), equal to 0.169, which is the final misfit, representing the inversion of this study.

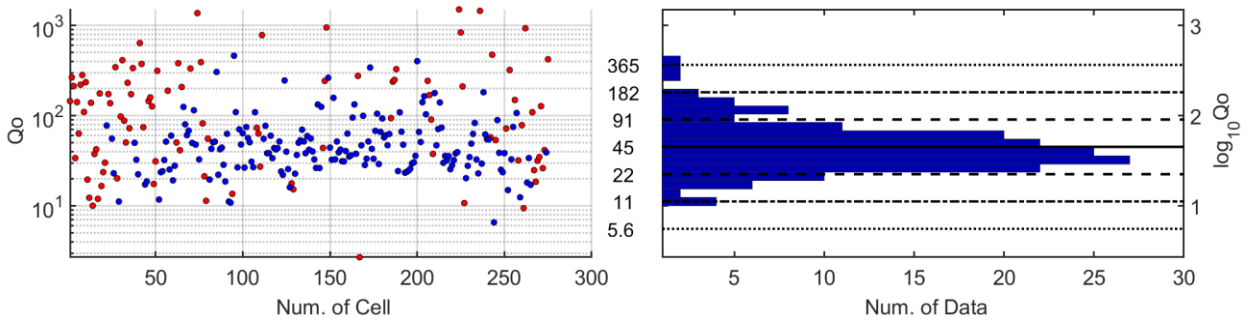

Figure 26. (**a**) The 275 Q_{o_n} computed for each cell "n" of **Figure 5**, in blue and red points for the corresponding CV(%) <15 and ≥15. (**b**) The histogram of the reliable considered $log_{10}(Q_{o_n})$ with CV <15 %. The average Q_{o_n} value in logarithmic scale and the corresponding standard deviation range, are also depicted.

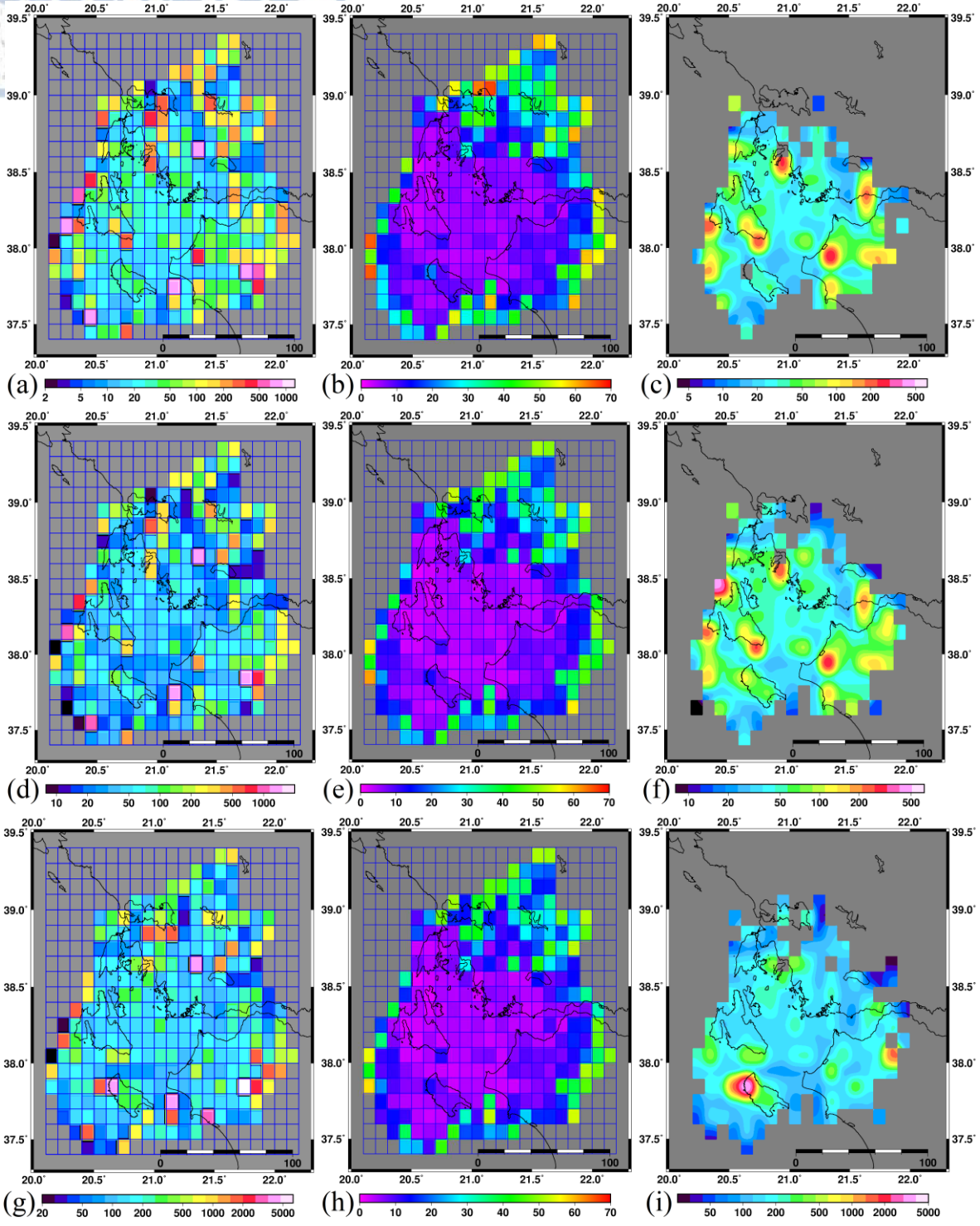

Figure 27. Three lines of maps corresponding to the computed $Q_{s_n}(f)$ (**Appendix K**, Eq. [7]) for frequencies 0.5, 1 and 5 Hz, respectively. The maps of the 1st column (a,d,g) show the computed $Q_{s_n}(f)$ for the 275 (total 406) sub-areas. The maps of the 2nd column (b,e,h) show the coefficient of variation, CV (%) for these $Q_{s_n}(f)$, in relation to their computed standard deviation. The maps of the 3rd column (c,f,i) represent the smoothed maps of the 1st column (a,d,g), respectively, taking into account only cells where CV < 15%.

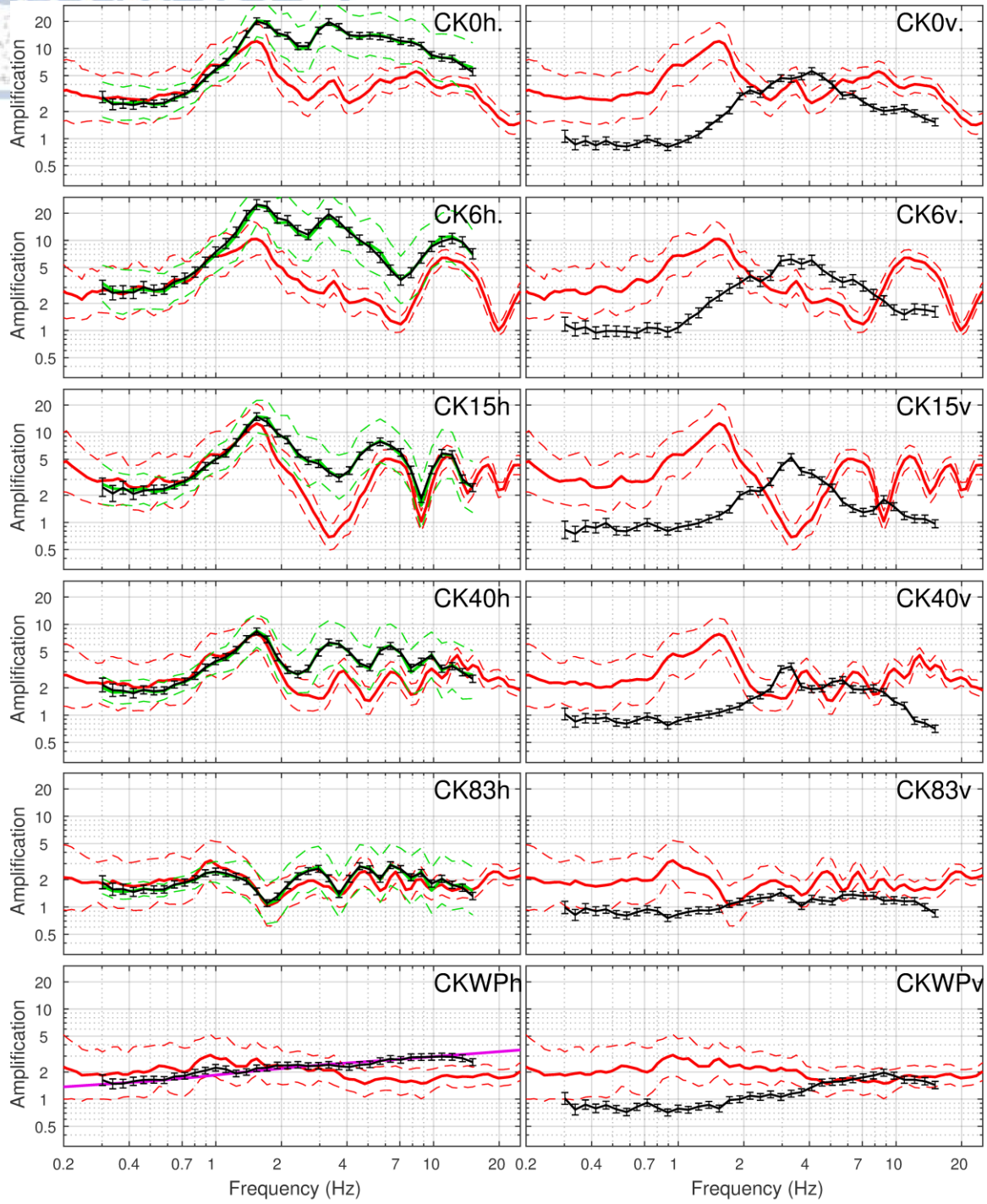

Figure 28. The 24 site amplification factors (black lines), $S_j(f_k)$ (Eq. [7]), computed in this study, for each station, j (**Appendix C**) and for each component (horizontal, "STATIONh" and vertical, "STATIONv", left and right columns, respectively) and the corresponding HVSR (red) (**Appendix L**). The horizontal components $S_j(f_k)$ (blue) computed previously in this chapter (**Figure 21**), for the broader Aegean region dataset, the SSR (green) of the horizontal components of the ARGONET stations (CK..), and ARG2, computed by ***Grendas et al., (2021c)*** and the generic amplification (purple) of site Class "B" (**Table 5**) are also shown.

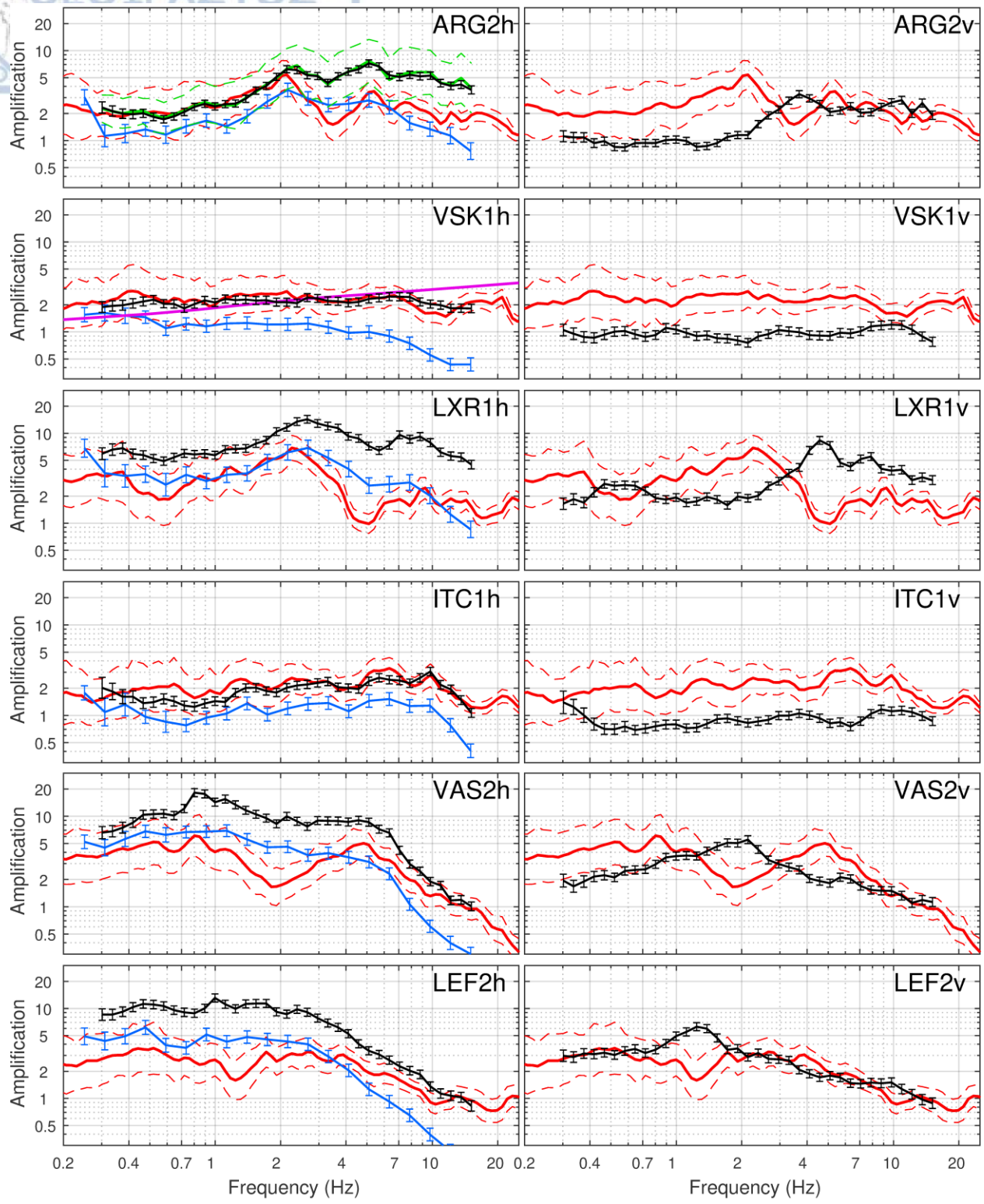

Figure 28. (continued)

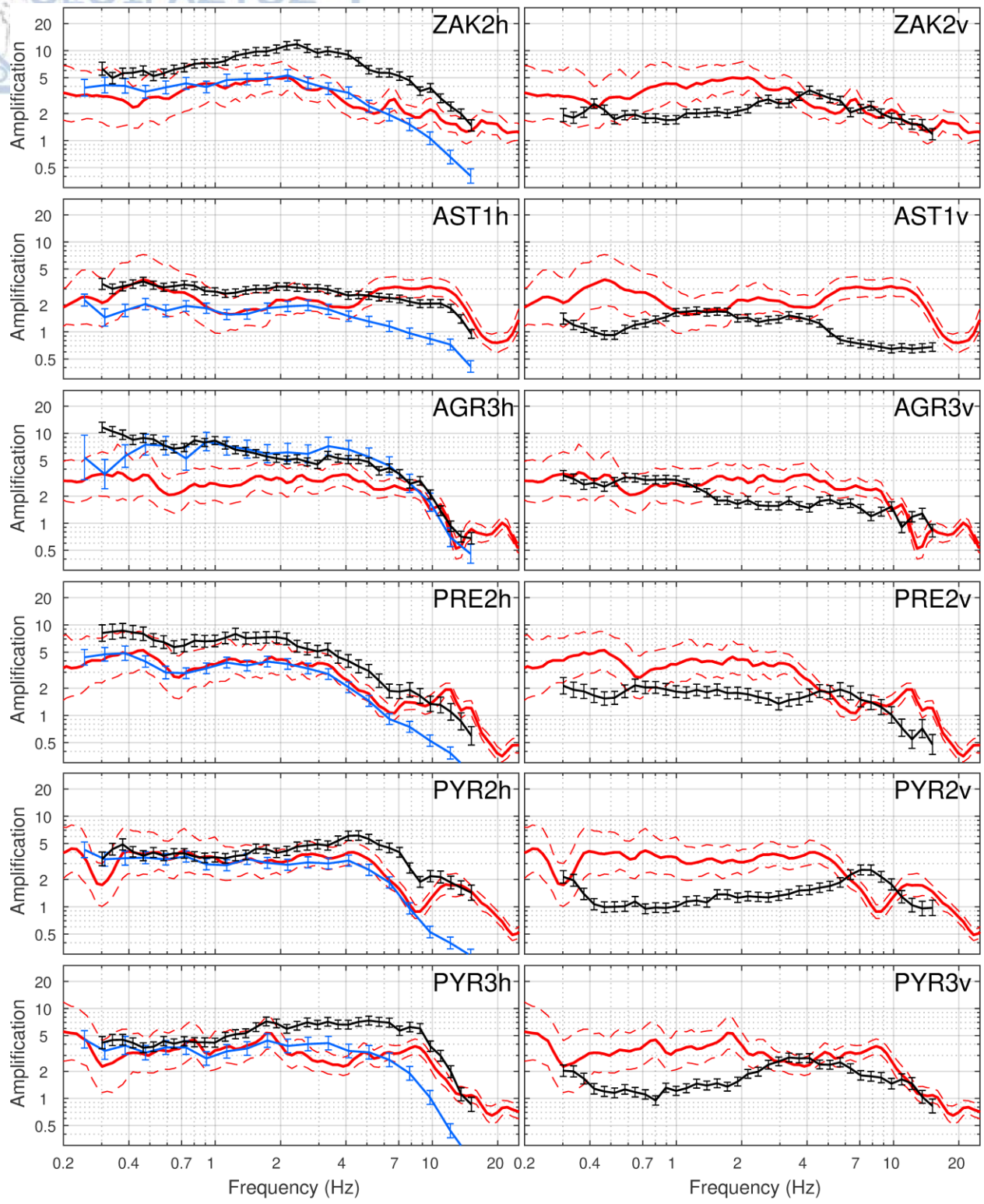

Figure 28. (continued)

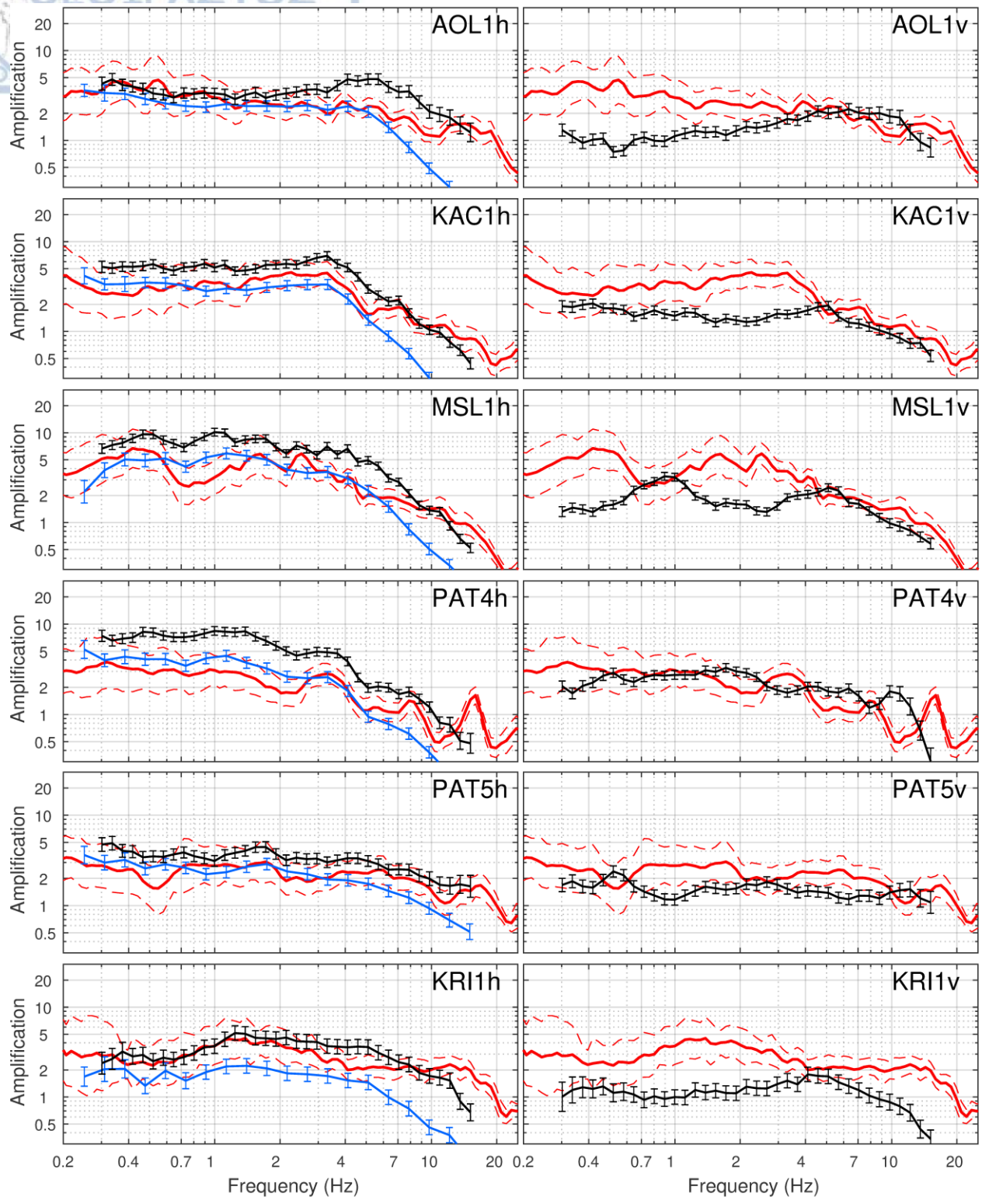

Figure 28. (continued)

Finally, the residuals of the misfit quantity, $Z_{D_{real}}$ - $Z(m_M)_D$ (Eq. [10]), for the data depicted in **Figure 29a**, have been plotted separately for each frequency (**Figure 31**), showing the same, distribution around zero (**Figure 32**). The corresponding standard deviations at each frequency, range between ~0.158 and 0.22 as presented in **Figure 32**, where the higher standard deviations ($\geq$ ~ 0.2) are observed for the lower frequencies (f $\leq$ 0.8 Hz), while a decrease of the standard deviations (from 0.2 down to 0.158) is obtained with frequency increase up to ~10 Hz. A short trend of standard deviation increase is also observed for f > ~10 Hz. In addition, the lower the number of data used, the higher the standard deviation (**Figure 32**).

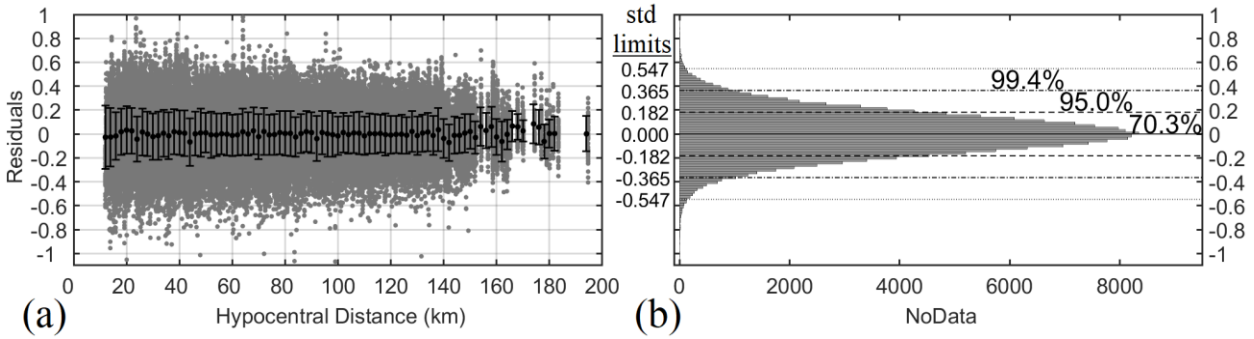

Figure 29. (**a**) The residuals "$Z_{D_{real}}$ - $Z(m_M)_D$" (Eq. [10]) of each data (grey points) and the average values (black points) and their standard deviation (error bars) of all the groups of residuals, corresponding to 2 km intervals, computed for all the hypocentral distance range (12-200 km). (**b**) Histogram corresponding to the distribution of the residuals of **Figure 29a**. The one, two and three standard deviation (std) ranges (dashed and dotted lines) and their corresponding values, are presented, including the 70.3%, 95% and 99.4% of the total Number of Data (NoData).

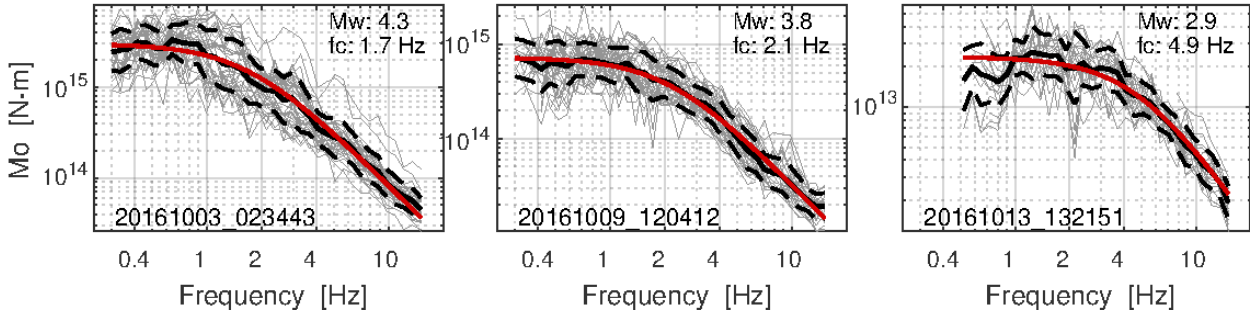

Figure 30. Three examples of the (post-inversion) computed (from Eq. [7]) (details into the text) non-parametric source spectra (grey lines), for each S-wave FAS of three earthquakes of **Appendix B**. With black lines the average values (in logarithmic scale) and their standard deviation (black dashed lines) are presented. With red lines the corresponding parametric source spectra, computed from the inversion based on Brune's source model (Eq. [7]) (***Brune, 1970***) and the calculated seismic moment, M_w and corner frequency, f_c, are shown.

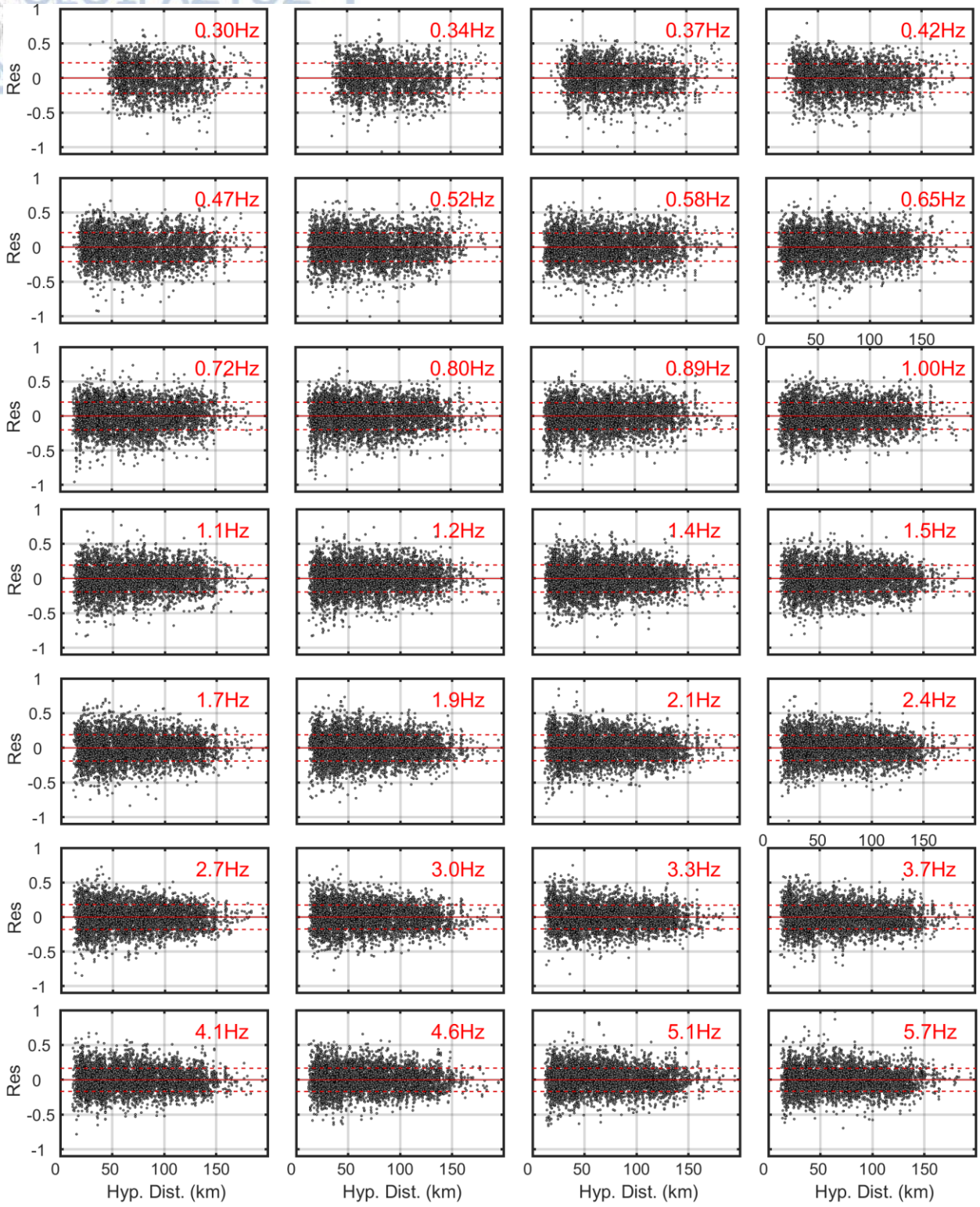

Figure 31. The residuals, $Z_{D_{real}}$ - $Z(m_M)_D$ (Eq. [10]) of **Figure 29**, corresponding to each discrete frequency of the 37 examined in this study (black points), versus the hypocentral distance. The corresponding average and ±std values are depicted in solid and dashed red lines, respectively.

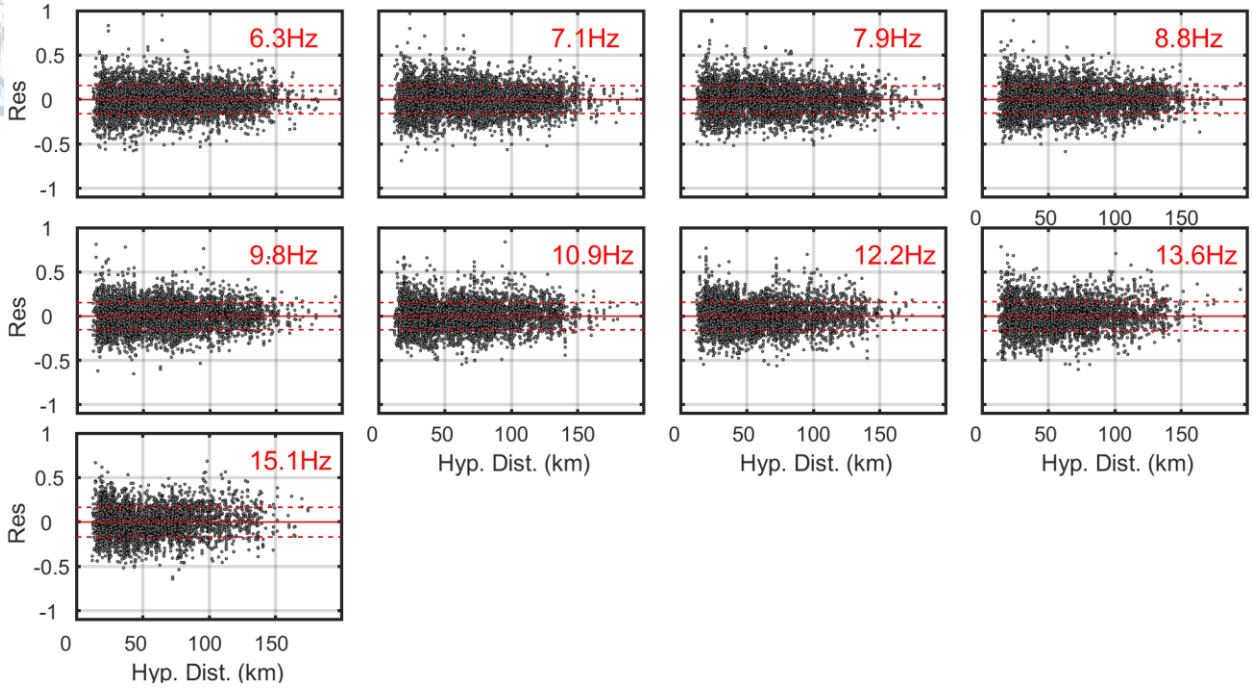

Figure 31. (continue)

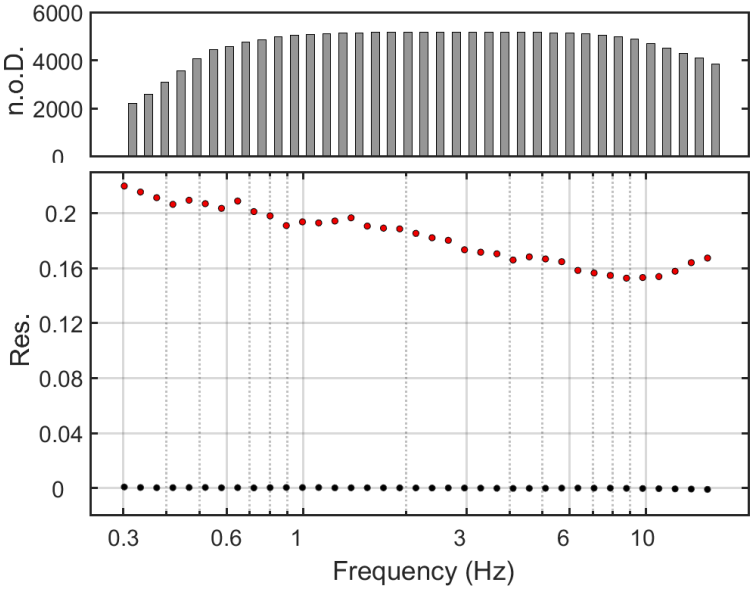

Figure 32. (**bottom**) The average (black points) residual values corresponding to each frequency separately and the corresponding standard deviation (red points), based on the values of **Figure 31**. (**top**) The number of Data (noD) of the Residuals (**Figure 29a**) corresponding to each discrete frequency, regarding the bottom figure and the values in **Figure 31**.

4 SITE AMPLIFICATION FACTOR (SAF) ESTIMATION BASED ON SPECTRAL FACTORIZATION OF CODA WAVES (SFC): DEVELOPMENT, APPLICATION AND VALIDATION OF A NEW ALGORITHM

4.1 Introduction

The main goal attempted to be achieved in this chapter refers to the introduction of a technique aiming at the Site Amplification Factor, ($SAF(f)$), estimation. This technique is based mostly on the minimum phase Source Time Function ($mpSTF$) estimation methodology introduced by ***Sèbe et al., (2018)*** and partially on the rationale of the broadly used in seismology Standard Spectral Ratio (SSR) (***Borcherdt, 1970***) technique. Briefly, the $mpSTF$ estimation methodology of small to moderate magnitude earthquakes (***Sèbe et al., 2018***), for which the STF is not complicated, corresponds to the real STF and is based on the Spectral Factorization Method of Coda waves (SFC). This method has the advantage that can be applied on a single station earthquake record. The existence of the distance independent site effect into the coda wave records, as outlined in the Introduction (*ch.* 1), implies that the estimated STF includes the $SAF(f)$ factor for the examined site, and consequently the STF is more suitable to be referred as apparent STF. Based on this consideration and assuming that no significant effects of the source directivity exist for the low-to-moderate magnitude earthquakes (i.e. the STF is independent of the seismic source azimuth and expected to be same in all examined sites), the comparison of two apparent $STFs$ estimated for the same seismic source in two stations, should reveal their relevant $SAF(f)$. In the specific case where one of the stations is considered as reference, as in the application of SSR technique, their relevant $SAF(f)$ should correspond to the $SAF(f)$ of the target site.

The analysis of the apparent STF in terms of Fourier Amplitude Spectrum (FAS), to the real $STF(f)$ and to the $SAF(f)$, and the way of $SAF(f)$ computation based on the comparison of the apparent STFs at two sites, are the main issues analyzed in this chapter. In addition, the investigation of the two assumptions, mentioned above (i.e. the existence of the distance independent site effect in coda wave records and the absence of significant effects related to the source directivity), is also an issue examined in this chapter.

For the needs of the apparent STF analysis here and of its use in the $SAF(f)$ estimation in a target site, a new SFC algorithm was developed, modifying that developed by ***Sèbe et al., (2018)***. The intent of this new algorithm development is to satisfy several modifications and general optimization of the ***Sèbe et al., (2018)*** algorithm. Moreover, error propagation is attempted to be estimated from the data of the apparent STF and consequently of the $SAF(f)$, controlling the reliability of the results. In this chapter, the new SFC algorithm is applied using records of two groups of earthquakes occurred at two areas of different seismotectonic regimes (western Greece, **Figure 7** and southeastern France, **Figure 8**) and of different level of seismicity (high and low to moderate, respectively). During the apparent STF analysis and $SAF(f)$ estimation study, the comparison between the $SAF(f)$ effect of an input wavelet at a reference and a target site, in time

domain, $SAF(t)$, is also investigated in this chapter, revealing some main characteristics of source wavelet amplification and lengthening caused by the $SAF(t)$ effect.

Finally, the validity and reliability of the minimum phase $mpSTF$ computation for 4 earthquakes of moderate to large magnitudes (M_w~$4, 5, 6, 7$), is investigated in this chapter. The latter is carried out aiming at further understanding the potential of the SFC method in estimating the real STF of the large magnitude earthquakes, for which the isotropic source radiation pattern scenario and the minimum phase assumption, are not absolutely realistic and reasonable assumptions.

4.2 Methodology

The flowchart described in **Table 6** presents a total of ten steps, nine of which are related to the prior computation of the minimum phase $mpSTF$ and the last one is referred to the $SAF(f)$ estimation at the target site. While the overall approach of the STF computation follows directly the methodology of ***Sèbe et al., (2018),*** several of the computation steps, presented here actually refer to some modifications. These modifications include details on tricky steps of the STF computation, as well as the assessment of its uncertainties and consequently the uncertainties of the $SAF(f)$ estimation.

Modifications of the new developed SFC algorithm, presented in this study, can be summarized in the following steps: (a) an alternative approach regarding the initial selection of coda wave window on the basis of signal-to-noise ratio, (b) a slightly different strategy followed for the derivation of the coda-Q quality factor and the stationarization of the considered coda window, (c) a slightly different (but equivalent) implementation of the retrieval of the minimum phase Source Time Function ($mpSTF$) from the corrected coda waveform, (d) correction of the low frequency $mpSTF$ part, and scaling, with respect to seismic moment, M_o and (e) tracking the propagation of uncertainties from the initial data to the estimated $mpSTF$ and M_o. The last one is necessary for ensuring the robustness and reliability of SAF(f) estimates, assessing the associated uncertainties, and thus evaluating the applicability potential of the proposed estimation technique.

Following the flowchart (**Table 6**) of the SAF(f) estimation technique, the ten steps are described below at each sub-chapter, along with their mathematical and physical basis.

Table 6. Flowchart of the Site Amplification Factor, SAF(f) estimation at a target site, after modification of the ***Sèbe et al., (2018)*** STF estimation methodology.

1) Signal pre-processing (at each component of seismic record) (*ch.* 4.2.1).
2) Selection of Coda wave window with satisfactory frequency band-width signal quality with respect to noise (SNR process, *ch.* 4.2.2 - each component of seismic record) (e.g. **Figure 33**).
3) Estimation of the coda quality factor, $Q_c(f)$ model (*ch.* 4.2.4) (following the Coda wave decomposition, *ch.* 4.2.3), in four steps:

- Frequency and time dependent, Energy $J(f_{cen}, t')_{\text{comp}}$ determination for each component of seismic record (e.g. **Figure 34a**)
- Total Energy $J(f_{cen}, t')$ computation from $J(f_{cen}, t')_{\text{comp}}$ (e.g. **Figure 34b**)
- $Q_c(f_{cen})$ computation at each examined frequency, f_{cen} (based on Eq. [23]) (e.g. **Figure 34b**)
- Average earthquake-station $Q_c(f)$ model estimation (e.g. **Figure 35**), based on $Q_c(f_{cen})$.

4) Attenuation Factor Removal (*ch.* 4.2.5), from each coda wave record component, based on the computed $Q_c(f)$ model. Three "stationary" waveforms, (Eq. [27]) are determined for each component, scaled by the *F* factor (Eq. [28]) and affected by the Site Amplification Factor ($SAF(f)$) (e.g. **Figure 36a**).

5) Scaled FAS(f) of velocity $S\dot{T}F_{comp}$ estimation (for each component seismic record) (*ch.* 4.2.6) ($SAF(f)$ and low frequency noise affected) (e.g. **Figure 36f**).

6) Scaled FAS(f) of velocity $S\dot{T}F$ estimation (*ch.* 4.2.7) ($SAF(f)$ and low frequency noise effects) (e.g. **Figure 37a**).

7) Scaled displacement minimum phase STF estimation (*ch.* 4.2.8) ($SAF(f)$ and low frequency noise affected):
   - Minimum phase $S\dot{T}F$ (velocity) estimation (e.g. **Figure 37b**)
   - Integration, after a High Pass filtering at the lowest required Fourier Transform frequency (1/40 Hz) of the 40 s $S\dot{T}F$
   - Minimum phase STF (displacement) estimation (scaled and $SAF(f)$ affected) (e.g. **Figure 37c** for reference site and **Figure 38a** for non-reference site)

8) Scaled STF low frequency correction (*ch*. 4.2.9) ($SAF(f)$ affected) (e.g. **Figure 37c,d** for reference site and **Figure 38a, b** for non-reference site).

9) STF scaling correction and seismic moment, M_o computation – uncertainties, if possible (*ch*. 4.2.10).

10) Site Amplification Factor, $SAF(f)$, estimation (*ch*. 4.2.11) at a target site, with respect to a distant reference station.

4.2.1 Signal pre-processing

The original methodology presented in ***Sèbe et al., (2018)*** involves classical seismological recordings corresponding to velocity time histories. For this reason, all 3-components accelerograms were initially converted to velocity time histories. The converting process consists firstly of applying a *Butterworth* (2nd order, or more) High-Pass filter at 0.05 Hz (the lower

frequency limit of the accelerometers used) and then of integrating the time acceleration histories (and checking the high-pass filtering allows to remove non-physical low frequency trends). Then, the S-wave arrival time, necessary for the selection of coda window onset, was manually picked.

4.2.2 Selection of Coda window with satisfactory frequency band-width signal quality with respect to noise level

The proposed SAF estimation technique is based on the analysis of the coda part of the seismogram. The selection of the appropriate coda wave window constitutes therefore a pre-requisite for the reliability of the approach. It depends on two factors: (a) the selection of the onset of coda window and (b) the selection of its duration on the basis of an acceptable signal quality with respect to background noise.

Before presenting the strategy followed in this study for the coda window selection, it is worth noting that the onset time of "coda waves", t_c, still remains an open issue, ranging between $2t_s$ and $3t_s$ (where t_s is the lapse time between the earthquake origin time and the S-wave arrival at the considered site) in order to avoid inclusion of source-generated surface waves (among others, see ***Rautian and Khalturin, 1978***). Here, the coda wave onset time was selected as $t_c = 2t_s$ (t_s the S-waves arrival time) following ***Aki, (1969)***, but modified, when necessary to ensure that t_c is always greater than 30 s after the earthquake origin time (i.e, typically for earthquakes located at less than 40–50 km from the considered site). This criterion was applied to avoid as much as possible the inclusion of the source-generated surface waves, but also to avoid very early coda waves that could probably be contaminated by other kinds of surface waves generated locally by the interaction of the main S-wave phase with the local underground and surface geometry (valley and surface topography effects). Such contamination was actually confirmed by observations at several cases in the examined dataset (see for instance ***Imtiaz et al., 2021***), for the composition of the wavefield around the ARGONET sites.

The determination of the quality of coda waves is achieved for each component separately, in frequency and in time domain, up to the end of the available record, or up to the appearance of a new earthquake record. The strategy followed aims at an optimum choice of coda wave window satisfying a minimum Signal to Noise Ratio (SNR) threshold over a large enough frequency bandwidth. This strategy is based on two specific items.

The first one deals with the selection of the "optimal" length of the analysis of coda windows, with respect to the reduction of the signal amplitude, in time, for the different frequency ranges. For this reason, different sets of consecutive coda windows with 50% overlap are considered from the t_c onset time up to the end of the earthquake record (**Figure 33a**). Each set has a fixed duration L_c, long enough for the detection of the lower frequencies signal evolution and shorter for the higher frequencies one. This is implemented because long duration coda windows cannot precisely capture small changes of high frequency amplitude with time, while short-time widows cannot provide robust estimates of low frequency content. For example in **Figure 33a**, three L_c durations of 5, 10 and 20 s were initially used to compute the FAS (**Figure 33b**) and the corresponding theoretical frequency ranges are: 0.2 - (f_s/2) Hz (f_s sampling frequency), 0.1 - (f_s/2) Hz and

0.05 - (f_s/2) Hz, respectively. As longer durations cannot reliably capture high-frequency changes, the shorter durations (L_c = 5 s) are kept for the high frequency part, while longer durations are considered only for the low frequency part which is not covered by shorter ones.

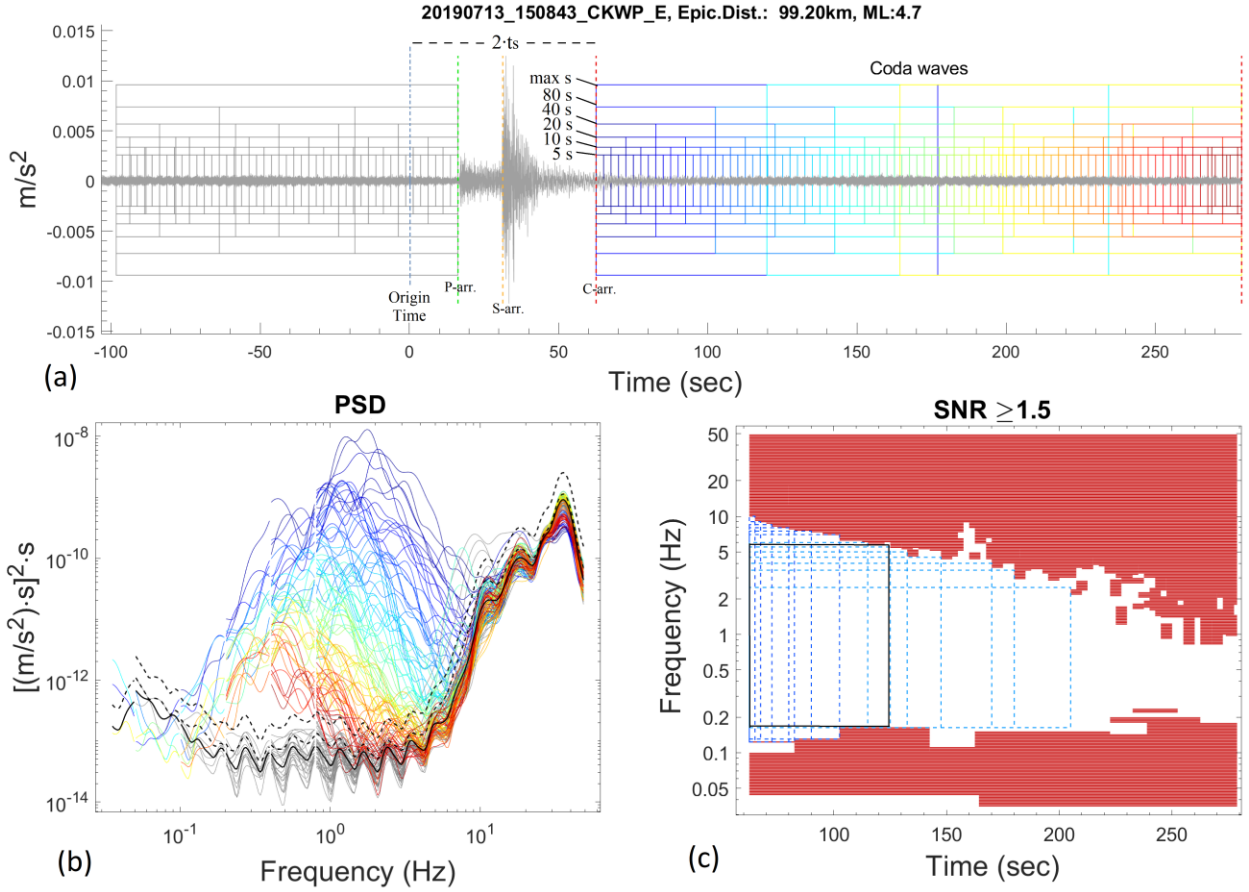

Figure 33. (**a**) The acceleration record ("E-W" component) of an earthquake at the station "CKWP". The several consecutive and half-overlapped noise and coda wave examined window with different durations (5, 10, 20, 40, 80 s and the maximum examined window, details into the text) are depicted (grey and multi-colors, respectively). P, S and Coda wave arrival time are also depicted (green, orange and red vertical dashed lines). (**b**) The Power Spectral Density of the corresponding in **Figure 33a** windows. Geometrical Mean Spectrum (GMS) of Noise (solid black line), GMS plus one standard deviation (lower dashed line) (the considered noise level), and 2.25 times the noise level (1.5 at the FAS) (upper dashed lines) used for the reliable coda waves selection (step 2, flowchart-**Table 6**). (**c**) The coda wave Fourier Amplitudes per record time depicted with red and white, for SNR < 1.5 and SNR ≥ 1.5, respectively. The several cyan-blue dashed lines define the potential coda wave time windows that can be used for the specific reliable frequency ranges. The black rectangle defines the desirable 60 s coda wave window, corresponding to the maximum possible frequency range (0.18-6 Hz), of this example, which can be used as reliable for the SFC analysis. Its selection is based on the determination of the several dashed-blue rectangles.

Thus, in the above example, the frequency examined ranges for the 5, 10 and 20 s windows, will be the: 0.2 - (f_s/2) Hz, 0.1-0.2 Hz and 0.05-0.1 Hz, respectively. However, as the theoretical low frequency limit corresponding to each examined duration, $f_{min} = 1/L_c$ covers only one signal

cycle, it was thought more reliable to consider results only for frequencies corresponding to more than four cycles, i.e. $f_{min} = 4/L_c$ (Perron et al., 2018b). As a consequence, coda wave durations of 5, 10, 20, 40 and 80 s (where possible) were considered for the frequency ranges: 0.8 - (f_s/2) Hz, 0.4 - 0.8 Hz, 0.2 - 0.4 Hz, 0.1 - 0.2 Hz and 0.05 - 0.1 Hz, respectively. No attempt was made to consider frequencies lower than 0.05 Hz, because of the instrument type (see *ch*. 2.2) and the high pass filtering above 0.05 Hz. In case where this frequency limit is lower, then longer window should be examined.

The second item of the SNR process was applied in order to determine the most representative pre-event noise level. For this reason, a long enough time window (e.g. 120 s) before the P-wave arrival (**Figure 33a**), was used so that to detect the average noise, FAS_n. This spectrum was computed based on the geometric mean, FAS_n of several sets of consecutive noise time windows (**Figure 33a, b**), of the same duration as the ones used for the coda wave windows, mentioned above. Finally, the plus one standard deviation limit of the geometric mean, $FAS_n \cdot \sigma_n(f)$ (**Figure 33b**), was considered as the noise spectral level for which the SNR $\geq$ 1.5 is applied (**Figure 33c**) for the final selection of the satisfying quality coda wave window.

The minimum required length of the coda wave window, as well as the shorter desirable frequency range, constitute the two factors controlling the final reliable signal window that will be used for the STF estimation. When the selected coda time window is increased, the reliability bandwidth is usually decreased at high frequencies, as it can be observed in the example of **Figure 33c**. The rectangles marked by blue dashed lines represent the longest windows that can be considered for different frequency ranges. In this study, a relatively long coda wave time window of 60 s, was chosen in order to reliably estimate the low frequency plateau of the STF, since this plateau is necessary for obtaining the seismic moment, M_o. A minimum frequency-range from 0.5 Hz to 3 Hz, was required for all the examined records, both to capture - as much as possible - the low frequency STF part, and because this frequency range of SAF is of engineering interest.

4.2.3 Coda wave spectral decomposition

The non-stationary exponential decay of the coda wave energy has been firstly described by ***Aki, (1969)*** and ***Aki and Chouet, (1975)***, who considered the coda waves as the superposition of scattered seismic wavelets which are mainly body S-waves on randomly distributed inhomogeneities in the lithosphere (among others: ***Aki, 1980a***). Scattered waves arrive later in the "tail" of an earthquake record and therefore correspond to waves of larger travel distances, with lower and lower amplitudes in time, as they are affected by geometrical spreading, anelastic attenuation and scattering effects.

"Single Scattering" (***Aki and Chouet, 1975; Sato, 1978***) and "multiple scattering" (***Kopnichev, 1977***), are two commonly used theoretical models describing the "mechanism" that may control the coda wave energy reduction from source to site, in addition to the classical geometrical spreading. Both assume a spherical radiation from the seismic source for the total energy in an infinite elastic medium with scatterers. The results in the present study are based on

the "single scattering" model, in which the backscattering process is assumed to be relatively weak, since each wavelet is considered to be backscattered only once. We choose to examine the "single-scattering" model in this study, recommending however the use of the "multiple-scattering" one, in a future analysis. The formalism would be the same for the "multiple-scattering" model, modifying only the value of the geometrical spreading parameter.

In terms of energy the relation between the Power Spectral Density (PSD), $R_{ij}(f,t')$ of the coda waves (in velocity) at a station, j, corresponding to an earthquake, i, for a specific travel time, t', is described by the following formula in frequency domain (***Aki, 1969; Aki and Chouet, 1975; Sato, 1977; Sèbe et al., 2018***):

$$R_{ij}(f,t') = W_i(f) \cdot E_c(f) \cdot |A_C(f,t')|^2 \cdot N_j(f) \quad [18]$$

where the $E_c(f)$ and $|A_C(f,t')|^2$ terms correspond to the total, distance-dependent attenuation factor, while the $W_i(f)$ and $N_j(f)$ terms, are related to the seismic source and site effect factors, respectively. $N_j(f) = \mathrm{SAF}_j(f)^2$ and the $W_i(f)$ source factor is given by ***Vassiliou and Kanamori, (1982)***:

$$W_i(f) = \frac{\left|\dot{\Omega}_i(f)\right|^2}{10\pi\rho\beta^5} \quad [19]$$

under the assumption of an isotropic source radiation, which is considered as a pre-condition in this study for the earthquakes used ($M_L \leq 5.1$). The $\dot{\Omega}_i(f)$ factor corresponds to the FAS of the STF in velocity domain. The denominator of the above ratio constitutes the seismic source scaling factor, which is controlled by the density, ρ (in *kg/m^3*) and the shear wave velocity, β (in *m/s*), of the medium close to the seismic source.

The attenuation factor (Eq. [18]), according to the "single scattering" attenuation model (***Aki and Chouet, 1975; Sato, 1978***), in energy domain adopted in this study, is controlled by the product of the excitation factor $E_c(f)$, with the factor:

$$|A_c(f,t')|^2 = \frac{1}{(v_s \cdot t')^{\eta}} e^{-\frac{2\pi f t'}{Q_c(f)}} \quad [20]$$

where t' is the travel time of the signal, v_s (in *m/s*) is the average shear wave velocity considered for the area that coda waves travelled and $Q_c(f)$ is the frequency dependent quality factor for coda waves.

The first term, $(v_s \cdot t')^{-\eta}$ of Eq. [20] controls the loss of energy due to geometrical spreading, where for the single scattering model, it is $\eta = 2$ (***Aki and Chouet, 1975; Sato, 1977; Sato et al., 2012***). The exponential term of Eq. [20] controls the loss of energy due to both anelastic (intrinsic) and scattering attenuation of S-waves. These two "causes" of attenuation (anelasticity of the medium and wave scattering), are related to the physical properties of the medium, as well as to its heterogeneous "character" (among others: ***Soham and Abhishek, 2016***), expressed by the

velocity variabilities and by the existence of complex geological structures (e.g. faults, folds, etc.), respectively. It is worth noting that these two attenuation factors, are merged in the second part of Eq. [20], being impossible to isolate them in this study.

The frequency dependent excitation factor $E_c(f)$ (Eq. [18]), included into the single scattering attenuation model, indirectly expresses the fractional loss of energy per unit travel distance of the waves from the source to the receiver, due to the wave scattering by the lithosphere heterogeneities. In fact, this factor controls the intensity of scattering and is considered as an independent scaling factor of attenuation with dimensions of *length*$^{-1}$. Following ***Sèbe et al., (2018)***, based on ***Herraiz and Espinosa, (1986)***, it can be written:

$$E_c(f) = \frac{1}{\pi \cdot l(f)} \quad [21]$$

where $l(f)$ (in *m*) is the frequency dependent mean free path (***Sato, 1978***), indirectly characterizing the distribution of the scatterers. Mean free path is an *a priori* unknown "free" parameter and describes the wave propagation providing information about the tectonic setting.

Under the assumption of a reference site (no spectral amplification, i.e. $N_j(f) = 1$), ***Sèbe et al., (2018)*** refer to the exponential model of crustal heterogeneities distribution, supported by *in situ* observations (***Dolan et al., 1998***) and by suitable measurements analysis (***Gusev and Abubakirov, 1996***). Based on the above, they theoretically consider that for the single scattering model where the attenuation factor $A_C(f, t')$ affects the exponential decay of coda wave amplitudes, the mean free path could also be considered as frequency independent, $l(f) = l$, so that Eq. [21] becomes:

$$E_c(f) = E_c \quad [22]$$

Thus, the corrected by $A_C(f, t')$ coda waveform can be considered as the convolution of many similar wavelets of the "apparent" STF (characterized by their PSD: $W_i(f) \cdot N_j(f)$, according to Eq. [18]) at random arrival times, with the square root of the constant (time and frequency independent) coda excitation term, $\sqrt{E_c}$.

4.2.4 Estimation of the coda quality factor, $Q_c(f)$

The derivation of coda quality factor $Q_c(f)$ is based on the analysis of the time decay rate of coda wave envelopes, as outlined by ***Aki and Chouet, (1975)***. This analysis follows the principle of energy conservation between source and receiver, in continuous wave arrival times, based on the single scattering model (Eq. [20]). It is implemented by applying a series of successive narrow band-pass filters to the selected coda signal, centered on a set of 25 central frequencies f_{cen}, equally distributed on logarithmic scale between 0.06 and 30 Hz. The corresponding Q_c is determined for each value of f_{cen} according to the four-step approach proposed by ***Margerin et al., (1999)***, as it is detailed below.

Firstly, the coda wave record, at each component, is bandpass filtered (*Butterworth*, 3rd order) around each central frequency f_{cen}, with a narrow bandwidth taken equal to the 2/3 of the central frequency f_{cen}. Thereafter the analytical filtered signal is determined by using the *Hilbert* Transform to the filtered signal and its modulus (absolute value) is computed at each time, *t*.

For the 25 filtered signals, the frequency dependent energy, $J(f_{cen}, t')_{\text{comp}}$ for each component (e.g. **Figure 34a**) at each consecutive in central time, t' coda envelope of duration $T_{cen} = 1/f_{cen}$ seconds (1.5 s time step), is computed by summing up the square of the corresponding analytical filtered signal amplitudes, determined above. The time t' corresponds to the middle time of each examined coda envelope. The same process is applied on the pre-event noise record (e.g. **Figure 34a**). The geometric mean value of the noise energy, $J_n(f_{cen}, t')_{\text{comp}}$ is considered as the average noise energy level (at each frequency) and a SNR threshold of 1.5, in terms of energy was applied to detect the reliable values of $J(f_{cen}, t')$ for the $Q_c(f)$ estimation analysis (e.g. **Figure 34a**).

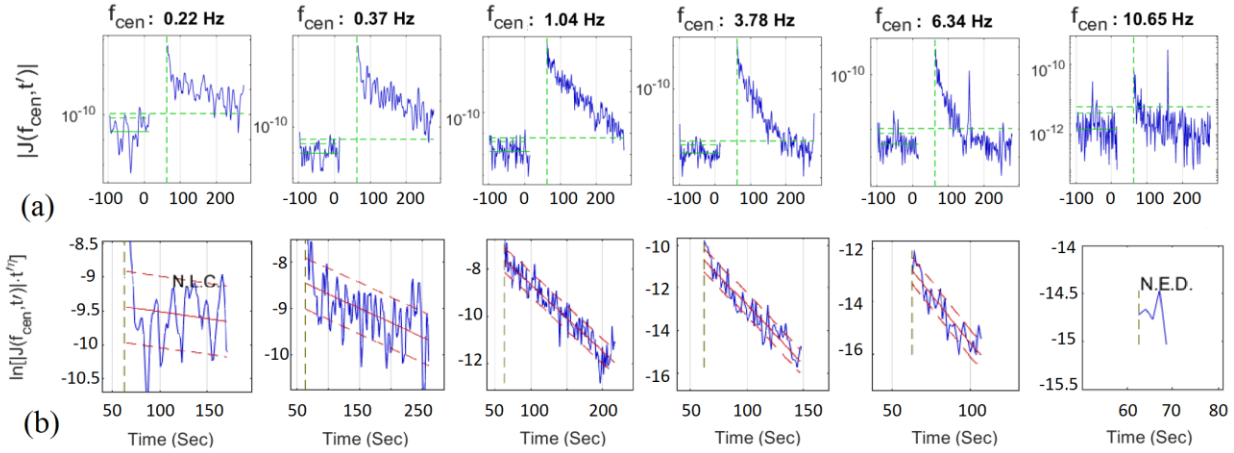

Figure 34. (**a**) (upper) Examples of the $|J(f_{cen}, t')|$ energy (blue line) of each component, at each time t' of the band-passed signal (pre-event noise and coda waves) for 6 central frequencies (f_{cen}) (for the record of **Figure 33a**). S-wave arrival time, t_s (vertical green dashed lines), Average Noise Level (AVL) (horizontal solid green line), the AVL + one standard deviation (horizontal green bottom dashed lines), and the final considered noise level (horizontal green upper dashed lines), are also depicted. (**b**) (bottom) Plots of the $\ln[J(f_{cen}, t') \cdot t'^{\eta}]$ quantity (Eq. [23]), corresponding to **Figure 34a**, computed only for the coda wave part, versus time. The least square analysis (solid red line) with its standard deviation (red dashed lines) are depicted, where N.L.C and N.E.D., indicate the "Non Linear-Correlation" and "Not Enough Data" according to the criteria described in the text.

Secondly, the total coda wave energy $J(f_{cen}, t')$ of the 3-component earthquake records is computed (e.g. **Figure 34b**), by summing up the partial energies, $J(f_{cen}, t')_{\text{comp}}$ of each component (e.g. **Figure 34a**), for each time, where they are considered reliable with the SNR criterion.

The third step consists in deriving the resulting coda quality factor $Q_c(f_{cen})$ by a least square (L-S) fit of $\ln[J(f_{cen}, t') \cdot t'^{\eta}]$ versus time, t', according to Eq. [23], for each central frequency, f_{cen} (**Figure 34b**). Eq. [23] results after taking natural logarithms of Eq. [18] and using Eq. [20].

$$\ln\left[J(f_{cen}, t') \cdot t'^{\eta}\right] = V(f) - \frac{2\pi f_{cen} t'}{Q_c(f_{cen})} \quad [23]$$

where:

$$V(f) = \ln\left[W_i(f) \cdot E_c(f) \cdot \frac{1}{v_s^{\eta}} \cdot N_j(f)\right] \quad [24]$$

$V(f)$ factor includes all the time independent factors of Eq. [18].

Standard deviations of $Q_c(f_{cen})$ are also determined together with the mean values. It should be noted that the L-S fit is implemented only if the duration of the examined filtered signal is greater than 10 times (signal cycles) of the corresponding T_{cen} ($1/f_{cen}$) (e.g. for f_{cen} = 0.2 Hz, 50 s minimum signal is considered), with a minimum threshold of 30 s (e.g. **Figure 34b**, mentioned as: N.E.D.-"Not Enough Data") and a maximum of 180 s. Moreover, the $Q_c(f_{cen})$ computed from the L-S fit at each f_{cen} and which did not present linear correlation according to Eq. [23] (minimum absolute linear correlation coefficient of 0.55, e.g. **Figure 34b**, mentioned as: N.L.C.-"Non Linear Correlation"), were not taken into account at the next step of the $Q_c(f)$ model estimation (e.g. **Figure 34b**). These empirical criteria were taken into account based on our observations, in order: (a) to conclude to reliable and robust slopes related to $Q_c(f_{cen})$ computation and (b) to avoid distant enough, regional attenuation effects (changes in slopes by variation of quality factors).

Finally, the fourth step consists in using the measured $Q_c(f_{cen})$ values to fit an analytical frequency dependent model $Q_c(f)$, as it is needed for the subsequent determination of minimum phase STF. The $Q_c(f)$ was initially fitted by the classical power-law $Q_c(f)$ model given by Eq. [25] following ***Aki, (1980b)*** and ***Singh and Herrmann, (1983)***:

$$Q_c(f) = Q_c \cdot f^{a} \quad [25]$$

Such a model is generally satisfactory for f > ~1 Hz. However, for lower frequencies (f < 1 Hz), ***Herraiz and Espinosa, (1986)*** based on computations of ***Sato (1982)*** and on Aki's conjecture (***Aki, 1980a***), outlined that the $Q_c(f)$ may stabilize or even increase with decreasing frequency. In this study, the $Q_c(f)$ model required for the attenuation factor removal in time domain (Eq. [20]), could be fitted according to Eq. [25] down to 1 Hz, but most recordings also indicated some Q_c increase below ~1 Hz. Thus, such a $Q_c(f)$ "behavior" was modeled by allowing higher polynomial degrees in the fit between $ln[Q_c(f_{cen})]$ and $ln(f_{cen})$. Depending on the observed $Q_c(f_{cen})$ results, a 3rd, 2nd or sometimes a 1st degree (same as Eq. [25]) polynomial were found, as it is shown at the characteristic examples of **Figure 35**.

In this regression analysis, standard deviations of $Q_c(f_{cen})$ are taken into account and finally the standard deviation of the computed polynomial is also used in the following mpSTF computation process.

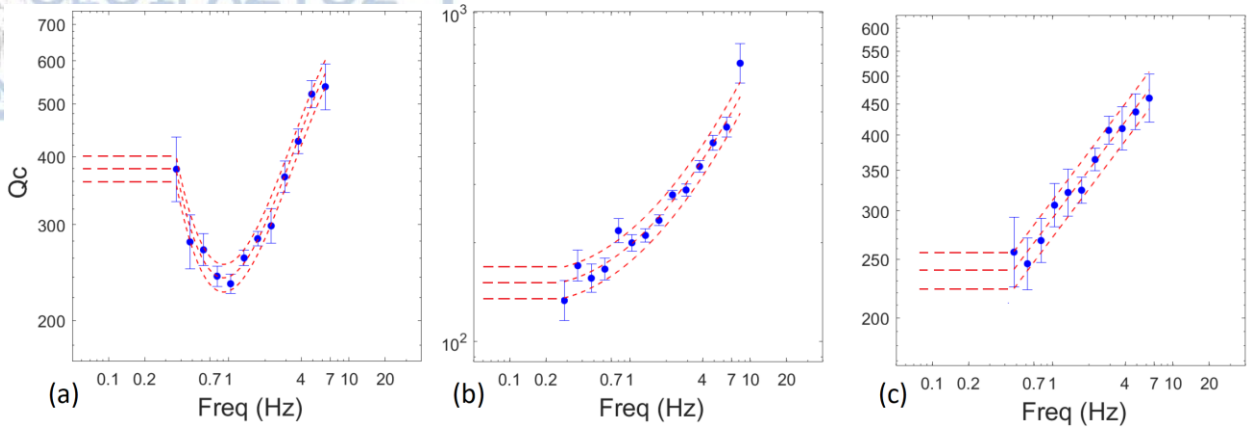

Figure 35. Three characteristic examples of the $Q_c(f)$ (± one standard deviation) model based on regression analysis (red dashed lines) between $\ln(Q_c(f_{cen}))$ and $\ln(f_{cen})$ (the blue points), for a 3rd, 2nd and 1st degree polynomial (**a**,**b** and **c**, respectively). **Figure 35a** corresponds to the $Q_c(f_{cen})$ calculation from the example of **Figure 34a**.

4.2.5 Attenuation Factor Removal

The removal of attenuation from the coda record is required, for each component, in order to obtain a stationary waveform at each component (**Figure 36a**) from which the apparent source time function can be retrieved. This removal is based on the analytical process presented in ***Sèbe et al., (2018)***. Here it's worth noting that the attenuation factor removal is separately applied on each earthquake-station pair (single) record, based on the corresponding computed $Q_c(f)$ model (e.g. **Figure 35a**). The common computed $Q_c(f)$ model of an examined region is also recommended to be investigated with this methodology, in case where enough records will be available.

Briefly, this process is achieved by deconvolving all the sliding 60 s minimum phase wavelets, $A_C(t,t')^{min}$ (based on $A_c(f,t')$ spectrum of Eq. [20], except for the frequency independent factor $v_s^{-\eta}$, here), for each progressive central time t', from the corresponding 60 s sliding coda stationary waveform windows (zero padded where it is needed), tapered by a *Hanning* window. Finally, the stationary waveform is "constructed" in time by all the specific amplitude values, which correspond to the median values, t' of each one of the sliding deconvolved signals. The $A_C(t,t')^{min}$ wavelets (scaled for the factor $v_s^{-\eta/2}$), scaled for the factor $v_s^{-\eta}$ (Eq. [20]), are constructed based on the inverse Fourier Transform of the frequency and time-dependent part of $A_C(f,t')$ (Eq. [20], except for the frequency independent factor $v_s^{-\eta}$), from the coda waveform.

$$A_c(t,t')^{min} = \frac{1}{2\cdot\pi}\cdot\int_{-\infty}^{\infty}|A_C(f,t')\,|\cdot e^{-i(2\pi f t+\varphi(f)_{min})}\,df \qquad [26]$$

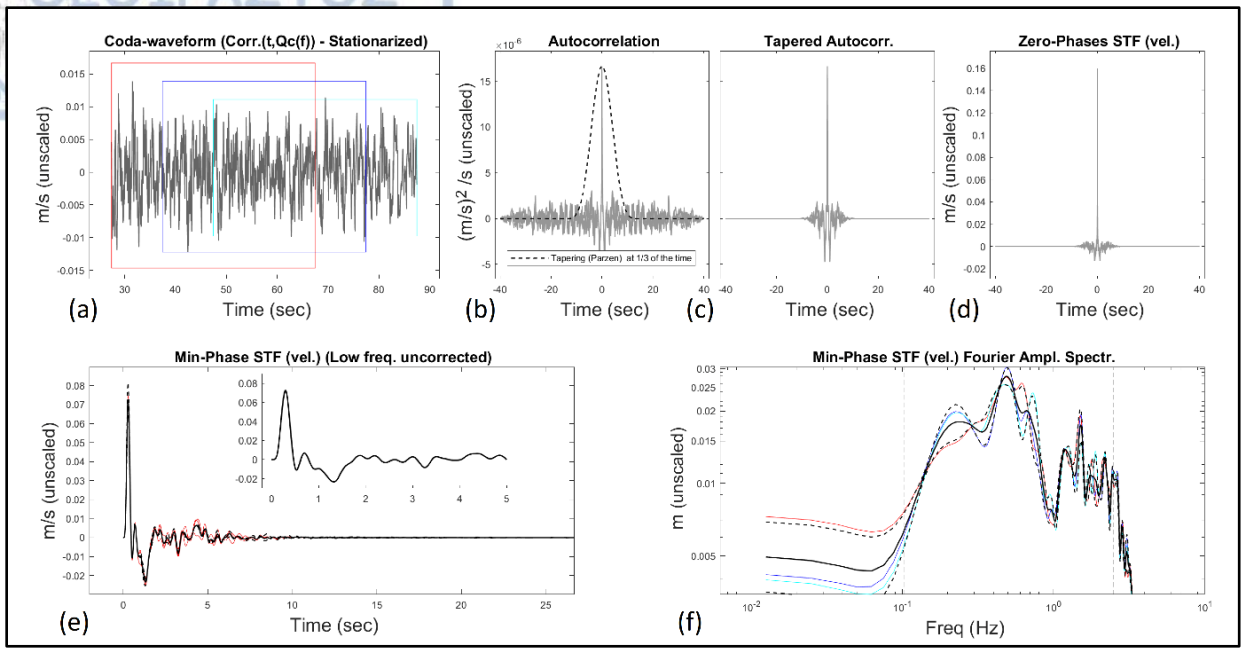

Figure 36. (**a**) An example of a 60 s corrected (stationary) velocity coda waveform of an earthquake (20151117_123756, M_L = 4.5, Epic. Dist. = 38 km) recorded at a rock site (ITC1) and the three consecutive 40 s examined time windows (75% overlapped, red, blue, cyan). (**b**) The 3 normalized autocorrelation functions (overlapped) of the 40 s time windows of (**a**) and the applied tapering function in a descriptive way (*Parzen* window, dashed line). (**c**) The 3 smoothed by tapering autocorrelation functions (T.A.F.) (overlapped) of (**b**). (**d**) The 3 zero-phases (symmetric) wavelets computed from the T.A.F. of (**c**), (details into the text). (**e**) The 3 minimum phase wavelets (M.P.W.) of wavelets shown in (**d**) (red), and their average one (black). (**f**) The 3 Fourier Amplitude Spectra of M.P.W. shown in (**e**), (colors correspond to Fig. **a**) and their geometric mean Spectrum (solid black) $\pm$ one standard deviation in log scale (dashed black lines). The vertical black dashed lines indicate the reliable part of the spectrum as it was studied in SNR process (**Figure 34**).

Regarding the $A_C(f,t')$ spectrum computation (Eq. [26]), as it exhibits a continuous dependence on $Q_c(f)$, the polynomial model obtained from the least-square fit between $ln[Q_c(f_{cen})]$ and $ln(f_{cen})$ as described in the previous section (e.g. **Figure 35**), is used at each frequency. Since this fit cannot be extrapolated to very low frequencies, needed for the 60 s windows, it is assumed that $Q_c(f)$ = constant = $Q_c(f_{cen}^{low})$ for frequencies f below the lowest frequency f_{cen}^{low} , for which $Q_c(f_{cen}^{low})$ can be reliably estimated (left points in **Figure 35**). This consideration can be reasonably applied when the f_{cen}^{low} is ~0.5 Hz, since the unknown potential $Q_c(f < f_{cen}^{low})$ variability does not significantly affect the final computed STF, as experimentally observed for the examined low to moderate magnitude earthquakes. Moreover, it's worth noting that at these low frequencies ($f < f_{cen}^{low}$) the FAS of the STF mainly belongs to the unreliable part, which does not affect the STF and it is appropriate and reliably corrected as described below.

In this study, the $A_C(t,t')^{min}$ wavelets computation is indirectly implemented, by firstly applying a zero phase inverse Fourier Transform (iFT) to the $A_C(f,t')$ spectra obtained for each time t', leading to a time domain wavelet, $A_C(t,t')^{zero}$, and then deriving its minimum phase

equivalent $A_C(t,t')^{min}$, by using the "rceps" Matlab function (*Matlab 2017* and later), based on the real cepstrum construction (***Oppenheim and Ronald, 1975***; ***Weinstein, 1979***).

Finally, the corresponding coda windows centered on t' are then deconvolved from these sliding $A_C(t,t')^{min}$ wavelets, by applying a "water-level" deconvolution process (***Margrave, 1998; Margrave et al., 2011***) for a "water level" of 5% of the maximum spectral amplitude of the examined stationary coda waveform window.

In order to account for the uncertainty in coda quality factor, this deconvolution process is repeated 3 times considering three different $Q_c(f)$ models (average and average ± one standard deviation, e.g. **Figure 35**), leading to three different "stationarized coda waveforms – for each component and finally to nine "stationarized coda waveforms" for all the components. The amplitudes of these waveforms are corrected for the hypocentral distance, but are still affected by the several, frequency independent, scaling factors (Eq. [24]).

4.2.6 Scaled FAS(f) of velocity STF_{comp} estimation

After the removal of the frequency and t' dependent attenuation factor ($|A_C(f,t')|^2$) (Eq. [20], except for the term $v_s^{-\eta}$) from the coda waves at each component, separately, the corresponding stationary waveform is retrieved and from now on will be called as $X_{ij}(t,t')$ (**Figure 36a**). The symbol of time t' in $X_{ij}(t,t')$ simply characterizes the central time of each potentially examined window of the total retrieved coda stationary waveform, X_{ij}. The corresponding PSD, $C_{ij}(f,t')$ of $X_{ij}(t,t')$ corresponds to $e^{V(f)}$ factor (Eq. [24]) and is expressed according to Eq. [23] and [24] ($\eta = 2$, Eq. [20]), based on Eq. [19], [21] and [22], as:

$$C_{ij}(f,t') = \frac{\left|\dot{\Omega}_i(f)\right|^2}{10\cdot\pi\cdot\rho\cdot\beta^5} \cdot \frac{1}{\pi\cdot l} \cdot \frac{1}{v_s^2} \cdot N_j(f) \qquad [27]$$

In Eq. [27], the quantities: $\frac{1}{10\pi\rho\beta^5}$, $\frac{1}{\pi\, l}$ and $\frac{1}{v_s^2}$ are constant factors (frequency and time independent), directly controlling the scale of the Fourier Amplitude Spectrum, $\dot{\Omega}_i(f)$, albeit the second and the third factors refer to the propagation path. Thus, from now on their product will be referred as "*F*" factor, where:

$$F = \frac{1}{10\cdot\pi^2\cdot\rho\cdot\beta^5\cdot l\cdot v_s^2} \qquad [28]$$

Consequently, taking into account Eq. [28], Eq. [27] can be written as:

$$C_{ij}(f,t') = \left|\dot{\Omega}_i(f)\right|^2 \cdot N_j(f) \cdot F \qquad [29]$$

The above equation represents, in the frequency and energy domain, the relation between the "raw" coda stationary waveform of each component, obtained after the previous step, and the scaled by

the factor F (Eq. [28]), apparent $\dot{ST}F_{comp}^{sc}$ (in velocity) at the recording site, i.e., the product of the frequency dependent, source and site terms.

The goal of this study is to recover the scaled apparent source term (Eq. [29]) of an earthquake *i*, at every receiver *j*, based on the spectral factorization method and then (i) to recover the scaled "true" source term from sites which can be considered as reference sites (i.e., without any amplification: $N_j(f) = \mathrm{SAF}_j(f)^2 = 1$), and (ii) to recover the site term $N_j(f) = \mathrm{SAF}_j(f)^2 \neq 1$, for all other sites, by comparing with the scaled source terms at reference sites. The stage (i) allows to obtain an estimate of the seismic moment if it is properly corrected for the scaling factor (F in the energy domain and $\sqrt{F}$ for the real amplitudes in the time and frequency domain). The present chapter describes in detail this particular stage.

In principle, the most straightforward way to estimate $C_{ij}(f, t')$ is to derive it simply by taking the square of the Fourier Transform of each considered, coda stationary waveform window $X_{ij}(t, t')$ (**Figure 36a**). However, the methodology proposed by ***Sèbe et al., (2018)*** allows a more robust estimate of $C_{ij}(f, t')$ through the use of the ***Wiener-Khinchin*** theorem. The latter links the PSD, $C_{ij}(f, t')$ of the stationary corrected coda waveform, $X_{ij}(t, t')$, to the Fourier Transform of the autocorrelation function, $A_{XX}(\tau, t')$ of $X_{ij}(t, t')$, as expressed in Eq. [30]:

$$C_{ij}(f, t') = \int_{\tau=-\infty}^{+\infty} A_{XX}(\tau, t') \cdot e^{-i \cdot 2 \cdot \pi \cdot f \cdot \tau} \, d\tau \qquad [30]$$

where:

$$A_{XX}(\tau, t') = E\{X_{ij}(t, t') \cdot X_{ij}(t - \tau, t')\} \qquad [31]$$

for lag time, τ.

As illustrated in **Figure 36b, c**, the tapering of $A_{XX}(\tau, t')$ function, allows to eliminate what is, more likely, "noise" at large lag times, so that the *Fourier Transform* of the tapered $A_{XX}(\tau, t')$ function (Eq. [30]) is probably less contaminated by noise than the direct *Fourier Transform* of $X_{ij}(t, t')$. In addition, applying this process to successive coda windows centered on different travel times t', allows estimating both the average $C_{ij}(f, t')$, and the corresponding variability / uncertainty.

From a practical viewpoint, in the example of **Figure 36, t**hree 40 s autocorrelation time functions, $A_{XX}(\tau, t')$, 75% overlapped, are computed (**Figure 36b**) from the 60 s coda stationary window, $X_{ij}(t, t')$ (**Figure 36a**). The resulted, symmetric in time domain 80 s long (40 s right and left from zero time), symmetric in time domain $A_{XX}(\tau, t')$ are then tapered with a 26.7 s (80/3 s) long *Parzen* window (**Figure 36b, c**), also symmetric in zero time, keeping only the 1/3 of each $A_{XX}(\tau, t')$, as the reliable part of the autocorrelation function, removing the same time the late "lag" noise.

To derive the minimum phase wavelets of the "apparent"- scaled (Eq. [29]), $S\dot{T}F(t')_{comp}^{sc}$ (in velocity), of each examined 40 s coda stationary window $X_{ij}(t,t')$ at central time t', the procedure is implemented in two steps. The first one is to obtain its corresponding Fourier Amplitude Spectrum, $FAS[S\dot{T}F(t')_{comp}^{sc}]$ which is equal to the square root of the PSD, $C_{ij}(f,t')$, ($|\dot{\Omega}_i(f)|\cdot\sqrt{N_j(f)}\cdot\sqrt{F}$, Eq. [29]) and is simply computed from the square root of the FAS of the tapered autocorrelation function (Eq. [30] right term). The second step is to derive the source time function wavelet by assuming it is a minimum phase signal (see ***Sèbe et al., 2018***, for detailed discussion on this assumption). In the present study, the latter minimum phase derivation was performed in two steps: a) obtaining, an easy to be created, "zero-phases" wavelet (imaginary part, $I(f) = 0$, of the Fourier Transform, at each frequency, f), which is of equivalent FAS to the source time function, by simply computing the *inverse Fourier Transform* of the estimated $FAS[S\dot{T}F(t')_{comp}^{sc}]$ (**Figure 36d**) (real part, $R(f) = FAS[S\dot{T}F(t')_{comp}^{sc}]$, since $I(f) = 0$) and then deriving its minimum phase equivalent (**Figure 36e**) with the "*rceps*" Matlab function (***Oppenheim and Ronald, 1975***; ***Weinstein, 1979***; ***Matlab 2017b*** and later).

There are as many estimates of the minimum phase, $S\dot{T}F(t')_{comp}^{sc}$ as the number of considered (stationarized) coda windows $X_{ij}(t,t')$ at central times t'. Here, implementing the aforementioned procedure separately for each component, the geometric mean $FAS[S\dot{T}F_{comp}^{sc}]$ of the three $FAS[S\dot{T}F(t')_{comp}^{sc}]$ computed for each 40 s examined stationary window $X_{ij}(t,t')$ (**Figure 36a**), centered at time t', as well as its one standard deviation range, are determined (**Figure 36f**) and the corresponding three minimum phase, $S\dot{T}F_{comp}^{sc}$ (average and its ± std) are also derived (**Figure 36e**).

To be sure that the minimum phase $S\dot{T}F_{comp}^{sc}$ is not contaminated by high-frequency noise, all the minimum phase wavelets are low-pass filtered with a 4th or higher order Butterworth filter, with a cut-off frequency corresponding to the upper limit of the reliable frequency band provided the SNR analysis (step 2, flowchart-**Table 6**, e.g. **Figure 33**).

4.2.7 Scaled FAS(f) of velocity STF estimation

The aforementioned procedure is applied separately for each component and the total of the three components scaled for the factor $\sqrt{F}$ (Eq. [29]), $FAS[S\dot{T}F^{sc}]$ in velocity) is estimated by the three $FAS[S\dot{T}F_{comp}^{sc}]$ (step 5, flowchart-**Table 6**), according to Eq. [32] (e.g. **Figure 37a**):

$$FAS[S\dot{T}F^{sc}] = \sqrt{FAS[S\dot{T}F_{EW}^{sc}]^2 + FAS[S\dot{T}F_{NS}^{sc}]^2 + FAS[S\dot{T}F_{Z}^{sc}]^2} \qquad [32]$$

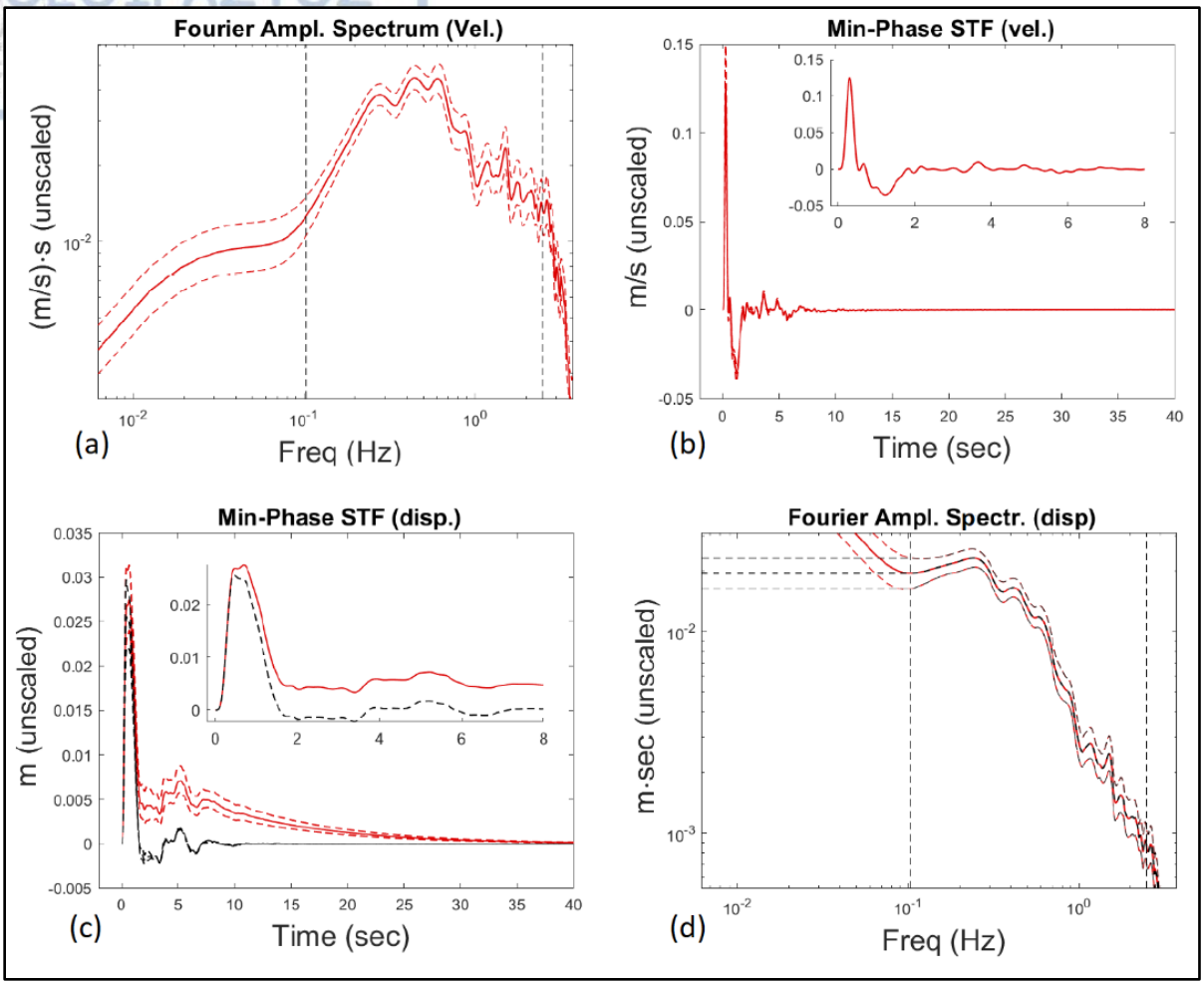

Figure 37. (**a**) The common "apparent"-scaled velocity $FAS[S\dot{T}F^{sc}]$ corresponding to the example of **Figure 36**. (**b**) The $mpS\dot{T}F^{sc}$ (vel.) corresponding to the FAS of **a**. (**c**) The $mpSTF^{sc}$(disp.) after integration of the corresponding velocity one shown in (**b**) (red line) and the corresponding one (black dashed lines), corrected for the low frequency plateau (details in the text). (**d**) The two "average" $FAS[mpSTF^{sc}]$ of the two $mpSTF^{sc}$ in **c** (red and black lines, respectively) (identical for frequencies greater than ~ 0.1 Hz) and their std range.

The corresponding standard deviation of $FAS[S\dot{T}F^{sc}]$, (in logarithmic scale), is also computed (**Figure 37a**), taking into account the propagation of the corresponding standard deviation obtained for each component.

Finally, the minimum phase "apparent"-scaled (Eq. [29]) Source Time Function, $mpS\dot{T}F^{sc}$ (in velocity) and its corresponding upper-lower standard deviation wavelets are determined (**Figure 37b**), following the same minimum phase computation process mentioned above.

4.2.8 Scaled displacement minimum phase STF estimation

The next step is to estimate the minimum phase "apparent" - scaled (Eq. [29]) Source Time Function, $mpSTF^{sc}$, in terms of displacement. This is done by integrating the corresponding

velocity $mpS\dot{T}F^{sc}$ and re-computing its minimum phase wavelet with the same procedure, mentioned above.

To avoid zero frequency issues, the velocity wavelets are high-pass filtered with a 2-order *Butterworth* filter at the lowest frequency limit (df = 1/40 Hz) associated to their duration (40 s). After filtering and integration, the displacement Fourier amplitudes are maintained equal to the corresponding velocity ones divided by the angular frequency, $\omega_k = 2\pi f_k$ ($f_k \neq 0$). Such a procedure is applied to the three velocity wavelets, $mpS\dot{T}F^{sc}$ (average and average ± one standard deviation) obtained in the previous step (related to Eq. [32], step 6, flowchart-**Table 6**).

In terms of amplitude, the so-derived displacement $mpSTF^{sc}$ is still scaled by the $\sqrt{F}$ factor and by site factor, $\mathrm{SAF}_j(f)$ (Eq. [29], $\mathrm{SAF}_j(f) = \sqrt{N_j(f)}$) (e.g. **Figure 37c**) and may be contaminated by low frequency noise because of poor SNR ratio at these frequencies (e.g. **Figure 33**). Consequently, its FAS is under the same scaling, by definition.

The next step is intended to account for this low-frequency contamination before estimating the seismic moment from the low-frequency plateau level.

4.2.9 Scaled STF low frequency correction

The effect of low frequency noise in seismic record is "propagated" also to the Fourier Amplitude Spectrum ($FAS[mpSTF^{sc}]$) of the $mpSTF^{sc}$ which is identical to the $FAS[STF^{sc}]$ of the real far-field STF, as it can be seen in the example of **Figure 37d**. In fact, this effect starts close to the lowest reliable frequency detected by the SNR process (step 2, flowchart-**Table 6**, e.g. **Figure 33**).

Theoretically, the far-field Source Time Function (STF) computed by the aforementioned methodology at a reference site (free of spectral amplification) (e.g. **Figure 37c**) should be a positive wavelet, representing the amount of energy (scaled by the constant $\sqrt{F}$ factor Eq. [28] and [29]) which is released during the seismic source rupture. Consequently, the scaled seismic Moment, $M_{o_{sc}}$, representing the total "scaled" energy released, must correspond to the "area" of the $mpSTF^{sc}$, while its $FAS[mpSTF^{sc}]$ is expected to present a low-frequency plateau below the corner frequency, f_c ($f_c = 1/T_c$, T_c: rupture duration), for which the following relation holds:

$$FAS[mpSTF^{sc}](f < f_c) \approx FAS[mpSTF^{sc}](0) \propto M_{o_{sc}} \qquad [33]$$

However, the low frequency noise "contamination" can definitely affect the shape of the retrieved "apparent" - scaled (Eq. [29]) $mpSTF^{sc}$, (e.g. **Figure 37c**) and consequently the estimation of the seismic moment $M_{o_{sc}}$. Nevertheless, as long as the lower-limit of reliable bandwidth, f_{LR}, derived from the SNR analysis, is significantly smaller than the corner frequency, the "raw" STF spectrum should exhibit a detectable flat part from which the $M_{o_{sc}}$ can be estimated based on Eq. [33].

This is, for instance, the case in **Figure 37d**. It is then possible to extend the source term $FAS[mpSTF^{sc}]$ at all frequencies $f \leq \sim f_{LR}$ (f_{LR} the lowest frequency for which $FAS[mpSTF^{sc}]$

is considered reliable according to SNR procedure, step 2, flowchart-**Table 6**) by simply taking it constant and equal to the $FAS[mpSTF^{sc}]$ at ~ f_{LR} as shown in **Figure 37d** (dotted black lines).

Eventually, the corresponding scaled minimum phase displacement source time function can be recomputed (black line in **Figure 37c**). A similar process can be applied on recordings from non-reference sites (site amplification included), as long as the site amplification does not affect too low frequencies and there is still a frequency band just over ~f_{LR} where $\mathrm{SAF}_j(f)$ ($N_j(f) = \mathrm{SAF}_j(f)^2$, Eq. [29]) is close to 1. Simple H/V analysis of coda as well as S-wave recordings can provide reliable indications on the site fundamental frequency f_{0j}, and whenever the ratio f_{0j}/f_{LR} is larger than ~3–4, one may reasonably assume the low-frequency part of the retrieved $FAS[mpSTF^{sc}]$ is not affected by the site amplification and may be used in the same way as for a reference site to perform a low-frequency correction of the apparent source term and to estimate the seismic moment. Such an example is presented in **Figure 38a, b** for a recoding obtained at station "CK0" located at the center of the Argostoli-Koutavos basin with a fundamental frequency of 1.4 Hz (***Theodoulidis et al., 2018***).

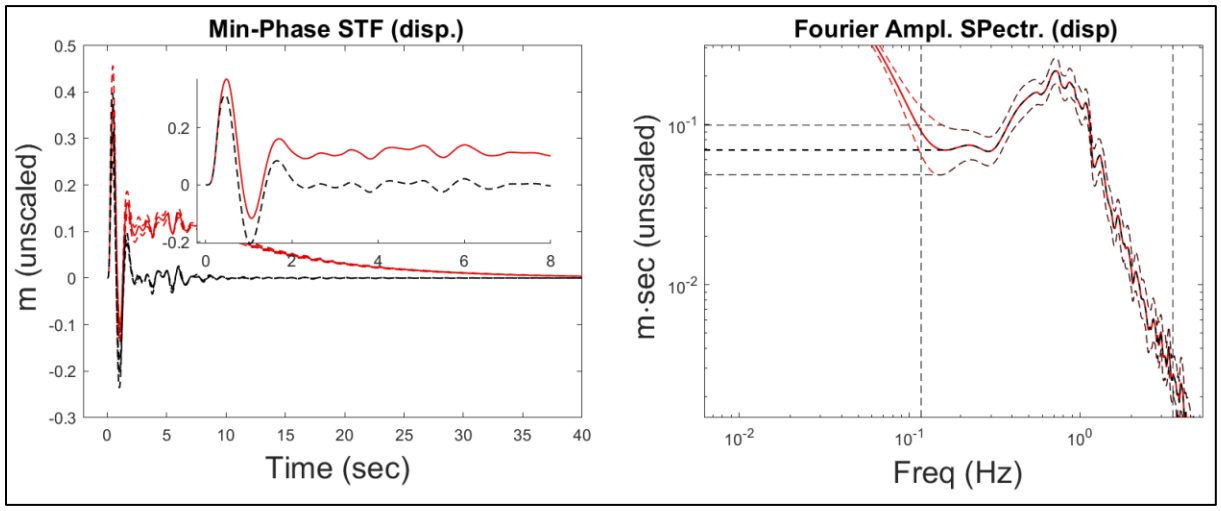

Figure 38. (**a**) (similar to **Figure 37c**) An example of a scaled (Eq. [28]) $mpSTF^{sc}$ (site effect included) of an earthquake recorded at the "VAS2" sedimentary basin site (uncorrected and corrected for the low frequency plateau, in red and black line, respectively) and (**b**) (similar to **Figure 37d**) their corresponding $FAS[mpSTF^{sc}]$ (red and black lines, respectively), identical for frequencies greater than ~0.1 Hz.

4.2.10 STF scaling correction and M_o computation - uncertainties

Since the SAF estimation technique, applied in this study, is based on the STF estimation, it is necessary to investigate all the elements that contribute to the scaling of STF (Eq. [29]) and seismic moment M_o, which, in turn, controls the absolute SAF amplitudes.

As repeatedly indicated, the processing detailed in the previous sections leads to estimates of a minimum phase "apparent"-scaled source time function $mpSTF^{sc}$, which include the $\sqrt{F}$ scaling factor (Eq. [29]). Whenever site amplification is negligible at low frequency, the scaled

seismic moment, $M_{o_{sc}}$ may be estimated from the scaled displacement spectrum plateau (step 8, flowchart-**Table 6**), according to Eq. [33] and the real seismic moment, M_o can be retrieved by the following equation:

$$M_{o_{sc}} = M_o \cdot \sqrt{F} \quad [34]$$

However, the knowledge of the factor, F, and consequently the estimation of seismic moment, M_o, remains an issue. Two computation strategies can be applied for determining the F factor and consequently M_o.

The first one is simply based on the M_o scaling of an examined earthquake in comparison to another one located in the same area and recorded at the same station, for which the M_o is already reliably estimated from a different methodology. Thus, computing the scaled STF of the second one and knowing its M_o, the $\sqrt{F}$ factor can be directly obtained from Eq. [34], without separately knowing all the crustal parameters involved in Eq. [28]. Consequently, correcting the scaled STF of the examined earthquake by the $\sqrt{F}$, its M_o is also computed from Eq. [34]. While such a strategy could contribute to the seismic moment estimation of low magnitude earthquakes for which M_o, cannot be computed from other methodologies, it requires the existence of another well characterized event at similar location, for which both the STF estimation process can be applied, and the M_o, can be computed with another reliable approach.

The second strategy is based on a direct computation of the scaling factor, $\sqrt{F}$ (Eq. [28]). This could be achieved by using representative values for the density (ρ) and the shear wave velocity (β) of the medium close to the seismic source (Eq. [19]), as well as for the mean free path l (Eq. [21]) and the average shear wave velocity along the propagation path v_s, (Eq. [20]). Although these parameters are unknown, several reasonable values can be considered in order to estimate the average STF and the seismic moment, M_o, as well as their variability/uncertainty.

More specifically, regarding the average shear wave velocity, v_s for the upper crust which is commonly used as 3.5 km/sec, a range of v_s values from 3.0 km/s to 4.0 km/s is assumed for the estimation of the average STF, M_o and their uncertainties and eventually of the moment magnitude M_w and its corresponding variability/uncertainty.

According to ***Hanks and Kanamori, (1979)***, M_w is provided by the following equation:

$$M_w = [log_{10}(M_o) - 9.1]/1.5 \quad [35]$$

where according to Eq. [34] it is:

$$M_w = \left[log_{10}\left(M_{o_{sc}}\right) - log_{10}\left(\sqrt{F}\right) - 9.1\right]/1.5 \quad [36]$$

and finally, the moment magnitude, M_w is directly and independently related to the v_s value but also to the ρ, β and l (Eq. [21] and [22]) through the following equation:

$$M_w = \left[log_{10}\left(M_{o\,sc}\right) + \frac{log_{10}(l)+log_{10}(\rho)+log_{10}\left(10\cdot\beta^5\right)}{2} + log_{10}(\pi\cdot v_s) - 9.1\right]/1.5 \qquad [37]$$

Thus, for an average computed moment magnitude, M_w, determined for v_s = 3.5 km/s and for its predefined range of values, 3.0 – 4.0 km/s, the maximum corresponding range of M_w is inversely computed as ±0.0446. This is defined based on the difference between the two corresponding M_w standard deviation limits (higher and lower) in comparison to the average one.

The same average and variation of shear wave velocities values, β, 3.0 - 4.0 km/s are considered for the medium close to the seismic source. In this case, also based on Eq. [37], the corresponding maximum range of the average computed moment magnitude, M_w is ±0.1116.

Following the same computation strategy, a representative density value of the Earth's crust (ρ ~ 2.8 g/cm^3), ranging from 2.5 to 3.1 g/cm^3 was considered, resulting in a variation range of ±0.0164 (**Figure 36**).

The total maximum "artificial" M_w expected variation range based on the combination of the corresponding individual ranges of the three scaling parameters (v_s, β and ρ), can, according to Eq. [37], cumulatively reach up to a maximum ±0.173 (±0.0446, ±0.1116, ±0.0164), lower than the usually routinely estimated standard deviation of ±0.2 (and higher), for moment magnitudes.

Regarding the initially unknown Mean Free Path, l which controls the excitation factor, E_c (Eq. [21], and [22]) and can significantly vary in different tectonic regimes, it can be considered equal to the mean free path under isotropic scattering conditions (***Sato, 1978***). The corresponding typical l values at these conditions can mainly range between 10 to 1000 km, according to measured values from several studies (***Hatzidimitriou, 1996; Lacombe et al., 2003; Margerin et al., 1999; Sato, 1978***). This range can be considered as a reasonable variation range with a geometric mean value of 100 km, for the STF and M_o computation strategy. However, based on these values of l, and on the same strategy followed above regarding the variation of v_s, β and ρ scaling parameters (Eq. [37]), the corresponding maximum M_w variation becomes significant (±0.333).

Consequently, in case that the second computation strategy is chosen for the STF scaling correction and M_o estimation, a total potential range of moment magnitude ±0.504 (0.171+0.333) must be considered, independently of the standard deviation range computed for the scaled STF and M_o.

4.2.11 Site Amplification Factor (SAF) estimation

The corrected $mpSTF^{sc}$ (displacement) obtained as presented in the previous sections, is in fact considered as the apparent $mpSTF$ (Eq. [29]) multiplied by the frequency independent factor $\sqrt{F}$ (Eq. [28]). This is theoretically true only after the low frequency part is modified by the plateau extension down to zero frequency (e.g. **Figure 37d** and **Figure 38b**). The last process can reasonably be considered as achievable for all sites where low frequency amplification can be considered negligible, i.e., both reference rock sites and all sedimentary sites with a fundamental

frequency above around 1 Hz (at least for the present study where coda waves exhibit a good signal-to-noise ratio down to around 0.2 Hz). Nevertheless, some sites over very thick deposits, or presenting intense topography, may exhibit low frequency amplification hampering the low frequency correction, and this deserves specific investigations through a comparison with other approaches to derive the SAF.

In any case (reference or non-reference site) the FAS of the $mpSTF^{sc}$, remains valid in the reliable frequency part (estimated with the SNR analysis, step 2, flowchart-**Table 6**), and independent of the fact that FAS values are affected by noise at low frequency.

Therefore, the Site Amplification Factor at a target site, $SAF(f)_{targ}$, could reasonably be estimated with the ratio of the Fourier Amplitude Spectra (FAS) of the real apparent STF (site effect included), computed from the same earthquake at the target site and at another one, whenever the latter can be assumed as a reference site (SAF$(f)_{ref}$ = 1). This relation is valid under the assumption of an isotropic source energy radiation, which in principle is acceptable for the coda waves of low-to-moderate magnitude earthquakes and is expressed by Eq. [38]:

$$\frac{FAS[STF]_{targ}}{FAS[STF]_{ref}} = \frac{FAS[real.STF]\cdot SAF(f)_{targ}}{FAS[real.STF]\cdot SAF(f)_{ref}} = \frac{SAF(f)_{targ}}{SAF(f)_{ref}} = SAF(f)_{targ} \qquad [38]$$

where the $FAS[STF]_j$ of the real "apparent" STF estimated at a site, j (target and reference), is simply considered as the product of the common $FAS[real.STF]$ of the real STF, free of site amplification, with the $SAF(f)_j$ of the corresponding site.

A similar relation can be established for the observed "scaled" $FAS[mpSTF^{sc}]$ obtained before their correction with the unknown factor $\sqrt{F}$ (Eq. [29]) since:

$$FAS[STF] = FAS[mpSTF^{sc}]/\sqrt{F} \qquad [39]$$

Thus, based on Eq. [39], [27] and [28], the Eq. [38] can be analyzed as:

$$SAF(f)_{targ} = \frac{FAS[STF]_{targ}}{FAS[STF]_{ref}} = \frac{FAS[mpSTF^{sc}]_{targ}/\sqrt{F_{targ}}}{FAS[mpSTF^{sc}]_{ref}/\sqrt{F_{ref}}} =$$

$$= \frac{FAS[mpSTF^{sc}]_{targ}\cdot v_{s_{targ}}\sqrt{10\pi^2\rho\beta^5 l_{targ}}}{FAS[mpSTF^{sc}]_{ref}\cdot v_{s_{ref}}\sqrt{10\pi^2\rho\beta^5 l_{ref}}} = \frac{FAS[mpSTF^{sc}]_{targ}\cdot v_{s_{targ}}\cdot\sqrt{l_{targ}}}{FAS[mpSTF^{sc}]_{ref}\cdot\ v_{s_{ref}}\cdot\sqrt{l_{ref}}} \qquad [40]$$

Eventually, taking into account Eq. [40] three simple conclusions can be extracted:

(i) The ratio of the scaled FAS[STF] of the "apparent" STF at the two sites (target and reference) can provide the $SAF(f)$ of the target site, only under the condition that both scaling factors, F_{targ} and F_{ref}, are known, or unknown but similar. The latter means that the average shear wave velocity v_s corresponding to the coda waves path from the earthquake focus to the target and

reference site ($v_{s_{targ}}$ and $v_{s_{ref}}$), as well as the corresponding mean free paths, $l_{targ}$and l_{ref}, must be similar, so that the $SAF(f)$ is not biased by a constant factor.

(ii) Taking into account the considered variation of v_s and l parameters, (3–4 km/sec and 10–1000 km, respectively), as mentioned above ($ch.$ 4.2.10) and following the same strategy with respect to the $SAF(f)$ instead of the seismic moment, M_w, the maximum difference between the computed $SAFs(f)$ at a target site from several earthquakes can reach a factor up to ~ 7 (lower or higher) between each other. This range is defined based on the $v_s{\cdot}\sqrt{l}$ ratio (Eq. [40]) between the target and the reference site, according to the range of their values. Nevertheless, when the reference and target sites are located at the same region, sharing the same seismotectonic regime, the path-related parameters v_s and $\sqrt{l}$ are unlikely to vary as much.

(iii) Although the absolute SAF$(f)_{targ}$ amplitudes depend on v_s and l parameters, the relative SAF$(f)_{targ}$ amplitudes values of the discrete frequencies are independent of these parameters and can be theoretically revealed by Eq. [40]. In other words, the shape of the SAF(f) is expected to be stable and independent of the scaling factor F.

4.3 Results

4.3.1 SAFs estimation based on SFC application to western Greece data

To estimate the SAF(f) at the 24 stations of **Figure 7**, the first two steps of the corresponding SAF estimation technique described in the flowchart (**Table 6**), were implemented, aiming at detecting the reliable 3-component records. Finally, 739 earthquake-station pairs (**Figure 7)**, were considered reliable to be examined for their STF computation, taking into account the SNR of the records.

To compute the apparent-scaled (Eq. [29]) $mpSTF^{sc}$, the coda $Q_c(f)$ model was estimated for each earthquake-station pair (**Figure 39**, **Appendix N**), following the 3rd step of the flowchart in **Table 6**. For all stations a general agreement of the $Q_c(f)$ model (**Appendix N**), is observed for the broader study area (western Greece). However, this observation cannot lead to the conclusion of an absolute agreement between the computed $Q_c(f)$ models since some discrepancies are presented in several earthquake-station pairs. These discrepancies could be due to epistemic uncertainties of the single-scattering model used, due to the uppermost layers effect of the coda waves especially in the sedimentary basin, or due to computational issues related to the single-scattering model.

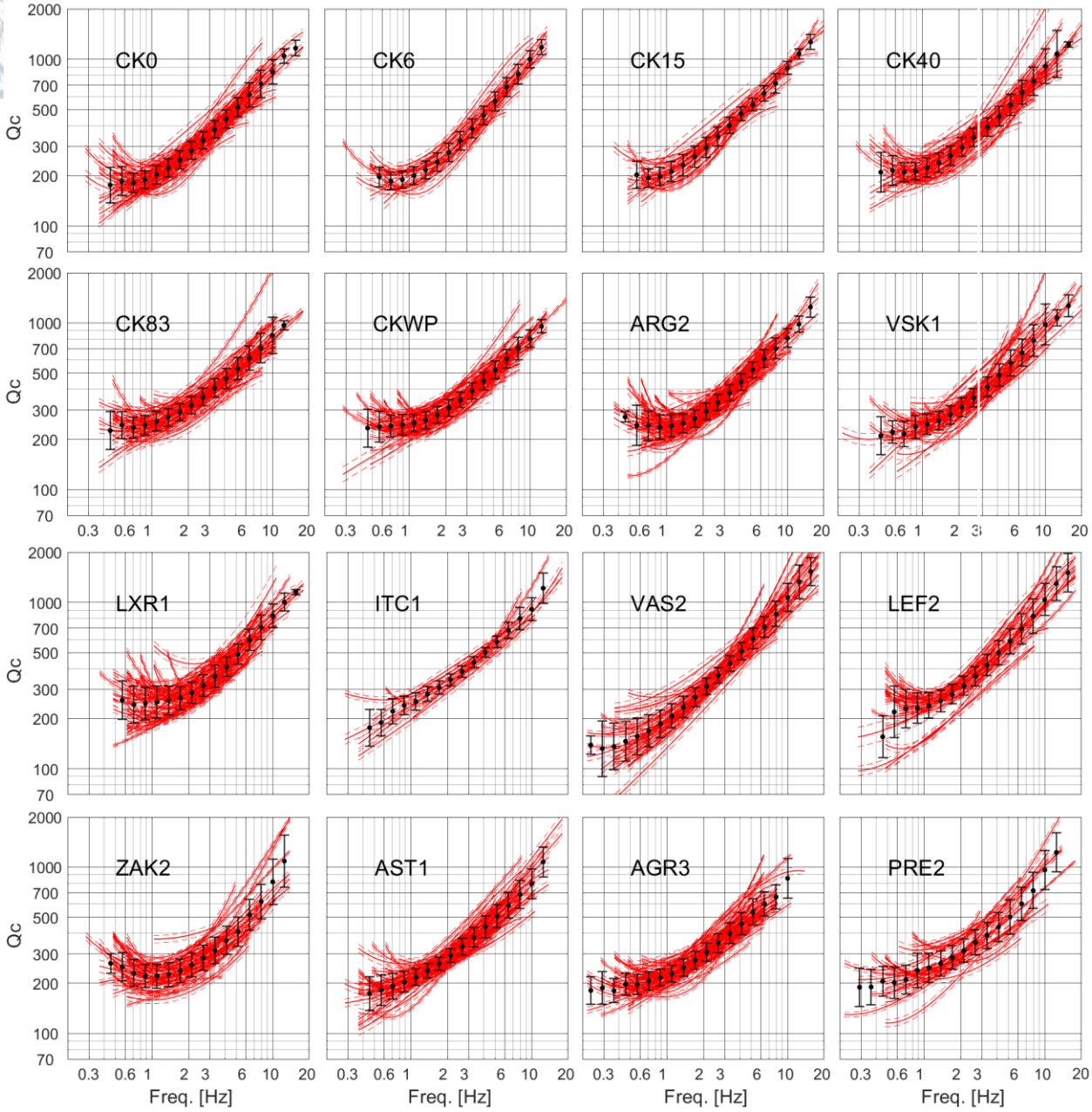

Figure 39. The $Q_c(f)$ models (red lines) computed from each pair of earthquake-station for the 24 examined sites (**Figure 7**). The geometric mean curve (Q(f), black lines) and the corresponding standard deviation range, at each station (sub-plot), is also displayed.

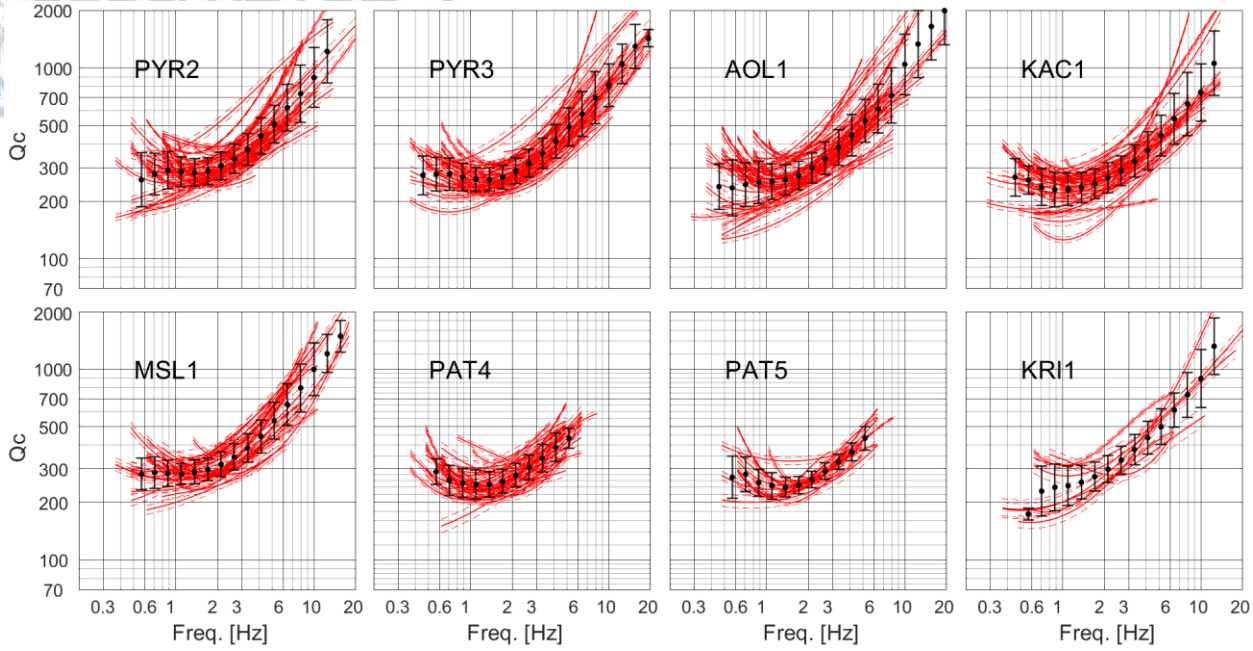

Figure 39. (continued)

Thereafter, based on these $Q_c(f)$ models, 739 scaled $mpSTF^{sc}$ of the 89 examined earthquakes (**Figure 7**) for the 24 sites were computed, following the 4th to 7th steps of the SAF(f) estimation technique of the flowchart (**Table 6**). Then applying the 8th step of the flowchart, these apparent $mpSTF^{sc}$, were corrected for the required low frequency plateau.

Consequently, the 9th flowchart step was applied to the low frequency corrected apparent $mpSTF^{sc}$, retrieving the corresponding seismic moment, M_o for each earthquake-station pair. Three different values of M_o were computed for each apparent $mpSTF^{sc}$, corresponding to the mean free path l values of 10 km, 100 km and 1000 km (see step 9, flowchart-**Table 6**). Based on these M_o, the corresponding moment magnitudes, M_w were calculated based on Eq. [35].

In **Figure 40** the differences between the M_w obtained in the present study and the corresponding local magnitude, M_L (http://geophysics.geo.auth.gr/ss/, **Appendix B**), are presented for each station of **Figure 7,** as a function of epicentral distance. What is firstly observed in **Figure 40** is that the scaling of the computed $mpSTF^{sc}$ is mainly controlled by the mean free path variation and not significantly by the representative values of the rest scaling factors (ρ, β, v_s, Eq. [37]). This is supported by the relatively low computed variation range (~ 0.17) of the M_L - M_w difference, separately estimated for each one of the three mean free path l values (10, 100 and 1000 km) , which correspond to the expected corresponding range (±0.17) of the computed M_w based on the reasonable ranges of ρ, β, v_s, parameters (step 9, flowchart-**Table 6**). Moreover, it is obvious that the three examined, mean free path, l values, "cover" the unknown value of the real l, since at least one of them lies close to the zero M_L - M_w difference, or within its standard deviation range (±0.2) corresponding to the typical one of M_L. This observation indirectly confirms that the l values range, more or less, between 10 km and 1000 km, supporting the computational

validity of the STF methodology proposed by ***Sèbe et al., (2018)*** and slightly updated in this study. Moreover, these mean free path values are in good agreement to the ~55 km at 1.5 Hz and ~192 km around 1 Hz, observed by ***Hatzidimitriou, (1996)***, based on coda waves and on macroseismic intensity data analysis, respectively, for the region of Northern Greece.

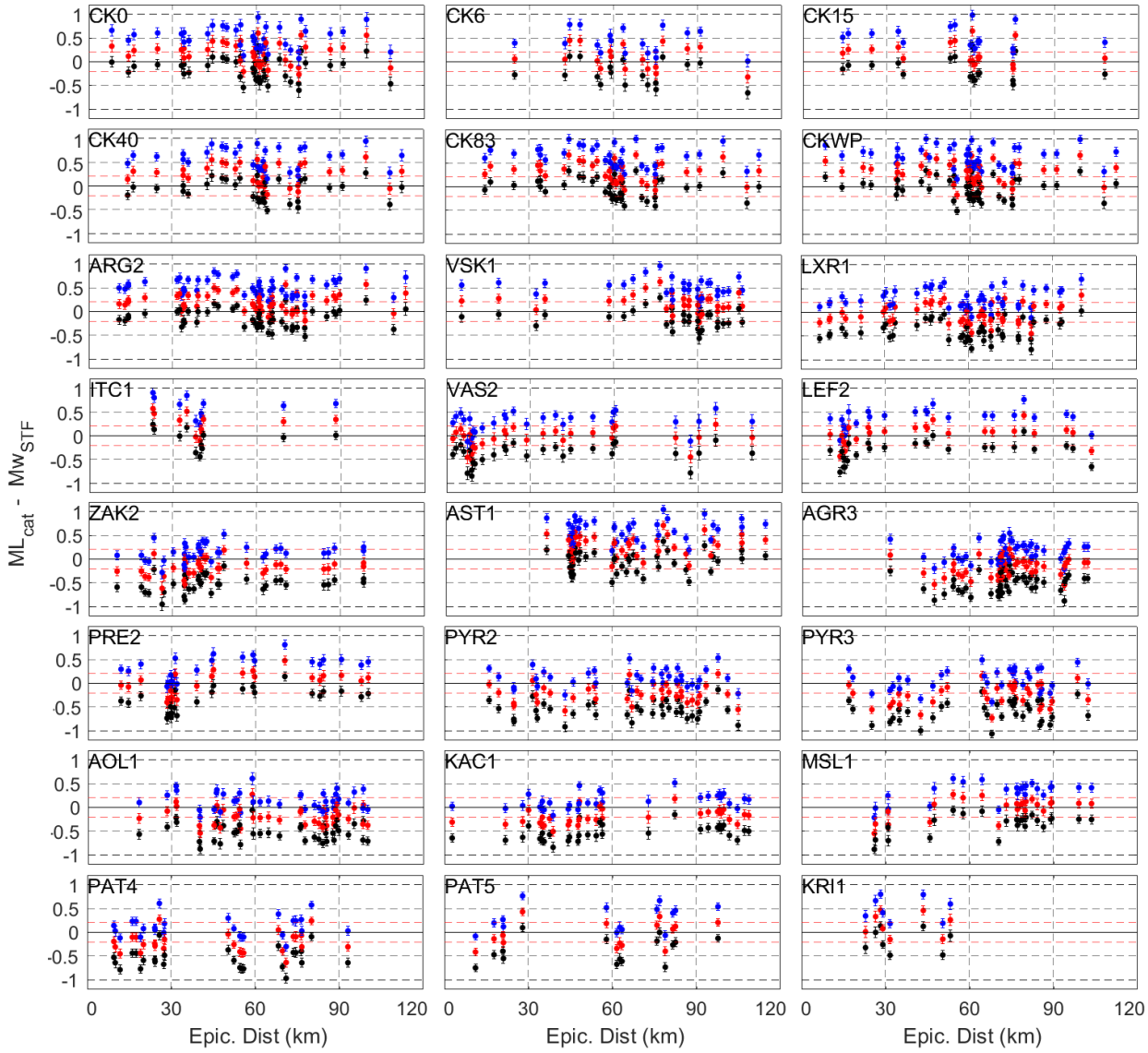

Figure 40. The difference between the local magnitude M_{Lcat} from catalogue (**Appendix B**) and the computed moment magnitude, M_{wSTF} based on the 2nd computation step of the (flowchart- **Table 6**) for three different mean free paths: 10 km, 100 km and 1000 km (blue, red, black points, respectively).

Trying to have a better understanding of the mean free path variability, which is significant for the SAF(f) estimation as explained above (step 10, flowchart-**Table 6**), the mean free paths, l, were inversely computed (**Figure 41**) for each earthquake-station pair of **Figure 7**, solving Eq. [37] for the mean free path, l, based on the moment magnitudes, M_w computed in GIT study

(see. *ch.* 3, **Appendix B**), for the common earthquakes and on the scaled seismic moment $M_{o_{sc}}$ of each scaled computed STF (Eq. [33] and [34]). This solution takes into account the average values considered for ρ, β, v_s, as given in step 9 in the flowchart of **Table 6**. The computed l values corresponding to each computed STF for each earthquake-station pair are shown in **Figure 41**. No clear correlation is observed between l and azimuth or epicentral distance, as well as not absolutely stable l values are observed at each station. However, two groups of sites can be roughly observed: one with average mean free path l < 200 km and a second with l > 200 km. This may indicate that mean free path could be partly site dependent, something that is analyzed below. The latter indication is investigated and discussed below.

Finally, the $SAF(f)$ are computed (step 10, flowchart-**Table 6**, Eq. [40]) without the knowledge of the values of shear wave velocity, v_s and mean free path, l, for both target and reference site, but considering that they are similar ($\mathrm{v}_{\mathrm{s}_{\mathrm{targ}}} \approx \mathrm{v}_{s_{ref}}$, $\mathrm{l}_{\mathrm{targ}} \approx \mathrm{l}_{ref}$), so that to be eliminated according to Eq. [40], avoiding thus the 9th step of the flowchart in **Table 6**. In fact, this assumption is a main issue of the study, the solution of which is approached by the results presented below, aiming at confirming the three conclusions mentioned above in the "Site Amplification Factor, $SAF(f)$ estimation" section (step 10, flowchart-**Table 6**).

The $SAF(f)$ referring to the 24 stations examined in this study (**Figure 7**, **Appendix C**), were computed by using only the horizontal components of the reliable FAS part of the "apparent" - scaled and low frequency corrected, $mpSTF^{sc}$ (step 8, flowchart-**Table 6**) ($FAS[mpSTF^{sc}{}_{hor}]$, Eq. [32]). They were determined with respect to the following two stations, "CKWP", "VSK1", which were considered as reference based on the combination of the following criteria: (a) installation on rock sites, based on *in-situ* geological observation; (b) measured or inferred average shear wave velocity over the 30 first meters of rock (Vs_{30}) greater than ~ 760 m/s (**Appendix C, *Margaris et al., 2021*** for the "VSK1" and ***Cushing et al., (2020)*** for the "CKWP"); and (c) flat shape of average Horizontal to Vertical Spectral Ratio (eHVSR) at least up to ~ 10 Hz, with HVSR < 3, (**Appendix L**). Two extra stations (the "ITC1" and "AST1", **Appendix C**), are conventionally examined here as reference up to ~10 Hz, albeit their inferred Vs_{30} is ~450 m/s (since the real one is unknown) (**Appendix C**). These stations are examined as reference ones, due to the fact that they are installed very close to surface rock outcrop sites (based on *in-situ* observation), their eHVSR curves are approximately flat and lower than 3 (**Appendix L**), as well as the computed SAF(f) of these two sites computed based on the GIT application for the same regions (western Greece) was found close to ~1 (no amplification) (**Figure 28**).

The minimum distance between these, reference considered, stations is ~5 km and the maximum ~65 km (**Figure 7a**) while the distances between the target and reference stations range from ~ 0.4 km to ~ 110 km.

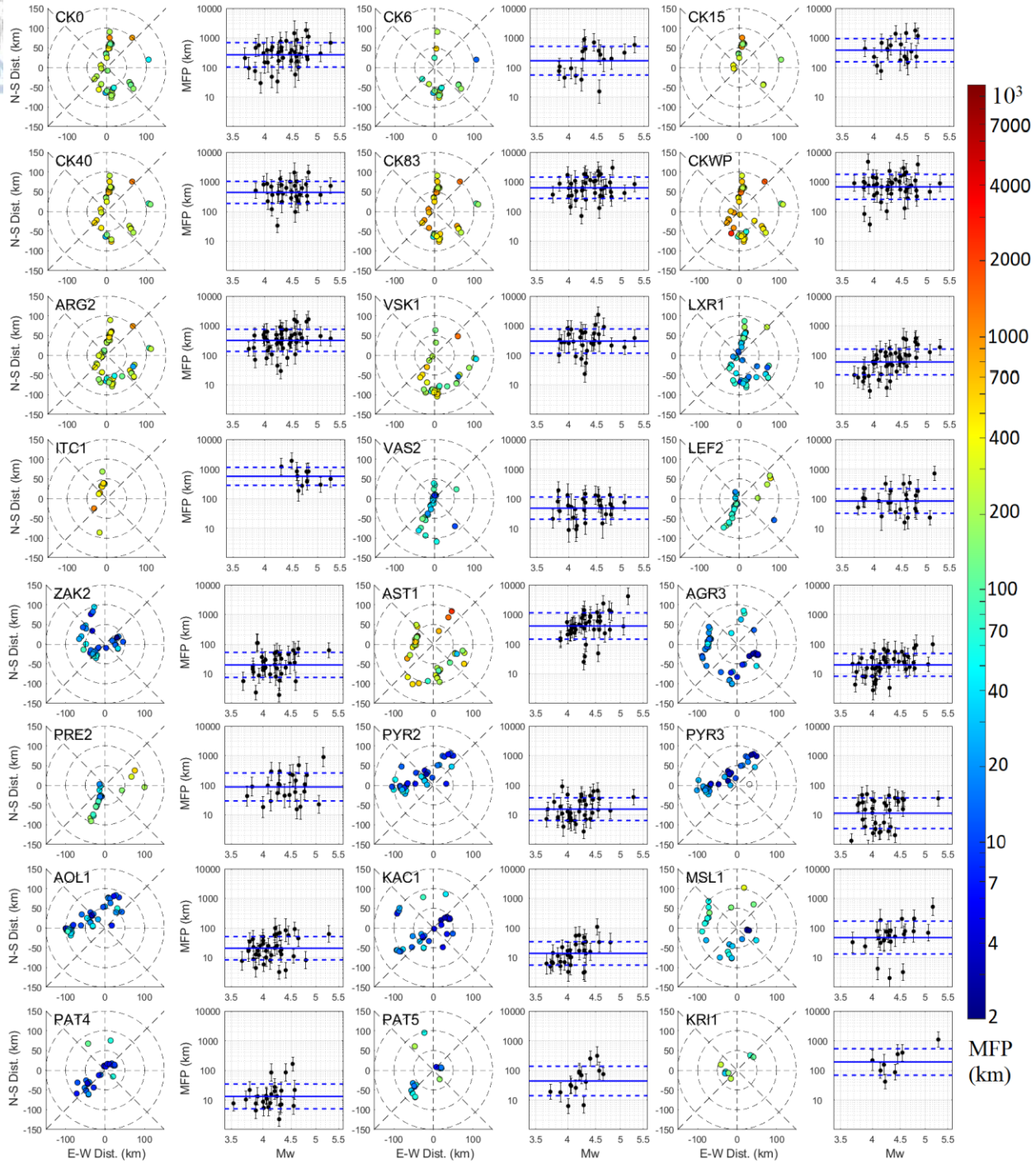

Figure 41 Three column of pairs of subfigures which correspond to the 24 stations (**Figure 7**), where: the **left** depict the epicenters of the earthquakes, colored according to the inversely computed Mean Free Path (km) (the center of each sub-figure (0,0) corresponds to the position of the examined station) and the dashed cycles correspond to 50, 100 and 150 km radius). The **right** column-subfigures depict the computed Mean Free Paths (MFP) vs M_L (see details into the text).

It is worth noting that the SAF(f) computations could also be directly achieved from the $FAS[\text{STF}^{sc}{}_{hor}]$ (Eq. [32]), of the $mp\text{STF}^{sc}$ in velocity, estimated earlier at the 6th step of the SFC analysis (**Table 6**), overcoming by this way the 7th and the 8th steps, for two reasons: (1) The low frequency FAS correction of the STF (displacement) at the 8th step is applied on the non-reliable frequency part does not affect the reliable FAS part, used in SAF(f) computation and (2) The FAS ratio of the $mpSTF^{sc}$, in displacement (step 7, flowchart-**Table 6**) between the two examined stations (reference and target), is equal to the corresponding one from velocity $mp\dot{S}\dot{T}F^{sc}$ (step 6, flowchart-**Table 6**), since the angular frequencies, ω ($2\pi f$), used as coefficient of velocity to displacement FAS conversion (at the reliable $FAS[\dot{S}\dot{T}F^{sc}{}_{hor}]$ part, $f \neq 0$ Hz), at both the reference and target $mp\dot{S}\dot{T}F^{sc}$, are eliminated at the FAS ratio (Eq. [30]).

Before the computation of the horizontal component $SAF(f)$ and their comparison to the corresponding ones based on the SSR technique of S-waves, the theoretical correctness application of the $SAF(f)$ estimation by using the horizontal component FAS must be firstly investigated. The latter is required, because the application of the proposed $SAF(f)$ estimation technique is based on the conservation of energy of the same seismic source at two different sites and its correct implementation should take into account all three components (Eq. [32]). However, proving that the Horizontal to Vertical Spectral Ratio (HVSR) of the computed $FAS[\text{STF}^{sc}{}_{comp}]$ is identical to the corresponding one computed by the direct body S-waves (same dataset), the energy distribution will be the same between Horizontal and Vertical components for the direct and coda S-waves. Thus, the comparison between the $SAF(f)$ computed from SSR and from the proposed technique will be theoretically valid. The above consideration is confirmed, since the computed HVSR, at each examined site (**Figure 7**, **Appendix C**), of the direct body S-wave FAS (**Appendix L**) and of the $FAS[\text{STF}^{sc}{}_{comp}]$ (**Appendix O**), are similar (**Figure 42**).

In **Figure 43** the computed SAF(f) of the 24 stations, are presented by using the CKWP as a reference station. Their geometrical mean is also computed separately for each site. Focusing at each individual station, the relevant stability of the SAF(f) shape, and their maximum difference which is generally much lower than 7 times between each other separately confirm the second and the third conclusion which were theoretically extracted at the "*Site Amplification Factor,* SAF(f) *estimation*" analysis (step 10, flowchart-**Table 6**).

The first conclusion which refers to the average shear wave velocity and mean free path similarity resulting in stable SAF(f) amplitudes, is supported by the relatively satisfactory agreement of the computed SAF(f) (**Figure 43**, grey lines), for each site, at least up to ~92 km. The event-to-event variability of the SAF(f) estimations may be characterized, for each site and frequency, f, by their logarithmic standard deviation around the logarithmic SAF(f) average (geometric mean) (**Figure 43**, black lines), as is usually done for every method for estimating a site attribute (SSR, GIT, HVSR). To quantify this variability with a single scalar value over the whole considered frequency range, the weighted root mean square (rms) formula, based on the $Y_i(f) = \log_{10}(\text{SAF}(f))$ and on the corresponding logarithmic average $\overline{Y}(f)$, was computed for each data i, at each station separately, as follows:

$$rms = \sqrt{\frac{\sum_{f_{min}}^{f_{max}}\{\sum_{i=1}^{N}\{w_i(f)\cdot[Y_i(f)-\bar{Y}(f)]^2\}\}}{\sum_{f_{min}}^{f_{max}}\{\sum_{i=1}^{N} w_i(f)\}}} \quad [41]$$

where $w_i(f) = df/f$ (df is the "fft" sampling frequency) balance the logarithmic weights of the numerator quantity, with respect to the logarithmic weights of the computed $FAS(f)$ values in frequency axis.

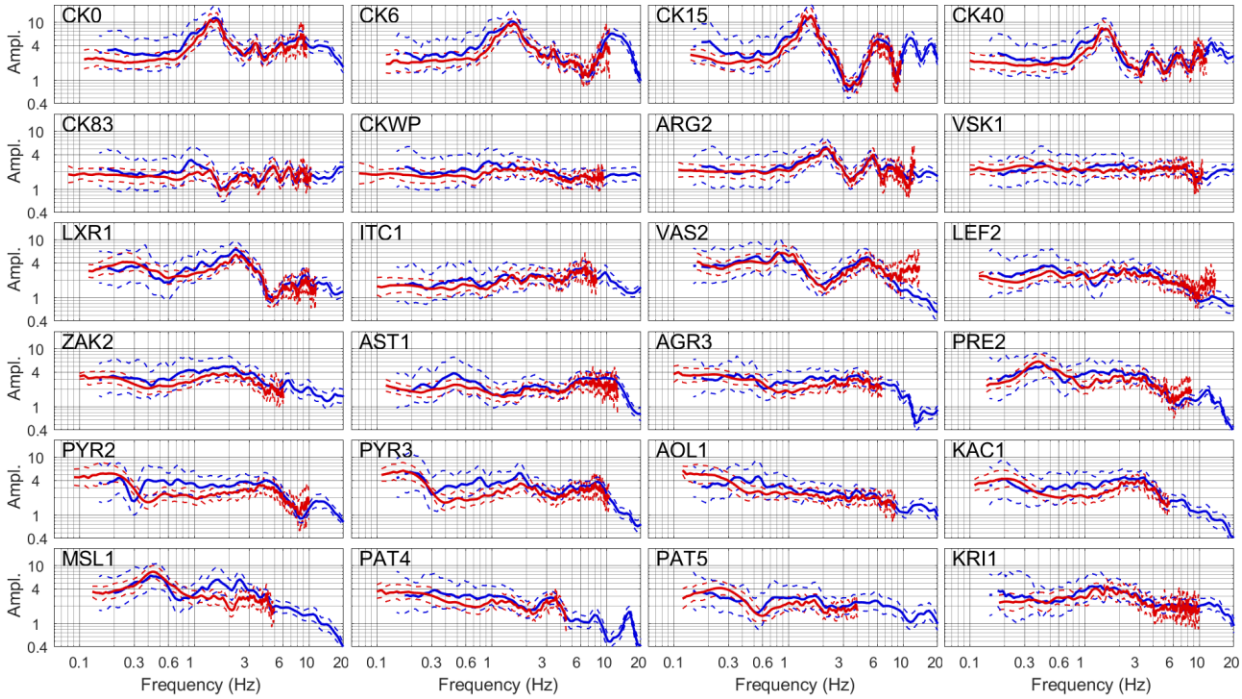

Figure 42. The "average" (geometric means) HVSRs (blue lines), of the 24 examined sites (**Appendix C**), computed from the direct S-wave data used above in this study (*ch.* 2.1, **Appendix L**) and from the $FAS[mpSTF^{sc}]$ (red lines) computed in this chapter (**Appendix O**) based on the SFC method.

Figure 44a displays this variability of the computed SAF(f) (**Figure 43**, grey lines), for each station - reference distance, through the rms quantity (Eq. [41]), leading to two main observations: There is a clear trend for increasing variability with distance (**Figure 44a**), but the scattering remains relatively limited (less than 0.2, which is comparable to SSR variability). At short distance however, corresponding to all CK stations (**Figure 44a**), the average value is less than 0.1, which is very limited and is similar, or even lower, than the scattering on HVSR ratios (see for instance: ***Field and Jacob, 1995; Theodulidis et al., 1996; Theodulidis and Bard, 1995)***.

The geometric means of the computed SAF(f) are also compared to the corresponding ones computed by other methods. More specifically, the SSR (***Borcherdt, 1970***) of the 5 ARGONET borehole stations, "CK" (CK0, CK6, CK15, CK40, CK83) (**Appendix C**), computed by ***Grendas et al., (2021c)*** based on ***Kishida et al., (2016)*** and ***Perron et al., (2018)*** S-wave duration selection

and using the nearby (~0.4 km) CKWP reference station, are compared with the corresponding SAF(f) computed in this study (**Figure 43**). Moreover, the SAF(f) of the 24 stations (**Appendix C**) estimated by the Generalized Inversion Technique (GIT) application, implemented in this study (*ch.* 3, **Figure 28**), are also compared with the corresponding SAF(f) computed in this study (**Figure 43**). These GIT SAF(f) have been "corrected" so that the CKWP station being considered as absolute reference station (no amplification) and the SAF(f) computed by the two methodologies (SFC and GIT), being comparable. This correction has been implemented just by dividing all the GIT SAF(f) by the SAF(f) of the CKWP (**Figure 28**).

The SSR $SAFs(f)$ of the 5 "CK" sites which constitute reliable amplification estimates, are in good agreement compared with the corresponding SAF(f) resulting from the proposed SFC technique (**Figure 43**), both using the station CKWP as reference site. Moreover, for most of ITSAK stations, satisfactory agreement is also observed between the SAF(f) computed in the present chapter and those estimated by the GIT (*ch.* 3, **Figure 28**). For these SAF$s(f)$, observed disagreements, mainly in absolute amplification at some sites (VAS2, LEF2, ZAK2, AGR3, PRE2, KAC1, MSL1) that undergo high amplifications, can be related to several factors. Among these factors could be considered: the potential surface waves contamination of coda, the choice of the significant shorter S-wave windows used as data in GIT in comparison to the long ones examined here, or the effect on SAF(f) by the average attenuation factor controlled by the broader Aegean area in the GIT. However, it can be reasonably considered that these results tend to approach satisfactorily the actual SAF(f).

The SAF(f) computed in this study with respect to the CKWP reference station (**Figure 43**) seem to statistically agree with those obtained with alternative methods at least where reference-target site distance is less than ~60 km. This observation comes from a visual "inspection" of the average of the alternative methods (**Figure 43**, blue and red lines), so that to approximately fall within the standard deviation range of the computed in this study SAF(f) (black lines). It is worth noting that geometric mean of the 5 "CK" SAF(f), computed by the proposed SFC technique (black lines, **Figure 43**), indicated a small overestimation at the higher amplification part (around 1–2 Hz) in comparison to the corresponding SAF(f) computed by SSR (red lines, **Figure 43**). However, this overestimation lies below the +1 standard deviation of the SSR values and is progressively reduced, when the target site is moved from the surface to borehole bottom, or when the intense site spectral amplification at the specific frequency part (1–2 Hz) is decreased (or alternatively when the contribution of surface waves to ground motion is decreased). For example, for station CK83 at the bottom of the borehole, the SAF(f) computed by the SSR and the proposed technique are identical. Generally, all the estimated SAF(f) at least up to ~60 km seems to have similar shape to the one computed by the GIT, while for those sites at which a fundamental frequency exists and an intense amplification is presented (e.g. VAS2, **Figure 43**), the SAF(f) at this frequency range, is slightly overestimated. The average rms value that characterizes the maximum expected variability at ~60 km is ~0.15 (**Figure 44a**).

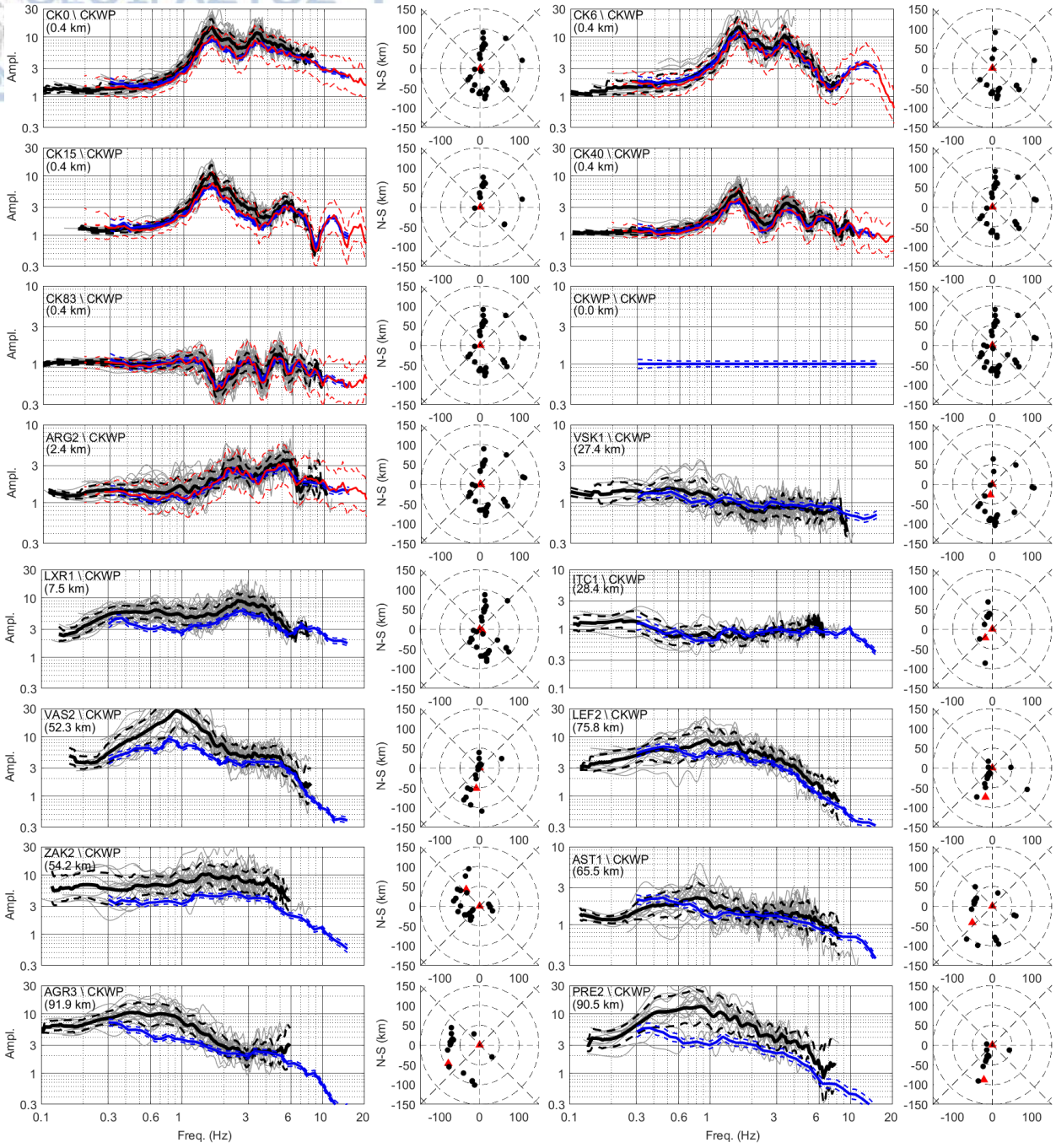

Figure 43. Two columns of pairs of subfigures where the **left** depict the SAF(f) for the 24 examined sites (**Figure 7**) computed by: (1st) the proposed technique based on SFC method (grey lines, black line the geometric mean) using the "CKWP" as a reference station. (2nd) the SSR technique (red lines) for the 5 CK stations, with respect to "CKWP" (3rd) the GIT application implemented above in this study (blue lines). These SAF(f) (blue line), are the corrected one, with respect to "CKWP" (details into the text). The distance between targets and reference site is also given. The **right** subfigures depict the epicenters of the examined earthquakes (black points) at the SFC method, with respect to the examined station location (middle-red triangle). In red triangle (non-middle), the reference location is depicted, with respect to the examined station one.

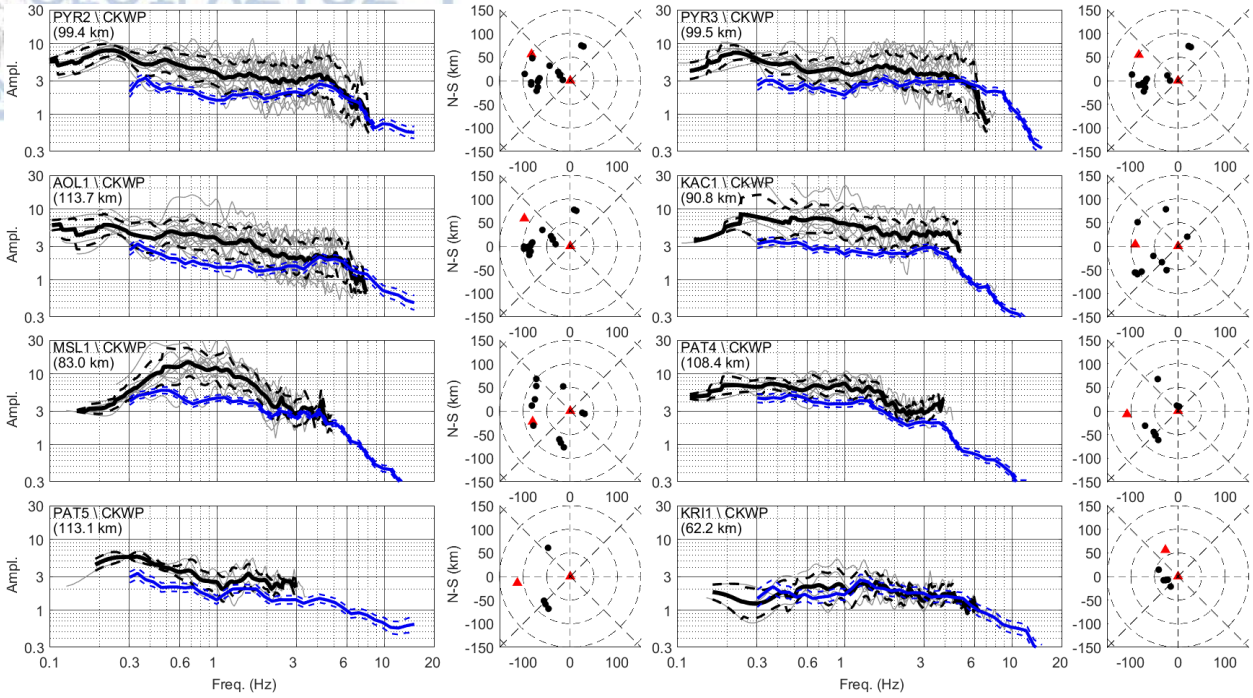

Figure 43. (continued)

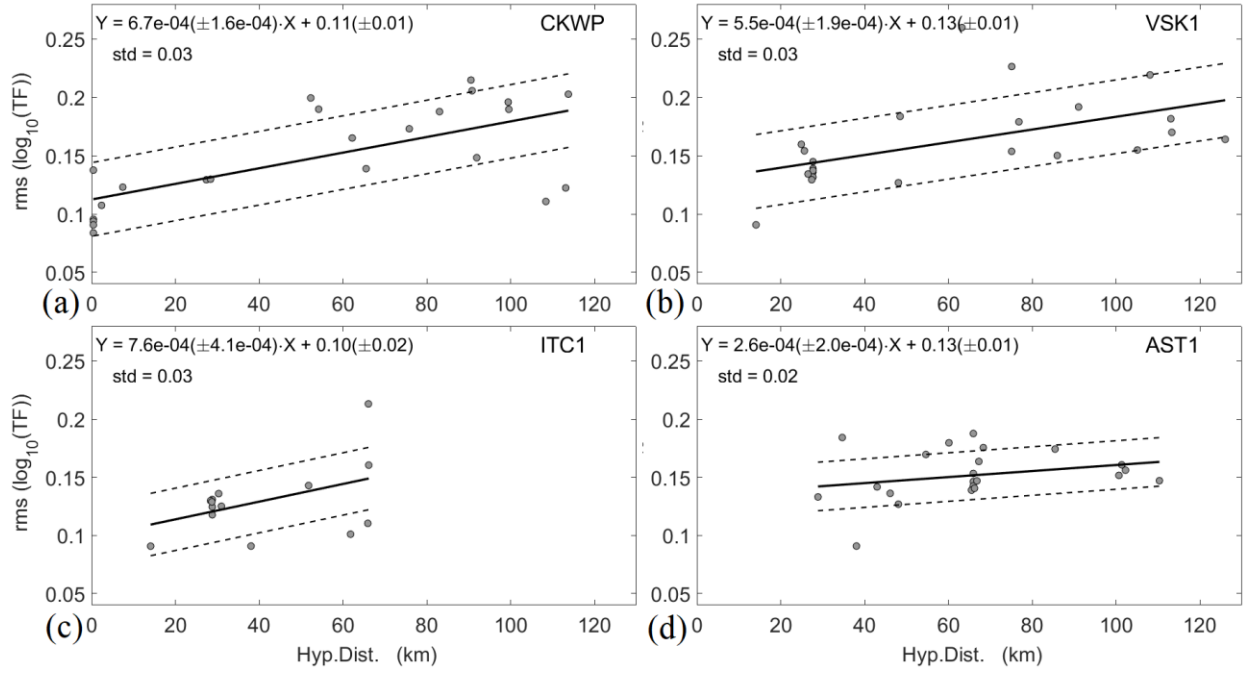

Figure 44. (**a**) The rms quantity (Eq. [41]), of the estimated log10($SAF(f)$) (grey lines in **Figure 43**) from the corresponding logarithmic average (geometric mean) (black lines in **Figure 43**), for each site, versus reference-target site distance, with respect to the "CKWP" reference station. (**b**), (**c**) and (**d**) are similar to the **Figure 44a**, but refereeing to log10($SAF(f)$) from **Figure 45**, **Appendix P** and **Appendix Q**, for the VSK1, ITC1 and AST1 "reference" stations, respectively.

The above observations are in agreement with the one presented by ***Margheriti et al., (1994)***, comparing SSR results obtained by using "S" and coda waves (for adjacent stations). They claimed that "*the coda amplification generally yields upper bounds for the S-wave amplifications on the frequency band (0.5 to 10 Hz)*", mainly at cases where site amplification is intense, while in different cases the $SAFs(f)$ are going to be of similar amplification level. Similar conclusions derived by ***Seekins et al., (1996)***, comparing SSRs of S-waves and coda waves. Also, similar observation has been extracted by the most recent study of ***Ito et al., (2020)***, where the comparison between SAF retrieved from S-waves and from the entire earthquake waveform, indicates overestimation of the former by the latter one, at stations of intense spectral amplification below a frequency of ~2Hz. This observations is also in agreement with the conclusion extracted by ***Bard and Bouchon, (1985)*** and by ***Kawase and Aki, (1989)***, where for surface sites at deep sedimentary basins, the strong basin effects create larger amplification and longer duration, since the wave energy is trapped into the valley, due to 2D/3D effects and the coda amplification assumption for the body wave incidence in no longer valid in the lower frequency range (< 2 Hz).

The SAF(f) were also computed using as reference the "VSK1" rock station and they are presented in **Figure 45**. A similar increase of the scattering between the computed SAF(f) (**Figure 45**) and the corresponding geometric mean SAF(f), expressed by the single scalar quantity of rms (Eq. [41]), is presented (**Figure 44b**), with a minimum ~ 0.13 value at zero distance between reference-target sites. For this reference site, the corresponding SAF(f) estimated by GIT application (*ch.* 3, **Figure 28**), seem to slightly diverge from values close to one. For this reason the computed geometric mean (black lines) of the SAFs estimated for the 18 ITSAK sites (ARG2, VSK1, LXR1, ITC1, VAS2, LEF2, ZAK2, AST1, AGR3, PRE2, PYR2, PYR3, AOL1, KAC1, MSL1, PAT4, PAT5 and KRI1), were "corrected" (blue lines) for the absolute SAF(f) (**Figure 28**) of the reference "VSK1" site (**Figure 45**), by a similar process as above in **Figure 43**, so that the comparison of the SAF(f) computed by SFC (black lines) and GIT (blue lines) methodologies being compatible and valid. Moreover, the computed SSR (red lines, ***Grendas et al., 2021c***) for the ARGONET sites (CK0, CK6, CK15, CK40, CK83), with respect to the reference CKWP, were also "corrected" by multiplying them with the computed SAF(f) (black line) of the CKWP, so that being comparable.

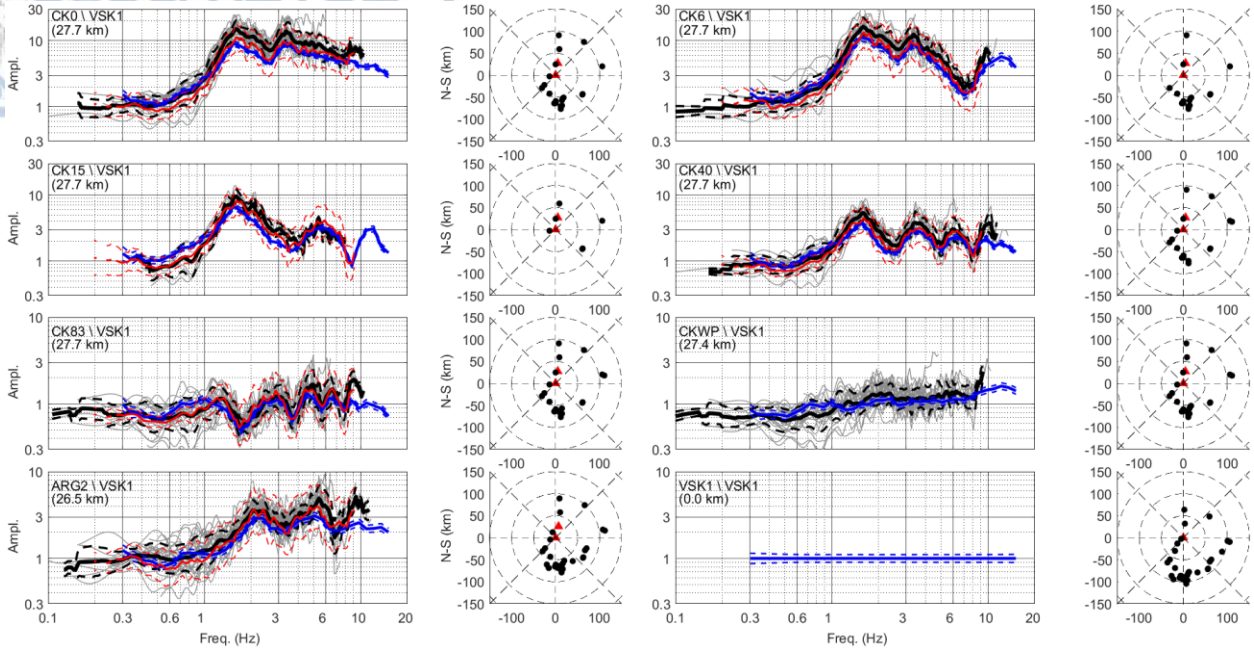

Figure 45. The corresponding to **Figure 43**, SAFs using station "VSK1" as reference (black lines). The SSR results of the 5 CK_. stations with respect to "CKWP" (red lines), have been adapted- corrected for the computed average SAFs of the "CKWP", computed here.

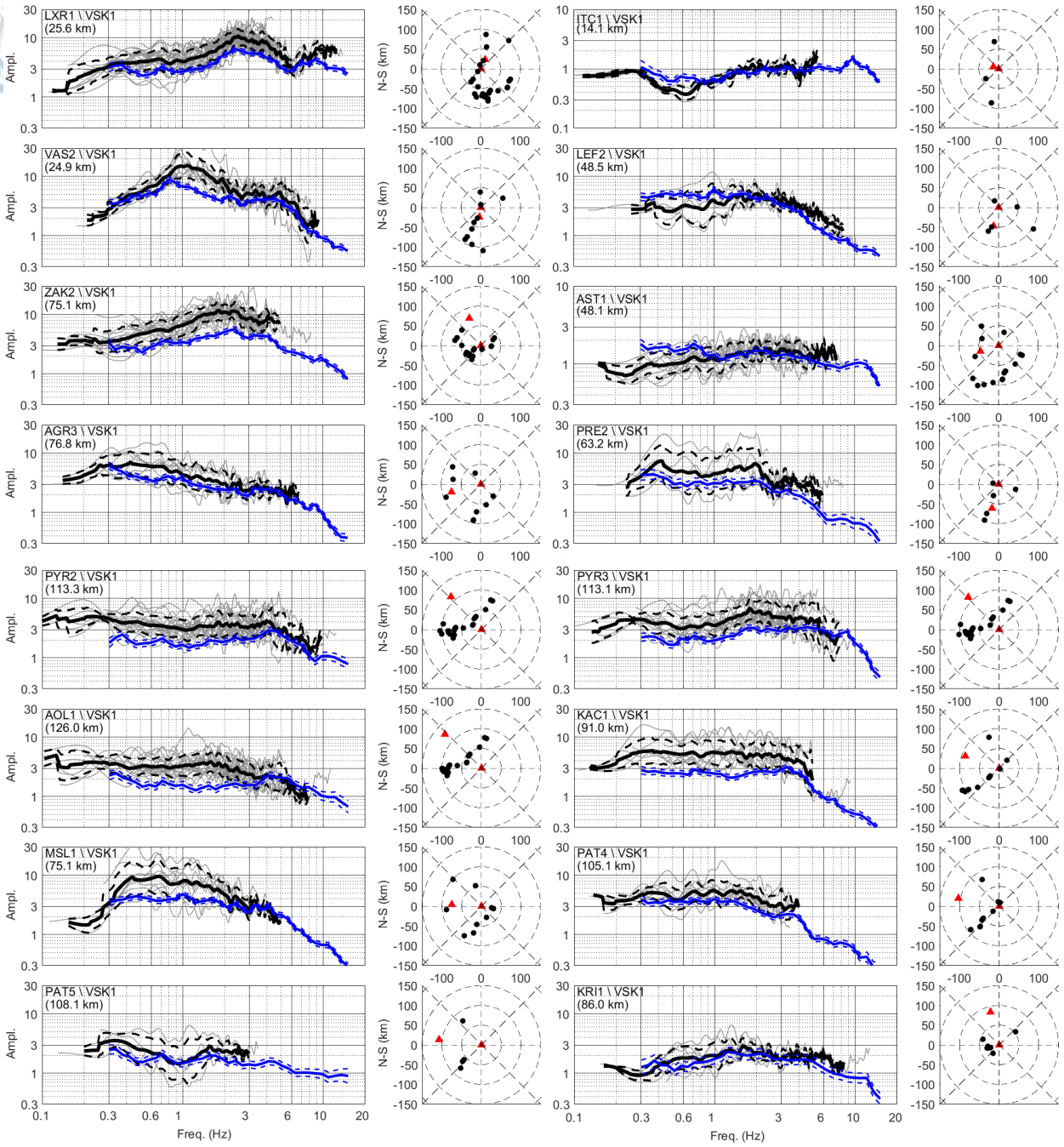

Figure 45. (continued)

The SAF(f) results presented in **Figure 45** using the VSK1 as the reference site, are similar with those derived by using the CKWP station as reference even though the distance between VSK1 and CKWP reference stations is 27.4 km. In addition, the SAF(f) computed by the SFC method (**Figure 45**, black lines), present a relatively satisfactory agreement with those computed by alternative methods at least when the reference to site distance is up to ~ 60 km, after a visual "inspection" of the average SAF(f) of the alternative methods (**Figure 45**, blue and red lines), so

that to approximately fall within the standard deviation range of the computed in this study SAF(f) (**Figure 45**, black lines). The variability of the SAF(f) computed by the SFC method is expressed by rms equal to 0.15 (**Figure 44b**). Similar results were also extracted by computing the SAF(f) based on the SFC method, with respect to the "ITC1", and "AST1" sites (**Appendix P** and **Appendix Q**), that were considered as "reference", since their SAF(f) computed by GIT (*ch.* 3, **Figure 28**) tend to be of similar amplitude level to the corresponding ones estimated using the stations CKWP and VSK1 as reference ones. Similar agreement in the increase of rms (Eq. [41]) of the computed $\log_{10}$(SAF(f)) (**Appendix P** and **Appendix Q**) at each site, in comparison to reference-target site distance, is presented in **Figure 44c, d** , respectively, with a minimum of ~0.1 and ~0.13 at zero distance and an average expected one up to ~0.15 at ~60 km. Based on the minimum values of rms estimated for the four reference stations (**Figure 44**) an average of ~0.12 for the minimum scattering of the SAF(f) can be considered, while an average value of ~0.15 can be considered for target-reference site distance up to 60 km.

Based on the satisfactory stability of the results presented with respect to all four distant reference considered stations (expressed by rms ~0.15), the "interaction" between the SAF(f) and the inversely computed mean free paths, l of **Figure 41** was further investigated. More specifically, all the computed FAS[STF^{sc}] of the apparent STFs, were corrected (divided) for the corresponding geometric mean SAF(f) for each site, computed with respect to the VSK1 reference station (**Figure 45**). At those low frequencies for which no SAF(f) was computed, a linear interpolation (in log-log scale) of SAF(f) was implemented, between the lowest frequency, f_{Low} determined $SAF(f_{Low})$ value (**Figure 45**) and the $SAF(0.01) = 1$, considering negligible generic amplification for the low frequency f = 0.01 Hz, independently on the site conditions (***Boore and Joyner, 1997***). The corrected FAS[STF^{sc}] results for all the earthquake-station pairs, are provided in **Appendix R**, presenting a relevant stability between each other, for each site, at each earthquake, separately.

After this correction the mean free path, l values were re-computed (like the one in **Figure 41**), with respect to the moment magnitudes retrieved by the GIT application above in this thesis for all the corresponding earthquakes (**Figure 23**, **Appendix B**). The new computed, l, are displayed in **Figure 46** (given in **Appendix B**) for all the stations and they clearly present a better stability to higher values as well as lower variability, than the one displayed in **Figure 41**. These observations are similar to all stations and they are confirmed by the MFPs scattering presented in **Figure 47a** and **Figure 47c**. At these figures the MFP distribution seems to be "improved" after the site effect correction (**Figure 47b** vs **Figure 47d**), presenting a sharp normal shape (of the logarithmic MFP values), with a geometric mean of l around ~253 km (on average) and a standard deviation range between 88 km and 727 km (the corresponding values computed without correcting for the SAF(f) ranges for one standard deviation between 16-498 km with a geometric mean ~89 km). The latter supports the topic of this study regarding the use of a distant reference station, in SAF(f) estimation, under the relatively similar excitation factor (Eq. [21]) of the study area.

Finally, based on the geometric mean values of the SAF(f) for the 6 ARGONET sites computed with respect to the VSK1, the corresponding minimum phase $mpSAF(t)$ were also computed (**Figure 48**) attempting to present site effects in time domain. For this reason an experimental positive-pulse wavelet based on the Brune's source model (***Brune, 1970***), with duration, T_{cen} = 1 s ($T_{cen} = 1/f_{cen}$) and of maximum amplitude equal to one was convolved with the corresponding $mpSAF(t)$ at each one of the 6 ARGONET sites (**Figure 49**). The resulting wavelets clearly indicate a resonant-type amplification, characterized by more cycles and larger amplitudes, as the depth decreases from the bottom of the borehole (CK83) to the surface (CK0), while the dominant frequency remains the same over the top 40 m.

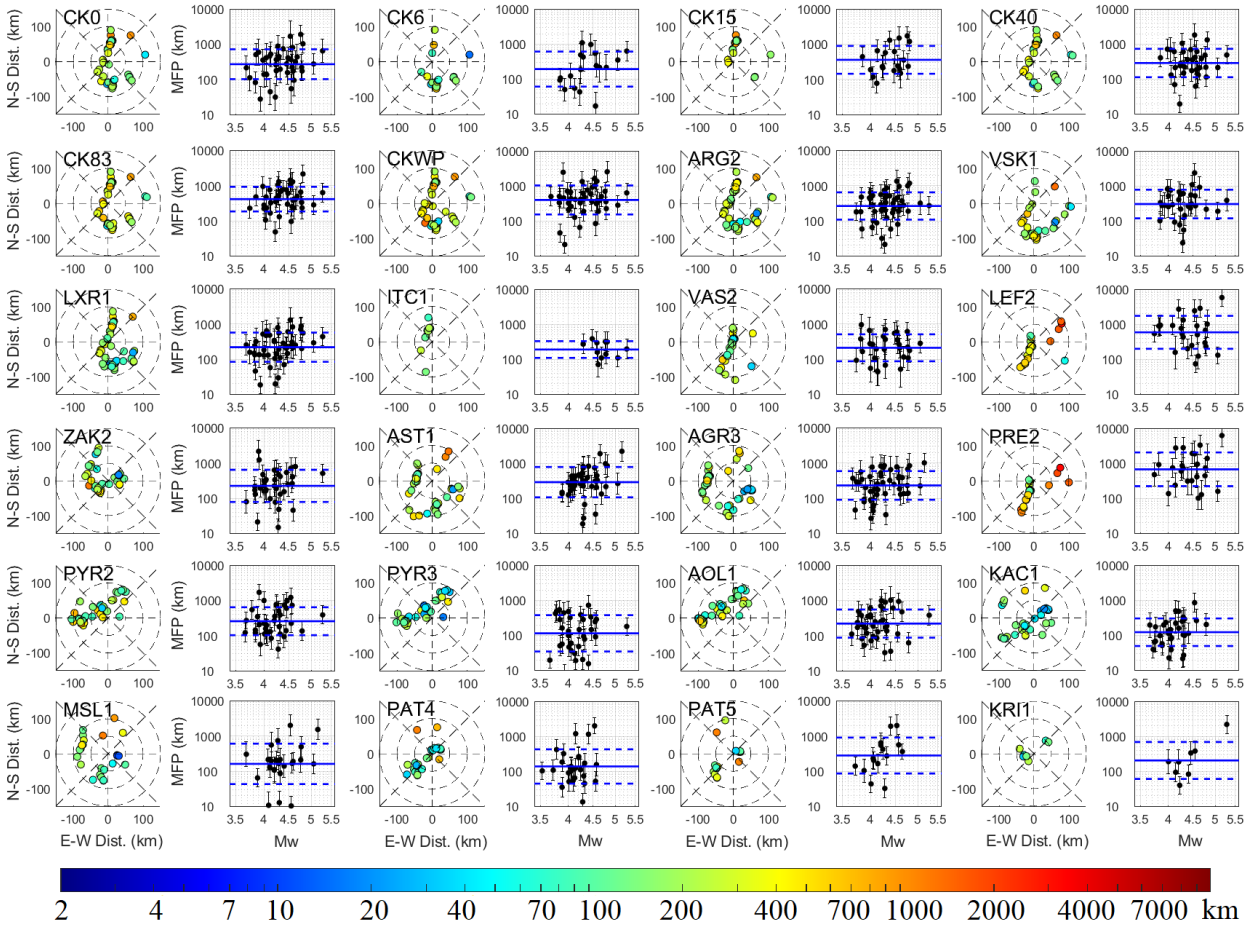

Figure 46. The Mean Free Path (km) values similar to **Figure 41** after the correction for the "average" $SAF(f)$ of **Figure 45** (same color bar), estimated from each earthquake-station pair for the 24 stations (**Figure 7a**). The center of each sub-figure (0,0) corresponds to the position of the station. Dashed cycles correspond to 50, 100 and 150 km radius. Mean Free Path versus moment magnitude, is also presented, as well as their geometric mean and their corresponding standard deviation (given in **Appendix C**).

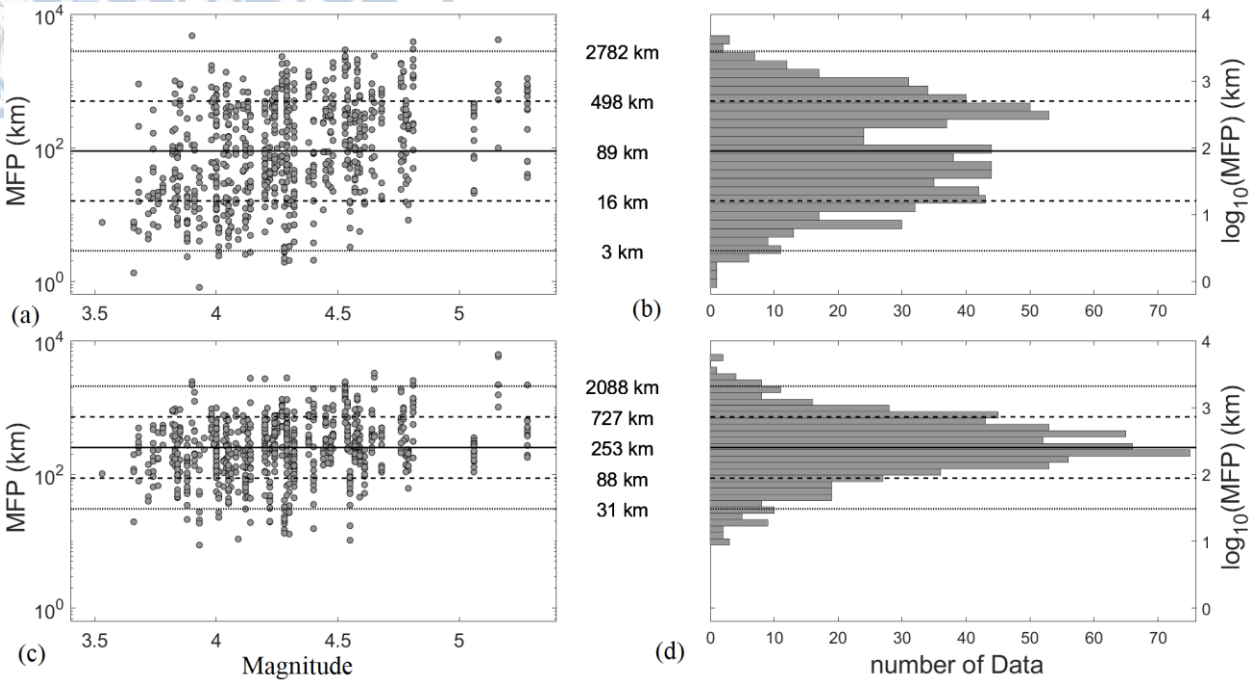

Figure 47. (**a**) The distribution of the computed Mean Free Paths of **Figure 41** vs the magnitude M_w of the examined earthquake (**Appendix B**) and (**b**) the corresponding histogram. (**c**) The geometric mean and the corresponding one and two standard deviation ranges are shown (similar to the figure **a**) for the corrected MFP of **Figure 46** and (**d**) the corresponding histogram.

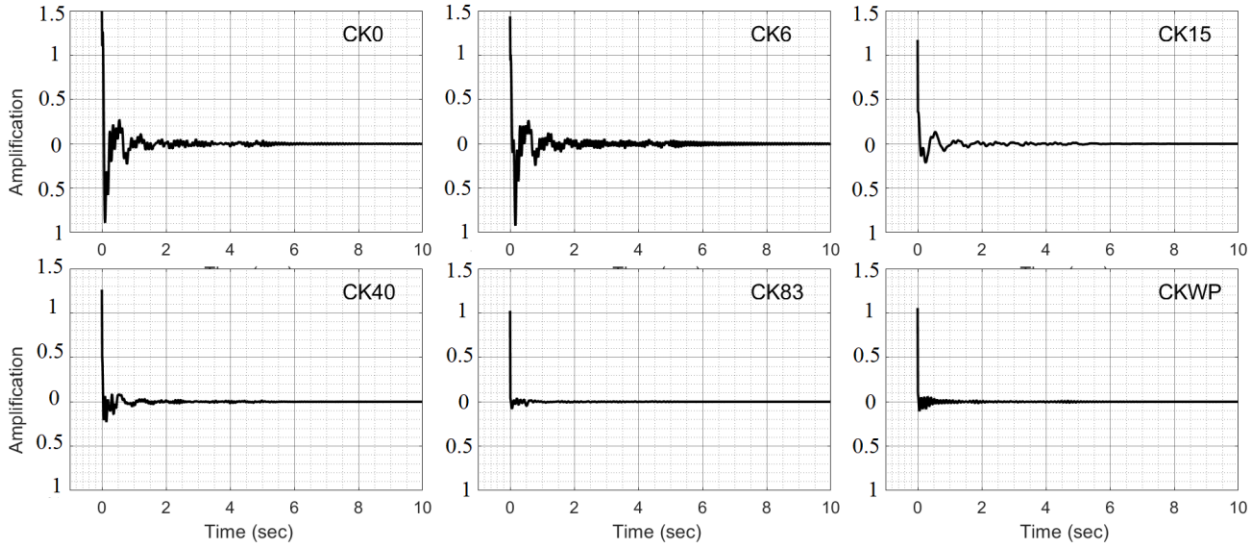

Figure 48. The minimum phase SAF(t) wavelets computed for the 6 stations of ARGONET, based on the corresponding "average" SAF(f) with respect to the "VSK1" reference station. shown in **Figure 45**.

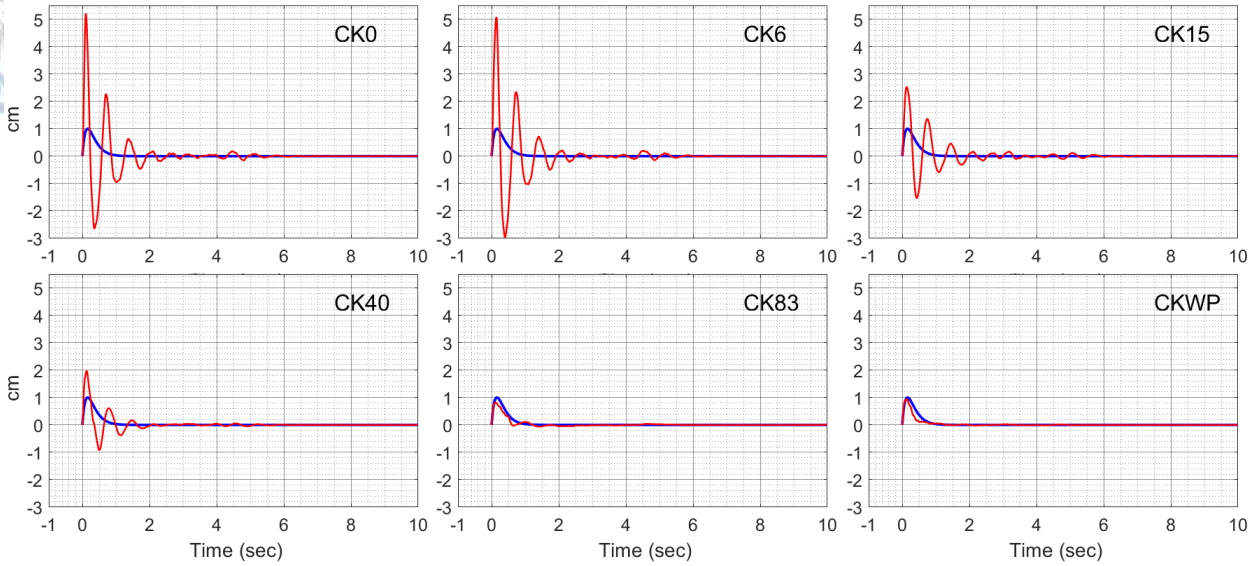

Figure 49. An example of an input wavelet (blue) and of the corresponding output with site effects one (red) after convolutions of the former with the corresponding mpSAF(t) wavelet presented in **Figure 48**, for each one of the 6 stations of ARGONET, with respect to the VSK1 reference station.

4.3.2 SAFs estimation based on SFC application to southeastern France data

The SFC method was applied also to the data (3rd examined group, *ch.* 2.3) collected from 16 stations (**Appendix D**) installed in southeastern France (**Figure 8**), in order to estimate their SAF(f). Following the same process as applied to the western Greece data (*ch.* 4.3.1), the first two steps of the SAF(f) estimation technique provided in the flowchart of **Table 6** were implemented after detecting the reliable part of the 3-component records. After this step, 144 earthquake-station pairs (**Figure 8**) were finally considered reliable for the estimation of the apparent-scaled (Eq. [29]) $mpSTF^{sc}$. Thereafter, the 3rd step of the flowchart in **Table 6** was implemented, to determine the coda $Q_c(f)$, corresponding to each earthquake-station pair (**Figure 50**) and then to remove it from the corresponding coda wave record (step 4, flowchart-**Table 6**). Finally, the scaled $mp\dot{S}TF^{sc}$ (in velocity) of the 35 examined earthquakes (**Figure 8**) for the 16 sites, were computed, based on the 5th and 6th steps of the flowchart in **Table 6**.

Avoiding the computation of the scaled $mpSTF^{sc}$(in displacement) of each coda wave record for each earthquake (step 7, flowchart-**Table 6**) and of their low frequency and scaling corrections (step 8 and 9 respectively), the SAF(f) estimation (step 10, flowchart-**Table 6**) for each station was directly applied on the already determined scaled $mp\dot{S}TF^{sc}$ (in velocity). This estimation was implemented with respect to two reference stations, considering that the excitation factor remains similar for the entire examined area and is satisfactorily constrained. The stations "BSTF_00_HH" and "CA01_21" were considered as reference stations, based both on their geological site conditions and housing characteristics (**Appendix D**) and on their computed HVSR curves (**Appendix S**) which show a flat shape at least up to ~10 Hz.

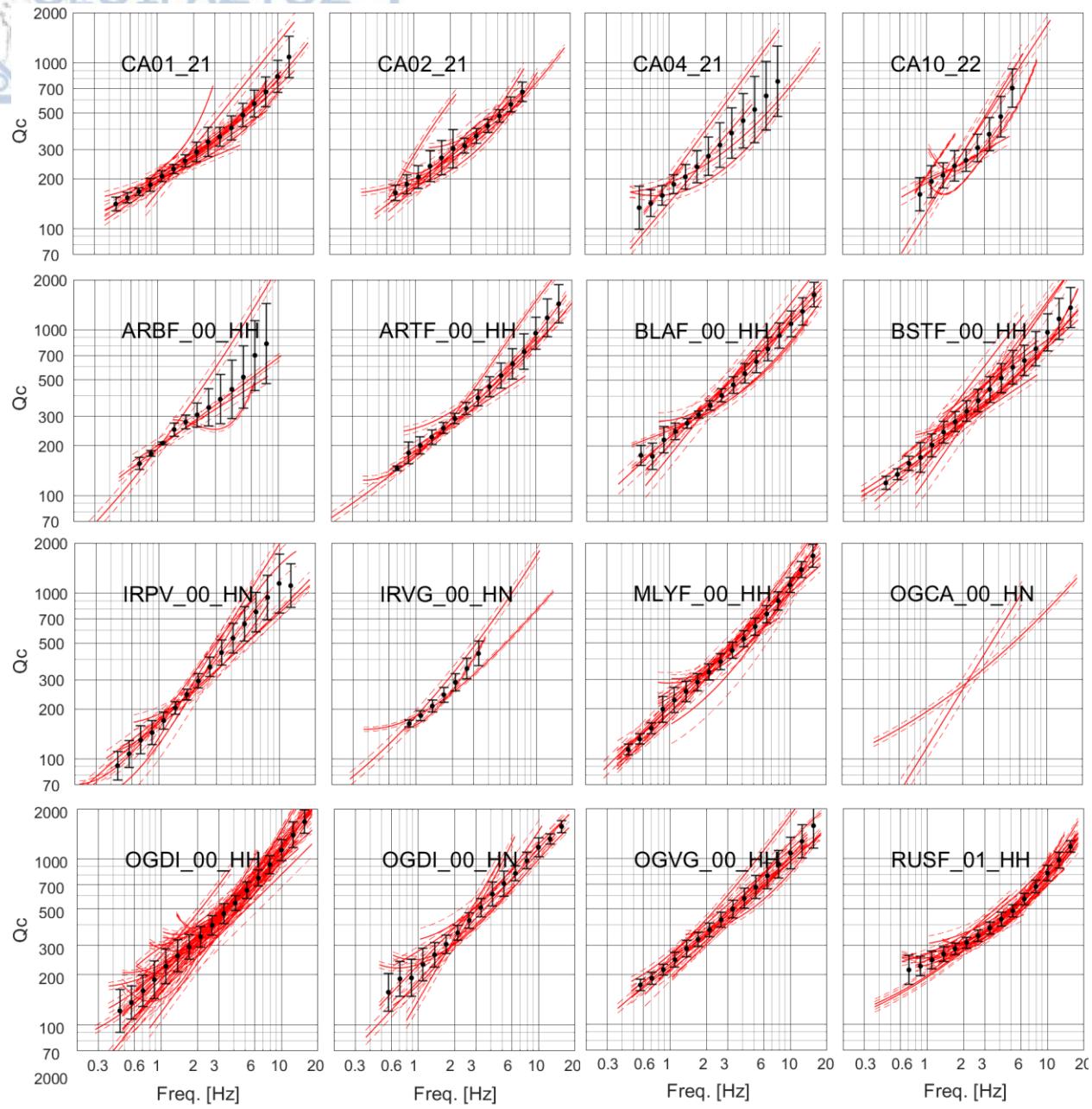

Figure 50. The$Q_c(f)$ models (red lines) and their standard deviation range (red dashed lines) computed for each earthquake-station pair for the 16 examined sites of **Figure 8**. The geometric mean curve ($Q_c(f)$, black lines) and the corresponding standard deviation range, at each station (sub-plot), is also displayed.

In **Figure 51** the computed SAF(f) of the 16 stations of **Figure 8** (**Appendix D**), with respect to the "BSTF_00_HH" station, are depicted (grey lines) and their geometric mean (black lines) were computed when more than two values per frequency were available. Although the examined group of data do not result in large number of SAF(f) estimations for each one of the 16 sites, they present a general stability at least when the distance between target and reference site is up to ~60 km, similar to the results of the SFC application to western Greece data (*ch.* 4.3.1) which is

around 60 km. In **Figure 52a** the variability of the computed SAF(f) shown in **Figure 51** with grey lines, for each station versus the target-reference distance, is presented through the rms quantity (Eq. [41]), confirming a similar conclusion extracted for the western Greece data (**Figure 44**), i.e. (i) a clear trend of increasing variability with distance and (ii) the dispersion of the computed SAF(f) remains relatively limited (less than ~0.2) and lower than ~0.15 for target-reference distance up to ~50 km.

The SAF(f) results (**Figure 51**) were compared to the corresponding SSR results, of the Cadarache (CA02_21, CA04_21 and CA10_22) sites computed with respect to the reference site CA01_21, considered as rock sites. It's worth noting that these SSRs presented in **Appendix T**, were computed using data from all the 58 earthquakes, that were initially examined in this study (3rd group of data, *ch. 2.3*). The S-wave records used for the SSR estimation, were selected based on the same process applied on S-wave records of the 1st group of data (*ch.* 2.1). The SSR results in **Figure 51**, have been appropriately adjusted in order to be comparable to the SAF(f) results computed based on the SFC method (**Figure 51**), with respect to the "BSTF_00_HH" reference stations. This adjustment was applied by multiplying the SSR results (**Appendix T**) of the three Cadarache sites with the average computed SAF(f) of the CA01_21, based on the SFC method. A satisfactory agreement between the SAF(f) (applying SFC method) and the adjusted SSR is observed, similar to the one observed for western Greece (e.g. **Figure 41**).

In addition, these SAF(f) were compared to the corresponding results computed by GIT applications (**Figure 51**). More specifically, 4 GIT applications were implemented (***Traversa, P., 2021***, personal communication), based on two different algorithms (a parametric and a non-parametric one), using different reference condition (the sum of all the stations and the OGDI_00_HN station). These site factors resulted using the GIT were also adjusted in order to be comparable to the SAF(f) resulted by the application of the SFC method, for which the "BSTF_00_HH" station was considered as reference. This adjustment was applied by dividing all the SAF(f) of GIT, with the corresponding SAF(f) (also by GIT) of the "BSTF_00_HH" reference station. In **Figure 51** all the 4 adjustment GIT cases present identical results between each other and are also in relatively good agreement with those computed by the SFC method.

In **Figure 53** the corresponding SAF(f) computed based on the SFC method are shown using the station CA01_21 as a reference one, in comparison with the SSR results for the Cadarache stations. A relevant good agreement between them is observed, while a similar stability of the SAF(f) results at each site (grey lines) to those shown in **Figure 51**, for target-reference distance up to ~50 km is also observed, confirming the relatively low variability of the SAF(f) results (grey lines), around their corresponding geometric mean (**Figure 52b**).

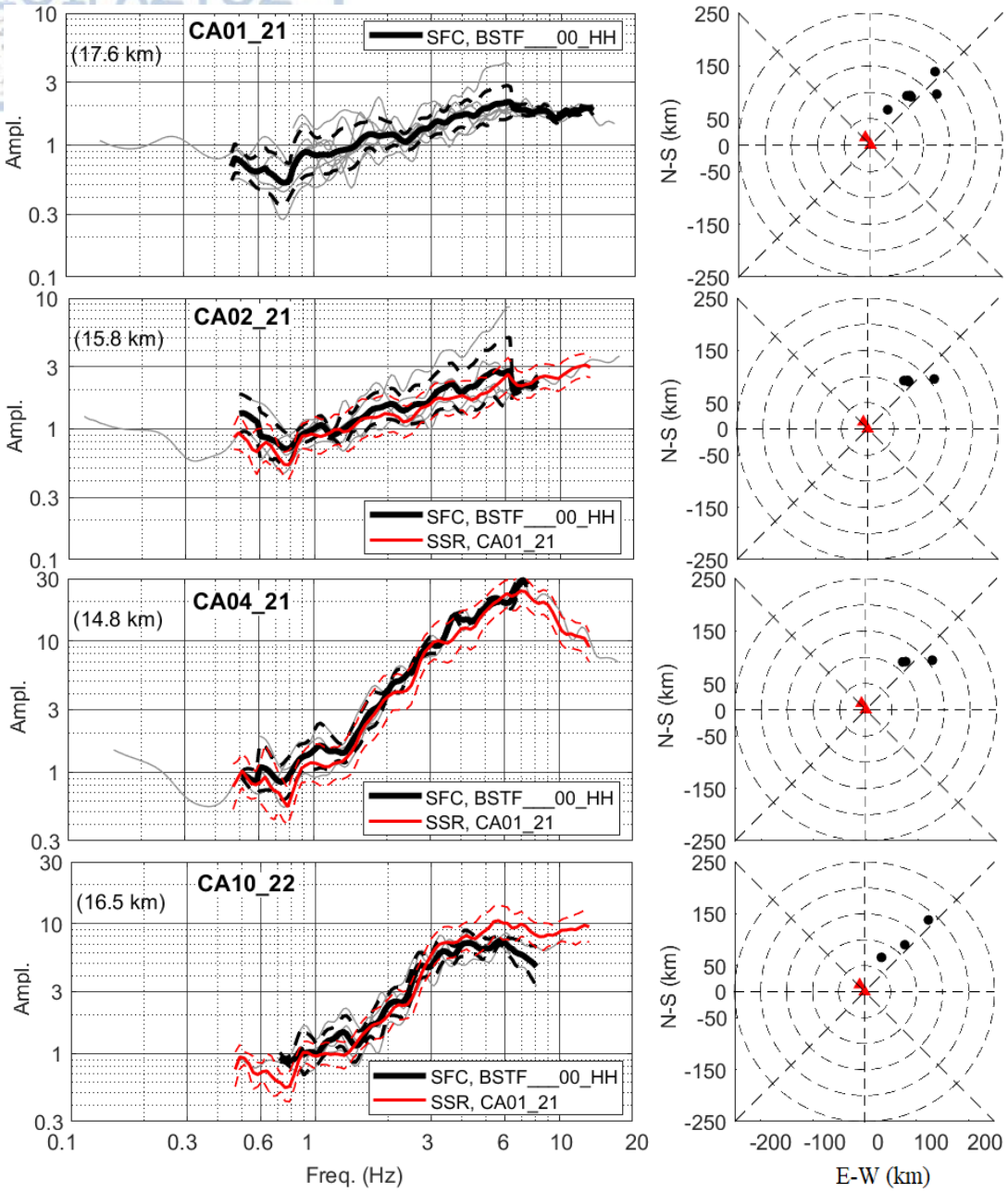

Figure 51. Two columns of pairs of subfigures where the **left** depict the computed SAF(f) for the 16 stations of **Figure 8** (**Appendix D**) based on the SFC method (grey lines, solid black line is the geometric mean and dashed lines are the standard deviation limits), with respect to the "**BSTF_00_HH**" reference station. The adjusted SSR results (red lines, **Appendix T**) for the 3 Cadarache (CA..) stations with respect to the CA01_21, are also presented. In yellow, cyan, brown and purple (they are all identical to purple) the adjusted GIT results (***Traversa, P, 2021***, personal communication) computed for parametric (p) and non-parametric (np) cases are depicted, by using either the sum of all the stations as reference (all), or the OGDI_00_HN station (the legends are shown in BSTF_00_HH subfigure). The right subfigures depict the epicenters of the examined earthquakes (black points) at the SFC methodology (grey lines), with respect to the examined station location (middle-red triangle). In red triangle (non-middle), the reference location is depicted, with respect to the examined station one.

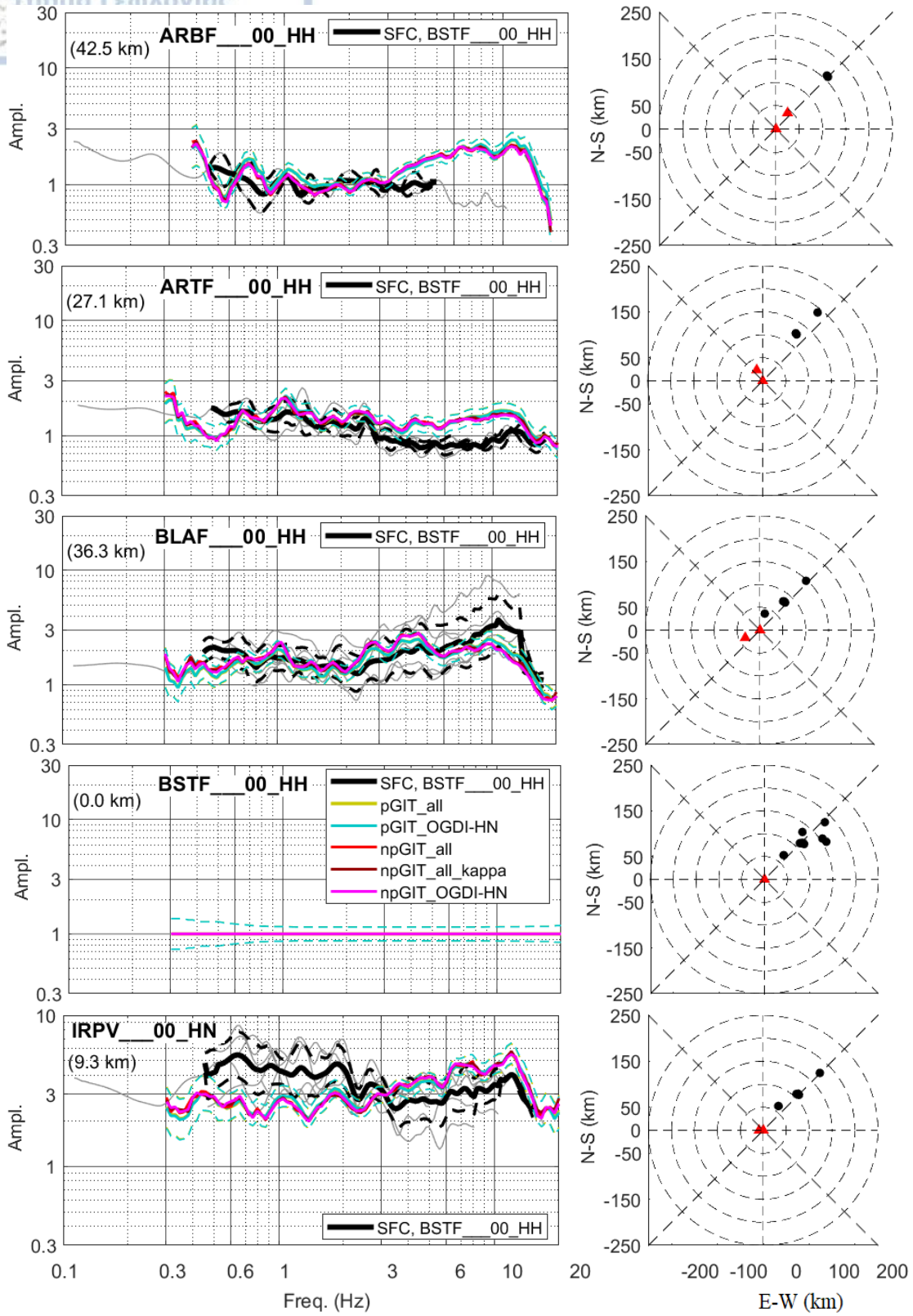

Figure 51. (continue)

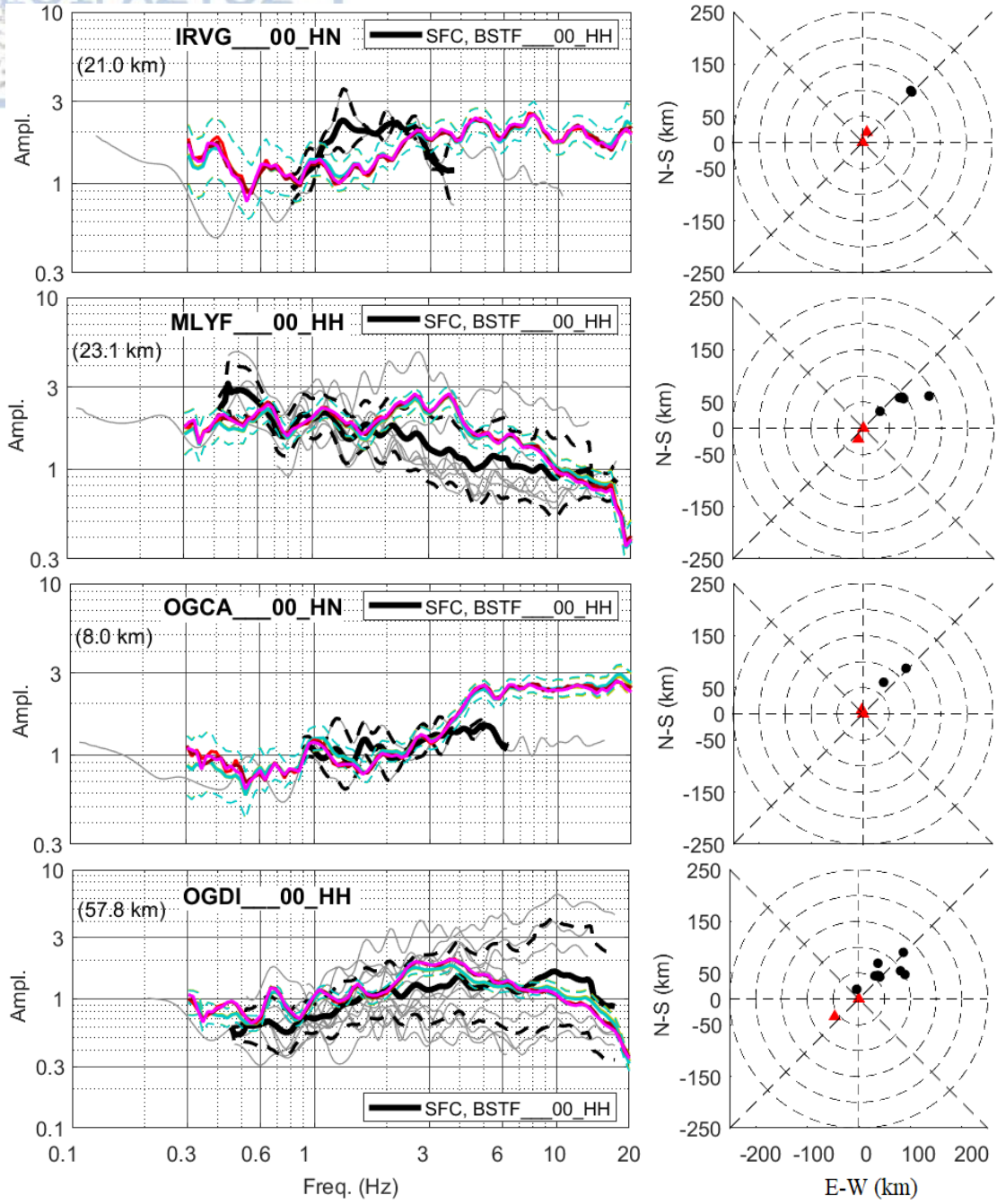

Figure 51. (continue)

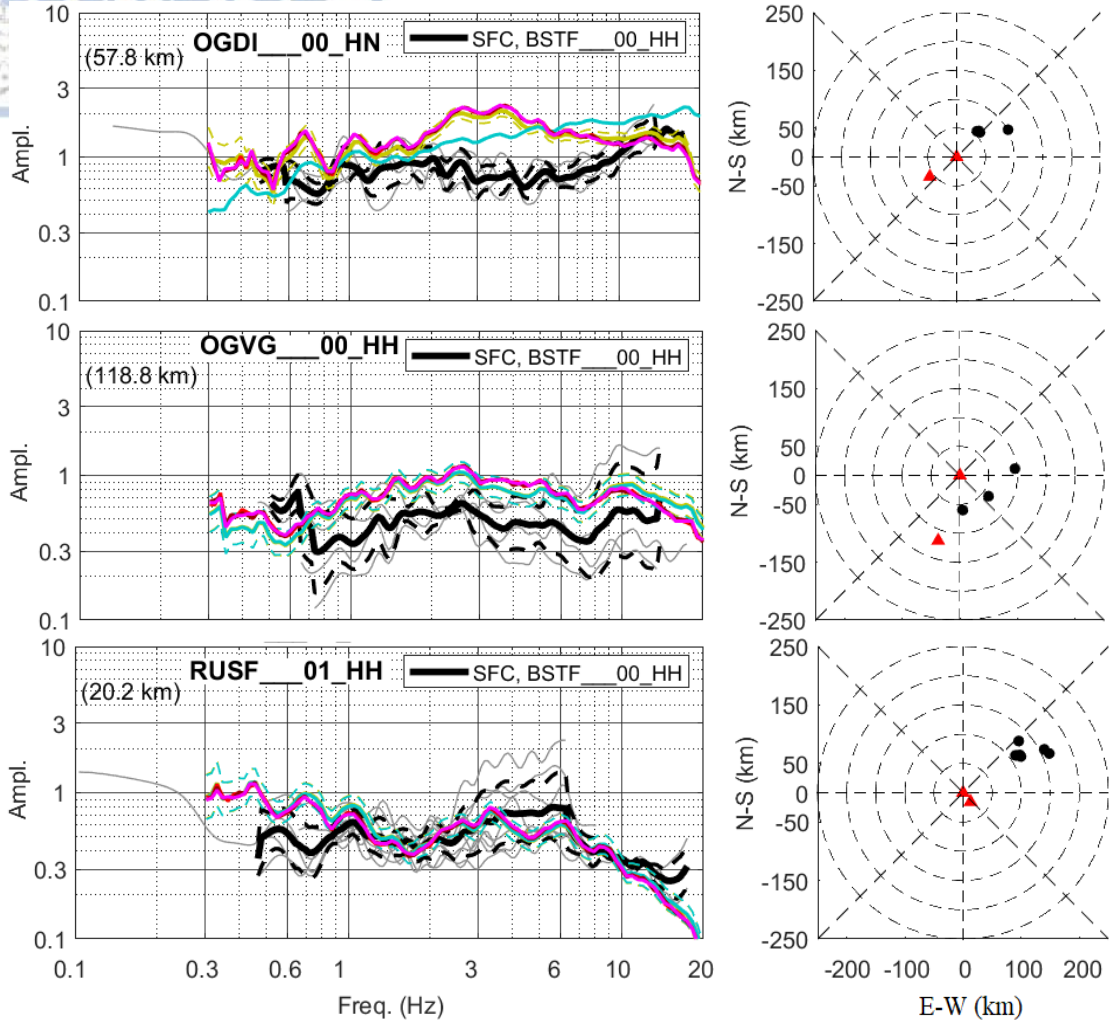

Figure 51. (continue)

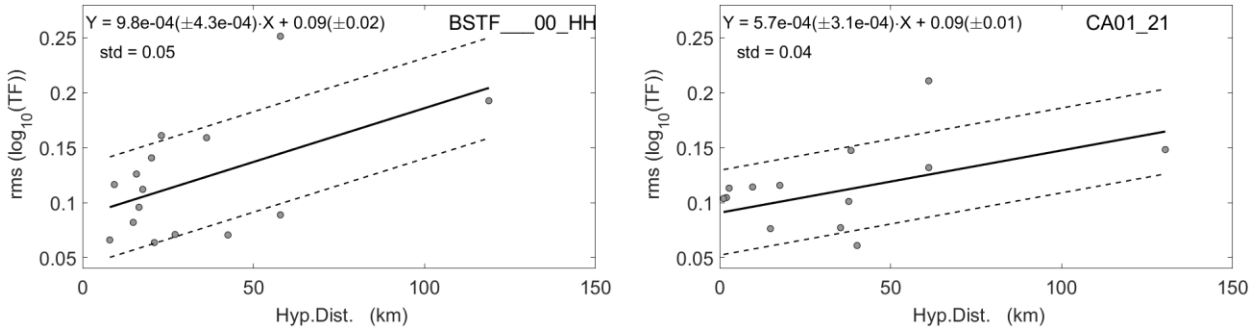

Figure 52. (**a**) The rms line (Eq. [41]), of the estimated for each site, log10($SAF(f)$) of **Figure 51** (grey lines) from the corresponding logarithmic average (geometric mean) (black lines), versus reference-target site distance, with respect to the "BSTF_00_HH" reference station. (**b**) similar to (**a**) but refereeing to log10($SAF(f)$) from **Figure 53**, for CA01_21 reference station.

In **Figure 54** the corresponding 16 SAF(f) computed by the SFC, with respect to the "OGCA_00_HN" reference station, are presented. In this figure, although the data is limited (only one SAF(f) is retrieved for most of the stations), the results are similar with those extracted from **Figure 51** and **Figure 53**, for the "BSTF_00_HH" and "CA01_21" reference stations, while the distance between these two stations and "OGCA_00_HN" is 8 km and~10 km, respectively.

Finally, based on the already computed $mpS\dot{T}F^{sc}$ (in velocity) of the 35 examined earthquakes (**Figure 8**) for the 16 sites, the scaled $mpSTF^{sc}$(in displacement) of each coda wave record were computed only for the horizontal components (step 7th, flowchart-**Table 6**) and the low frequency correction was applied (step 8th). All these scaled $mpSTF^{sc}$ were divided for the geometric mean $SAF(f)$ for each site, estimated by using "BSTF_00_HH" as reference station (**Figure 51**). For those low frequencies for which SAF(f) was not feasible to be computed, a linear interpolation (in log-log scale) of SAF(f) was implemented between the lowest frequency, f_{Low} determined $SAF(f_{Low})$ value (**Figure 51**) and the $SAF(0.01) = 1$ (negligible generic amplification for the low frequency f = 0.01 Hz, independently on the site conditions, ***Boore and Joyner, (1997)***). This adjustment was also applied on the western Greece data, above in this study. By this correction the scaled seismic moment, $M_{o_{sc}}$.(Eq. [34]), was determined for each scaled $mpSTF^{sc}$ and then based on the moment magnitude of each earthquake (**Appendix F**) and on Eq. [37], the mean free path, l corresponding to each coda wave record was computed (**Figure 55**). The computed l values present relevant high values (**Figure 56**), with a geometric mean ~835 km, ranging mainly between 186 km and 3750 km (the one standard deviation range). These average, l values are overestimated with respect to those of the early coda waves (~250 km) estimated for the crust of the broader France region by ***Lacombe et al., (2003)*** for frequency ~3 Hz. Here, it's worth noting that ***Lacombe et al., (2003)*** observed a frequency dependance of the mean free path for this region from ~300 km at 2 Hz to ~15 km at 5 Hz, as well as they also outline the quite higher values (~1000 km) of the mantle free path, due to the lower number of heterogeneities than those in the crust.

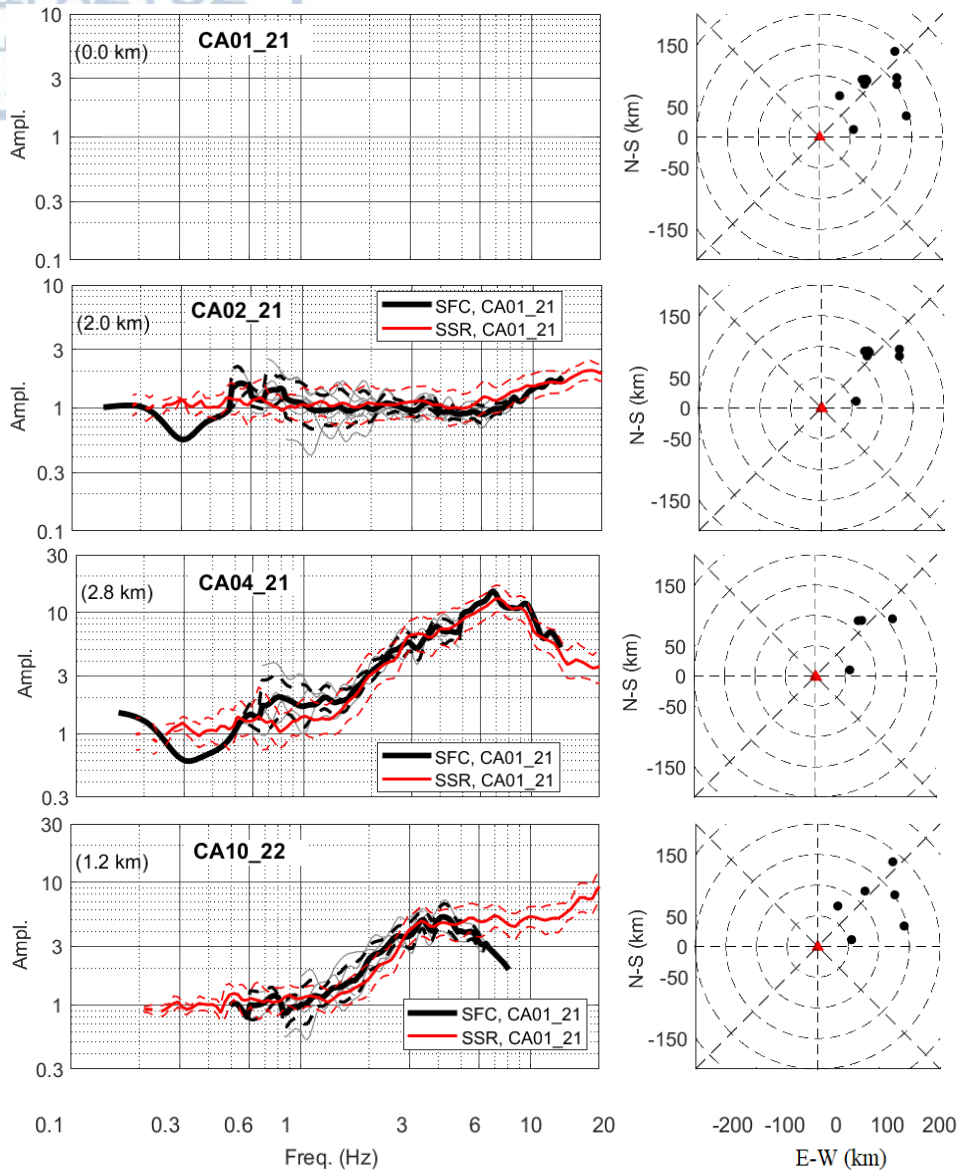

Figure 53. Two columns of pairs of subfigures where the **left** depict the computed SAF(f) for the 18 stations of **Figure 8** (**Appendix D**) based on the SFC method (grey lines, solid black line is the geometric mean and dashed lines are the standard deviation limits), with respect to the "**CA01_21**" reference station. The SSR results (red lines, **Appendix T**) for the 3 Cadarache (CA..) stations with respect to the CA01_21, are also presented. The right subfigures depict the epicenters of the examined earthquakes (black points) at the SFC methodology (grey lines), with respect to the examined station location (middle-red triangle). In red triangle (non-middle), the reference location is depicted, with respect to the examined station one.

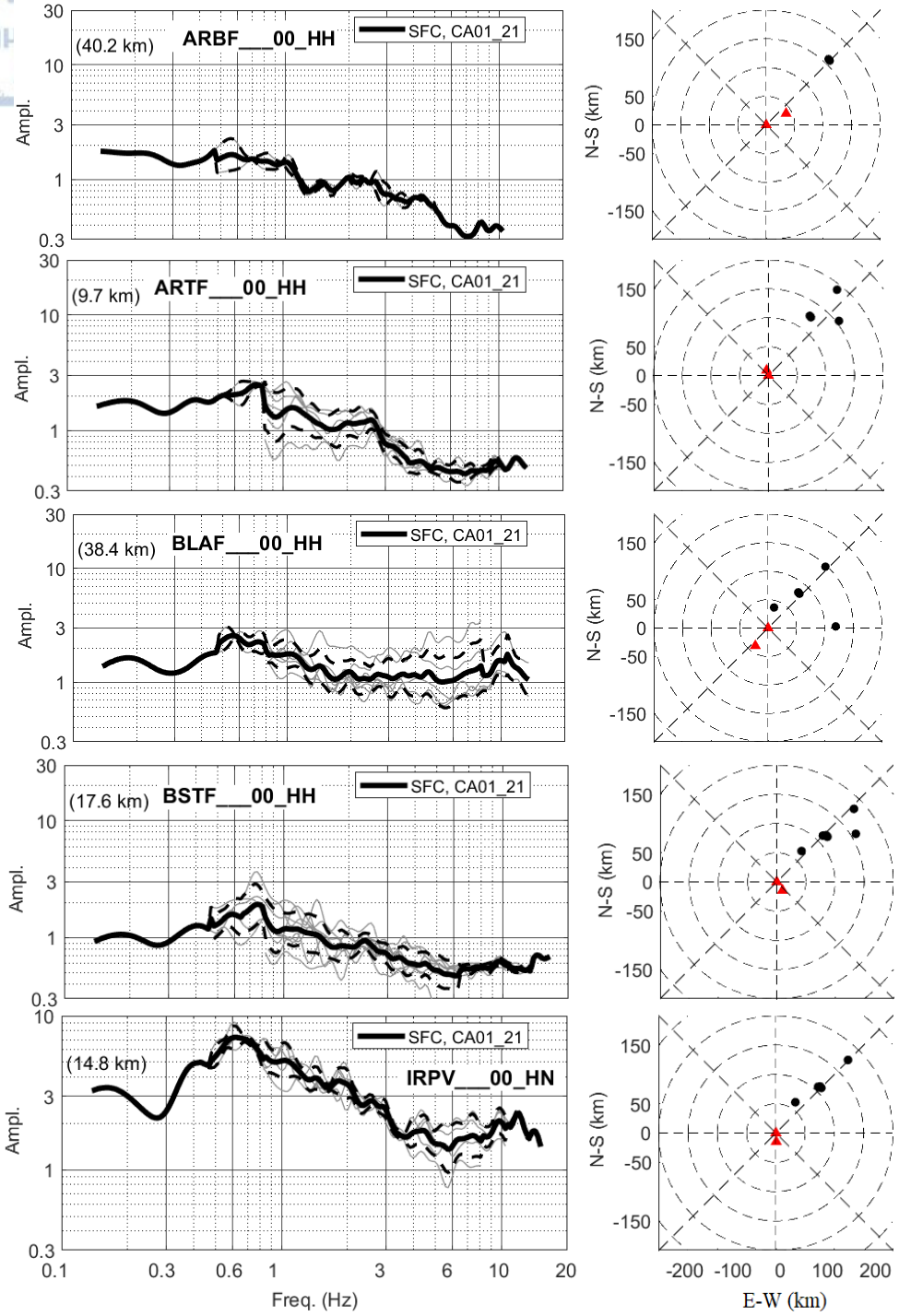

Figure 53. (continued)

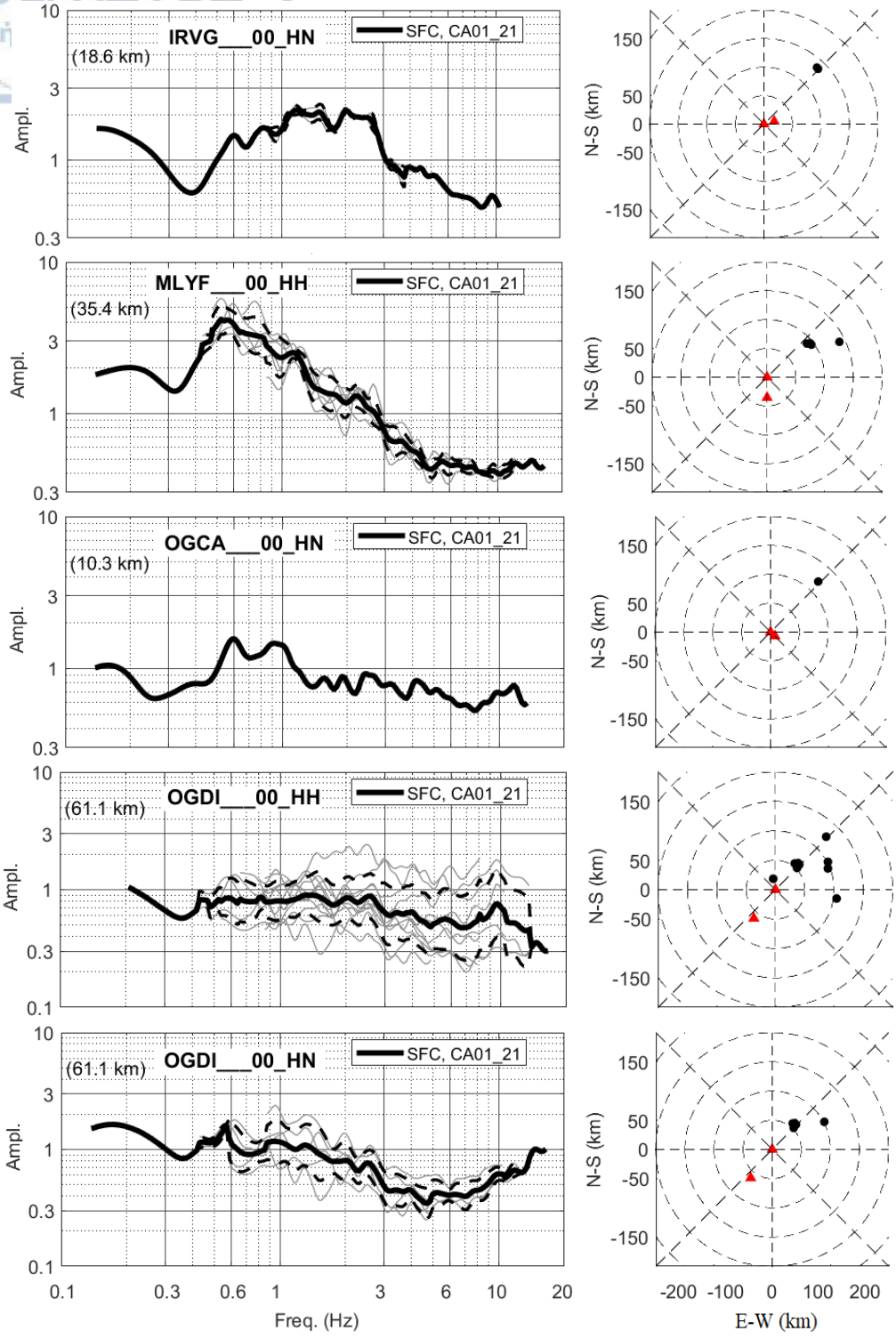

Figure 53. (continued)

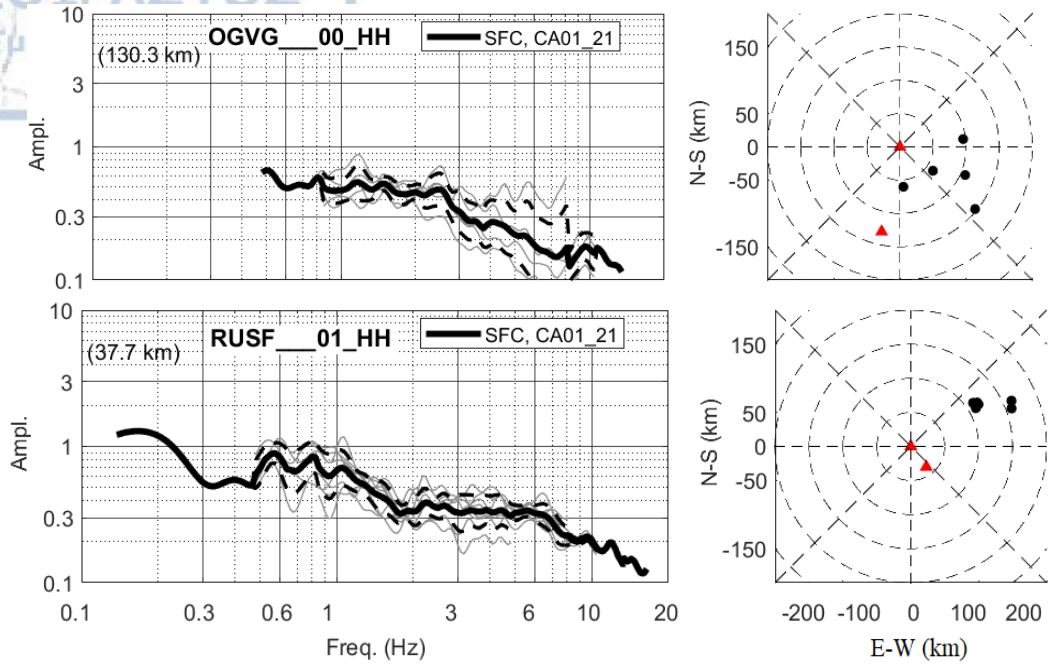

Figure 53. (continued)

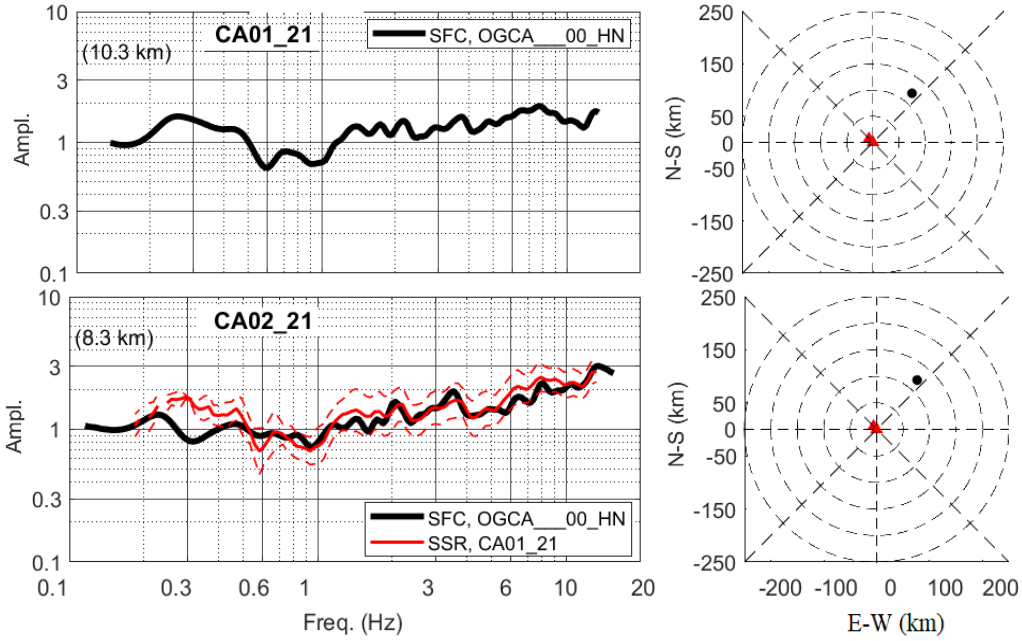

Figure 54. (similar to **Figure 51**) The SAF(f) for the 16 stations of **Figure 8** (**Appendix D**) computed based on the SFC method (grey lines, black line is the geometric mean), with respect to the **OGCA_00_HN** reference station. The adjusted SSR results (red lines, **Appendix T**) for the 3 Cadarache (CA..) stations with respect to the CA01_21, are also presented. In yellow, cyan, brown and purple (they are all identical to purple) the "corrected" GIT results (***Traversa, P., 2021***, personal communication) computed for parametric (p) and non-parametric (np) study cases, by using either the sum of all the stations as reference (all), or the OGDI_00_HN station.

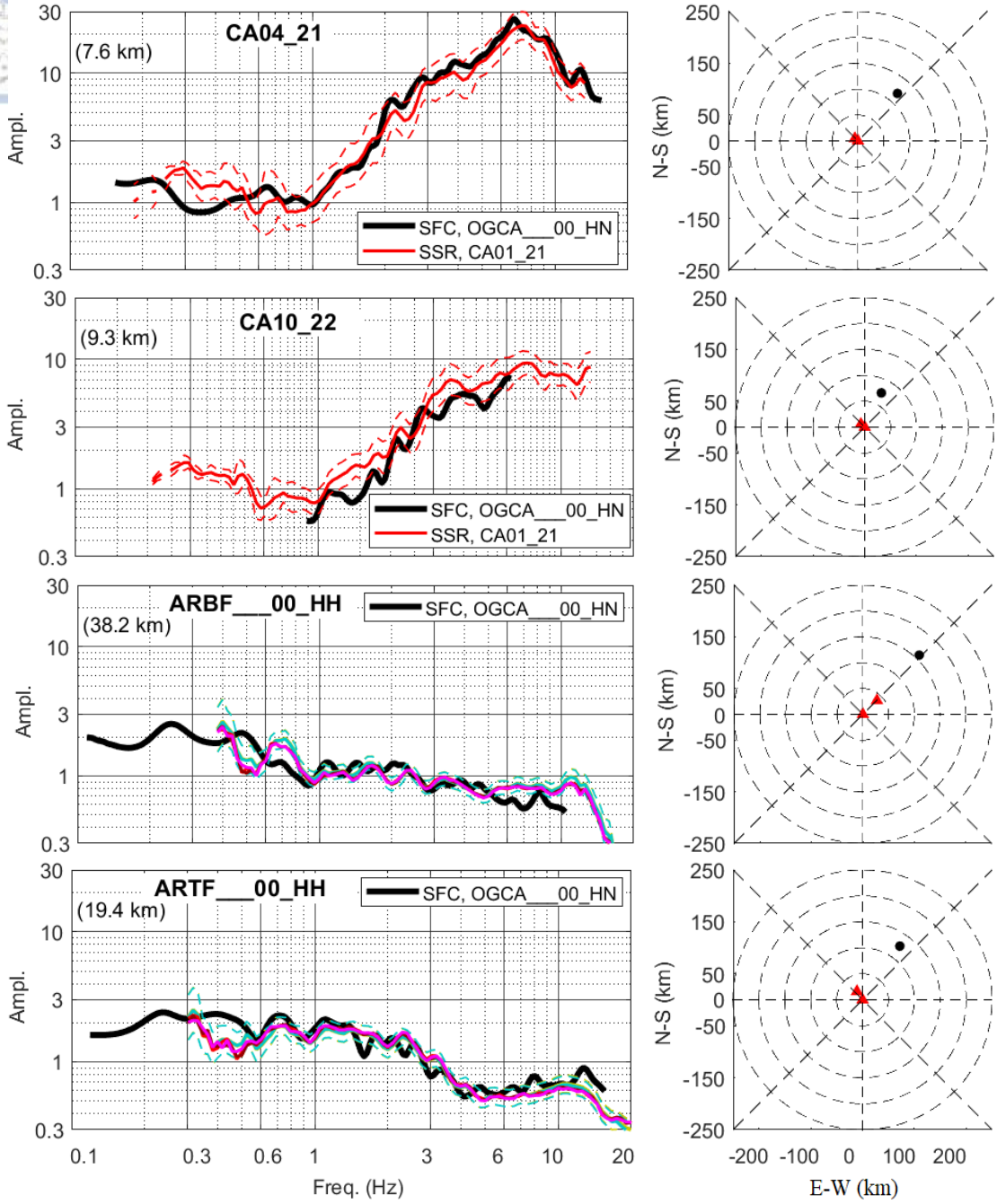

Figure 54. (continued)

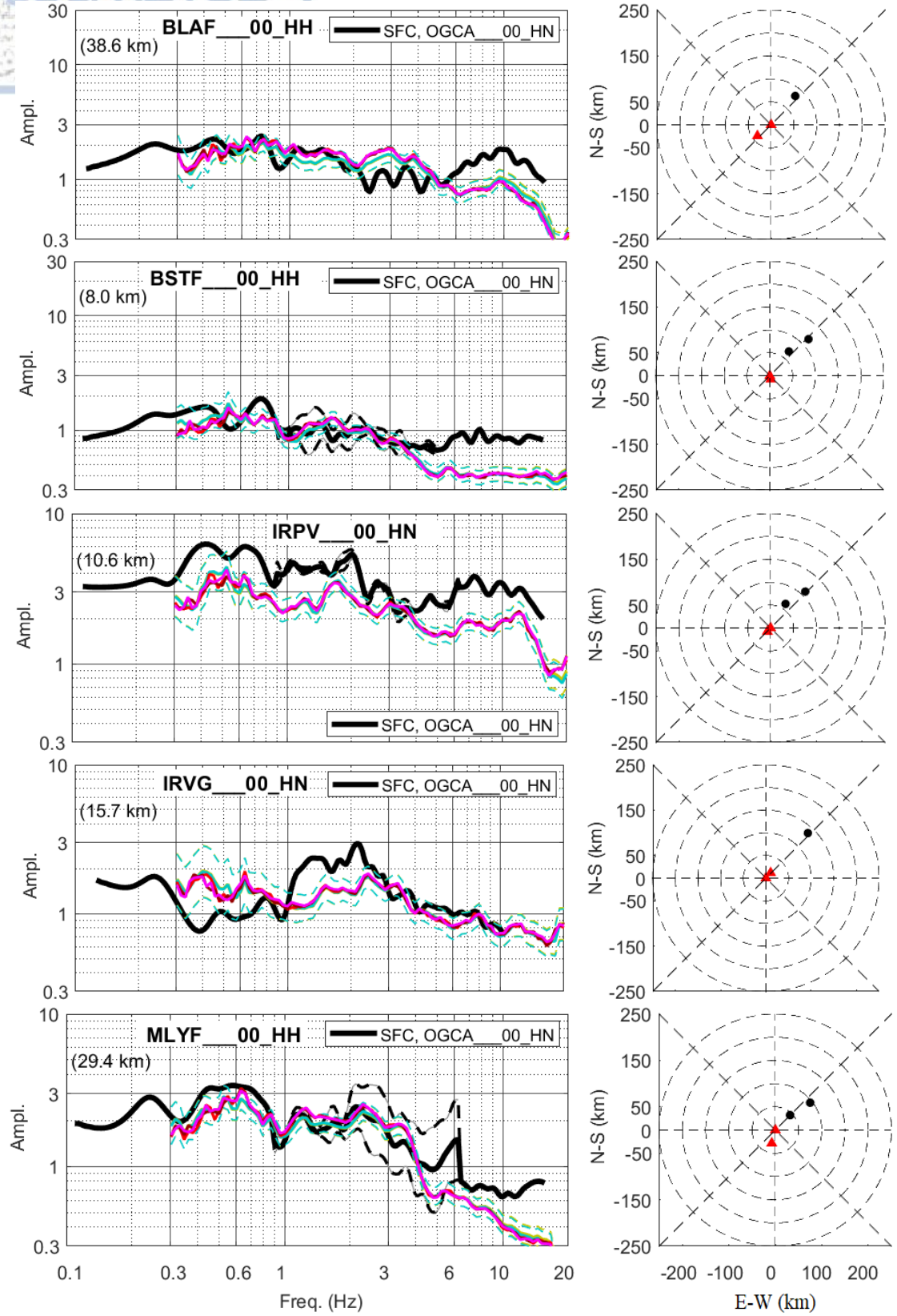

Figure 54. (continued)

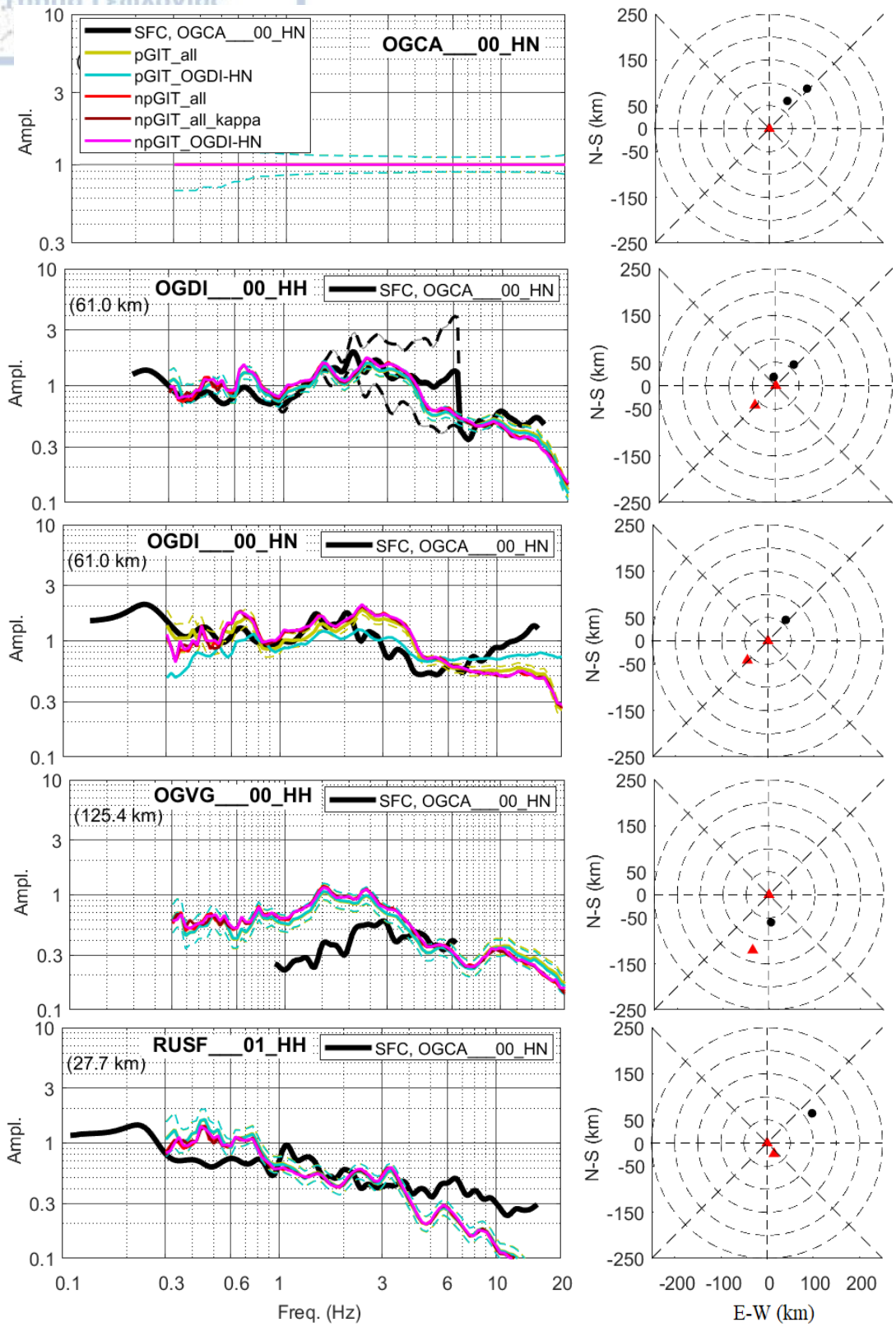

Figure 54. (continued)

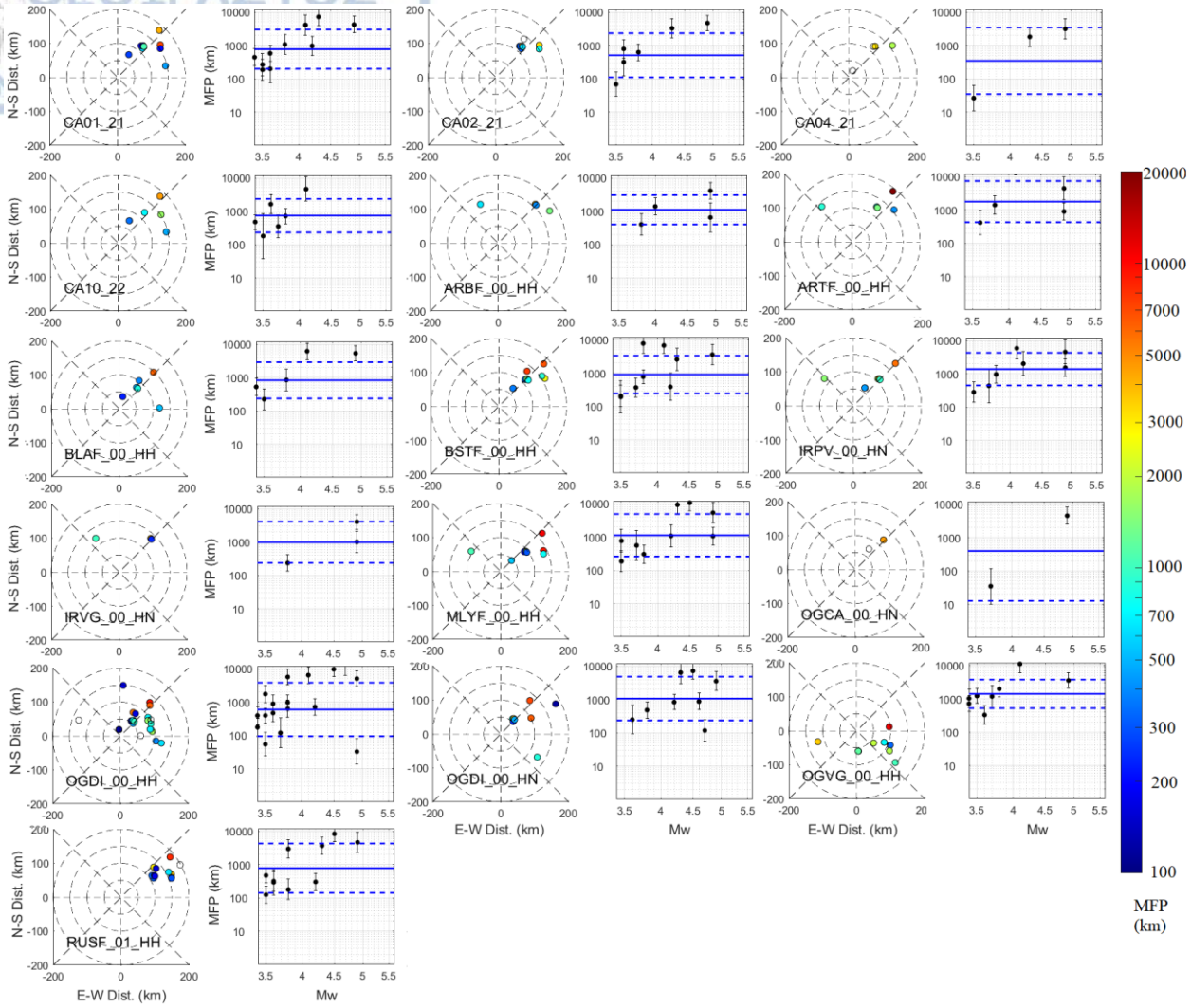

Figure 55. (Similar to **Figure 46**). The Mean Free Path (km) are presented after the correction for the "average" $SAF(f)$ of **Figure 51** (same color bar), estimated from each earthquake-station pair for the 16 stations (**Figure 8a**). The geometric mean and the corresponding standard deviation of the Mean Free Paths computed at each site, are given in **Appendix D**.

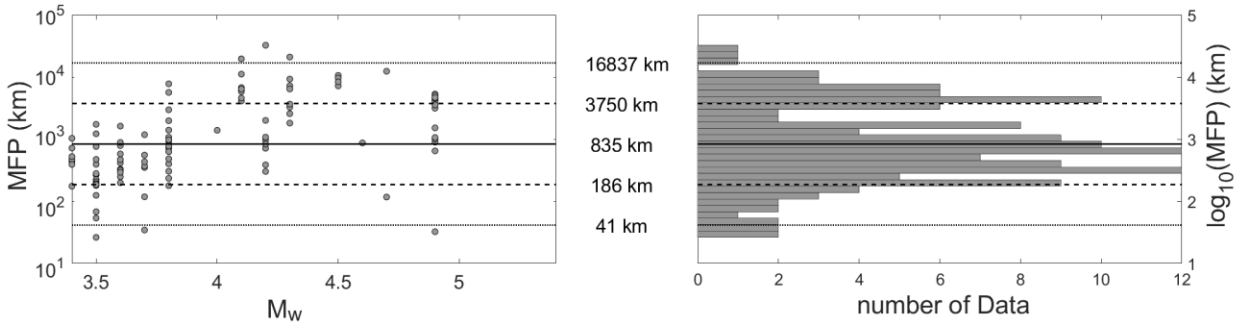

Figure 56. The distribution of the computed Mean Free Paths of **Figure 55** vs the corresponding M_w of the examined earthquakes (**Appendix D**) and the corresponding histogram. The geometric mean and the one and two standard deviation ranges are also depicted.

4.3.3 SFC application on four low-to-large magnitude earthquakes and evaluation of their mpSTF

Based on the SFC analysis mentioned above in this chapter the minimum phase Source Time Functions were estimated for four earthquakes of the 4th group of data of this study (*ch. 2.4*), at each examined station and they are presented in this section. The most appropriate mean free path values, which are discussed at each case, have been taken into account.

Earthquake Id: 20120226_223756, M_w~ 4.2

Regarding the first earthquake occurred in Southeastern France (M_w= 4.15 earthquake id: 20120226_223756, 4th group of data, *ch. 2.4*), the scaled for the F factor (Eq. [28]) Fourier Amplitude Spectra, $FAS[S\dot{T}F^{sc}]$ (in velocity) (Eq. [32], for the horizontal components) at each station (**Figure 9a**) were firstly estimated based on the first 6 steps of the SFC algorithm (**Table 6**). Before the estimation of the scaled minimum phase Source Time Function, $mpSTF^{sc}$ (in displacement) (based on the 7th and 8th steps of the algorithm) and its scaling correction (9th step), the available Site Amplification Factors, SAF(f) of the examined sites, were firstly removed from the corresponding $FAS[S\dot{T}F^{sc}]$. More specifically this correction was achieved by firstly computing the minimum phase of each available SAF(f) ($mpSAF(t)$), as in the example of **Figure 48** and deconvolving them from the mp$S\dot{T}F^{sc}$. The SAF(f) of each station used for the correction per examined earthquake, were the average one computed based on the BSTF_00_HH station (**Figure 51**). For those stations that no SAF(f) was available (**Appendix E**), no correction was applied to the mp$S\dot{T}F^{sc}$. However, it must be mentioned that no significant site effects are expected at these sites, since they are installed on rock conditions.

After this site effect correction of the $FAS[S\dot{T}F^{sc}]$ at each station, the 7th and 8th steps of the SFC algorithm were applied to retrieve the scaled and corrected for the low frequency plateau, $mpSTF^{sc}$. Thereafter, the scaling correction of the $mpSTF^{sc}$ was applied based on the 9th step of the SFC algorithm, by computing the F factor (Eq. [28]), considering the mean free path, l = 835 km. This value is the average one estimated in this study (**Figure 56**) by the application of the SFC method to lower magnitude earthquakes occurred in the broader area of Southeastern France (**Figure 8**). Moreover the l = 3750 km and 186 km, were used to retrieve the ±1 standard deviation limits of the $mpSTF$, based on the values obtained in **Figure 56**. Finally, the seismic moment magnitudes, M_w corresponding to each $mpSTF$ of each earthquake-station pair were determined, based on the already computed seismic moment, M_o and on Eq. [35].

In **Figure 57** the $mpSTF$s of the current examined earthquake (M_w= 4.15 earthquake id: 20120226_223756) computed at each examined station of **Figure 9a**, are presented, in comparison with three different cases of the total seven apparent STF estimated by ***Courboulex et al., (2013)***, presented in **Figure 58** and which include high frequency rupture directivity effect. These apparent STFs were computed based on a high frequency analysis using Empirical Greens Function (EGF), applying the deconvolution method developed by ***Vallée, (2004)***, between the mainshock and a small aftershock at the same region. The three cases presented in **Figure 57**

represent the two "extreme" cases of the higher duration-lower STF peak and lower duration-maximum STF peak, that is the STF of the OGAG and ISO station, respectively, expressed by the Doppler's effect, as well as the average STF, computed based on the available seven apparent STFs provided by ***Courboulex et al., (2013)*** (**Figure 58**).

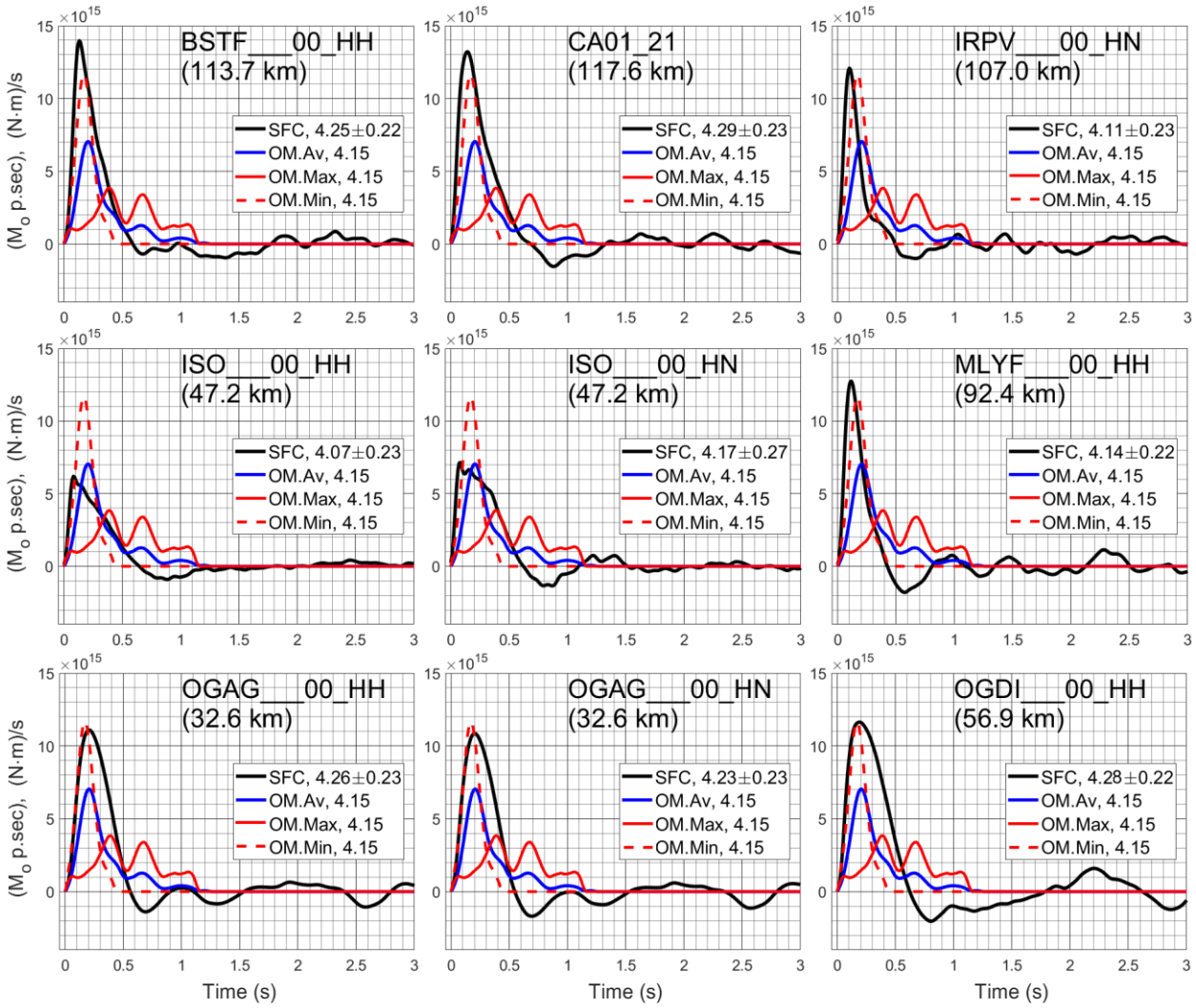

Figure 57. The *mpSTF* computed in this study, for the M_w= 4.15 earthquake (id: 20120226_223756), at each examined station, based on the SFC method (black line). The corresponding apparent STFs computed by other method (***Courboulex et al., 2013***) for the following two extreme cases: the minimum duration-high peak (OM.Min - red line) and the maximum duration-low peak (OM.Max - red dashed line), as well as the average computed by all the available apparent STF (OM.Av. - blue line). The corresponding computed M_w of each case is also presented.

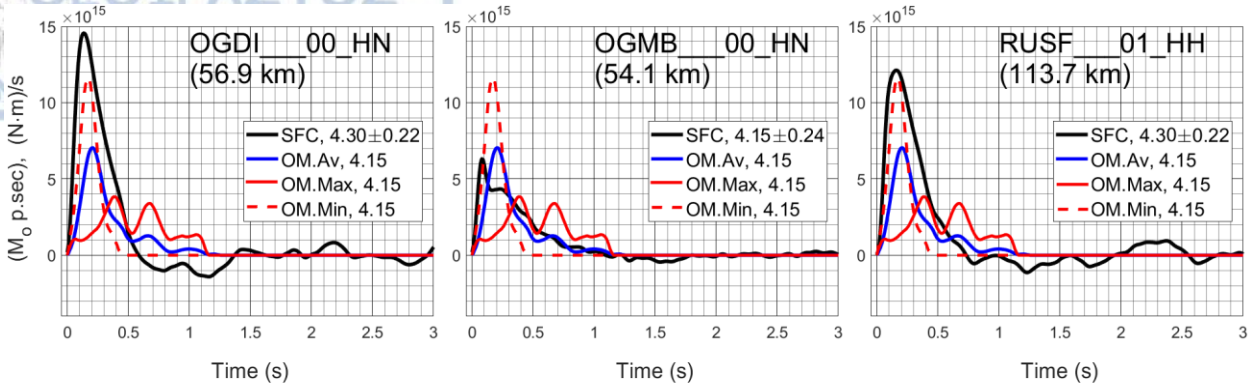

Figure 57. (continue)

It's worth noting that the $mpSTF$ (**Figure 57**) present some low, non-reasonable negative values, that are probably related to some low site effect "contamination" in high frequencies, that were not absolutely reduced by the average SAFs(f) used for the site effect correction. However, this $SAF(f)$ correction, converges to $mpSTF$ results, which satisfactorily approach the moment magnitude, M_w= 4.15 computed by ***Courboulex et al., (2013)***, but also approach its rupture duration, which seems to vary between 0.4 s and 1.2 s, as presented in **Figure 57**. More specifically, regarding the M_w computed at each site depending only on the stable value of the low frequency plateau of the $FAS[mpSTF]$ (**Figure 59**), it seems that all satisfactorily approach the M_w= 4.15, taking into account their standard deviation range. Also, based on **Figure 57**, it can be observed that most of the $mpSTF$ approach the "minimum duration-high peak" apparent STF, or at least the average computed one, in terms of duration. This observation albeit it is related to the minimum phase assumption regarding the energy release at the beginning of the STF, obviously agree to the observed corner frequency, f_c at the corresponding FAS[$mpSTF$] presented in **Figure 59**, independently of the minimum phase assumption. Most of the FAS[$mpSTF$] present $f_c \geq 1$ Hz, which correspond to source duration, $T_c \leq 1$ s, in agreement to range 0.4 s to 1.2 s, obtained by the ***Courboulex et al., (2013)***. The station OGMU_00_HN, is the only one at which $f_c \sim 1$ Hz (**Figure 59**) ($T_c \sim 1$ s, **Figure 57**), indicating a partial directivity effect, in relevant agreement to the one extracted by ***Courboulex et al., (2013)***, for the stations at the opposite side (towards NNW) of the rupture direction (**Figure 58**). However, not obvious correlation is extracted between the $mpSTF$ and the directivity effects of the source rupture, as presented in **Figure 60a,b**, determining mainly the average source duration ($T_c \sim$ 0.5-1 s). Finally, the average computed M_w based on all the computed ones of the $mpSTF$ (**Figure 57**), is 4.21 ± 0.15 (**Figure 60**), in quite good agreement to the M_w = 4.15 ± 0.2, computed by ***Courboulex et al., (2013)***.

Finally, regarding the use of the minimum phase scenario of the STF estimation based on its FAS, it seems that at this case where the STF is not so complicated, with a relevant low duration (~1 s), is in a relatively good agreement with the STF estimated by ***Courboulex et al., (2013)***.

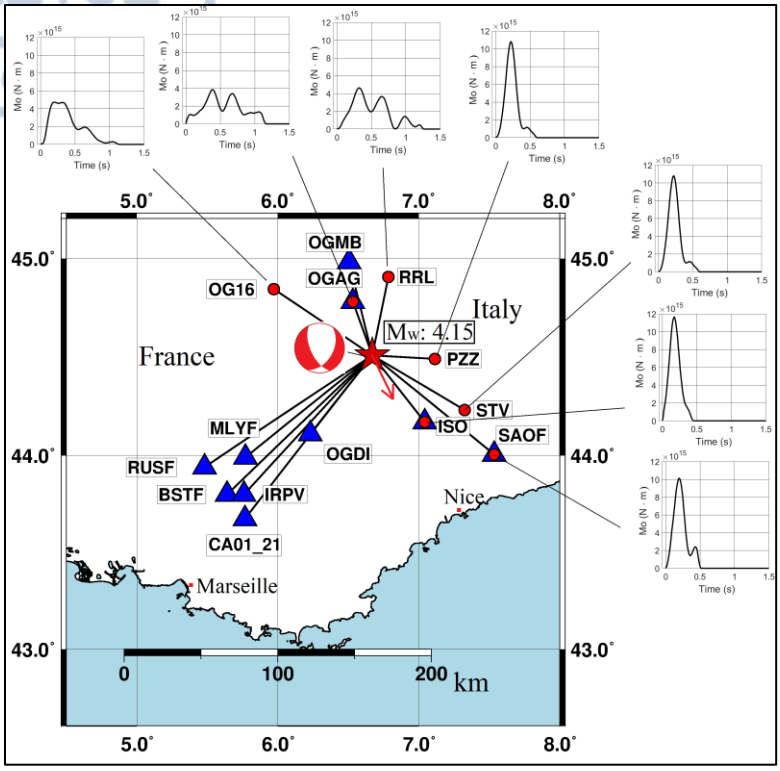

Figure 58. The same map displayed in **Figure 9a,** where the apparent STFs computed by ***Courboulex et al., (2013)*** at the seven specific stations (red cycles) are now presented.

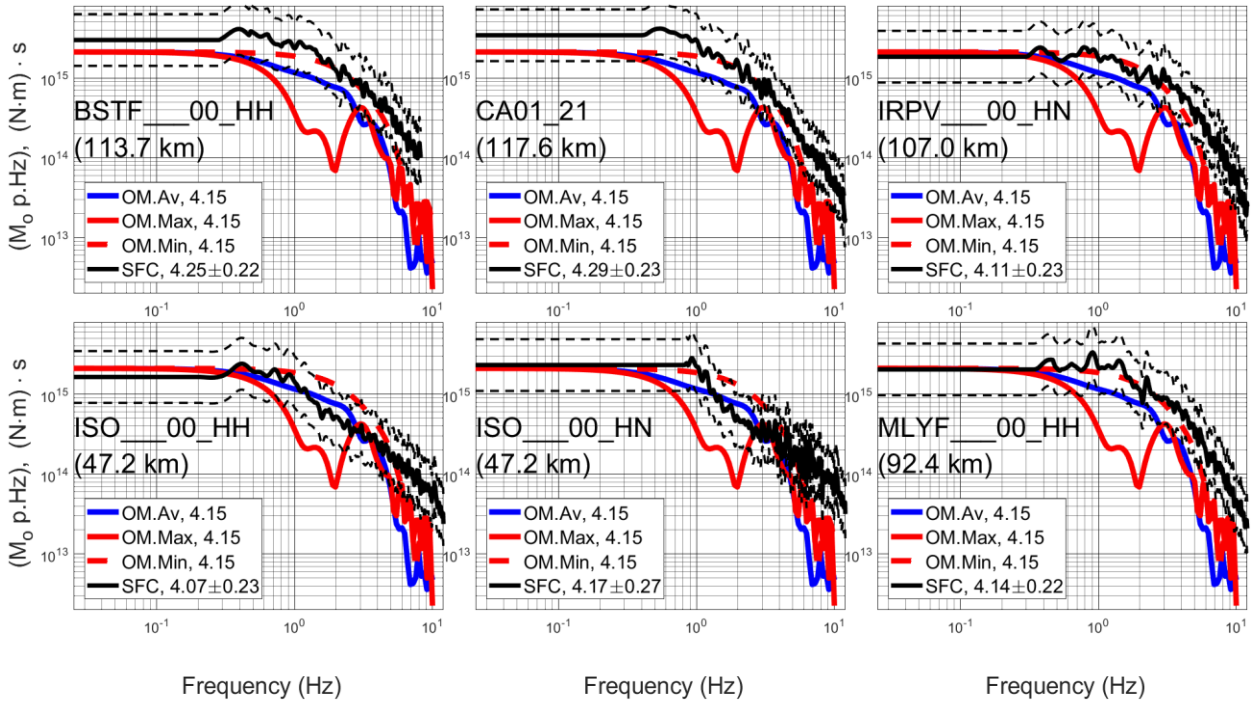

Figure 59. The corresponding FAS of the apparent STF presented in **Figure 57**.

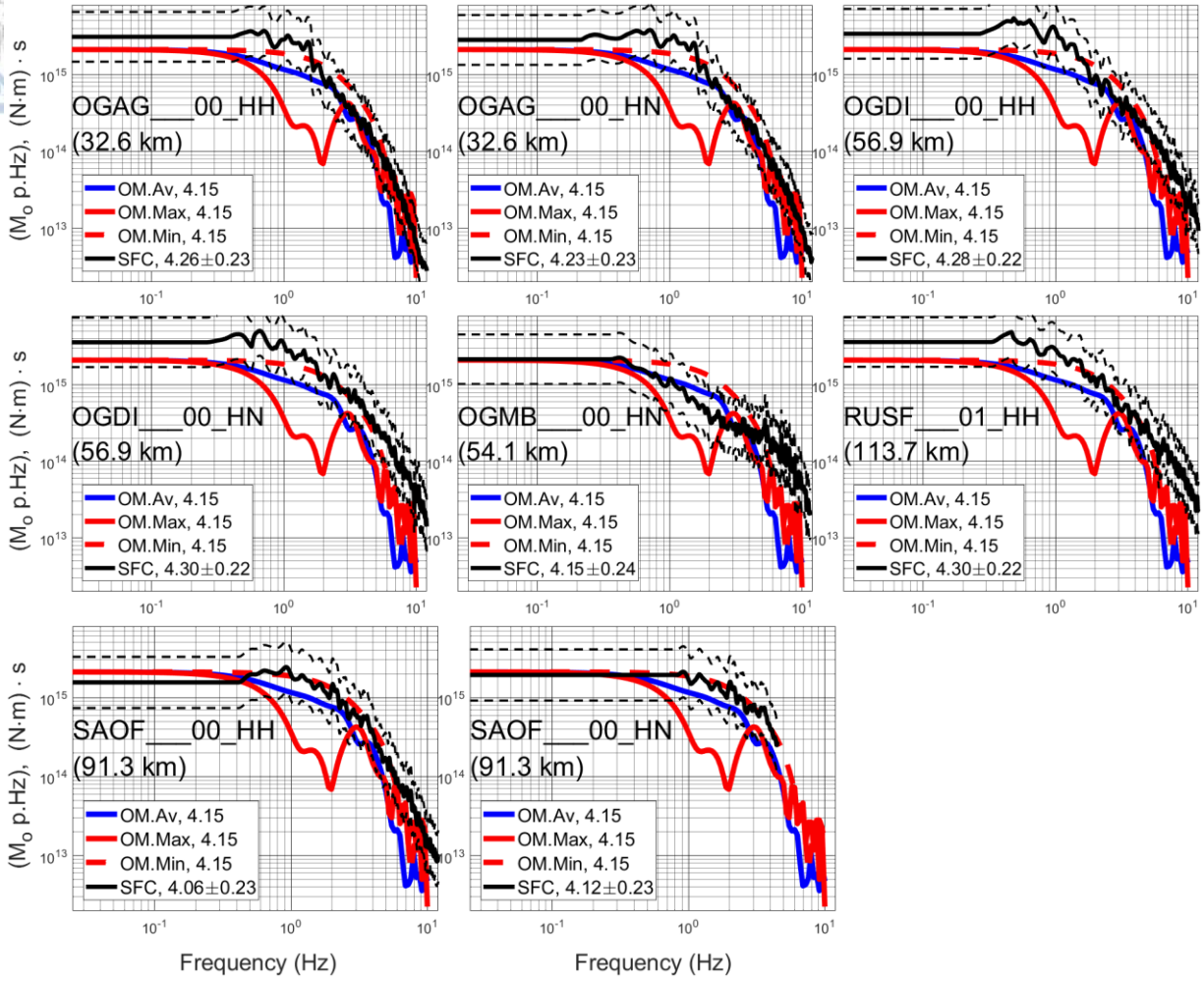

Figure 59. (continue)

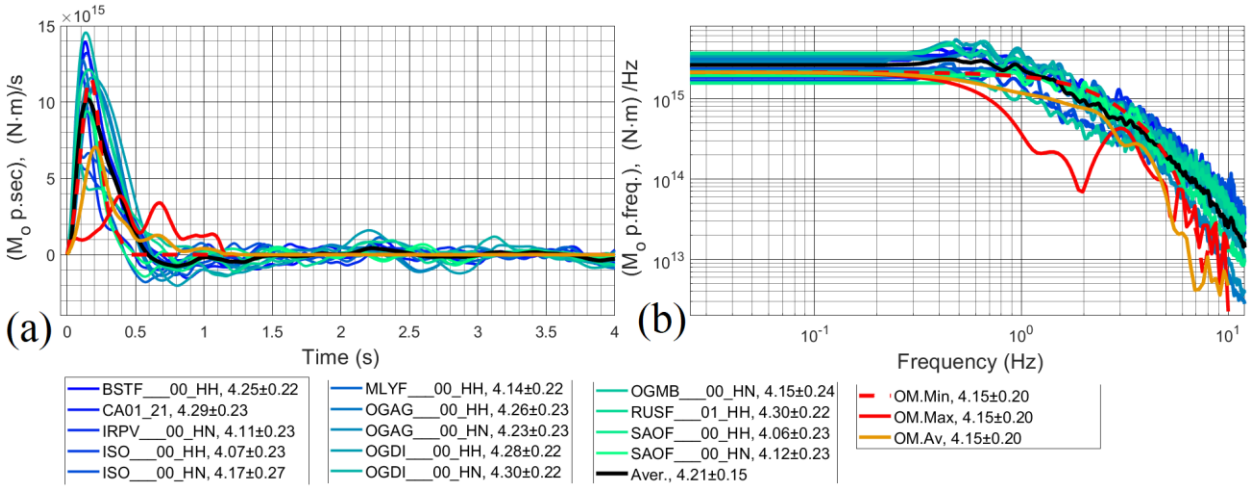

Figure 60. (**a**) The *mpSTF* of all the examined stations (**Figure 58**) based on the SFC method (multi color lines) and their average computed one (black line) vs the three cases of the apparent STFs (OM.Min, OM.Max and OM.Av), as presented in **Figure 57**. (**b**) The corresponding FAS of the STF of Fig. **a**.

Earthquake Id: 20191111_105245, M_w~ 4.9

Regarding the second earthquake occurred also in Southeastern France (M_w= 4.85 earthquake id: 2019111_105245, mentioned at the 4th group of data, *ch. 2.4*), the same process as the one mentioned above for the first examined earthquake in the same area was applied for the $mpSTF^{sc}$, correcting it by the same scaling factor, (l = 835 km, one standard deviation range: l = 186-3750 km, **Figure 56**). In **Figure 61** all the determined $mpSTF$ (**Appendix U**) computed based on the SFC method for the examined stations (**Figure 9b**) are presented in comparison to the two extreme cases of the real STF (the minimum duration-higher STF Peak and the maximum duration-lower STF peak) and the average one as estimated by ***Causse et al., (2021)***. In this case albeit all the station are located perpendicular to the bilateral rupture directivity of the fault (see **Figure 9b**), the $mpSTF$s "fit" better to the shape of the apparent STF related to the minimum duration and higher STF peak (**Figure 61a**). This is not an effect of the minimum phase scenario, since also all the FAS of the $mpSTF$ (**Figure 61b**) "fit" better to the corresponding FAS of the minimum duration-maximum energy peak STF (see in **Appendix V**). Regarding the minimum phase scenario, seems to be a good hypothesis for this earthquake, since the $mpSTF$ approaches a simple pulse wavelet. Thus, the $mpSTF$ can reveal information about the source duration. All the $mpSTF$ indicate duration up to ~1 s, which is in quite good agreement to the shorter duration STFs estimated by ***Causse et al., (2021)***, ranging between 1 s and~4 s.

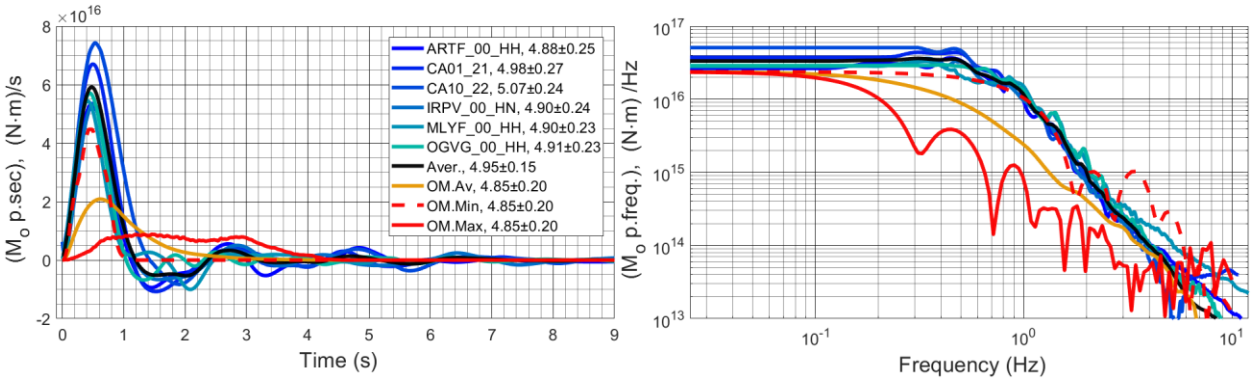

Figure 61. The corresponding to **Figure 60**, for the M_w= 4.85 (earthquake id: 2019111_105245). The apparent real STF and their FAS are based on ***Causse et al., (2021)***.

Earthquake Id: 20140226_135543, M_w= 6.1

Regarding the third earthquake which was occurred in western Greece (M_w= 6.05 earthquake id: 20140226_135543, mentioned in the 4th group of data, *ch.* 2.4) the same process as the one mentioned above for the first examined earthquake, was applied for the $mpSTF^{sc}$. The scaling factor correction was based on the average mean free path computed above in this study for this region, l = 253 km (**Figure 47c, d**), based on lower magnitude earthquakes. The computed average ±1 standard deviation range of the mean free path (l = 88 km – 727 km, **Figure 47c, d**) was used to determine the standard deviation range of the $mpSTF$ and the corresponding M_w. In

Figure 62a all the determined *mpSTF*s (**Appendix W**) computed based on the SFC methodology for the examined stations (**Figure 10a**) are presented in comparison with the average real STF estimated by ***Sokos et al., (2015)*** (**Figure 62a**). As at the previous two cases for the $M_w \sim 4$ and $M_w \sim 5$, the M_w of this earthquake estimated from each coda wave record are in quite good agreement to the M_w= 6.05 (±0.20) determined by ***Sokos et al., (2015)*** (**Figure 62a,b**), where their average is M_w= 6.08±0.20. Moreover, the FAS[*mpSTF*] are in quite good agreement to the corresponding FAS of the real STF up to ~0.2 Hz, which is its computational high frequency limit (***Sokos et al., 2015***). Regarding the real moment rate function (STF), it is obvious that the minimum phase scenario is not appropriate to approach the real STF shape. This is confirmed by the disagreement of the total energy release in time, of each *mpSTF* (**Figure 62c**), to the one computed from the real STF determined by ***Sokos et al., (2015)***. However, what can be extracted from this figure, is the source duration corresponding to the 95%, 97% and 99% of the total energy (**Figure 62d**). It seems that the duration of the real STF (***Sokos et al., 2015***) ($T_c \sim 12$ s), can be estimated, based on the ~95% of the total energy released by the *mpSTF*.

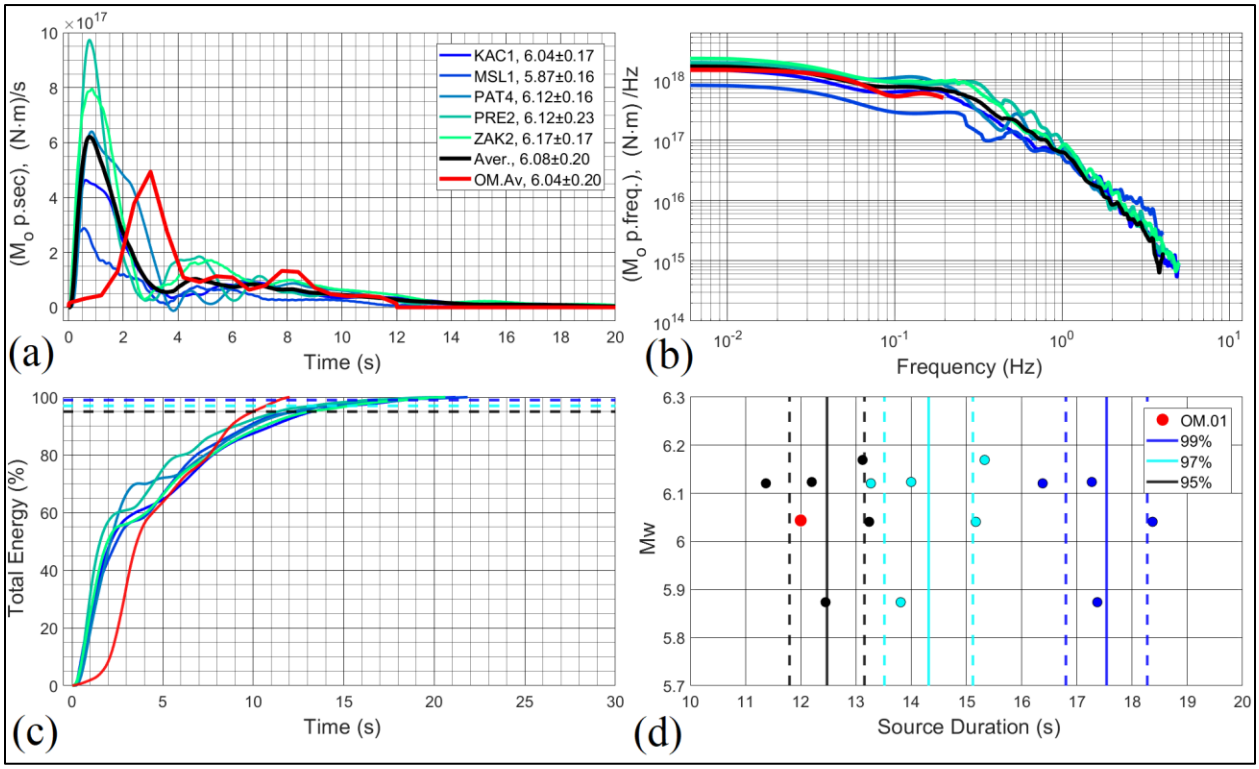

Figure 62. (**a**) The *mpSTF* of the 5 examined stations for the M_w= 6.05 (earthquake id: 20140226_135543) based on the SFC method (multi color lines) and their average computed one (black line) vs the average real STF (for the frequency range 0 - 0.2 Hz) based on ***Sokos et al., (2015)*** (based on Other Methodology, red line). (**b**) The corresponding FAS of the STFs of Fig. **a**. (**c**) The total energy release of each *mpSTF*s of Fig. (**a**) and of the real STF (**d**) The durations of the *mpSTF* corresponding to the 95%, 97% and 99% percent of their energy released in time depicted in **Figure 62c**. The duration of the real STF is also depicted.

It's worth noting that in this case, for all the $mpSTF$, the low frequency plateau begins at frequency very close to the lower reliable frequency limit (0.05 Hz) where the high pass filtering is applied on the recordings. This means that the M_w estimated by the $mpSTF$ could exhibit slightly higher values, than those already determined.

Earthquake Id: 20201030_115125, M_w= 7.0

The last (fourth) examined earthquake for its $mpSTF^{sc}$, (mentioned at the 4th group of data, *ch.* 2.4), has occurred in the Northern coasts of Samos island, in eastern Greece (M_w= 7.0, id: 20201030_115125). Albeit the mean free path has not been specifically determined for this region, it was conventionally considered, l = 253 km, equal to the average one estimated for the western Greece, taking into account the corresponding ±1 standard deviation range (l = 88 km – 727 km). Moreover, the *SAF(f)* factor has not been removed from the computed FAS[mpSTF] at the examined sites, since they have not been determined based on the SFC method by other, lower magnitude earthquakes. However, because of the large magnitude of this earthquake, the lower frequency plateau is expected to be presented at very low frequencies (f < 0.1), for which site effects are not expected. This means that the estimation of the moment magnitude based on the FAS[mpSTF], will not be affected by any possible site effects in higher frequencies. The same is expected for the apparent corner frequency, expecting that the total source duration computed based on the mpSTF, will not be affected by site effects. Both M_w and source duration are discussed below.

In **Figure 63** all determined $mpSTF$s (**Appendix Y**) computed by the SFC method for the examined stations (**Figure 10b**) are presented in comparison with the average STF estimated by the United States Geological Survey (USGS, https://earthquake.usgs.gov/earthquakes), as well by ***Lentas et al., (2021)***. As in the previous three cases for M_w ~ 4, M_w ~ 5 and M_w ~ 6, the M_w of this earthquake estimated from their coda wave recordings, are in quite good agreement with the M_w= 7.0 (±0.20) determined by the studies mentioned above, where their average is M_w= 6.88±0.20. Moreover, the FAS[$mpSTF$] (**Figure 63b**, **Appendix Z**) are in quite good agreement with the corresponding FAS of the real STF determined both by USGS and ***Lentas et al., (2021)*** up to ~0.5 Hz, which is their computational high frequency limit. Similar to the application for the Cephalonia earthquake (M_w ~ 6) examined in the previous subchapter the provided by Other Methodology (OM) real moment rate functions (STF) are not expressed by a minimum phase scenario. This is confirmed by the disagreement of the total energy release in time, of each $mpSTF$ (**Figure 63c**), to the ones computed from the two real STFs. What can be extracted from this figure, is that the source duration estimated based on the ~98% of the energy release (**Figure 63c**), for the half of the examined stations (MYT1, NAX1 and SMG1), is in agreement to the one estimated by ***Lentas et al., (2021)*** (~15 s), while for the rest stations (APE, CHOS and SGR1) the source duration estimated based on the ~95% of the energy release (**Figure 63c**), approaches to the one estimated by the USGS (~23 s).

Similar to the Cephalonia earthquake (M_w ~ 6) examined at the previous sub-chapter, the low frequency plateau begins at frequency very close to the lower reliable frequency limit (0.05 Hz

for the accelerographs and 0.01 for the seismographs) at which the high pass filter is applied for the accelerographs. This means that the M_w estimated by the $mpSTF$ could have a bit higher values, than the one already determined, but for sure no lower M_w could be extracted.

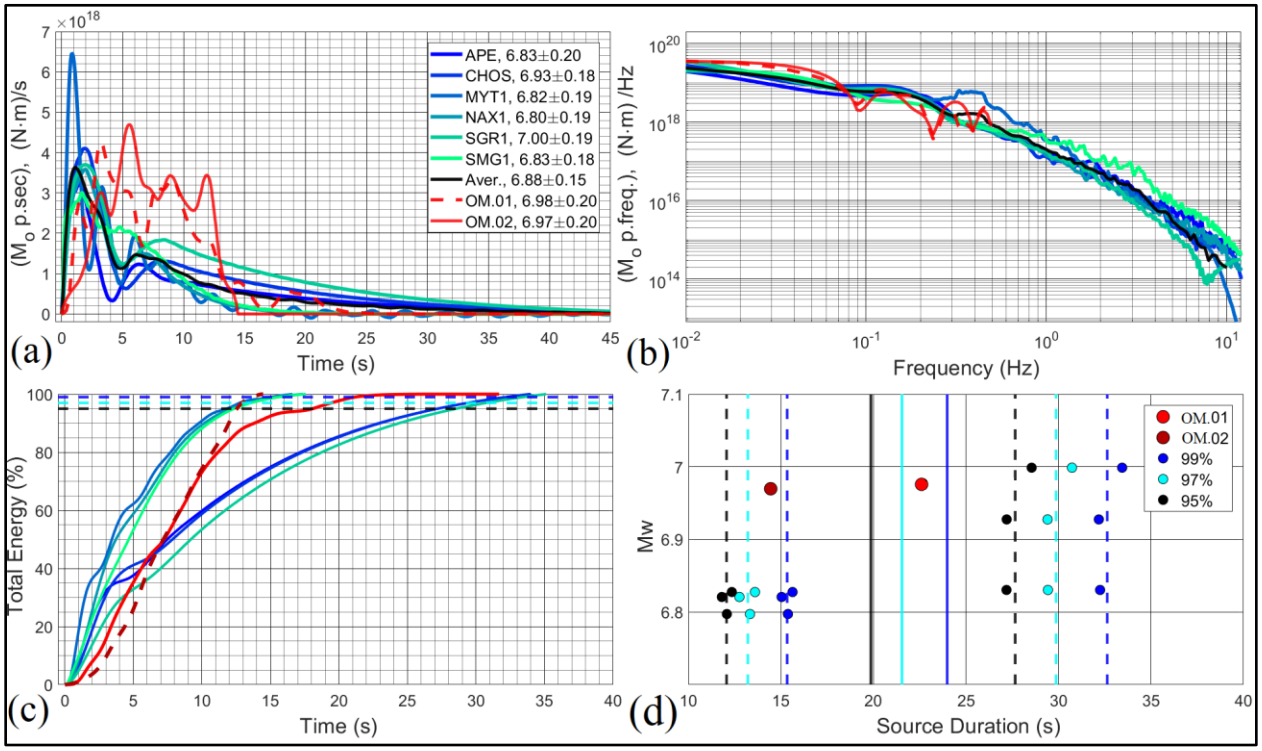

Figure 63. (**a** and **b**) the corresponding to **Figure 60**, for the M_w= 7.0 (earthquake id: 20201030_115125). The presented real STFs (OM.01 and OM.02) and their FAS, as have been provided by USGS and by ***Lentas et al., (2021)***, respectively based on other methodologies than the SFC one. (**c**) The total energy release of each $mpSTF$ of Fig. (**a**) and of the two real STFs (**d**) The durations of the $mpSTF$ corresponding to the 95%, 97% and 99% percent of their energy released in time depicted in Fig. (**c**). The durations of the two real STFs are also depicted.

5 CONCLUSIONS AND DISCUSSION

The main objective of this thesis refers to the study of the factors controlling seismic motion on surface geological formations, i.e. the seismic source, attenuation due to propagation path and site effects. This study is implemented through two methodologies, that is, the Generalized Inversion Technique (GIT), based on S-wave seismic motion and the Spectral Factorization of Coda waves (SFC). Both methodologies aim at investigating in frequency domain, all three factors that control seismic motion, while the latter can provide information about the Source Time Function and Site Amplification Factor, in time domain as well. In the framework of this thesis, two algorithms in MATLAB programming, have been developed and implemented, corresponding to GIT and SFC methodologies and can be used as seismological tools for corresponding future studies.

The first methodology analyzed in this study (the GIT, *ch.* 3), deals with the inversion of the Fourier Amplitude Spectra of the S-wave seismic motion, of several earthquakes at several stations and can lead to the determination (i) of the moment magnitude and the corner frequencies of the earthquakes examined, (ii) of the average Site Amplification Factors of each site (station location), as well as (iii) of a regional dependent anelastic attenuation model and a distance dependent geometrical spreading factor. The latter constitutes the main advantage of the new developed GIT algorithm in this study.

Regarding the implementation and results of the new GIT algorithm, four groups of inversion tests on synthetic data created in this study were implemented, confirming its effective applicability and the following conclusions are drawn and highlighted for future use:

- Significant stability and accuracy are presented in seismic moment, M_o computations, independently of the *a priori* values in the initial parameters model and of the use or not of reference site conditions.
- Similar stability has been observed in corner frequency, f_c computations, that fall into the data frequency range, while the inversion algorithm computing potential is weak in estimating f_c out of this frequency range. To face this issue, an *a priori* application of several inversions with different initial f_c values (e.g. corresponding to $\Delta\sigma$ = 10 and 400 bar) can be used for a preliminary evaluation of the f_c of the examined earthquakes, in order to investigate any instability of their estimation and consequently to be removed from the dataset before a final GIT implementation.
- A correlation between the average level of the geometrical spreading factor, gamma, γ and the average level of computed Site Amplification Factors, $S_j(f_k)$ exists and has been mainly observed through the 2nd inversion group of tests on synthetic data, when using different initial values of site factors, $S_j(f_k)$. The use of a reference site condition, or a geometrical spreading reference value, can help to better approach the investigated parameters, converging at a unique solution of the model parameters.

- The relative amplifications between the $S_j(f_k)$ remain similar in all tests, which is encouraging for the computation reliability of the algorithm. In other words, this means that the shape of the computed $S_j(f_k)$ is stable and independent of any correlation with the geometrical spreading factor as has been mentioned above.
- Regarding the computational capability of the proposed GIT algorithm to estimate the regional dependent anelastic attenuation factor, $Q_s(f_k)$, it seems that it constitutes a new satisfactory approach. The $Q_s(f_k)$ of several examined sub-areas can be successfully approximated for most of them while less successfully for a few cases, which mainly lie either at the edge of the examined area, or/and they do not include a satisfactory number of ray paths crossing them. This result is expressed by the relevantly high values of the corresponding standard deviations computed by GIT.
- The efficient computing power of the new GIT algorithm and the achievement of its goal to improve the already developed one by ***Drouet et al., (2008a)***, were satisfying by the comparison of the results retrieved from the application of both algorithms on the same dataset, for the following reasons:
  - (i) The dataset processed and investigated by ***Grendas et al., (2018)*** using the previously developed GIT algorithm for a uniform attenuation model in the broader Aegean area, was inverted here as well. A relevantly low (~9%) but non-negligible reduction of the total misfit between the real and inverted data was observed, indicating the improvement of the algorithm by providing a misfit even closer to zero.
  - (ii) Regarding the inversion of the real dataset, mentioned in bullet (i), except for the desired misfit reduction, the computed factors of source, path and site effects, indicate also improvement of the new GIT algorithm implementation. The estimated moment magnitudes, M_w, for some earthquakes are in a better agreement with the corresponding ones of the catalogue while the rest remain stable in general (**Figure 14a**). Stability in shape is observed for the determined site factors $S_j(f_k)$ and most of them show amplification equal or higher than those corresponding to the HVSR method using the same data set, as it would be expected (***Haghshenas et al., 2008***). This is significantly supported by the fact that the $S_j(f_k)$ computed for stations located in Thessaloniki city, are now identical to those computed by the SSR technique using station 'SEIS' as a reference site. In addition, the geometrical spreading and the quality factor, seem to diverge from stable and homogeneous values for the entire examined area, as have been derived by the previous GIT algorithm. Finally, the inverted stress drop parameter, $\Delta\sigma$, the average of which is equal to ~29 bar (**Figure 14b**), are slightly lower than the corresponding previous study (~56 bar), while extreme and irrational $\Delta\sigma$ values (e.g. > 800 bar) are not observed after implementation of the new GIT algorithm.

Finally, during the GIT analysis presented in *ch. 3*, a quite analytical inversion study in terms of attenuation, was implemented to a dataset of S-wave records acquired within the high seismicity

area of western Greece, including the Ionian islands of Cephalonia, Lefkas, Zakynthos and Ithaca. More than five thousand S-wave FAS (both vertical and horizontal components), obtained from 180 earthquakes occurred in this area, with M_w range from 2.4 to 5.2 (M_L 3.0-5.4), were inverted based on the new GIT algorithm and the following conclusion for this application, are extracted:

- Regarding the attenuation factor dominating in western Greece and Ionian Sea, a close to spherical geometrical spreading, ${r_{ij}}^{-0.98}$, (Eq. [7]) of S-waves was computed for distances up to ~ 40 km (**Table 4**, **Figure 25**), while a smooth reduction up to ${r_{ij}}^{-0.77}$, prevails for longer distances (up to ~ 200 km).
- Moderate to high anelastic attenuation (attenuation due to scattering is included) characterizes the examined area, where the quality factor, Q_s (Eq. [7]) varies between 22.5 and 90.5 with geometric mean of Q_s = 45 (**Figure 27**, **Appendix K**), considering an average crustal shear wave velocity, v_s = 3500 m/s. The alpha, $a,$ parameter (Eq. [7]) ranges between 0.56 and 1.09, including the 86% of the data with CV < 15%, with an average value 0.86 ± 0.23.
- The site factors, $S_j(f_k)$ (Eq. [7]) of the horizontal and vertical components were computed for the 24 stations (**Appendix C**), of the study area. These factors include the real generic amplification with respect to the crustal-bedrock conditions (Vs~3.5 km/sec) and the expected high frequency attenuation due to surface bedrock weathered layers. Both generic amplification and high frequency attenuation factors included in $S_j(f_k)$, remain unknown, since they interact with each other resulting to the final $S_j(f_k)$ values. Regarding the considered as "reference" stations VSK1 and CKWP for which a generic amplification (**Table 5**) of rock site of class "B" was considered, it seems that this amplification satisfactorily contributes to the actual site factor $S_j(f_k)$ estimation at least up to ~8 Hz, assuming that no significant high frequency attenuation affects these sites. Moreover, the agreement between the fundamental frequencies revealed by the $S_j(f_k)$ with those of the HVSRs curves, indicates a satisfactory performance of the new GIT algorithm.
- Seismic source spectra seem to satisfy the Brune's source model (***Brune, 1970***) (Eq. [7]), for the examined earthquake for $M_w \leq 5.2$, with an average RMS = 0.158 (**Figure 32**, **Appendix B**). In addition, the non-parametric approach of earthquake source spectra were *a posteriori* determined as presented in **Appendix M**, based on site and attenuation factors, computed by the GIT algorithm, providing more details of the source spectra. The aforementioned conclusions encourage the reliable computation of moment magnitude even for low moment magnitude earthquakes ($M_w < 4$), which is not easy to be implemented by other routine methods.
- Regarding the estimated stress drop, $\Delta\sigma,$ of the examined earthquakes in western Greece, a low trend of $\Delta\sigma$ increase, is estimated from 5.8 bar to 54.5 bar for M_w range from 2.5 to 5.2, respectively. Moreover, the 85% of these $\Delta\sigma$ have values range between 5.8 to 40 bar, with a geometric mean of 15 bar, indicating thus a low to moderate stress drop seismotectonic regime, dominating the study area at least for low to moderate magnitude earthquakes.

The aforementioned results and especially those related to the attenuation and site factors, can be easily used to directly determine the source spectra of future earthquake in this area, for the frequency range examined in this study (0.3-15.1 Hz), for the 24 specific sites (**Appendix C**). In turn, these source spectra could lead to the estimation of the moment magnitude, M_w, of this earthquake, in near-real time, at least for moment magnitudes, $M_w < 5.2$. Moreover, these parameters can be used to even more reliable seismic hazard assessment in the examined region, by improving the performance of stochastic S-wave simulations when using the point source stochastic method of ***Boore (1983;2003)***, as well as the rational application of EXSIM code, (***Assatourians and Atkinson, 2012***), making direct use of the regional attenuation coefficients, gamma, γ and $Q_s(f)$ (Eq. [7]).

Regarding the GIT algorithm some future steps may be suggested to further improve the investigated model parameters. For seismic sources, it seems reasonable to assume that higher magnitude events, do not follow exactly the Brune's source model, especially for the higher frequency part of their Fourier spectra. For this reason, the investigation of non-parametric seismic source spectrum, as is studied by the non-parametric GIT algorithms (e.g. ***Oth et al., (2009a)***), is suggested. Moreover, the study of anelastic attenuation parameters varying with depth constitutes an important step towards an improvement of the model parameters and inversion misfit reduction.

The second methodology examined in this study (*ch.* 4) is the SFC, introduced by ***Sèbe et al., (2018***) and is used here aiming mainly at the estimation of the Site Amplification Factor, SAF(f) in a target site with respect to a distant reference site. The rational of this SAF(f) estimation method proposed here, is similar to the Standard Spectral Ratio technique (***Borcherdt, 1970***), with relaxation of the reference station requirement close enough to the target one, since the minimum phase scaled Source Time Function ($mpSTF^{sc}$) retrieved by SFC methodology, can be considered as free of path effects. The SFC method is modified here to include the 9 steps STF algorithm, as shown in the flowchart of **Table 6**, by applying several alternative computational approaches.

Regarding the SFC algorithm application for SAF(f) estimation of the 24 sites in western Greece and for the 18 sites in southern France, with respect to four (CKWP, ITC1, VSK1 and AST1) and three (BSTF_00_HH, CA01_21 and OGCA_00_HN) reference stations, respectively, the following conclusions can be extracted:

- At the 8th step of the algorithm flowchart (**Table 6**) the low frequency $FAS[mpSTF^{sc}]$ plateau observed at target sites, could be misleading. That is, the correct computation of the scaled by the mean free path moment magnitude is not always feasible to be achieved. For instance, such a misleading fact is confirmed by the estimated SAF(f) at the CK0 and AGR3, target sites (e.g. **Figure 43** and **Figure 45**), where for the first station, no amplification in low frequencies is observed, while for the second one stable amplification up to 4, contaminates the low frequency $FAS[mpSTF^{sc}]$ plateau. This contamination is not easy to be detected and removed during the low frequency correction since only a flat amplification is apparent. This contamination can lead to an overestimation bias of the apparent mean free path, l, values by including site amplification in lower frequencies, as those shown in **Figure 41**, presenting thus

an apparent high dispersion and lower mean free path, l, for the area of western Greece, compared to the corrected for the "average" SAF(f), l values, presented in **Figure 46** (**Appendix C**), leading to lower scattering of l.

- The average mean free path, l values estimated for the western Greece area after the correction for the "average" SAF(f), is ~283 km (**Figure 46c,d**) ranging mainly from ~88 km to ~727 km (the one standard deviation range) and ~835 km (**Figure 56**), ranging mainly between 186 km and 3750 km (the one standard deviation range), for the southeastern France.
- The SAF(f) estimation technique presented in this study, is based on the "apparent" minimum phase STF computation (in displacement, step 9, flowchart-**Table 6**), for a pair of sites; the reference and the target one. However, the implementation of the STF scaling correction is not always feasible because of the large impact of poorly known parameters, mainly the mean free path l and to a lesser degree the average shear wave velocity, v_s along the propagation path, used for the estimation (Eq. [28]) of the scaling factor, F (step 9, flowchart-**Table 6**, Eq. [37]). This effect can potentially lead to moment magnitude variability σ_{M_w}~0.333 and ~0.045, for the corresponding l and $v_s$variability, which can progressively provide amplitude differences in the finally computed SAF(f) up to ~7 times. However, the results of this study regarding the SFC application, show quite lower discrepancy than this theoretical estimation, related to the next conclusions.
- The SAF(f) estimation can be directly achieved, based on the scaled $FAS[mpSTF^{sc}]$ in velocity (step 6, flowchart-**Table 6**), in both examined sites (reference and target), avoiding the scaling of the $mpSTF^{sc}$ (step 9, flowchart-**Table 6**). The valid and correct SAF(f) estimation based on this step, depend on the precondition of the same scaling factor for the two computed $FAS[mpSTF^{sc}]$, with the SAF(f) being included, which is the first assumption extracted in the Site Amplification Factor estimation section (step 10, flowchart-**Table 6**). To estimate SAF(f)s in this study, the above precondition of the scaling factor similarity can be safely considered for reference-to-target site distances up to ~50-60 km, while it can be considered relatively satisfactory for longer distances, based on an adequate number of SAF(f)s. The SAF(f) results of this study, for 24 sites in western Greece and 16 sites in southern France, were computed with respect to four (CKWP, ITC1, VSK1, AST1) and three (BSTF_00_HH, CA01_21 and OGCA_00_HN), reference stations, respectively. These reference stations are abstaining from each other between 8 and 65 km.
- The computed SAF(f)s of the examined sites in western Greece and southeastern France, with respect to different and distant between each other reference stations, present an increase of their scattering, ranging from 0.12 at short distances up to 0.2 (rms in logarithmic values) for the distant ones, as it is shown in **Figure 44** and **Figure 52** (scattering range around 0.15 for target-reference distance ~55 km).
- The computed SAF(f)s of the examined sites, confirm the third conclusion derived in SAF(f) estimation section, pinpointing that the SAF(f) "shape" is almost stable and independent of the constant scaling factors (mean free path, shear wave velocity) and of the reference-to-target site distance.

- It is worth noting that the estimated average SAF(f) in the frequency range where the amplification is intense, seems to lie close to +1 standard deviation limits of the corresponding SSRs (e.g. CK0 in **Figure 43**, **Figure 45**, **Appendix P** and **Appendix Q**). This observation is in good agreement with those of ***Ito et al., (2020); Margheriti et al., (1994)*** and ***Seekins et al., (1996)***, when comparing SSR−SAF(f) based on direct S-, on coda and on entire duration of records. However, for sites of low amplifications, the computed SAFs seem to be identical to the corresponding SSRs (e.g. CK83 in **Figure 43**, **Figure 45**, **Appendix P** and **Appendix Q**). The latter confirms that the $mpSTF^{sc}$ computed according to the methodology of ***Sèbe et al., (2018)***, based on coda waves, undoubtedly includes site effects. The SAF(f) characterizing the site effects, seems to affect seismic motion through a resonant-type amplification, potentially leading to more cycles and larger amplitudes in time domain (e.g. **Figure 49**), with respect to the level of SAF(f) amplitudes.

Regarding the application potential of the proposed study for estimation of SAF(f), it can be reasonably considered that an average SAF(f) of a site could be used as a "pseudo-reference" site (of known amplification) for another distant site, for which the comparison with a real reference site with no amplification, is not feasible. In such a case the computed "pseudo-reference" standard deviation must be propagated to the SAF(f) of the target site.

Furthermore, it is important to mention that the applicability of the proposed SAF(f) estimation technique is based on the hypothesis of an isotropic source energy radiation pattern. This seems to be true for the earthquakes examined in this study (M_L = 3.2 - 5.4) and it is confirmed by the similar "shape" between the computed SAF(f)s. Probably the seismic sources of these low to moderate magnitude earthquakes, are reasonably represented by a simple pulse wavelet considered by ***Sèbe et al., (2018)*** and the energy radiation can be considered independent of the azimuth. Further research regarding the $FAS[mpSTF]$ computed by the SFC algorithm, based on four moderate-to-large magnitude earthquakes ($M_w \sim 4, 5, 6, 7$) for which STFs were computed by independent methodologies, was carried out. The results of the $FAS[mpSTF]$ of these earthquakes computed for several stations, led to the following conclusions:

- The SFC method can provide encouraging results for the magnitude and the average *STF* duration of the examined earthquake.
- Moreover, it seems that the minimum phase scenario is an appropriate hypothesis for earthquakes with $M_w \sim 4$ and ~5, while it cannot satisfy the real phases (energy release rate) for earthquakes of greater magnitudes, say $M_w > 6$.
- Finally, regarding the source directivity effects, it seems that not clear indication of their existence is observed in the computed $FAS[mpSTF]$, providing rather an average $FAS[mpSTF]$, or the corresponding one close to the minimum STF duration approach. The latter probably represents the convolution of several randomly reflected apparent STFs in the entire region from several azimuths with respect to the source, smoothing thus the azimuthal dependence due to radiation pattern and focal mechanism, according to the generation concept of coda waves. Regarding source directivity effects and azimuthal dependence of the

$FAS[mpSTF]$, certainly further research is needed to clarify their relation, by using an adequate number of records, covering a wide azimuthal source-to-station range and examining a satisfactory number of high magnitude earthquakes.

BIBLIOGRAPHY

Aki, K., 1969. Analysis of the Seismic Coda of Local Earthquakes as Scattered Waves. J. Geophys. Res. 74, 615–631.

Aki, K., 1980a. Scattering and attenuation of shear waves in the lithosphere. J. Geophys. Res. 85, 6496–6504.

Aki, K., 1980b. Attenuation of shear-waves in the lithosphere for frequencies from 0.05 to 25 Hz. Phys. Earth Planet. Inter. 21, 50–60.

Aki, K., Chouet, B., 1975. Origin of coda waves: Source, attenuation, and scattering effects. J. Geophys. Res. 80, 3322–3342.

Aki, K., Richards, P., 2002. Quantitative seismology, 2nd ed. W.H. Freeman and Company, pp. 700.

Anderson, B.Y.J.G., Hough, S.E., 1984. A model for the shape of the Fourier Amplitude Spectrum of accelertion at high frequencies. Bull. Seismol. Soc. Am. 74, 1969–1993.

Andrews, D.J., 1986. Objective determination of source parameters and similarity of earthquakes of different size. Earthq. source Mech. 37, 259–267.

Arias, A., 1970. Measure of Earthquake Intensity. Seism. Des. Nucl. Power Plants 438–483.

Assatourians, K., Atkinson, G., 2012. EXSIM12: a Stochastic Finite- Fault Computer Program in FORTRAN.

Bard, P.-Y., Bouchon, M., 1985. The Two-Dimensional Resonance of Sediment-Filled Valleys. Bull. Seismol. Soc. Am. 75, 519–541.

Bard, P.Y., Gariel, J.C., 1986. Seismic Response of Two-Dimensional Sedimentary Deposits With Large Vertical Velocity Gradients. Bull. Seismol. Soc. Am. 76, 343–366.

Baroux, E., Pino, N.A., Valensise, G., Scotti, O., Cushing, M.E., 2003. Source parameters of the 11 June 1909, Lambesc (Provence, southeastern France) earthquake: A reappraisal based on macroseismic, seismological, and geodetic observations. J. Geophys. Res. Solid Earth 108.

Baskoutas, I., Panapoulou, G., Rontouanni, T., 2000. Seismic attenuation in two geologically distinct regions of central Greece. Boll. di Geofis. Teor. ed Appl. 41, 233–242.

Benetatos, C., Kiratzi, A., Roumelioti, Z., Stavrakakis, G., Drakatos, G., Latoussakis, I., 2005. The 14 August 2003 Lefkada Island (Greece) earthquake: Focal mechanisms of the mainshock and of the aftershock sequence. J. Seismol. 9, 171–190.

Billi, A., Faccenna, C., Bellier, O., Minelli, L., Neri, G., Piromallo, C., Presti, D., Scrocca, D., Serpelloni, E., 2011. Recent tectonic reorganization of the Nubia-Eurasia convergent boundary heading for the closure of the western Mediterranean. Bull. la Soc. Geol. Fr. 182, 279–303.

Bindi, D., Pacor, F., Luzi, L., Massa, M., Ameri, G., 2009. The Mw 6.3, 2009 L'Aquila earthquake: Source, path and site effects from spectral analysis of strong motion data. Geophys. J. Int. 179, 1573–1579.

Boore, D., Boatwright, J., 1984. Average body-wave radiation coefficients. Bull. - Seismol. Soc. Am. 13, 576.

Boore, D.M., 1983. Stochastic simulation of high-frequency ground motions based on seismological models of the radiated spectra. Bull. Seismol. Soc. Am. Soc. Am. 73, 240.

Boore, D.M., 2003. Simulation of ground motion using the stochastic method. Pure Appl. Geophys. 160, 635–676.

Boore, D.M., Joyner, W.B., 1997. Site Amplifications for Generic Rock Sites. Bull. Seismol. Soc. Am. 87, 327–341.

Borcherdt, R., 1970. Effects of Local Geology on Ground Motion Near San Francisco Rbay. Bull. Seismol. Soc. Am. 60, 29–61.

Brune, J.N., 1970. Tectonic stress and the spectra of seismic shear waves from earthquakes. J. Geophys. Res. 75, 4997–5009.

Burton, P.W., Xu, Y., Qin, C., Tselentis, G.A., Sokos, E., 2004. A catalogue of seismicity in Greece and the adjacent areas for the twentieth century. Tectonophysics 390, 117–127.

Burton, P.W., Xu, Y., Tselentis, G.A., Sokos, E., Aspinall, W., 2003. Strong ground acceleration seismic hazard in Greece and neighboring regions. Soil Dyn. Earthq. Eng. 23, 159–181.

Cadet, H., Bard, P.-Y., Rodriguez-Marek, A., 2012. Site effect assessment using KiK-net data: Part 1. A simple correction procedure for surface/downhole spectral ratios. Bull. Earthq. Eng. 10, 421–448.

Castro, R.R., Anderson, J.G., Singh, S.K., 1990. Site response, attenuation and source spectra of S waves along the Guerrero, Mexico subduction zone. Bull. Seismol. Soc. Am. 80, 1481–1503.

Causse, M., Cornou, C., Maufroy, E., Grasso, J.-R., Baillet, L., Haber, E.E., 2021. Exceptional ground motion during the shallow Mw 4.9 2019 Le Teil earthquake, France. Commun. Earth Environ.

Courboulex, F., Dujardin, A., Vallée, M., Delouis, B., Sira, C., Deschamps, A., Honoré, L., Thouvenot, F., 2013. High-frequency directivity effect for an Mw 4.1 earthquake, widely felt by the population in southeastern France. Bull. Seismol. Soc. Am. 103, 3347–3353.

Cushing, E.M., Hollender, F., Moiriat, D., Guyonnet-Benaize, C., Theodoulidis, N., Pons-Branchu, E., Sépulcre, S., Bard, P.Y., Cornou, C., Dechamp, A., Mariscal, A., Roumelioti, Z., 2020. Building a three dimensional model of the active Plio-Quaternary basin of Argostoli (Cephalonia Island, Greece): An integrated geophysical and geological approach. Eng. Geol. 265, 105441.

Danciu, L., Sokos, E., Tselentis, G., 2007. Probabilistic Seismic Hazard Assessment in Terms of Engineering Parameters in Greece. Int. Symp. Seism. risk Reduct. 26–27.

Davatgari, F.T.M., Bora, S.S., Mirzaei, N., Ghofrani, H., Kazemian, J., 2021. Erratum: Spectral models for seismological source parameters, path attenuation and site-effects in Alborz region of northern Iran (Geophysical Journal International DOI: 10.1093/gji/ggab227). Geophys. J. Int. 227, 969.

Dobry, R., Idriss, I., Ng, E., 1978. Duration characteristics of horizontal components of strong-motion earthquake records. Bull. Seismol. Soc. Am. 68, 1487–1520.

Dolan, S.S., Bean, C.J., Riollet, B., 1998. The broad-band fractal nature of heterogeneity in the upper crust from petrophysical logs. Geophys. J. Int. 132, 489–507.

Drouet, S., Assumpção, M., 2013. Spectral analysis of Brazilian data and comparison with ground-motion models. 13th Int. Congr. Brazilian Geophys. Soc. EXPOGEF, Rio Janeiro, Brazil, 26–29 August 2013 1745–1749.

Drouet, S., Bouin, M.P., Cotton, F., 2011. New moment magnitude scale, evidence of stress drop magnitude scaling and stochastic ground motion model for the French West Indies. Geophys. J. Int. 187, 1625–1644.

Drouet, S., Chevrot, S., Cotton, F., Souriau, A., 2008a. Simultaneous inversion of source spectra, attenuation parameters, and site responses: Application to the data of the French accelerometric network. Bull. Seismol. Soc. Am. 98, 198–219.

Drouet, S., Cotton, F., Guéguen, P., 2010. VS30, κ, regional attenuation and Mw from accelerograms: Application to magnitude 3-5 French earthquakes. Geophys. J. Int. 182, 880–

898.

Drouet, S., Triantafyllidis, P., Savvaidis, A., Theodulidis, N., 2008b. Comparison of site-effects estimation methods using the Lefkas, Greece, 2003 earthquake aftershocks. Bull. Seismol. Soc. Am. 98, 2349–2363.

Duverger, C., Mazet-Roux, G., Bollinger, L., Guilhem Trilla, A., Vallage, A., Hernandez, B., Cansi, Y., 2021. A decade of seismicity in metropolitan France (2010-2019): The CEA/LDG methodologies and observations. BSGF - Earth Sci. Bull. 192.

Edwards, B., Rietbrock, A., Bommer, J.J., Baptie, B., 2008. The acquisition of source, path, and site effects from microearthquake recordings using Q tomography: Application to the United Kingdom. Bull. Seismol. Soc. Am. 98, 1915–1935.

Field, E.H., Jacob, K.H., 1995. A comparison and test of various site-response estimation techniques, including three that are not reference-site dependent. Bull. - Seismol. Soc. Am. 85, 1127–1143.

Flerit, F., Armijo, R., King, G., Meyer, B., 2004. The mechanical interaction between the propagating North Anatolian Fault and the back-arc extension in the Aegean. Earth Planet. Sci. Lett. 224, 347–362.

Ganas, A., Serpelloni, E., Drakatos, G., Kolligri, M., Adamis, I., Tsimi, C., Batsi, E., 2009. The Mw 6.4 SW-achaia (Western Greece) earthquake of 8 june 2008: Seismological, field, GPS observations, and stress modeling. J. Earthq. Eng. 13, 1101–1124.

Grendas, I., Hollender, F., Theodoulidis, N., Hatzidimitriou, P., Bard, P.Y., Perron, V., 2021a. Sprectral amplification estimation, based on distant reference station. 6th IASPEI / IAEE Int. Symp. Eff. Surf. Geol. Seism. Motion, August.

Grendas, I., Theodoulidis, N., Bard, P.Y., Perron, V., Hatzidimitriou, P., Hollender, F., 2022. Can site effects be estimated with respect to a distant reference station? Performance of the spectral factorization of coda waves. Geophys. J. Int. 230, 1–28.

Grendas, I., Theodoulidis, N., Hatzidimitriou, P., Margaris, B., Drouet, S., 2018. Determination of source, path and site parameters based on non-linear inversion of accelerometric data in Greece. Bull. Earthq. Eng. 16, 5061–5094.

Grendas, I., Theodoulidis, N., Hollender, F., Hatzidimitriou, P., 2019. Improved Generalized Inversion Technique (GIT) and its implementation to a synthetic dataset , to retrieve seismic source , propagation path and site factors. 15th Int. Congr. Geol. Soc. Greece, Athens, 22-24 May.

Grendas, I., Theodoulidis, N., Hollender, F., Hatzidimitriou, P., 2021b. A GIT algorithm for simultaneous estimation of seismic source, site response and regional-distance dependent attenuation parameters: application to synthetic and real data. J. Seismol. 1–24.

Grendas, I., Theodoulidis, N., Hollender, F., Hatzidimitriou, P., 2021c. Effects of the S-wave time-window selection on Standard Spectral Ratio (SSR): Application to the ARGONET vertical array, Greece. 6th Int. Conf. Earthq. Eng. Seismol.

Gusev, A.A., Abubakirov, I.R., 1996. Simulated envelopes of non-isotropically scattered body waves as compared to observed ones: another manifestation of fractal heterogeneity. Geophys. J. Int. 127, 49–60.

Gutenberg, B., Richter, C.F., 1944. Frequency of earthquakes in California. Bull. Seism. Soc. Am. 34, 185–188.

Haghshenas, E., Bard, P.Y., Theodulidis, N., Atakan, K., Cara, F., Cornou, C., Cultrera, G., Di Giulio, G., Dimitriu, P., Fäh, D., De Franco, R., Marcellini, A., Pagani, M., Rovelli, A., Savvaidis, A., Tento, A., Vidal, S., Zacharopoulos, S., 2008. Empirical evaluation of

microtremor H/V spectral ratio. Bull. Earthq. Eng. 6, 75–108.
Hanks, T.C., Kanamori, H., 1979. A moment magnitude scale. J. Geophys. Res. 84, 2348–2350.
Hartzell, S.H., 1978. Earthquake aftershocks as Green's functions. Geophys. Res. Lett. 1–4.
Hashida, T., Stavrakakis, G., Shimazaki, K., 1988. Three-dimensional seismic attenuation structure beneath the Aegean region and its tectonic implication. Tectonophysics 145, 43–54.
Hatzfeld, D., Kassaras, I., Panagiotopoulos, D., Amorese, D., Makropoulos, K., Karakaisis, G., Coutant, O., 1995. Microseimicity and strain pattern in northwestern Greece. Tectonics 14, 773–785.
Hatzidimitriou, P., 1996. Backward scattering coefficient and attenuation of shear waves in the crust in Northern Greece. In: First Congress of the Balkan Geophysical Society. pp. 36–37.
Hatzidimitriou, P., Papazachos, C., Kiratzi, A., Theodulidis, N., 1993. Estimation of attenuation structure and local earthquake magnitude based on acceleration records in Greece. Tectonophysics 217, 243–253.
Hatzidimitriou, P.M., Papadimitriou, E.E., Mountrakis, D.M., Papazachos, B.C., 1985. The seismic parameter b of the frequency-magnitude relation and its association with the geological zones in the area of Greece. Tectonophysics 120, 141–151.
Herraiz, M., Espinosa, A.F., 1986. Scattering and attenuation of high-frequency seismic waves development of the theory of coda waves. US Geol. Surv. 86–455.
Hollender, F., Cornou, C., Dechamp, A., Oghalaei, K., Renalier, F., Maufroy, E., Burnouf, C., Thomassin, S., Wathelet, M., Bard, P.Y., Boutin, V., Desbordes, C., Douste-Bacqué, I., Foundotos, L., Guyonnet-Benaize, C., Perron, V., Régnier, J., Roullé, A., Langlais, M., Sicilia, D., 2018. Characterization of site conditions (soil class, VS30, velocity profiles) for 33 stations from the French permanent accelerometric network (RAP) using surface-wave methods. Bull. Earthq. Eng. 16, 2337–2365.
Hough, S.E., Seeber, L., Lerner-Lam, A., Armbruster, J.C., Guo, H., 1991. Empirical Green's function analysis of Loma Prieta aftershocks. Bull. Seismol. Soc. Am. 1737–1753.
Imtiaz, A., Cornou, C., Bard, P.Y., Hobiger, M., 2021. Diffracted wavefield decomposition and multidimensional site effects in the Argostoli valley, Greece. Geophys. J. Int. 224, 1849–1869.
Ito, E., Nakano, K., Nagashima, F., Kawase, H., 2020. A method to directly estimate s-wave site amplification factor from horizontal-to-vertical spectral ratio of earthquakes (Ehvsrs). Bull. Seismol. Soc. Am. 110, 2892–2911.
Iwata, T., Irikura, K., 1988. Source parameters of the 1983 Japan sea earthquake sequence. J. Phys. Earth 36, 155–184.
Kagami, H., Duke, C.M., Liang, G.C., Ohta, Y., 1982. Evaluation of site effect upon seismic wave amplification due to extremely deep soil deposits. Bull. - Seismol. Soc. Am. 987–998.
Karakostas, V., Papadimitriou, E., Mesimeri, M., Gkarlaouni, C., Paradisopoulou, P., 2015. The 2014 Kefalonia Doublet (Mw6.1 and Mw6.0), central Ionian Islands, Greece: Seismotectonic implications along the Kefalonia transform fault zone. Acta Geophys. 63, 1–16.
Kassaras, I., Kapetanidis, V., Karakonstantis, A., 2016. On the spatial distribution of seismicity and the 3D tectonic stress field in western Greece. Phys. Chem. Earth 95, 50–72.
Kawase, H., Aki, K., 1989. A study of the response of a soft basin for incident S, P, and Rayleigh waves with special reference to the long duration observed in Mexico City. Bull. - Seismol. Soc. Am. 79, 1361–1382.
Kawase, H., Sánchez-Sesma, F.J., Matsushima, S., 2011. The optimal use of horizontal-to-vertical spectral ratios of earthquake motions for velocity inversions based on diffuse-field theory for

plane waves. Bull. Seismol. Soc. Am. 101, 2001–2014.
Kennett, B.L., Kerry, N.J., 1979. Seismic waves in a stratified half space. Geophys. J. R. Astron. Soc. 57, 557–583.
Kijko, A., 2011. Seismic Hazard. Gupta H.K. Encycl. Solid Earth Geophys. Springer, Dordrecht.
Kiratzi, A.A., 2014. Mechanisms of Earthquakes in Aegean. Encycl. Earthq. Eng. 1–22.
Kishida, T., Ktenidou, O.J., Darragh, R.B., Walter, S., 2016. Semi-automated procedure for windowing time series and computing Fourier amplitude spectra (FAS) for the NGA-West2 database.
Klin, P., Laurenzano, G., Priolo, E., 2018. Gitanes: A Matlab package for estimation of site spectral amplification with the generalized inversion technique. Seismol. Res. Lett. 89, 182–190.
Konno, K., Ohmachi, T., 1998. Ground-motion characteristics estimated from spectral ratio between horizontal and vertical components of microtremor. Bull. Seismol. Soc. Am. 88, 228–241.
Kopnichev, Y.F., 1977. The role of multiple scattering in the formation of seismogram's tail. Izv. Acad. Sci. USSR, Phys. Solid Earth 13, 394–398.
Koutrakis, S.I., Karakaisis, G.F., Hatzidimitriou, P.M., Koliopoulos, P.K., Margaris, V.N., 2002. Seismic hazard in Greece based on different strong gound motion parameters. J. Earthq. Eng. 60, 75–109.
Kovachev, S.A., Kuzin, I.P., Shoda, O.Y., Soloviev, S.L., 1991. Attenuation of S-waves in the lithosphere of the Sea of Crete according to OBS observations. Phys. Earth Planet. Inter. 69, 101–111.
Lacombe, C., Campillo, M., Paul, A., Margerin, L., 2003. Separation of intrinsic absorption and scattering attenuation from Lg coda decay in central France using acoustic radiative transfer theory. Geophys. J. Int. 154, 417–425.
Le Breton, E., Handy, M.R., Molli, G., Ustaszewski, K., 2017. Post-20 Ma Motion of the Adriatic Plate: New Constraints From Surrounding Orogens and Implications for Crust-Mantle Decoupling. Tectonics 36, 3135–3154.
Lekkas, E., Mavroulis, S., Carydis, P., Alexoudi, V., 2018. The 17 November 2015 Mw 6.4 Lefkas (Ionian Sea, Western Greece) Earthquake: Impact on Environment and Buildings, Geotechnical and Geological Engineering. Springer International Publishing.
Lentas, K., Gkarlaouni, C., Kalligeris, N., Melis, N., 2021. The 30 October 2020, Mw 7.0, Samos Earthquake: Aftershock Relocation, Slip Model, Coulomb Stress Evolution and Estimation of Shaking.
Lermo, J., Chavez-Garcia, F.J., 1993. Site effect evaluation using spectral ratios with only one station. Bull. - Seismol. Soc. Am. 83, 1574–1594.
Louvari, E., Kiratzi, A.A., Papazachos, B.C., 1999. The Cephalonia Transform Fault and its extension to western Lefkada Island (Greece). Tectonophysics 308, 223–236.
Makropoulos, K., Kaviris, G., Kouskouna, V., 2012. An updated and extended earthquake catalogue for Greece and adjacent areas since 1900. Nat. Hazards Earth Syst. Sci. 12, 1425–1430.
Makropoulos, K.C., Burton, P.W., 1985. Seismic hazard in Greece. I. Magnitude recurrence. Tectonophysics 117.
Manchuel, K., Traversa, P., Baumont, D., Cara, M., Nayman, E., Durouchoux, C., 2018. The French seismic CATalogue (FCAT-17). Bull. Earthq. Eng. 16, 2227–2251.
Mandal, P., Dutta, U., 2011. Estimation of earthquake source parameters in the Kachchh seismic zone, Gujarat, India, from strong-motion network data using a generalized inversion

technique. Bull. Seismol. Soc. Am. 101, 1719–1731.
Margaris, B., Athanasopoulos, G., Mylonakis, G., Papaioannou, C., Klimis, N., Theodulidis, N., Savvaidis, A., Efthymiadou, V., Stewart, J.P., 2010. The 8 june 2008 Mw6.5 Achaia-Elia, Greece earthquake: Source characteristics, ground motions, and ground failure. Earthq. Spectra 26, 399–424.
Margaris, B., Scordilis, E.M., Stewart, J.P., Boore, D.M., Theodoulidis, N., Kalogeras, I., Melis, N.S., Skarlatoudis, A.A., Klimis, N., Seyhan, E., 2021. Hellenic Strong-Motion Database with Uniformly Assigned Source and Site Metadata for the Period 1972–2015. Seismol. Res. Lett.
Margaris, B.N., Boore, D.M., 1998. Determination of Δσ and κο from response spectra of large earthquakes in Greece. Bull. Seismol. Soc. Am. 88, 170–182.
Margaris, B.N., Hatzidimitriou, P.M., 2002. Source spectral scaling and stress release estimates using strong-motion records in Greece. Bull. Seismol. Soc. Am. 92, 1040–1059.
Margerin, L., Campillo, M., Shapiro, N.M., Van Tiggelen, B., 1999. Residence time of diffuse waves in the crust as a physical interpretation of coda Q: Application to seismograms recorded in Mexico. Geophys. J. Int. 138, 343–352.
Margheriti, L., Wennerberg, L., Boatwright, J., 1994. A comparison of coda and S-wave spectral ratios as estimates of site response in the southern San Francisco Bay area. Bull. - Seismol. Soc. Am. 84, 1815–1830.
Margrave, G.F., 1998. Theory of nonstationary linear filtering in the Fourier domain with application to time-variant filtering. Geophysics 63, 244–259.
Margrave, G.F., Lamoureux, M.P., Henley, D.C., 2011. Gabor deconvolution: Estimating reflectivity by nonstationary deconvolution of seismic data. Geophysics 76, W15–W30.
MATLAB, 2017. The MathWorks, Inc., Natick, Massachusetts, United States.
Melis, N.S., Brooks, M., Pearce, R.G., 1989. A microearthquake study in the Gulf of Patras region, western Greece, and its seismotectonic interpretation. Geophys. J. Int. 98, 515–524.
Milana, G., Barba, S., Del Pezzo, E., Zambonelli, E., 1996. Site response from ambient noise measurements: new perspectives from an array study in Central Italy. Bull. Seismol. Soc. Am. 320–328.
Mueller, C.S., 1985. Source pulse enhancement by deconvolution of an empirical Green's function. Geophys. Res. Lett. 33–36.
Nakamura, Y., 1989. A method for Dynamic Characteristics Estimation of Subsurface using Microtremor on the Ground Surface. Railw. Tech. Res. Institute, Q. Reports.
Nakano, K., Matsushima, S., Kawase, H., 2015. Statistical properties of strong ground motions from the generalized spectral inversion of data observed by K-NET, KiK-net, and the JMA Shindokei network in Japan. Bull. Seismol. Soc. Am. 105, 2662–2680.
Nocquet, J.M., Calais, E., 2004. Geodetic measurements of crustal deformation in the Western Mediterranean and Europe. Pure Appl. Geophys. 161, 661–681.
Oppenheim, A. V., Ronald, W.S., 1975. Digital Signal Processing. In: Prentice-Hall. Englewood Cliffs, New Jersey.
Ortiz-Alemán, C., Reyes-Olvera, M., Iglesias-Mendoza, A., Orozco-Del-Castillo, M.G., Hernández-Gómez, J.J., 2017. Estimation of source; path and site effects at MASE array stations: A comprehensive study. Geofis. Int.
Oth, A., Parolai, S., Bindi, D., Wenzel, F., 2009. Source spectra and site response from S waves of intermediate-depth Vrancea, Romania, earthquakes. Bull. Seismol. Soc. Am. 99, 235–254.
Papaioannou, C.A., Papazachos, B.C., 2000. Time-independent and time-dependent seismic

hazard in Greece based on seismogenic sources. Bull. Seismol. Soc. Am. 90, 22–33.

Papanikolaou, D.J., Royden, L.H., 2007. Disruption of the Hellenic arc: Late Miocene extensional detachment faults and steep Pliocene-Quaternary normal faults - Or what happened at Corinth? Tectonics 26, 1–16.

Papazachos, B., Papazachou, C., 1997. The earthquakes of Greece, Ziti. ed. Thessaloniki.

Papazachos, B.C., 1990. Seismicity of the Aegean and surrounding area. Tectonophysics 178, 287–308.

Papazachos, B.C., Comninakis, P.E., Karakaisis, G.F., Karakostas, B.G., Papaioannou, C.A., Papazachos, C.B., Scordilis, E.M., 2000. A catalogue of earthquakes in Greece and surrounding area for the period 550BC-1999. Publ. Geoph. Lab., Univ. of Thessaloniki.

Papazachos, B.C., Papadimitriou, E.E., Kiratzi, A.A., Papazachos, C.B., Louvari, E.K., 1998. Fault plane solutions in the Aegean Sea and the surrounding area and their tectonic implication. Boll. Geof. teor. appl, 39, 199–218.

Papazachos, B.C., Papaioannou, C.A., Margaris, B.N., Theodulidis, N.P., 1993. Regionalization of seismic hazard in Greece based on seismic sources. Nat. Hazards 8, 1–18.

Papazachos, B.C., Papaioannou, C.A., Papazachos, C.B., Savvaidis, A.S., 1999. Rupture zones in the Aegean region. Tectonophysics 308, 205–221.

Papazachos, C., 1999. An Alternative Method for a Reliable Estimation of Seismicity with an Application in Greece and the Surrounding Area. Bull. Seismol. Soc. Am. 89, 111–119.

Papazachos, C., Kiratzi, A., 1996. A detailed study of the active crustal deformation in the Aegean and surrounding area. Tectonophysics 253, 129–153.

Papazachos, C.B., 1992. Anisotropic radiation modelling of macroseismic intensities for estimation of the attenuation structure of the upper crust in Greece. Pure Appl. Geophys. 138, 445–469.

Papoulia, J., Nicolich, R., Makris, J., Slejko, D., Mascle, J., Papadopoulos, G., Anagnostou, C.H., Camera, L., Daskalaki, E., Fasoulaka, C.H., Fokaefs, A., Fountoulis, I., Garcia, J., Gülkan, P., Mariolakos, I., Pomonis, A., Santulin, M., Tsambas, A., Wardell, N., Yalçiner, A., 2014. A new seismogenic model for the Kyparissiakos Gulf and western Peloponnese (SW Hellenic Arc). Boll. di Geofis. Teor. ed Appl. 55, 405–432.

Pérouse, E., Sébrier, M., Braucher, R., Chamot-Rooke, N., Bourlès, D., Briole, P., Sorel, D., Dimitrov, D., Arsenikos, S., 2017. Transition from collision to subduction in Western Greece: the Katouna–Stamna active fault system and regional kinematics. Int. J. Earth Sci.

Perron, V., Gélis, C., Froment, B., Hollender, F., Bard, P.Y., Cultrera, G., Cushing, E.M., 2018a. Can broad-band earthquake site responses be predicted by the ambient noise spectral ratio? Insight from observations at two sedimentary basins. Geophys. J. Int. 215, 1442–1454.

Perron, V., Laurendeau, A., Hollender, F., Bard, P.Y., Gélis, C., Traversa, P., Drouet, S., 2018b. Selecting time windows of seismic phases and noise for engineering seismology applications: a versatile methodology and algorithm. Bull. Earthq. Eng. 16, 2211–2225.

Polatidis, A., Kiratzi, A., Hatzidimitriou, P., Margaris, B., 2003. Attenuation of shear-waves in the back-arc region of the Hellenic arc for frequencies from 0.6 to 16 Hz. Tectonophysics 367, 29–40.

Rautian, T.G., Khalturin, V.I., 1978. The use of the coda for determination of the earthquake source spectrum. Bull. Seismol. Soc. Am. 68, 923–948.

Régnier, J., Laurendeau, A., Duval, A.-M., 2010. From heterogeneous set of soil data to Vs profile : Application on the French permanent accelerometric network (RAP) sites. 14th Eur. Conf. Earthq. Eng. Ohrid, Repub. Maced. 30 August-3 Sept. 2010.

Ritz, J., Baize, S., Delouis, B., Mathot, E., Larroque, C., Audin, L., Al, M.C., 2019. Surface rupture and shallow fault reactivation during the 2019 Mw 4.9 Le Teil earthquake, France. Commun. Earth Environ. 1–12.

Sachpazi, M., Hirn, A., Clément, C., Haslinger, F., Laigle, M., Kissling, E., Charvis, P., Hello, Y., Lépine, J.C., Sapin, M., Ansorge, J., 2000. Western Hellenic subduction and Cephalonia Transform: Local earthquakes and plate transport and strain. Tectonophysics 319, 301–319.

Sánchez-Sesma, F.J., Pérez-Ruiz, J.A., Luzón, F., Campillo, M., Rodríguez-Castellanos, A., 2008. Diffuse fields in dynamic elasticity. Wave Motion 45, 641–654.

Sato, H., 1977. Energy propagation including scattering effects single isotropic scattering approximation. J. Phys. Earth 25, 27–41.

Sato, H., 1978. Mean free path of S-waves under the Kanto district of Japan. J. Phys. Earth 26, 185–198.

Sato, H., 1982. Attenuation of S waves in the lithosphere due to scattering by its random velocity structure. J. Geophys. Res. Solid Earth 87, 7779–7785.

Sato, H., Fehler, M.C., Maeda, T., 2012. Seismic wave propagation and scattering in the heterogeneous earth, Vol. (496). ed. Springer, Berlin.

Scordilis, E.M., Karakaisis, G.F., Karacostas, B.G., Panagiotopoulos, D.G., Comninakis, P.E., Papazachos, B.C., 1985. Evidence for transform faulting in the Ionian sea: The Cephalonia island earthquake sequence of 1983. Pure Appl. Geophys. PAGEOPH 123, 388–397.

Scordilis, E.M., Kementzetzidou, D., Papazachos, B.C., 2016. Local magnitude calibration of the Hellenic Unified Seismic Network. J. Seismol. 20, 319–332.

Sèbe, O., Bard, P.-Y., Guilbert, J., 2005. Single station estimation of seismic source time function from coda waves: The Kursk disaster. Geophys. Res. Lett. 32, 1–4.

Sèbe, O., Guilbert, J., Bard, P.-Y., 2014. Estimation des effets de site par factorisation spectrale du signal de coda (Spectral factorization of seismic site effect from coda waves). Spec. issue "Hazard Geosci. 1157–741X, 37–42.

Sèbe, O., Guilbert, J., Bard, P.-Y., 2018. Spectral factorization of the source time function of an earthquake from coda waves, application to the 2003 rambervillers, France, earthquake. Bull. Seismol. Soc. Am. 108, 2521–2542.

Seekins, L.C., Wennerberg, L., Margheriti, L., Liu, H.P., 1996. Site amplification at five locations in San Francisco, California: A comparison of S waves, codas, and microtremors. Bull. Seismol. Soc. Am. 86, 627–635.

Singh, S., Herrmann, R.B., 1983. Regionalization of crustal coda Q in the continental United States. J. Geophys. Res. Solid Earth 88, 527–538.

Soham, B., Abhishek, K., 2016. Determination of seismic wave attenuation: A Review. Disaster Adv. 9.

Sokos, E., Gallovič, F., Evangelidis, C., Serpetsidaki, A., Plicka, V., Kostelecký, J., Zahradník, J., 2020. The 2018 Mw 6.8 Zakynthos, Greece, Earthquake : Dominant Strike-Slip Faulting near Subducting Slab. Seismol. Res. Lett. 91, 721–732.

Sokos, E., Kiratzi, A., Gallovič, F., Zahradník, J., Serpetsidaki, A., Plicka, V., Janský, J., Kostelecký, J., Tselentis, G.A., 2015. Rupture process of the 2014 Cephalonia, Greece, earthquake doublet (Mw6) as inferred from regional and local seismic data. Tectonophysics 656, 131–141.

Sokos, E., Zahradník, J., Gallovič, F., Serpetsidaki, A., Plicka, V., Kiratzi, A., 2016. Asperity break after 12years: The Mw6.4 2015 Lefkada (Greece) earthquake. Geophys. Res. Lett. 1–8.

Stavrakakis, G.N., Drakopoulos, J., 1995. Bayesian probabilities of earthquake occurrences in

Greece and surrounding areas. Pure Appl. Geophys. PAGEOPH 144, 307–319.
Steidl, J.H., Tumarkin, A.G., Archuleta, R.J., 1996. What is a reference? Bull. Seismol. Soc. Am. 86, 1743–1748.
Svigkas, N., Atzori, S., Kiratzi, A., Tolomei, C., Antonioli, A., Papoutsis, I., Salvi, S., Kontoes, C., 2019. On the segmentation of the Cephalonia-Lefkada Transform Fault Zone (Greece) from an InSAR multi-mode dataset of the Lefkada 2015 sequence. Remote Sens. 11.
Svigkas, N., Kiratzi, A., Antonioli, A., Atzori, S., Tolomei, C., Salvi, S., Polcari, M., Bignami, C., 2021. Earthquake source investigation of the kanallaki, march 2020 sequence (north-western greece) based on seismic and geodetic data. Remote Sens. 13, 1–16.
Tarantola, A., 2005. Inverse problem theory and methods for model parameter estimation. Soc. Ind. Appl. Math. 343.
Theodoulidis, N., Hollender, F., Mariscal, A., Moiriat, D., Bard, P.Y., Konidaris, A., Cushing, M., Konstantinidou, K., Roumelioti, Z., 2018. The ARGONET (Greece) seismic observatory: An accelerometric vertical array and its data. Seismol. Res. Lett. 89, 1555–1565.
Theodoulidis, N., Karakostas, C., Lekidis, V., Makra, K., Margaris, B., Morfidis, K., Papaioannou, C., Rovithis, E., Salonikios, T., Savvaidis, A., 2016. The Cephalonia, Greece, January 26 (M6.1) and February 3, 2014 (M6.0) earthquakes: near-fault ground motion and effects on soil and structures. Bull. Earthq. Eng. 14, 1–38.
Theodulidis, N., Bard, P.Y., Archuleta, R., Bouchon, M., 1996. Horizontal-to-vertical spectral ratio and geological conditions: The case of Garner Valley Downhole Array in southern California. Bull. Seismol. Soc. Am. 86, 306–319.
Theodulidis, N.P., Bard, P.Y., 1995. Horizontal to vertical spectral ratio and geological conditions: an analysis of strong motion data from Greece and Taiwan (SMART-1). Soil Dyn. Earthq. Eng. 14, 177–197.
Traversa, P., Maufroy, E., Hollender, F., Perron, V., Bremaud, V., Shible, H., Drouet, S., Guéguen, P., Langlais, M., Wolyniec, D., Péquegnat, C., Douste-Bacque, I., 2020. RESIF RAP and RLBP Dataset of earthquake ground motion in Mainland France. Seismol. Res. Lett. 91, 2409–2424.
Tselentis, G.A., 1998. Intrinsic and scattering seismic attenuation in W. Greece. Pure Appl. Geophys. 153, 703–712.
Tselentis, G.A., Danciu, L., Sokos, E., 2010. Probabilistic seismic hazard assessment in Greece - Part 2: Acceleration response spectra and elastic input energy spectra. Nat. Hazards Earth Syst. Sci. 10, 41–49.
Tselentis, G.A., Sokos, E., Martakis, N., Serpetsidaki, A., 2006. Seismicity and seismotectonics in Epirus, western Greece: Results from a microearthquake survey. Bull. Seismol. Soc. Am. 96, 1706–1717.
Vallée, M., 2004. Stabilizing the empirical Green function analysis: Development of the projected Landweber method. Bull. Seism. Soc. Am. 94, 394–409.
Vamvakaris, D.A., Papazachos, C.B., Papaioannou, C.A., Scordilis, E.M., Karakaisis, G.F., 2016a. A detailed seismic zonation model for shallow earthquakes in the broader Aegean area. Nat. Hazards Earth Syst. Sci. 16, 55–84.
Vamvakaris, D.A., Papazachos, C.B., Papaioannou, C.A., Scordilis, E.M., Karakaisis, G.F., 2016b. Seismic hazard assessment in the broader aegean area using time-independent seismicity models based on synthetic earthquake catalogs. Bull. Geol. Soc. Greece 50, 1463–1472.
Vassiliou, M.S., Kanamori, H., 1982. The energy release in earthquakes. Bull. Seismol. Soc. Am.

72, 371–387.
Weaver, R. l., 1982. On diffuse waves in solid media. Accoustical Soc. Am. 71, 1608–1609.
Weinstein, C.J., 1979. Programs for Digital Signal Processing. In: IEEE Press. New York.
Wessel, P., Smith, W.H.F., 1998. New, improved version of generic mapping tools released. Eos, Trans. Am. Geophys. Union 79, 579–579.
Γρένδας, Ι., Suroyo, P., Θεοδουλίδης, Ν., Hollender, F., Bard, P.-Y., Perron, V., Χατζηδημητρίου, Π., 2019. Εκτίμηση Επίδρασης Τοπικών Εδαφικών Συνθηκών με Ανάλυση Κυμάτων Ουράς Σεισμικών Καταγραφών. Πανελλήνιο Συνέδριο Αντισεισμικής Μηχανικής και Τεχνικής Σεισμολογίας, Αθήνα, 5-7 Σεπτεμβρίου, ΕΤΑΜ/ΤΕΕ.

APPENDICES

Appendix A. The pre-inversion process, corresponding to the new developed in this study (*ch.* 3) GIT algorithm and constitutes a necessary *a priori* application for the implementation of the algorithm.

The main concept of this pre-inversion process is to geometrically separate a seismic wave ray path, at a uniform attenuation area model (one anelastic attenuation factor) (**Figure 11a**), into ***n*** parts passing through ***n*** individual areas (cells) (***n*** anelastic attenuation factors). The ***n*** cells are shaped by the specific Meridians and Parallels (e.g. **Figure 11b**). This process uses the ray path based on its surface projection corresponding to the epicentral distance and is analyzed below at **Step 1**. At **Step 2,** the *a* posteriori connection of the epicentral distance to the hypocentral distance and the ray path is also analyzed in details.

Step 1

The detection of the partial ray paths that compose a ray path crossing each cell (e.g. **Figure 11b**) is simply based on the detection of the intersection points of the given surface ray path with the specific Parallels and Meridians (e.g. in **Figure 11b** four Meridians at: 20.35ºE 20.46ºE, 20.6ºE, 20.75º E longitudes and four Parallels at: 38.07ºN, 38.15ºN, 38.2ºN, 38.33º N are depicted). After the detection of these points, it is feasible to calculate the partial epicentral distances using open access formulas. In order to find these intersection points, the cross section between the Reference Ellipsoid Surface (the closest functional approach to the Earth's ellipsoid surface) and the plane defined by the earthquake source point, the station point and the central point of the reference Ellipsoid, has to be firstly defined. This cross section corresponds to a "great" cycle upon a sphere and the distance between the earthquake epicenter and the station location, on the Reference Ellipsoid surface actually consists the shortest distance between them.

The ellipsoid equation at a Cartesian coordinate system is defined by the equation:

$$\left(\frac{x^2}{{r_x}^2}\right) + \left(\frac{y^2}{{r_y}^2}\right) + \left(\frac{z^2}{{r_z}^2}\right) = 1, \qquad \text{Eq. [A1]}$$

where for the ***Reference Ellipsoid***: $r_x = r_y$ = 6378.1370 km, r_z = 6356.7523 km (***WGS84***). The parametric form of a biaxial ellipsoid, in terms of geographical coordinates, is given by:

$$x = V \cdot \cos(\varphi) \cdot \cos(\lambda), \qquad \text{Eq. [A2]}$$
$$y = V \cdot \cos(\varphi) \cdot \sin(\lambda), \qquad \text{Eq. [A3]}$$
$$z = V \cdot (1-e_x^2) \cdot \sin(\varphi), \qquad \text{Eq. [A4]}$$

where φ is the geographic latitude ($-\pi/2 \le \varphi \le \pi/2$), λ is the geographic longitude, ($-\pi \le \lambda \le \pi$), and V is given by the following equation:

$$V = r_x/\sqrt{1 - e_x^2 \cdot sin^2(\varphi)} \qquad \text{Eq. [A5]}$$

where:

$$e_x^2 = (r_x^2 - r_z^2)/r_x^2 \qquad \text{Eq. [A6]}$$

The plane formed by the earthquake epicenter point **A(x_a,y_a.z_a)**, station (surface) point **B(x_b,y_b.z_b)** and the central point of the reference ellipsoid, the zero point **O(*0,0,0*)**, is by definition perpendicular to the vector defined by the cross product:

$$\overrightarrow{OA} \times \overrightarrow{OB} = \vec{\boldsymbol{i}} \cdot (y_a \cdot z_b - z_a \cdot y_b) - \vec{\boldsymbol{j}} \cdot (x_a \cdot z_b - z_a \cdot x_b) - \vec{\boldsymbol{k}} \cdot (y_a \cdot x_b - x_a \cdot y_b) \qquad \text{Eq. [A7]}$$

where: $\vec{\boldsymbol{i}}$, $\vec{\boldsymbol{j}}$, $\vec{\boldsymbol{k}}$ are the unit vectors parallel to the *x, y*, *z* Cartesian coordinate system axes. The equation of this plane is given by equation:

$$\omega_1 \cdot x - \omega_2 \cdot y + \omega_3 \cdot z = 0 \qquad \text{Eq. [A8]}$$

where $\boldsymbol{\omega_1} = y_a \cdot z_b - z_a \cdot y_b$, $\boldsymbol{\omega_2} = x_a \cdot z_b - z_a \cdot x_b$, $\boldsymbol{\omega_3} = x_a \cdot y_b - y_a \cdot x_b$

Based on Eq. [A1] and [A8] the cross section between the Reference Ellipsoid surface and the plane formed by A, B and O points is mathematically represented by the geometric trace defined by the two following equations:

$$\left(\frac{1}{{r_x}^2} + \frac{{\omega_1}^2}{{r_z}^2 \cdot {\omega_3}^2}\right) \cdot x^2 - \left(\frac{2\,\omega_1\omega_2}{{r_z}^2 \cdot {\omega_3}^2}\right) x \cdot y + \left(\frac{1}{{r_x}^2} + \frac{{\omega_2}^2}{{r_z}^2 \cdot {\omega_3}^2}\right) \cdot y^2 = 1, \quad \omega_3 \neq 0 \qquad \text{Eq. [A9]}$$

$$z = \left({}^{1}/_{\omega_3}\right) \cdot (\omega_2 \cdot y - \omega_1 \cdot x), \;\; \omega_3 \neq 0 \qquad \text{Eq. [A10]}$$

The intersection points that are needed for the partial epicentral distances computations, lie on this geometric trace. In the specific case where $\boldsymbol{\omega_3 = 0}$ the vertical component, z of the cross product $\overrightarrow{OA} \times \overrightarrow{OB}$ is zero. Consequently, the plane formed by the A, B and O points is a plane vertical to the Parallels or in other words is a plane that certainly passes through a Meridian (and its antipode). Therefore, the intersection points of the above geometrical trace (where the ray path lies) with a specific Meridian are either infinite (in case where is collinear to the specific Meridian), or there are only two intersection points, the two Earth's poles. In this case where A and B points, (Earthquake and Station, respectively) are the Reference Ellipsoid poles with $z_a \neq z_b$, and $x_a = x_b = y_a = y_b = 0$ ($\omega_3 = 0$), there are no intersection points with any Meridian between earthquake and station points. In this case ($\boldsymbol{\omega_3 = 0}$) the ray path can intersect only the examined Parallels, if these are between the Earthquake and Station.

Based on Eq. [A2], [A3], [A4], [A5], [A9] and [A10] for the given Meridians and Parallels (specific longitudes and latitudes, respectively), the intersection points of the ray paths with the Meridians and Parallels can easily be found as it is detailed analyzed below:

Case 1: Obtaining the intersection point of a ray path with a specific Parallel.

A specific Parallel is characterized by one specific Latitude value, $\varphi_{\mathbf{PRL}}$. The intersection point that we are looking for, has the latitude of the specific Parallel crossed by the ray path and longitude calculated as explained below, based on Eq. [A9] and [A10]. Using the specific Latitude of the specific Parallel (here $\varphi_{\mathbf{PRL}}$) at Eq. [A10] and based on Eq. [A2], [A3] and [A4], it is obtained:

$$\omega_1 \cdot \cos(\lambda) = \frac{[\omega_2 \cdot \cos(\varphi_{\mathbf{PRL}}) \cdot \sin(\lambda)] - [\omega_3 \cdot \sin(\varphi_{\mathbf{PRL}}) \cdot (1 - e_x^2)]}{\cos(\varphi_{\mathbf{PRL}})}, \qquad \text{Eq. [A11]}$$

$$(\varphi_{\mathbf{PRL}} \neq \pm \pi/2)$$

It is obvious that the value of φ = ± π/2 cannot be used in order to separate the attenuation area.

From Eq. [A9] and using Eq. [A2], [A3] and [A6] the following equation is obtained:

$$[cos^2(\lambda) \cdot E + sin^2(\lambda) \cdot F - cos(\lambda) \cdot sin(\lambda) \cdot G] - 1 = 0 \qquad \text{Eq. [A12]}$$

where:

$$\boldsymbol{E} = H^2 \cdot cos^2(\varphi_{\mathbf{PRL}}) \cdot \left(1 + \frac{{\omega_1}^2 \cdot r_x^2}{{r_z}^2 \cdot {\omega_3}^2}\right)$$

$$\boldsymbol{F} = H^2 \cdot cos^2(\varphi_{\mathbf{PRL}}) \cdot \left(1 + \frac{{\omega_2}^2 \cdot r_x^2}{{r_z}^2 \cdot {\omega_3}^2}\right)$$

$$\boldsymbol{G} = H^2 \cdot \frac{cos^2(\varphi_{\mathbf{PRL}}) \cdot 2 \cdot \omega_1 \cdot \omega_2 \cdot {r_x}^2}{{r_z}^2 \cdot {\omega_3}^2}$$

and: $H^2 = [1 - e_x^2 \cdot sin^2(\varphi_{\mathbf{PRL}})]^{-1}$

Based on the trigonometric identity: $\cos^2\lambda = 1 - \sin^2\lambda$, and on Eq. [A11], Eq. [A12] can be written as:

$$sin^2(\lambda) \cdot \left[F - E - \frac{\mathrm{G} \cdot \omega_2}{\omega_1}\right] +$$

$$+ sin(\lambda) \cdot \left[\frac{G \cdot \omega_3 \cdot sin(\varphi_{\mathbf{PRL}}) \cdot (1 - e_x^2)}{\omega_1 \cdot cos(\varphi_{\mathbf{PRL}})}\right] + \qquad \text{Eq. [A13]}$$

$$+ (E - 1) = 0, \quad (\varphi_{\mathbf{PRL}} \neq \pm \pi/2)$$

which is a simple second-degree polynomial equation, where ***sin(λ)*** is the unknown since the other factors are known.

In case where the geometric trace defined by Eq. [A9] and [A10] is not collinear or parallel with the specific examined parallel, the intersection points according to Eq. [A13] are two points as it is normally expected. However, the ray path which lies on the "ring" formed by Eq. [A9] and

[A10] and is considered as the shortest distance between Earthquake and Station points and can intersect only once the parallel, if only the latitude of the parallel is between the Earthquake and Station latitudes. The process of finally recognizing the required $\boldsymbol{\lambda}$ of intersection point (in case that the studied parallel is between Earthquake and Station points) is affected by the "human" convention of the Earth Meridians relative to Greenwich Meridian that take values between -180º and 180º. Thus, an extra a posteriori process for estimating the required $\boldsymbol{\lambda}$ is presented directly below.

The longitude of the unique intersection point (if there is one) among the ray path and the specific parallel can be obtained, as it has already analyzed above, by the solution of Eq. [A13]. Because of the particular condition of the range in degrees of the Earth Meridians (-180º to 180º), in combination with the basic properties of the sine: $-1 \le \sin(\lambda) \le 1 \Leftrightarrow -90^o \le \lambda \le 90^o$, the other cases have to be examined, i.e. $-180^o \le \lambda < -90^o$ and $90^o < \lambda \le 180^o$. More specific, after the two solutions: $\lambda_{1,2} = \arcsin(\sin(\lambda)_{1,2})$ of the two $\sin(\lambda)_{1,2}$ unknowns from Eq. [A13], we have to consider the antipodal longitudes of these two $\lambda_{1,2}$ on the Earth's coordinate system (e.g. if $\lambda = 20^o$ the antipodal longitude is $\lambda = 20^o - 180^o = -160^o$ and if $\lambda = -20^o$ the antipodal longitude is $\lambda = 180^o - 20^o = 160^o$). Thus, instead of two λ, four λ values must finally be examined that cover all the possible cases for the intersection points. The point which is the unique intersection point of the ray path with the specific parallel (which exists only in case where the studied parallel is between Earthquake and Station points) is the one where the sum of the epicentral distances between Earthquake – intersection point and intersection point-Station, is the shortest.

Case 2: Obtaining the intersection point of a ray path with a specific meridian.

A specific meridian in the area under study is characterized by a specific longitude value, $\boldsymbol{\lambda_{PRL}}$. The intersection point, that we are looking for, has the longitude of this specific meridian and latitude calculated as is explained below based on Eq. [A9 and A10]. Using this given specific longitude ($\boldsymbol{\lambda_{PRL}}$ in Eq. [A10] and based on Eq. [A2], [A3], [A4], as well as taking into account that $r_x = r_y$ (*Reference Ellipsoid, **WGS84***), the following equation is obtained:

$$\begin{aligned} &cos^2(\varphi) \cdot H^2 \cdot cos^2(\boldsymbol{\lambda_{PRL}}) \cdot \left(1 + \frac{{\omega_1}^2 \cdot r_x^2}{{r_z}^2 \cdot {\omega_3}^2}\right) + \\ &+ cos^2(\varphi) \cdot H^2 \cdot sin^2(\boldsymbol{\lambda_{PRL}}) \cdot \left(1 + \frac{{\omega_2}^2 \cdot r_x^2}{{r_z}^2 \cdot {\omega_3}^2}\right) - \\ &- cos^2(\varphi) \cdot H^2 \cdot \frac{sin(\lambda_{\mathbf{PRL}}) \cdot cos(\lambda_{\mathbf{PRL}}) \cdot 2 \cdot \omega_1 \cdot \omega_2 \cdot {r_x}^2}{{r_z}^2 \cdot {\omega_3}^2} - 1 = 0 \end{aligned} \qquad \text{Eq. [A14]}$$

After computations and taking into account the trigonometric identity $\cos^2\lambda = 1 - \sin^2\lambda$, Eq. [A14] can be written as:

$$cos^2(\varphi) \cdot \left[\frac{{r_x}^2 \cdot [\omega_1 \cdot \cos(\boldsymbol{\lambda_{PRL}}) - \omega_2 \cdot \sin(\boldsymbol{\lambda_{PRL}})]^2}{{r_z}^2 \cdot {\omega_3}^2} - e_x^2\right] + e_x^2 - 1 = 0 \qquad \text{Eq. [A15]}$$

which is also a simple second-degree polynomial equation, where ***cos(φ)*** is the unknown.

There are two intersection points of the geometric trace given by Eq. [A9], [A10] with the meridian and they can be found by Eq. [A15] for the known earthquake and station points (Eq. [6]), as well as for the known longitude value of the specific meridian, $\boldsymbol{\lambda_{PRL}}$. However, the ray path which is the shortest distance between the earthquake and station along the line expressed by Eq. [A9] and [A10], can intersect only once the meridian, if only the longitude of the meridian lies between the earthquake and station longitudes. Eq. [A15] has a simple second-degree polynomial form and the two solutions are a double root solution of φ: $\varphi_1 = arc(+\cos(\varphi))$ and $\varphi_2 = arc(-\cos(\varphi))$. Taking into account that the calculated, φ = arc(cosφ), is positive ($-1 \leq \cos(\varphi) \leq 1 \Leftrightarrow 0^o \leq \varphi \leq 180^o$) and the cosine property $cos(\varphi) = cos(-\varphi)$, we must consider, and we have to examine four solution ($\pm\varphi_1$ and $\pm\varphi_2$). instead of two (φ_1 and φ_2), However, because the Earth's parallel range in degrees is between -90° and 90° we have to reduce the values that are out (φ < -90° and φ > 90°) of the range of the Earth's parallels to the corresponding values in the range -90° and 90°. Thus, for example: if $\varphi_1 = 80^o$ and $\varphi_2 = 100^o$, we will also examine the values -80°, -100° and in the Earth's parallels coordinate system, which is a closed cycle, the value of 100° parallel can be considered as the continuation after the maximum value of +90° and corresponds again to the same parallel of +80°. The same can be considered for -100°. Thus, from the four solutions we conclude at two that are in the parallel range (≥-90° and ≤90°). Finally, among these two φ values the one of the intersection points (if there is) is the value that lies between the earthquake and station latitude.

Step 2

The intersection points calculated in **Step 1,** according to Eq. [A13 and A15] and the procedures mentioned above, are useful for the estimation of the epicentral distances but not for the hypocentral distances. It's worth to note that for far-filed crustal earthquakes epicentral distances are usually used and a common accepted way of hypocentral distance computation is based on the following simple formula:

$$R_{hyp} = \sqrt{{R_{epic}}^2 + depth^2} \qquad \text{Eq. [A16]}$$

using the earthquake depth and considering also that epicentral distance is a straight line (**Figure A 1**).

Following these conditions, it is feasible to calculate the part of the hypocentral distances (**Figure A 1b**) that correspond to the same part of the epicentral distance (e.g. **Figure 11b**), which are indirectly computed through the intersection point detection (**Appendix A**, **Step 1**), crossing the initial given attenuation model space. Thus, for the straight lines BC and AC and taking into account that AB, DE, FG are parallel to each other it is concluded (similar triangles) that the ratios of the various lines segments BD, DF FC, BF, DC over along BC are proportional to the ratios of the various lines segments AE, EG, GC, AG, EC along AC. DE is parallel to FG in the case that parallels are examined, while in case where meridians are examined we can accept that DE is parallel to FG for shallow earthquake depths which in any case are much smaller than the Earth's

radius. Hypocentral distance between earthquake and station (e.g. AC at **Figure A 1b**) is conventionally calculated by Eq. [A16) as it is mentioned above, for the known epicentral distance BC and depth AB. Following the procedure just mentioned, it is easy to calculate any possible part of the hypocentral distance crossing a specific attenuation area for a 2-D attenuation model non-varied with depth.

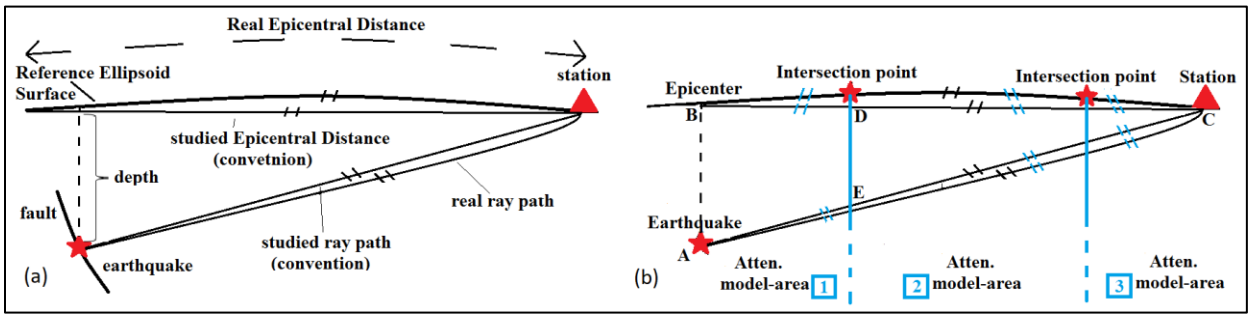

Figure A 1. (**a**) A sketch of Earth's cross section with depth that depicts, in a simple way, the earthquake point (red asterisk), the station (red triangle), a part of the Reference Ellipsoid surface and the real epicentral-hypocentral distances, as well as the commonly used epicentral-hypocentral distance after the convention of equality between the real and the studied (examined) ones.(**b**) The same sketch as in (**a**), where there are depicted 3 randomly chosen attenuation model-areas, separated by the blue vertical lines.

Appendix B. Information on the source parameters of the earthquakes used in this study, occurred in western Greece, given in the catalogues of the Seismologic Station of Aristotle University of Thessaloniki (AUTh) (http://geophysics.geo.auth.gr/ss/) (1st column: "C" refers to the events that were examined both by GIT (*ch.* 2.1) and SFC (*ch*. 2.2) methods, blank cells refer to earthquakes whose data were used only for the GIT. 2nd column: Date_Time, 3rd and 4th columns: Longitude and Latitude of the epicenters, 5th column: Focal Depth, 6th column: local magnitude, 7th column: moment magnitude, when available). Moreover, the information computed from the GIT in this study are also given (8th column: moment magnitude, 9th column: std of M_w, 10th column: corner frequency, 11th column: the corresponding standard deviation (in log scale) ($\log10(f_c)$ +/- $\log10(\sigma_{f_c}) \Leftrightarrow f_c \cdot/\div \sigma_{f_c}$), 12th: the Root Mean Square errors compute by the logarithmic values of the non-parametric source spectra in **Appendix M**).

	Earthquake_ID (YYYYMMDD_hhmmss)	Long. (°)	Lat. (°)	M_L (cat.)	D. (km	M_w (cat.)	M_w (inv.)	σ_{M_w} (inv.)	f_c (inv)	σ_{f_c} (inv)	RMS ($\log_{10}$)
	20150813_221356	20.4362	38.1588	3.3	14.5	-	3.17	0.02	4.10	1.06	0.21
	20150820_025647	20.4197	38.1505	3.4	17.6	-	3.53	0.02	3.85	1.06	0.24
	20150820_060359	20.4017	38.3283	3.1	12	-	3.17	0.02	5.47	1.07	0.18
	20150820_061503	20.4182	38.315	3.6	11.9	-	3.55	0.02	2.60	1.05	0.14
	20150919_035628	20.552	38.1268	3.5	18.8	-	3.06	0.02	4.94	1.06	0.20
	20150928_155339	20.7337	38.1887	3.2	14.3	-	3.39	0.02	3.27	1.05	0.19
C	20151023_171318	20.193	37.99	3.9	16.8	-	4.09	0.04	1.20	1.08	0.18
	20151117_072942	20.5862	38.6547	3.7	14	-	3.53	0.02	3.36	1.06	0.17
C	20151117_083340	20.557	38.6515	5.1	8.7	5	4.73	0.02	1.07	1.05	0.19
	20151117_090215	20.5535	38.5447	3.9	10.6	-	3.82	0.02	2.44	1.05	0.16
	20151117_104137	20.5142	38.4782	3.6	10.3	-	3.65	0.02	2.06	1.05	0.17
C	20151117_114945	20.4857	38.4862	4.1	7.5	4	4.07	0.02	1.30	1.05	0.19
C	20151117_115725	20.6145	38.7025	4.4	9.9	4.5	4.45	0.02	0.92	1.05	0.16
C	20151117_123756	20.6538	38.7022	4.5	4.8	4.7	4.57	0.02	0.91	1.05	0.16
	20151117_164001	20.5547	38.5303	3.4	13.1	-	3.4	0.02	3.66	1.05	0.14
	20151117_192316	20.5678	38.521	3.6	12	-	3.53	0.02	2.28	1.05	0.16
C	20151117_193934	20.6017	38.704	4.5	8.5	4.2	4.11	0.02	1.85	1.04	0.17
	20151117_211136	20.5425	38.527	3.7	13.4	-	3.68	0.02	2.51	1.05	0.17
C	20151118_051813	20.5177	38.4967	4.5	13.6	4.4	4.29	0.02	1.26	1.04	0.16
	20151118_052317	20.5267	38.4992	3.3	11	-	3.5	0.02	2.14	1.06	0.16
	20151118_085836	20.5692	38.6043	3.4	11.6	-	3.45	0.02	2.65	1.05	0.18
C	20151118_121538	20.5915	38.8443	4.9	17.2	5	4.73	0.03	1.16	1.06	0.17
C	20151118_130314	20.6288	38.7197	4.6	8.3	4.7	4.65	0.02	0.88	1.05	0.16
C	20151118_183007	20.628	38.7238	4.1	6.3	4.2	4.34	0.02	0.82	1.05	0.16
	20151119_061007	20.5417	38.5372	3.3	12.8	-	3.13	0.03	4.15	1.09	0.09
C	20151119_174555	20.4952	38.4623	4	12.5	-	3.76	0.02	2.38	1.04	0.16
	20151120_030528	20.5145	38.5025	3.8	10.8	-	3.8	0.02	1.82	1.05	0.15
	20151120_042757	20.5152	38.4957	3.3	11.6	-	3.37	0.03	3.47	1.08	0.11
C	20151120_051224	20.4875	38.4703	4.8	12.4	4.8	4.59	0.02	1.41	1.04	0.17
C	20151120_093314	20.583	38.6347	4.6	10.7	4.5	4.57	0.03	0.68	1.06	0.18
	20151120_103714	20.4753	38.455	3.6	14.6	-	3.52	0.02	2.53	1.05	0.20
	20151120_144232	20.4675	38.3673	3.3	11.5	-	3.36	0.02	2.91	1.05	0.15
	20151120_180737	20.478	38.4588	3.3	14.1	-	3.26	0.03	3.45	1.09	0.11
	20151120_214111	20.41	38.3715	3	15.8	-	3.18	0.02	3.47	1.06	0.16
C	20151120_233704	20.6172	38.7105	4.4	9	-	4.78	0.03	0.49	1.07	0.15
C	20151121_004156	20.617	38.7148	4.6	9.3	4.5	4.74	0.03	0.58	1.06	0.14

C	20151121_015825	20.5915	38.602	4.2	14.4	4.1	4.02	0.02	1.68	1.04	0.17
	20151121_035025	20.5013	38.5037	3.1	12.8	-	3.35	0.02	2.08	1.05	0.16
	20151122_002452	20.4523	38.4647	3.5	13	-	3.75	0.02	1.29	1.06	0.16
	20151122_023945	20.4675	38.457	3.7	12.2	-	3.74	0.04	1.58	1.09	0.10
C	20151123_093002	20.5818	38.5178	3.9	11.6	-	3.98	0.02	2.40	1.04	0.17
	20151123_152332	20.5608	38.5252	3.4	11.2	-	3.47	0.03	3.73	1.08	0.10
	20151124_003518	20.5757	38.5242	3.2	11.8	-	3.38	0.02	2.60	1.05	0.17
	20151124_115621	20.4657	38.3663	3.7	12.4	-	3.77	0.02	2.06	1.05	0.15
	20151124_122932	20.4617	38.4622	3.3	14.4	-	3.4	0.02	2.80	1.06	0.18
C	20151125_031447	20.545	38.5265	4.2	14.3	4.1	4.04	0.02	2.22	1.04	0.15
	20151125_073629	20.5703	38.5192	3.1	13.1	-	3.2	0.03	4.23	1.09	0.11
	20151125_152139	20.5595	38.5197	3.2	14.5	-	3.2	0.03	3.13	1.09	0.10
	20151128_044306	20.6237	38.6385	3.5	10.9	-	3.48	0.02	2.92	1.06	0.14
C	20151129_083609	20.6137	38.7228	4.1	7.5	-	4.18	0.03	1.09	1.08	0.11
	20151201_055733	20.4825	38.4297	3.1	10.6	-	3.28	0.03	2.42	1.08	0.12
	20151203_150021	20.5963	38.5282	3.2	12	-	3.56	0.03	3.83	1.08	0.10
	20151205_104645	20.4717	38.3953	3.2	13.8	-	3.24	0.03	3.34	1.09	0.10
	20151207_215206	20.5577	38.5317	3.2	14.2	-	3.1	0.03	4.12	1.09	0.11
	20151209_130629	20.4623	38.392	3.3	14.2	-	3.47	0.03	2.98	1.08	0.10
C	20151212_083445	21.1588	37.8318	4.6	28.9	4.5	4.28	0.02	2.13	1.05	0.21
C	20160104_072145	20.4012	38.3155	4	15	-	3.85	0.02	2.57	1.05	0.22
C	20160104_180055	20.5917	38.6037	4.3	14.1	4.2	4.11	0.02	1.56	1.05	0.18
	20160115_042151	20.5567	38.61	3	13.9	-	3.28	0.03	3.63	1.09	0.09
	20160211_022602	20.5538	38.4958	3.1	14.1	-	3.24	0.03	3.08	1.09	0.11
	20160217_164850	20.5713	38.2048	3	19.9	-	3.25	0.03	3.31	1.09	0.12
	20160305_084559	20.4747	38.3823	3	14.9	-	3.25	0.03	3.61	1.09	0.10
	20160313_032337	20.4163	38.2053	3	17.2	-	3.02	0.03	3.77	1.10	0.12
	20160317_043947	20.4377	38.149	3.2	16.4	-	2.9	0.03	7.76	1.13	0.16
	20160318_011522	20.4487	38.3852	3.1	13.2	-	3.52	0.04	1.41	1.09	0.11
C	20160329_214300	20.2793	37.661	3.8	15.4	-	3.93	0.04	2.26	1.09	0.15
C	20160411_185344	20.3325	38.2133	4.3	20.5	-	4.29	0.02	1.41	1.06	0.17
	20160423_103522	20.5413	38.497	3.5	15.5	-	3.1	0.02	4.63	1.09	0.13
	20160424_074156	20.4853	38.4685	3.5	17.8	-	3.25	0.03	3.38	1.09	0.10
C	20160426_141515	21.1042	37.8685	3.9	27.8	-	4.01	0.02	2.06	1.05	0.16
C	20160429_035053	20.6052	38.6967	3.9	9	-	3.95	0.02	1.52	1.04	0.15
	20160525_134010	20.4127	38.1225	3.1	17.1	-	2.47	0.03	12.37	1.19	0.13
C	20160604_163825	20.3477	38.1397	4.4	17	4.5	4.49	0.02	1.42	1.05	0.19
	20160605_071854	20.3397	38.1052	3.1	9.3	-	2.62	0.03	7.63	1.13	0.10
	20160605_073001	20.35	38.1558	3.5	17.1	-	3.62	0.03	2.75	1.09	0.10
	20160606_190905	20.491	38.3077	3	16.3	-	3.18	0.03	3.69	1.09	0.11
	20160607_045659	20.3483	38.1585	3.7	16.3	-	3.87	0.02	2.12	1.05	0.20
	20160607_062608	20.3633	38.1333	3	20.4	-	3.42	0.03	3.41	1.09	0.11
	20160611_101907	20.3677	38.15	3.2	14.9	-	3.45	0.03	2.73	1.09	0.11
	20160613_142412	20.3717	38.1417	3.2	17.9	-	2.51	0.03	9.02	1.15	0.13
	20160617_150034	20.216	37.9967	3.3	24	-	3.45	0.04	2.30	1.11	0.10
	20160622_112611	20.5483	38.5093	3	15.1	-	3.07	0.03	4.42	1.10	0.11
	20160722_033527	20.3858	38.0525	3.1	19.4	-	3.22	0.03	6.06	1.11	0.12
	20160723_183146	20.4772	38.2925	3.5	15.1	-	3.59	0.03	4.22	1.08	0.14
	20160827_041923	20.7058	38.446	3.1	13.8	-	3.43	0.03	2.38	1.09	0.10

	20160901_040753	20.591	38.4603	3.7	12.7	-	3.99	0.03	2.32	1.08	0.13
	20160901_075225	20.4017	38.2388	3	12.2	-	3.09	0.03	6.16	1.10	0.11
	20160902_080524	20.5658	38.4648	3.3	14	-	3.51	0.02	3.12	1.05	0.20
	20160907_051751	20.5988	38.4642	3.2	12.7	-	3.45	0.02	2.57	1.05	0.14
	20160907_084607	20.4022	38.3207	3.1	14.6	-	2.77	0.02	8.69	1.10	0.19
	20160908_153105	20.2318	37.9838	3.9	23	-	3.83	0.03	2.10	1.07	0.15
C	20160913_061449	21.2045	37.7758	4.1	15.3	-	4.13	0.02	2.34	1.05	0.19
C	20160914_022003	20.214	37.9628	3.9	19.4	-	4.03	0.04	1.22	1.09	0.15
C	20161003_023443	21.1967	37.7655	3.9	28.7	4.5	4.25	0.02	1.68	1.05	0.21
C	20161009_120412	20.2587	38.1703	3.9	17.9	4	3.84	0.02	2.14	1.06	0.18
	20161013_132151	20.6598	38.1273	3.1	13.2	-	2.85	0.02	4.87	1.07	0.15
	20161017_080959	20.4587	38.3725	3	13.7	-	3.39	0.02	2.05	1.06	0.16
	20161020_035838	20.256	37.976	3	10.6	-	3.44	0.03	1.34	1.07	0.18
	20161111_053643	20.4588	38.3022	3.3	8.6	-	3.32	0.02	3.74	1.05	0.18
	20161115_093442	20.669	38.1422	3.1	15.5	-	3.25	0.02	5.52	1.06	0.21
C	20161203_210435	21.979	38.0908	4.7	14.1	4.4	4.32	0.03	2.60	1.08	0.16
	20161214_091351	20.3698	38.1183	3.5	14.3	-	3.45	0.02	3.35	1.06	0.16
	20170102_011654	20.9615	37.9747	3.3	10.8	-	3.45	0.02	4.41	1.05	0.19
	20170108_233152	20.4168	38.1492	3	14.5	-	2.96	0.02	5.71	1.07	0.21
C	20170109_095316	21.7187	38.3368	4.5	2.7	4.6	4.55	0.02	1.29	1.05	0.17
C	20170110_124452	21.7197	38.3213	4.2	4.2	-	4.1	0.02	2.59	1.06	0.16
	20170120_164511	20.6143	38.6207	3.5	6.2	-	3.38	0.02	3.49	1.05	0.16
	20170224_223100	20.6065	38.4595	3.3	6.7	-	3.39	0.02	2.82	1.05	0.19
C	20170228_220201	20.1525	37.9028	4.1	7	4.1	4.07	0.04	1.20	1.10	0.18
	20170317_170843	20.5215	38.0975	3	18.3	-	3.23	0.02	4.14	1.07	0.20
	20170404_151227	20.4732	38.3855	3.3	10.9	-	3.35	0.02	2.35	1.06	0.19
C	20170405_154329	21.7722	38.3172	4.5	13.6	4.4	4.32	0.02	2.06	1.05	0.18
	20170406_201242	20.4773	38.3828	3.7	11.7	-	3.78	0.02	2.18	1.05	0.16
	20170406_224908	20.524	38.3825	3.3	8.8	-	3.48	0.02	2.28	1.05	0.13
	20170413_115117	20.5343	38.3797	3.2	3.7	-	3.37	0.02	2.51	1.05	0.20
C	20170415_013446	20.5067	38.3857	3.9	8.1	-	3.85	0.02	1.79	1.04	0.18
	20170424_144513	21.1053	37.861	3.9	18.5	-	3.72	0.02	3.79	1.05	0.19
C	20170514_044606	21.91	38.91	4.1	24	-	4.17	0.08	3.43	1.24	0.16
C	20170619_045537	21.2	38	4	10	-	4.15	0.02	1.03	1.05	0.19
C	20170627_035116	20.4188	38.2587	3.9	9.2	-	3.83	0.02	2.28	1.05	0.19
C	20170715_012203	21.99	38.34	4.1	4	-	4.04	0.04	2.38	1.10	0.17
C	20170715_030514	22.03	38.34	4.0	4	-	4.07	0.07	2.08	1.14	0.16
C	20170720_071545	21.94	38.39	4.1	5	-	4.03	0.03	2.14	1.08	0.15
C	20170910_083154	22.11	38.01	3.8	10	-	3.67	0.04	1.83	1.11	0.17
C	20170911_162015	21.53	39.15	4.9	8	-	4.69	0.06	0.95	1.17	0.17
C	20171104_095115	21.42	37.84	4.1	18	-	3.97	0.02	2.90	1.05	0.19
C	20171225_234705	20.5613	38.5937	4.4	4.7	4.3	4.27	0.02	1.24	1.05	0.19
C	20180221_234455	20.3462	37.7865	4.8	17.7	4.7	4.55	0.02	1.50	1.06	0.15
C	20180222_070750	21.62	38.13	3.9	20	-	3.8	0.02	3.12	1.06	0.19
	20180412_044529	21.3	38.6	3.7	18	-	3.71	0.02	3.18	1.06	0.20
C	20180424_052345	21.78	38.21	3.8	18	-	3.72	0.02	3.56	1.06	0.18
C	20180705_213905	21.29	37.96	4.4	4	-	4.22	0.02	1.53	1.05	0.20
C	20180714_050846	21.82	37.7	3.8	5	-	3.66	0.04	2.54	1.13	0.17
C	20180818_032649	21.82	38.38	3.8	10	-	3.54	0.03	1.94	1.07	0.23

C	20180831_071224	21.6307	39.2857	5	10.1	5.1	5.15	0.06	0.91	1.16	0.15
C	20180831_082623	21.61	39.35	4.1	6	-	4.19	0.06	1.53	1.19	0.15
C	20180918_024843	21.5687	38.1157	4	18.8	4	3.89	0.02	3.86	1.06	0.20
	20181023_220753	21.35	37.9	3.7	14	-	3.6	0.02	3.12	1.05	0.18
	20181026_001339	20.6712	37.466	4.5	5.7	-	4.6	0.04	1.12	1.12	0.10
	20181026_003255	20.3828	37.7262	4.4	10	-	4.52	0.04	1.12	1.10	0.11
	20181026_021733	20.5397	37.4798	4.1	8.2	-	4.2	0.04	3.46	1.14	0.10
	20181026_062051	20.4383	37.4698	4.4	5	-	4.24	0.04	2.84	1.23	0.09
	20181026_064408	20.521	37.4758	4.2	10	-	4.22	0.04	1.92	1.15	0.10
C	20181027_052846	20.6392	37.4743	4.6	5.1	4.4	4.44	0.03	2.40	1.08	0.17
	20181029_045211	20.5938	37.502	4.1	7.2	-	4.21	0.03	2.36	1.09	0.14
C	20181030_025959	20.5123	37.5938	5.4	6.9	-	5.25	0.03	0.64	1.06	0.23
	20181030_063413	20.5173	37.6515	4.2	8	-	4.38	0.04	0.92	1.09	0.10
C	20181105_064613	20.4863	37.6268	4.5	8.3	-	4.4	0.02	1.70	1.05	0.15
C	20181108_224600	20.4673	37.588	4.2	7	-	4.2	0.02	1.76	1.05	0.16
C	20181110_021338	20.4918	37.6482	4.2	7.7	-	4.02	0.02	1.98	1.05	0.15
C	20181111_233835	20.5055	37.6327	4.8	7	-	4.75	0.02	1.01	1.05	0.15
C	20181118_060644	20.3128	37.5557	4.3	7.5	-	4.48	0.1	1.52	1.16	0.15
C	20181119_055651	20.666	37.5437	4.1	16.3	-	4.19	0.02	1.91	1.06	0.17
C	20181129_002259	20.2648	37.6337	4.2	9.7	-	4.48	0.07	0.98	1.15	0.14
C	20181213_062641	20.6398	37.523	4.4	5.3	-	4.63	0.03	1.35	1.07	0.17
C	20190115_011149	20.4142	38.2898	4.2	11.2	-	4.09	0.02	2.08	1.04	0.17
C	20190115_012505	20.62	38.94	4.3	19	-	4.22	0.03	1.70	1.07	0.16
C	20190117_214639	20.6723	37.652	4.3	14.6	-	4.29	0.02	1.30	1.05	0.17
	20190125_225324	20.6485	37.6577	3.9	13.4	-	3.94	0.02	1.58	1.06	0.14
C	20190201_050200	20.9487	37.9522	3.9	13.4	-	3.93	0.02	2.42	1.05	0.16
C	20190205_022609	20.587	38.9803	5.2	13.2	-	5.04	0.03	0.96	1.07	0.15
C	20190216_015716	20.6875	37.6875	3.9	11.6	-	3.94	0.02	1.56	1.05	0.14
C	20190306_015445	22.02	38.36	3.9	9	-	3.74	0.05	4.69	1.14	0.14
C	20190325_062107	20.6172	37.6328	3.9	6.4	-	3.84	0.02	2.06	1.06	0.17
C	20190328_091301	21.94	38	4.1	10	-	3.87	0.03	2.01	1.07	0.16
C	20190416_010456	20.7129	37.7051	3.9	9	-	3.84	0.02	1.71	1.06	0.15
C	20190427_232557	20.6104	37.6025	3.9	11.2	-	3.83	0.02	2.34	1.06	0.17
C	20190513_165717	21.2695	37.6758	4.7	6.4	-	4.54	0.02	1.43	1.05	0.19
C	20190513_212733	21.27	37.69	4.3	11	-	4.19	0.02	1.44	1.05	0.20
	20190515_000241	21.27	37.91	3.7	6	-	3.7	0.02	1.45	1.05	0.19
C	20190521_085819	21.25	37.92	4.4	5	-	4.27	0.02	1.19	1.05	0.19
C	20190524_211759	21.24	37.94	3.9	5	-	3.88	0.02	1.47	1.05	0.19
C	20190619_232453	20.5289	38.0923	3.9	21.3	-	3.69	0.02	3.20	1.05	0.17
C	20190707_222218	20.57	37.52	3.9	18	-	3.92	0.03	1.95	1.08	0.14
C	20190713_150843	21.2498	38.8408	4.7	13.9	-	4.44	0.04	1.74	1.08	0.15
C	20190728_050253	20.5673	37.598	3.9	13.3	-	4	0.02	1.61	1.06	0.19
	20190828_054430	21.77	38.31	3.7	7	-	3.61	0.02	2.89	1.06	0.16
C	20191011_224320	20.93	37.7	4.4	9	-	4.35	0.03	1.18	1.06	0.18
C	20191012_064935	20.55	37.56	4.2	10	-	4.19	0.03	1.55	1.06	0.17
C	20191126_044929	21.88	38.37	4	8	-	4	0.03	1.54	1.08	0.18

Appendix C. The coordinates of the 24 stations located in western Greece. Column "El." gives the elevation, In the sixth column the values of "Vs_{30}" are given, where (M) and (I) refer to values measured where it was available or inferred, respectively, based on ***Margaris et al., (2021)*** for ITSAK stations and on ***Cushing et al., (2020)*** for the ARGONET ones. "N" characterizes the accelerometric network that each station belongs, where symbols "I" and "A" correspond to ITSAK (http://www.itsak.gr) and ARGONET (http://argonet-kefalonia.org/), respectively. "l", is the geometric mean of the mean free path presented in **Figure 46** and "*σ_l" the corresponding standard deviation (in log scale) (log10(l) +/- log10 (σ_l) $\Leftrightarrow$ $l \cdot/\div \sigma_l$). Stations with bold fonts are considered as "reference" ones in GIT study (*ch.* 3).

	Station	Long. (°)	Lat. (°)	El. (m)	Vs_{30} (M) m/sec	Vs_{30} (I) m/sec	N	l, (km)	*σ_l
1	CK0	20.506248	38.164152	4	~270	-	A	269	2.66
2	CK6	20.506248	38.164152	-2	~280	-	A	195	3.18
3	CK15	20.506248	38.164152	-11	~350	-	A	357	2.49
4	CK40	20.506248	38.164152	-36	~ 500	-	A	290	2.55
5	CK83	20.506248	38.164152	-79	≥ 690	-	A	416	2.24
6	**CKWP**	20.510489	38.166288	7	-	≥ 800	A	394	2.60
7	ARG2	20.4877	38.1783	5	-	381	I	265	2.44
8	**VSK1**	20.564	38.409	311	1183	-	I	301	2.57
9	LXR1	20.4374	38.2009	6	249	-	I	220	2.60
10	ITC1	20.7155	38.3645	7	-	438	I	188	1.74
11	VAS2	20.6081	38.6303	6	-	332	I	211	2.41
12	LEF2	20.7081	38.8302	2	331	311	I	585	2.96
13	ZAK2	20.8999	37.7878	3	-	352	I	226	2.86
14	AST1	21.0895	38.5416	9	-	461	I	287	2.72
15	AGR3	21.4161	38.5892	45	341	341	I	232	2.55
16	PRE2	20.7546	38.9576	2	-	384	I	669	3.04
17	PYR2	21.4505	37.6671	13	-	333	I	255	2.49
18	PYR3	21.4623	37.6787	24	225	-	I	115	3.31
19	AOL1	21.6247	37.6433	52	-	348	I	219	2.51
20	KAC1	21.5481	38.1379	40	337	-	I	124	2.48
21	MSL1	21.4243	38.3726	1	-	306	I	163	3.75
22	PAT4	21.7478	38.2341	33	350	-	I	137	3.10
23	PAT5	21.795	38.2959	53	-	423	I	281	3.24
24	KRI1	20.8171	37.6620	191	-	556	I	203	3.38

Appendix D. The coordinates of the 16 stations located in Southeastern France and which belong to the French network. The data of these station are included into the "RESIF-RAP" dataset (***Traversa et al., 2020***) . Column "El." Gives the elevation, and column Vs_{30} gives the values of the average shear wave velocity down to 30 m (where it was available). EC08 is the classification of each site according to Eurocode-08 (where available). "Loc" is the location of the stations, where "S" indicates that the stations is located into a structure, "FF" corresponds to Free Field installation, while "T" indicated installation into a tunnel. "N" characterizes the network that each station belongs, where symbol "C" correspond to the Cadarache network (seismometers), while "Fr" indicates the French accelerometric network (RAP) ***Régnier et al., 2010*** and ***Hollender et al., (2018)***. "l", is the geometric mean of the mean free path presented in **Figure 55** and "*σ_l" is the corresponding standard deviation (in log scale) (log10(l) +/- log10 (σ_l) ⇔ $l \cdot/\div \sigma_l$).

	Station	Long. (º)	Lat. (º)	El. (m)	Vs_{30} m/sec	EC08	Loc.	N	l, (km)	*σ_l
1	CA01_21	5.77	43.67	-	-	-	-	C	773	3.88
2	CA02_21	5.75	43.68	-	-	-	-	C	508	4.61
3	CA04_21	5.75	43.69	-	-	-	-	C	346	10.02
4	CA10_22	5.76	43.68	-	-	-	-	C	736	3.19
5	ARBF_00_HH	5.33	43.49	185	2400	A	S	Fr	1102	2.76
6	ARTF_00_HH	5.81	43.59	510	-	-	FF	Fr	1775	4.15
7	BLAF_00_HH	6.05	43.95	590	-	-	S	Fr	826	3.50
8	BSTF_00_HH	5.64	43.8	500	-	-	S	Fr	903	3.69
9	IRPV_00_HN	5.76	43.8	414	605	B	S	Fr	1374	3.09
10	IRVG_00_HN	5.54	43.63	499	2090	A	FF	Fr	984	4.16
11	MLYF_00_HH	5.77	43.99	765	-	-	S	Fr	1124	4.33
12	OGCA_00_HN	5.67	43.73	412	1383	A	FF	Fr	395	31.48
13	OGDI_00_HH	6.23	44.11	770	698	B	FF	Fr	596	6.39
14	OGDI_00_HN	6.23	44.11	770	698	B	FF	Fr	1067	4.54
15	OGVG_00_HH	6.11	44.82	6	1090	-	T	Fr	1408	2.68
16	RUSF_01_HH	5.48	43.94	499	2650	A	T	Fr	784	5.50

Appendix E. Similar Table as the **Appendix D**, for the extra 7 stations of the French accelerometric network (RAP), examined by the 4th group of data (see. *ch. 2.4*)

	Station	Long. (º)	Lat. (º)	El. (m)	Vs_{30} m/sec	EC08	Loc.	N
1	OGAG_00_HH	6.539745	44.78784	1280	972	A	T	Fr
2	OGAG_00_HN	6.539745	44.78784	1280	972	A	T	Fr
3	ISO_00_HH	7.05	44.184	910	2750	A	S	Fr
4	ISO_00_HN	7.05	44.184	910	2750	A	S	Fr
5	SAOF_00_HH	7.5532	43.986	595	2025	A	S	Fr
6	SAOF_00_HN	7.5532	43.986	595	2025	A	S	Fr
7	OGMB_00_HH	6.50576	44.9819	1575	573	B	FF	Fr

Appendix F. The information of the earthquakes used in this study (occurred in the broader Alps region), given by the catalogues of RAP (***Traversa et al., 2020***). (2nd column: Date_Time, 3rd: Longitude, 4th: Latitude, 5th local magnitude, 6th moment magnitude (if available), 7th Depth.

	Earthquake_ID (YYYYMMDD_hhmmss)	Long. (°)	Lat. (°)	M_L	M_w	Depth (km)
1	20000821_171429	8.28	44.89	5	4.7	5
2	20010225_183442	7.56	43.49	4.5	4.6	11
3	20050908_112718	6.88	46.04	4.9	4.7	7
4	20051220_235734	6.97	44.11	3.5	3.2	8
5	20060902_012131	7.73	43.91	4	3.8	2.8
6	20090419_123950	7.69	44.78	4.5	4.2	5
7	20110725_123121	7.32	44.99	4.8	4.5	5
8	20120226_223755	6.67	44.51	4.5	4.2	4
9	20120226_233934	6.69	44.52	3.6	3.3	10
10	20120227_163122	6.69	44.44	3.9	3.6	10
11	20120302_071552	6.64	44.51	3.8	3.5	5
12	20120325_080532	6.62	44.51	3.6	3.3	5
13	20120919_185601	5.875	43.868	3.6	3.3	5
14	20121003_092045	7.354	44.529	4.6	4.3	5
15	20121005_191043	7.247	44.594	3.6	3.3	10
16	20130107_042025	6.695	44.729	4.1	3.8	5
17	20130407_031313	7.399	44.22	3.8	3.5	7
18	20131015_024713	7.357	44.443	3.8	3.5	9
19	20140407_192659	6.713	44.514	5.2	4.9	8
20	20140612_114648	6.788	44.697	3.6	3.3	0
21	20140622_013214	6.718	44.512	3.6	3.3	12
22	20140713_100540	7.244	44.513	3.6	3.3	0
23	20150411_053314	6.684	44.517	3.5	3.3	7
24	20150910_065847	6.453	43.778	3.2	NaN	13
25	20151106_040303	6.739	44.491	4.1	3.8	12
26	20160314_133611	7.352	44.428	3.9	3.6	5
27	20160730_202137	7.324	44.914	4.4	4.1	5
28	20160903_191454	7.53	43.967	3.7	3.4	9
29	20161109_153511	6.177	44.276	3.8	3.5	15
30	20161110_024546	6.168	44.281	3.5	3.3	13
31	20161110_024813	6.168	44.277	4	3.7	13
32	20170408_095234	7.322	44.279	3.5	3.3	5
33	20171027_010951	6.329	45.447	3.7	3.4	3
34	20180717_181345	7.127	44.506	3.7	3.4	4
35	20191111_105245	4.6709	44.5178	5.2	4.9	1

Appendix G. The coordinates (latitude φ and longitude, λ), of the 60 station sites used for the creation of synthetic data (*ch*. 3.3.1). These stations consist a part of the permanent ITSAK accelerometric network (http://www.itsak.gr).

STAT.	Lat. (º), φ	Lon. (º), λ	STAT.	Lat. (º), φ	Lon. (º), λ	STAT.	Lat. (º), φ	Lon. (º), λ
AGR2	38.6319	21.4135	KAR2	39.3659	21.9194	PAT4	38.2341	21.7478
AGR3	38.5892	21.4161	KIF1	38.0772	23.8145	PAT5	38.2959	21.795
AIG2	38.2417	22.0724	KLV1	38.0325	22.1079	PER1	38.0119	23.7027
AKR1	38.1535	22.3132	KMV1	38.7793	22.7845	PET1	36.9638	21.9253
AOL1	37.6433	21.6247	KOR2	37.9401	22.9495	PIR1	37.9372	23.6425
ARE2	36.6663	22.3832	KRI1	37.662	20.8171	PIR2	37.9457	23.6708
ARG2	38.1783	20.4877	KRK1	39.6179	19.9163	PIR3	37.9572	23.6519
ARS1	37.6348	22.7293	KYM1	38.6338	24.1056	PLN1	39.998	23.575
ART2	39.1475	20.9937	KYP2	37.2497	21.667	PRE2	38.9576	20.7546
AST1	38.5416	21.0895	LAM2	38.9022	22.4317	PYL1	36.9141	21.6951
ATH5	37.9754	23.737	LAR4	39.6421	22.4218	PYR2	37.6671	21.4505
FRS1	39.2933	22.3844	LAR5	39.6403	22.4107	PYR3	37.6787	21.4623
GTH2	36.7602	22.5659	LEF2	38.8302	20.7081	SKO1	39.1233	23.7287
IGM2	39.4861	20.2592	LEO1	37.1688	22.8637	THV2	38.3161	23.3198
ITC1	38.3645	20.7155	LXR1	38.2009	20.4374	TRP1	37.5111	22.363
ITE1	38.4337	22.4272	MGP1	37.402	22.1378	VAS2	38.6303	20.6081
JAN2	39.664	20.8522	MOS1	37.9531	23.6819	VOL2	39.3659	22.9505
JAN3	39.6839	20.8378	MSL1	38.3726	21.4243	VOL3	39.3739	22.9353
KAC1	38.1379	21.5481	NMA1	37.8187	22.6627	VSK1	38.409	20.564
KAL3	37.0245	22.1029	NPS1	36.5126	23.0624	ZAK2	37.7878	20.8999

Appendix H. Information of the synthetic seismic sources used in this study. λ (Longitude) and φ (Latitude.) are the coordinates (**Figure 12**, **Appendix G**). The (1), (2) and (3) columns of M_w represent the synthetic, the initial at the inversion and the inversion resulted values of M_w, respectively. The synthetic depth is considered equal to zero. The initial magnitudes were created from the synthetic ones affected by standard input errors normally distributed around zero with a standard deviation 0.3.

ID	φ°	λ°	M_w			ID	φ°	λ°	M_w		
			(1)	(2)	(3)				(1)	(2)	(3)
1	36.6	20.2	3.1	3.1	3.12±0.02	**64**	36.6	22.3	3.4	3.4	3.39±0.02
2	37	20.2	3.7	3.7	3.72±0.02	**65**	37	22.3	6	5.9	5.98±0.05
3	37.4	20.2	2.2	2.3	2.22±0.02	**66**	37.4	22.3	3.7	3.7	3.71±0.02
4	37.8	20.2	3.7	3.6	3.71±0.02	**67**	37.8	22.3	3.4	3.6	3.40±0.02
5	38.2	20.2	1	0.9	1.01±0.02	**68**	38.2	22.3	1	1.4	1.01±0.02
6	38.6	20.2	3.4	3.3	3.41±0.02	**69**	38.6	22.3	2.2	2.3	2.20±0.02
7	39	20.2	3.7	3.6	3.72±0.02	**70**	39	22.3	1.6	1.8	1.60±0.02
8	39.4	20.2	2.8	2.6	2.81±0.02	**71**	39.4	22.3	5.2	5.2	5.21±0.02
9	39.8	20.2	4.9	4.7	4.91±0.03	**72**	39.8	22.3	2.8	2.6	2.80±0.02
10	36.6	20.5	4.6	5	4.62±0.03	**73**	36.6	22.6	1	0.7	1.00±0.02
11	37	20.5	1.6	1.2	1.62±0.02	**74**	37	22.6	4	3.8	4.01±0.02
12	37.4	20.5	2.8	2.5	2.81±0.02	**75**	37.4	22.6	3.7	3.8	3.71±0.02
13	37.8	20.5	1.3	1.5	1.30±0.02	**76**	37.8	22.6	1.3	1.8	1.30±0.02
14	38.2	20.5	2.8	3	2.81±0.02	**77**	38.2	22.6	2.8	2.7	2.81±0.02
15	38.6	20.5	4.3	4	4.32±0.02	**78**	38.6	22.6	2.5	2.3	2.51±0.02
16	39	20.5	1	0.9	1.01±0.02	**79**	39	22.6	3.1	3.5	3.11±0.02
17	39.4	20.5	3.4	3.1	3.39±0.02	**80**	39.4	22.6	2.2	2	2.21±0.02
18	39.8	20.5	3.1	3	3.10±0.02	**81**	39.8	22.6	2.5	2.3	2.51±0.02
19	36.6	20.8	1.3	1.4	1.32±0.02	**82**	36.6	22.9	1.9	1.7	1.89±0.02
20	37	20.8	2.8	2.7	2.81±0.02	**83**	37	22.9	1.3	1.4	1.30±0.02
21	37.4	20.8	4.6	4.5	4.61±0.02	**84**	37.4	22.9	2.5	2.5	2.50±0.02
22	37.8	20.8	1.9	1.5	1.90±0.02	**85**	37.8	22.9	3.1	3	3.11±0.02
23	38.2	20.8	4.3	4.5	4.31±0.02	**86**	38.2	22.9	3.4	3.6	3.42±0.02
24	38.6	20.8	1.6	1.8	1.61±0.02	**87**	38.6	22.9	4.6	4.6	4.60±0.02
25	39	20.8	3.4	3.7	3.40±0.02	**88**	39	22.9	2.2	2	2.20±0.02
26	39.4	20.8	4.3	4.5	4.31±0.02	**89**	39.4	22.9	4.9	4.8	4.93±0.02
27	39.8	20.8	1.9	2.2	1.90±0.02	**90**	39.8	22.9	1.3	1.6	1.29±0.02
28	36.6	21.1	1.6	1.7	1.62±0.02	**91**	36.6	23.2	1.3	1.3	1.29±0.02
29	37	21.1	3.1	3.4	3.11±0.02	**92**	37	23.2	4.3	4.3	4.29±0.02
30	37.4	21.1	1.6	1.2	1.61±0.02	**93**	37.4	23.2	1.9	2.1	1.91±0.02
31	37.8	21.1	1.9	2	1.90±0.02	**94**	37.8	23.2	1.3	1.2	1.31±0.02
32	38.2	21.1	1	1.1	1.01±0.02	**95**	38.2	23.2	4.9	5.2	4.90±0.02
33	38.6	21.1	5.5	5.7	5.52±0.03	**96**	38.6	23.2	1.9	2	1.89±0.02
34	39	21.1	4	3.8	4.01±0.02	**97**	39	23.2	4.9	5.2	4.92±0.02

35	39.4	21.1	3.4	3.3	3.41±0.02	**98**	39.4	23.2	1.6	1.5	1.62±0.02
36	39.8	21.1	1.9	2	1.91±0.02	**99**	39.8	23.2	4	3.9	4.00±0.02
37	36.6	21.4	1.3	1	1.31±0.02	**100**	36.6	23.5	2.2	2.4	2.19±0.02
38	37	21.4	1.3	1.4	1.30±0.02	**101**	37	23.5	1	1.2	0.99±0.02
39	37.4	21.4	2.2	2.5	2.21±0.02	**102**	37.4	23.5	4.3	4.1	4.29±0.02
40	37.8	21.4	2.2	2.2	2.21±0.02	**103**	37.8	23.5	4.6	4.6	4.60±0.02
41	38.2	21.4	2.5	2.4	2.50±0.02	**104**	38.2	23.5	1.6	1.7	1.61±0.02
42	38.6	21.4	1	1.1	1.01±0.02	**105**	38.6	23.5	1.3	1.5	1.30±0.02
43	39	21.4	2.2	2.3	2.20±0.02	**106**	39	23.5	2.5	2.6	2.52±0.02
44	39.4	21.4	2.2	2.2	2.21±0.02	**107**	39.4	23.5	3.7	3.6	3.71±0.02
45	39.8	21.4	1.6	1.5	1.60±0.02	**108**	39.8	23.5	1.9	1.5	1.91±0.02
46	36.6	21.7	1.9	2	1.91±0.02	**109**	36.6	23.8	2.8	3	2.79±0.02
47	37	21.7	1.9	1.9	1.90±0.02	**110**	37	23.8	4.6	4.6	4.59±0.02
48	37.4	21.7	1.3	1.3	1.30±0.02	**111**	37.4	23.8	1	1	1.01±0.02
49	37.8	21.7	2.8	2.4	2.80±0.02	**112**	37.8	23.8	1.6	1.6	1.60±0.02
50	38.2	21.7	3.1	3.1	3.11±0.02	**113**	38.2	23.8	4.3	4.4	4.31±0.02
51	38.6	21.7	4	3.7	4.01±0.02	**114**	38.6	23.8	5.2	5.4	5.22±0.03
52	39	21.7	2.5	2.4	2.49±0.02	**115**	39	23.8	1	1.4	0.99±0.02
53	39.4	21.7	3.1	3.4	3.10±0.02	**116**	39.4	23.8	1	1	1.02±0.02
54	39.8	21.7	2.8	2.7	2.79±0.02	**117**	39.8	23.8	1	1.3	0.99±0.02
55	36.6	22	2.5	2.4	2.51±0.02	**118**	36.6	24.1	3.7	3.7	3.70±0.02
56	37	22	5.5	5.2	5.51±0.03	**119**	37	24.1	3.4	3.7	3.40±0.02
57	37.4	22	2.5	2.5	2.50±0.02	**120**	37.4	24.1	1	1.2	1.01±0.02
58	37.8	22	5.2	5.2	5.21±0.02	**121**	37.8	24.1	1.3	1.4	1.31±0.02
59	38.2	22	1	1.3	1.00±0.02	**122**	38.2	24.1	2.5	2.2	2.51±0.02
60	38.6	22	4	3.6	4.02±0.02	**123**	38.6	24.1	1.6	1.9	1.61±0.02
61	39	22	3.1	2.9	3.10±0.02	**124**	39	24.1	5.5	5.5	5.53±0.04
62	39.4	22	4	4	4.01±0.02	**125**	39.4	24.1	1.9	2	1.90±0.02
63	39.8	22	2.2	2.1	2.19±0.02	**126**	39.8	24.1	1.6	1.9	1.60±0.02

Appendix I. Source parameters information used and computed in this study referring to the real dataset inverted also by ***Grendas et al., (2018),*** (**Figure 18**). In the second column the Earthquake (id) (date and time of each earthquake), in the third, fourth and fifth columns their coordinates (Latitude and Longitude) and focal depths reported by the Seismological Station of A.U.Th.(http://geophysics.geo.auth.gr/ss/) and in the sixth column the number of records used, are given, respectively. In the next columns their moment magnitudes M_w (cat) (from the catalogues of A.U.Th., and the computed from the application of GIT in this study M_w (inv) corner frequencies, $f_c(Inv)$, are given, respectively.

	Earthquake (id)	Lat. (°)	Long. (°)	D. (km)	Num. of Rec.	M_w (Cat.)	M_w (Inv.)	f_c (Inv.)
1	20101218_060541	37.228	20.19	7	6	4.8	4.83±0.05	0.18+1.40
2	20110222_203702	38.85	24.956	13	12	4.5	4.54±0.04	0.18+1.53
3	20110316_160724	38.453	20.486	1	10	4.5	4.54±0.04	0.16+1.64
4	20110403_235339	35.596	21.84	1	6	4.5	4.53±0.05	0.22-0.87
5	20110415_031829	36.614	22.873	6	10	4.5	4.37±0.04	0.17+1.59
6	20110508_065024	36.6752	27.2161	17	5	5.2	5.22±0.06	0.08-0.46
7	20110525_232750	37.9114	21.1121	14	12	5.1	5.00±0.04	0.06-0.62
8	20110526_125618	37.931	21.157	1	11	4.7	4.82±0.04	0.09-0.85
9	20110601_171858	36.37	22.287	11.4	12	4.5	4.49±0.04	0.12+1.11
10	20110719_071314	37.3929	20.1755	15	20	5.1	5.18±0.04	0.06-0.67
11	20110725_175721	40.8244	27.7474	12	8	5.1	4.98±0.05	0.14-0.79
12	20110807_143534	38.41	21.812	1	33	4.7	4.78±0.03	0.08+1.12
13	20110814_010502	37.231	22.009	1	13	4.6	4.74±0.04	0.08-0.86
14	20110914_033528	37.2	22.052	1	16	4.5	4.66±0.04	0.07-0.80
15	20111106_205650	35.79	25.647	11	13	5	4.94±0.05	0.12+1.02
16	20111110_172540	38.4	21.82	7	40	4.6	4.64±0.02	0.08+1.40
17	20111123_121754	34.2821	25.0778	11	6	5.5	5.46±0.06	0.06-0.37
18	20111205_081728	38.847	26.294	10	10	4.7	4.64±0.04	0.14+1.18
19	20120126_042459	36.0468	25.0538	22	7	5.2	5.21±0.05	0.09-0.73
20	20120127_013324	36.0558	25.0866	19	7	5.4	5.44±0.05	0.07-0.58
21	20120128_105055	36.05	25.04	11	6	4.7	4.74±0.05	0.14+1.06
22	20120129_095506	36.08	24.97	11	6	4.6	4.56±0.05	0.12-0.90
23	20120214_013439	40.1465	24.0754	12	29	5.2	5.25±0.03	0.05-0.65
24	20120304_033108	40.1696	24.0348	8	32	5.3	5.33±0.04	0.04-0.45
25	20120416_112342	36.719	21.6011	30	35	5.7	5.46±0.05	0.05-0.44
26	20120423_221534	34.901	25.343	10	6	4.6	4.54±0.05	0.16+1.33
27	20120501_144828	38.65	26.67	4	9	4.7	4.78±0.05	0.14-0.94
28	20120607_205421	40.8459	27.9342	8	6	5	5.06±0.05	0.19+1.17
29	20120610_124417	36.3847	28.9676	32	5	6.1	6.06±0.07	0.05-0.23
30	20120614_164607	36.386	29.018	5	5	4.5	4.50±0.06	0.23+1.05
31	20120625_130530	36.44	28.91	17	6	4.7	4.79±0.05	0.17-0.98
32	20120912_032747	34.8285	24.0647	30	14	5.4	5.28±0.05	0.06-0.51
33	20120921_084739	35.26	22.51	6	6	4.9	4.91±0.06	0.17-0.75
34	20120921_153916	35.369	22.679	10	5	4.6	4.57±0.05	0.30+1.59
35	20120922_035224	38.08	22.74	7	45	5.1	4.90±0.02	0.05-0.80

36	20120922_061557	40.15	20.83	8	38	4.6	4.64±0.03	0.06-0.79
37	20121023_152042	38.97	20.62	12	53	4.8	4.74±0.02	0.06+1.10
38	20121126_173541	36.66	28.006	1	20	4.8	4.76±0.04	0.09-0.77
39	20130108_141608	39.6681	25.5372	11	25	5.8	5.54±0.04	0.05-0.49
40	20130113_085515	39.67	25.57	9	23	4.5	4.69±0.03	0.13+1.54
41	20130406_112608	34.8226	24.1079	32	15	5.3	5.18±0.05	0.05-0.43
42	20130409_033627	36.5011	23.0159	18	58	4.6	4.85±0.02	0.09+1.44
43	20130523_140905	38.66	20.56	4	47	4.7	4.94±0.03	0.04-0.64
44	20130606_115348	36.8244	21.8841	42	49	5	4.97±0.03	0.07+1.02
45	20130615_161103	34.4507	25.044	22	11	6.3	6.27±0.07	0.01-0.10
46	20130615_162857	34.336	24.945	1	8	4.8	4.79±0.06	0.09-0.58
47	20130615_172206	34.328	25.047	1	5	4.5	4.54±0.05	0.14-0.92
48	20130616_213905	34.4242	25.1864	25	17	6.1	6.02±0.06	0.02-0.16
49	20130619_190508	34.282	25.037	1	9	4.7	4.68±0.05	0.14-0.92
50	20130702_104522	40.12	21.86	8	40	4.7	4.56±0.03	0.07+1.12
51	20130703_132823	40.12	21.85	7	38	4.8	4.72±0.03	0.05-0.66
52	20130807_090652	38.6885	22.6952	1	71	5.4	5.23±0.02	0.04-0.67
53	20130807_134432	38.7023	22.6593	1	64	5	4.90±0.02	0.04-0.74
54	20130809_114923	38.703	22.691	1	56	4.9	4.97±0.03	0.05-0.76
55	20130809_131010	38.702	22.659	1	55	4.7	4.84±0.02	0.05-0.91
56	20130908_045927	34.79	25.11	9	14	4.7	4.80±0.04	0.09-0.91
57	20130916_144240	38.68	22.71	6	64	4.6	4.75±0.02	0.05+1.01
58	20130916_150114	38.7062	22.729	8	66	5.3	5.12±0.03	0.04-0.60
59	20131112_180928	38.92	23.1	10	69	4.9	4.97±0.02	0.04-0.83
60	20140111_041257	37.8338	20.9713	1	51	5	4.88±0.02	0.05-0.84
61	20140126_184508	38.2313	20.3768	2	66	5.4	5.24±0.03	0.04-0.60
62	20140126_211535	38.145	20.352	8	51	4.7	4.76±0.02	0.06-0.95
63	20140128_051254	38.252	20.4	10	12	4.5	4.45±0.04	0.12+1.20
64	20140130_110618	38.414	20.444	1	58	4.5	4.70±0.02	0.05-0.82
65	20140201_081404	38.72	22.74	6	61	4.6	4.79±0.02	0.05-0.94
66	20140201_163338	38.176	20.305	3	56	4.5	4.75±0.03	0.05-0.76
67	20140203_030844	38.2665	20.323	10	64	6	5.91±0.04	0.03-0.31
68	20140206_192100	38.17	20.33	9	52	4.7	4.58±0.02	0.06+1.02
69	20140209_082259	38.186	20.349	9	49	4.5	4.60±0.02	0.06-0.94
70	20140212_103431	38.195	20.32	8	57	4.6	4.68±0.02	0.06-0.93
71	20140214_033832	38.16	20.28	6	50	4.8	4.88±0.03	0.05-0.68
72	20140215_073117	38.216	20.377	16	46	4.6	4.88±0.03	0.05-0.80
73	20140305_124921	38.109	20.352	11.6	14	4.8	4.88±0.04	0.07-0.73
74	20140414_204125	34.1335	25.8103	6	9	5.2	5.17±0.06	0.14-0.70
75	20140512_005433	39.761	20.272	4	19	5	4.91±0.03	0.11+1.21
76	20140601_120551	34.65	24.641	1	11	4.7	4.77±0.04	0.11-0.98
77	20140627_161427	38.25	25.15	8	27	4.4	4.72±0.03	0.14+1.35
78	20140703_050447	40.217	27.964	14	6	4.5	4.51±0.06	0.41+1.31
79	20140808_082048	34.788	24.835	13	19	4.8	4.66±0.04	0.10+1.10
80	20140822_042754	39.9352	23.4312	14	36	5.2	5.20±0.03	0.04-0.55

81	20140921_004340	38.351	21.833	11	58	4.6	4.98±0.03	0.04-0.56
82	20141003_222047	34.6202	26.283	1	16	5	4.95±0.05	0.06-0.51
83	20141004_122756	35.122	26.248	22.7	18	4.6	4.64±0.04	0.08-0.81
84	20141024_234315	38.9193	21.1252	1	62	5.3	5.37±0.03	0.03-0.50
85	20141107_074139	38.09	20.45	13	46	4.7	4.92±0.03	0.05-0.80
86	20141107_171300	38.2887	22.128	9	47	5.1	4.94±0.03	0.04-0.71
87	20141110_061640	37.099	28.765	1	8	4.5	4.65±0.05	0.16-0.90
88	20141113_093753	38.385	20.485	11	52	4.5	4.59±0.02	0.07+1.32
89	20141117_230556	38.6545	23.4328	1	70	5.3	5.23±0.02	0.04-0.67
90	20141117_230903	38.6455	23.4312	1	61	5.2	5.24±0.03	0.04-0.58
91	20141206_014507	38.9052	26.2613	14	16	5.1	5.09±0.04	0.06-0.59
92	20141206_062054	38.8962	26.2342	14	9	5	4.90±0.05	0.11-0.87
93	20141211_222423	38.39	20.41	20	52	4.5	4.69±0.02	0.10+2.03
94	20150102_061631	37.539	20.53	9	41	4.6	4.60±0.03	0.08+1.19
95	20150128_155435	34.2462	25.1413	1	14	5.3	5.29±0.06	0.07-0.47
96	20150313_133309	36.4	23.18	17	41	4.5	4.56±0.03	0.11+1.59
97	20150316_111834	37.338	20.101	1	27	4.5	4.74±0.04	0.11+1.18
98	20150416_180744	35.1463	26.888	1	19	6.1	5.98±0.05	0.04-0.36
99	20150416_185238	35.136	26.858	1	17	4.7	4.81±0.04	0.09-0.99
100	20150416_190215	35.142	26.809	1	18	4.6	4.84±0.04	0.08-0.90
101	20150417_020542	35.1575	26.7333	1	21	5.5	5.39±0.04	0.05-0.51
102	20150417_163943	35.119	26.68	1	19	4.6	4.57±0.03	0.10+1.21
103	20150418_164650	36.49	23.2	21	41	4.7	4.87±0.03	0.08+1.06
104	20150502_082345	34.447	25.796	1	14	4.7	4.80±0.04	0.10-0.87
105	20150609_010903	38.6402	23.4052	8	77	5.3	5.17±0.02	0.04-0.67
106	20150609_214948	35.0497	26.7158	1	20	5.4	5.31±0.04	0.05-0.54
107	20150620_195244	34.272	26.298	4	11	4.5	4.60±0.05	0.10-0.75
108	20150910_081246	38.82	26.28	11	11	4.6	4.60±0.04	0.18+1.41
109	20150913_025727	37.104	28.943	1	10	4.6	4.54±0.05	0.25+1.25
110	20150929_091240	34.76	24.594	15	16	4.5	4.44±0.04	0.10-0.99
111	20151117_071007	38.6733	20.5302	1	68	6.5	6.35±0.06	0.01-0.12
112	20151117_083340	38.6468	20.5718	7	65	5.1	4.96±0.03	0.03-0.53
113	20151117_115725	38.71	20.6	8	59	4.6	4.51±0.02	0.04-0.74
114	20151117_123754	38.72	20.58	8	57	4.9	4.69±0.02	0.05-0.81
115	20151117_193934	38.71	20.6	6	50	4.2	4.22±0.02	0.08+1.39
116	20151118_051813	38.5	20.52	9	51	4.6	4.46±0.02	0.05-0.95
117	20151118_121538	38.8628	20.5917	16	50	5	4.89±0.03	0.04-0.69
118	20151118_130314	38.74	20.6	14	56	5	4.67±0.03	0.04-0.72
119	20151120_051224	38.47	20.4442	14	56	5	4.62±0.02	0.05+1.02
120	20151120_093314	38.64	20.54	9	55	4.7	4.58±0.03	0.04-0.68
121	20151120_233703	38.73	20.6	3	50	4.5	4.58±0.03	0.04-0.56
122	20151121_004156	38.72	20.6	8	54	4.7	4.58±0.03	0.04-0.67
123	20160104_180055	38.58	20.6	10	52	4.3	4.21±0.02	0.06+1.15
124	20160205_230128	34.908	25.877	16	20	4.6	4.56±0.04	0.11+1.19
125	20160215_185500	37.58	21.7	18	57	5.2	5.14±0.03	0.04-0.57

126	20160312_124039	35.37	23.57	19	27	4.6	4.49±0.04	0.08-0.84
127	20160329_010528	37.38	19.988	1	41	5.3	5.13±0.04	0.06-0.62
128	20160403_004615	34.47	25.65	11	7	4.7	4.68±0.06	0.04-0.28
129	20160521_163308	41.278	21.068	1	32	4.8	4.65±0.04	0.11+1.09
130	20160521_164129	41.228	21.043	1	27	4.6	4.68±0.04	0.09-0.84
131	20160525_083615	34.918	26.261	7	21	5.6	5.42±0.04	0.05-0.55
132	20160604_163826	38.095	20.302	6	42	4.8	4.53±0.03	0.06-0.99
133	20160730_172624	35.23	22.855	18	10	5	5.11±0.05	0.09-0.62
134	20160912_082604	38.877	27.788	1	19	4.8	4.78±0.05	0.09-0.59
135	20160912_092938	38.895	27.774	3	19	4.5	4.56±0.05	0.09-0.65
136	20161015_201450	39.79	20.72	10	39	5.3	5.20±0.03	0.04-0.63

Appendix J. The Q_{s_n} and α_n values computed in this study for the 216 cells of **Figure 18**. The 69 sub-areas for which no ray paths passing through them, are not included to this Appendix and no Q_{s_n} and α_n parameters were computed for them (e.g the, n = 1, 2). The number of sub-areas starts from the upper left one (**Figure 18**) up to the bottom right one and consecutively counts for the columns of each line.

Number of Sub-Area, n	$Q_{s_n} \pm \sigma_{Q_{s_n}}$	$\alpha \pm \sigma_\alpha$	Number of Records	Number of Sub-Area, n	$Q_{s_n} \pm \sigma_{Q_{s_n}}$	$\alpha \pm \sigma_\alpha$	Number of Records
3	20.7±14.0	0.432±0.311	5	128	145.2±98.5	0.516±0.300	14
4	409.9±697.5	0.676±0.378	59	129	40.2±6.7	0.628±0.099	14
5	100.8±64.4	0.558±0.330	14	130	51.1±15.4	0.890±0.156	7
6	19.8±8.4	0.691±0.147	3	131	95.0±94.6	0.698±0.303	15
7	112.7±259.2	0.537±0.417	3	134	262.0±580.4	0.647±0.412	1
8	328.3±647.1	0.480±0.420	2	135	57.2±6.9	0.669±0.044	72
9	328.3±646.9	0.480±0.420	2	136	68.3±5.2	0.840±0.039	371
10	243.3±561.9	0.592±0.426	8	137	66.6±3.4	0.731±0.024	501
11	609.7±1398.6	0.629±0.426	18	138	73.2±4.0	0.722±0.025	434
12	53.7±15.8	0.607±0.182	19	139	121.5±11.2	0.495±0.042	347
13	586.4±1170.0	0.549±0.418	28	140	86.1±7.2	0.647±0.043	281
14	96.6±59.8	0.504±0.287	20	141	77.2±6.9	0.871±0.056	150
15	27.7±8.1	0.837±0.157	4	142	61.8±7.1	0.689±0.068	228
16	171.6±337.5	0.656±0.417	2	143	329.9±310.3	0.564±0.352	24
22	94.0±30.7	0.819±0.178	17	144	175.4±125.6	0.443±0.278	16
23	84.2±16.8	0.672±0.094	178	145	381.8±545.9	0.640±0.399	4
24	57.0±10.1	0.518±0.097	85	146	35.1±13.4	1.110±0.232	4
25	50.0±13.1	0.515±0.145	17	147	60.7±20.5	0.964±0.206	8
26	51.2±13.9	0.682±0.153	143	148	78.2±50.1	0.872±0.290	30
27	36.8±6.3	0.600±0.091	34	149	774.1±1652.7	0.659±0.420	9
28	242.5±240.4	0.780±0.378	10	150	61.4±43.0	0.711±0.240	16
29	39.9±8.2	0.637±0.119	25	151	260.1±532.3	0.602±0.410	5
30	145.1±50.6	0.302±0.165	48	153	477.7±1076.3	0.547±0.423	41
31	67.8±10.2	0.667±0.087	31	154	31.9±4.0	0.859±0.055	93
32	85.8±18.4	0.809±0.141	38	155	57.2±10.5	0.734±0.097	39
33	65.4±15.9	0.784±0.141	25	156	52.2±3.7	0.983±0.045	150
34	47.7±16.1	0.667±0.152	13	157	82.3±5.8	0.715±0.035	328
35	49.0±20.6	0.941±0.213	15	158	70.3±4.5	0.692±0.032	314
36	246.0±232.3	0.009±0.303	14	159	77.8±6.9	0.776±0.050	154
40	94.4±42.6	0.461±0.224	3	160	68.6±8.7	0.722±0.074	50
41	59.4±7.7	0.730±0.070	140	161	45.9±6.6	0.811±0.092	31
42	56.4±4.4	0.718±0.043	282	162	115.1±58.4	0.820±0.280	10
43	53.2±3.6	0.853±0.042	316	163	45.1±9.4	0.859±0.119	21
44	63.0±7.1	0.596±0.064	113	164	52.3±11.4	0.664±0.112	36
45	42.2±2.6	0.889±0.046	132	165	79.3±40.5	0.932±0.287	7
46	36.7±2.1	0.984±0.039	61	166	66.1±28.4	0.631±0.205	7
47	346.8±155.2	0.172±0.189	67	167	46.1±11.3	0.767±0.138	11
48	29.9±2.3	0.862±0.049	83	168	70.7±26.8	0.401±0.165	10
49	33.4±3.8	1.015±0.084	28	169	52.8±12.3	1.198±0.149	19

50	46.1±7.9	0.582±0.098	21	170	394.6±557.9	0.737±0.396	13
51	34.3±4.6	0.684±0.081	23	171	31.2±9.4	0.382±0.106	18
52	50.4±12.3	0.563±0.122	17	175	691.1±1437.5	0.586±0.421	7
53	316.2±419.0	0.503±0.385	12	176	48.2±6.6	1.057±0.076	211
54	42.8±10.9	0.972±0.160	12	177	87.5±10.7	0.637±0.061	145
55	65.7±37.0	0.741±0.190	8	178	80.8±7.5	0.755±0.049	158
58	112.3±140.0	0.333±0.391	57	179	70.4±8.0	0.948±0.077	168
59	343.7±265.2	0.268±0.278	48	180	55.2±9.9	0.867±0.113	14
60	62.9±5.1	0.777±0.044	316	181	1061.5±2332.	0.706±0.423	6
61	75.5±4.9	0.659±0.033	302	182	36.6±7.2	0.840±0.115	11
62	58.5±2.9	0.811±0.028	252	183	127.9±38.9	0.755±0.176	26
63	104.8±11.1	0.519±0.055	249	184	443.2±314.4	0.082±0.287	14
64	57.1±4.7	0.728±0.052	95	185	34.2±5.6	1.029±0.130	6
65	70.6±7.2	0.549±0.053	93	186	93.9±36.0	0.393±0.186	13
66	89.4±13.2	0.593±0.081	63	187	421.2±495.6	0.232±0.376	9
67	52.3±5.7	0.767±0.067	29	188	409.1±434.9	0.227±0.349	28
68	47.0±4.9	0.986±0.076	28	189	552.5±712.6	0.611±0.382	48
69	130.7±39.2	0.443±0.140	61	190	599.8±729.4	0.221±0.367	18
70	411.1±361.1	0.254±0.330	69	195	249.7±225.6	0.408±0.340	8
71	353.6±389.9	0.691±0.370	25	196	115.3±39.3	0.667±0.171	27
72	604.8±888.1	0.569±0.400	13	197	66.8±13.2	0.802±0.110	30
73	154.6±118.9	0.540±0.275	11	198	42.0±3.6	0.899±0.050	132
77	61.3±18.4	0.610±0.152	28	199	73.7±15.0	0.839±0.113	51
78	70.7±12.4	0.613±0.085	72	200	149.7±100.4	0.566±0.282	17
79	64.8±3.8	0.734±0.030	457	201	52.4±9.4	0.996±0.118	25
80	62.2±3.2	0.808±0.027	379	202	46.4±6.7	0.842±0.092	73
81	84.3±5.8	0.665±0.036	341	203	65.8±12.9	0.670±0.107	32
82	63.8±3.4	0.770±0.029	337	204	52.8±9.2	0.805±0.116	16
83	51.8±2.5	0.778±0.028	259	205	47.5±8.9	0.854±0.121	18
84	60.9±4.7	0.868±0.049	125	206	146.5±80.0	0.781±0.278	15
85	94.7±15.3	0.611±0.094	93	207	203.5±86.7	0.706±0.216	97
86	118.7±25.6	0.360±0.101	40	208	416.5±312.3	0.335±0.297	94
87	58.4±9.7	0.655±0.096	47	209	50.1±19.3	1.126±0.198	16
88	54.9±7.5	0.810±0.093	46	214	146.3±182.5	0.525±0.301	6
89	111.9±30.2	0.462±0.137	44	215	51.4±17.0	0.756±0.163	3
90	55.3±8.3	0.975±0.094	43	216	85.0±30.5	0.641±0.174	11
91	87.2±28.5	0.865±0.199	17	217	91.5±23.6	0.694±0.131	33
92	64.3±19.8	1.002±0.179	15	218	245.9±125.5	0.879±0.272	73
93	295.7±635.5	0.547±0.414	10	219	71.5±10.4	1.023±0.097	115
96	85.9±57.7	0.656±0.315	4	220	198.5±68.2	0.910±0.199	50
97	85.3±11.0	0.959±0.083	174	221	69.0±8.2	1.141±0.088	48
98	73.8±3.9	0.867±0.024	1182	222	75.2±12.1	0.930±0.105	41
99	95.3±6.7	0.616±0.032	671	223	64.7±8.4	1.058±0.094	29
100	76.9±4.6	0.588±0.030	435	224	64.2±9.8	0.983±0.110	47
101	71.3±4.2	0.709±0.030	441	225	67.1±11.5	1.082±0.110	91
102	58.6±3.0	0.716±0.024	652	226	167.6±114.2	0.890±0.296	91
103	90.7±8.3	0.601±0.039	382	227	116.3±141.0	0.660±0.387	5
104	50.3±3.6	0.821±0.045	121	234	47.1±48.4	0.310±0.356	1
105	73.7±9.7	0.810±0.080	116	235	81.5±44.3	0.623±0.195	21

106	66.8±10.2	0.443±0.075	76	236	82.2±27.4	0.373±0.130	24
107	37.9±3.8	0.763±0.065	29	237	156.1±50.4	0.642±0.150	79
108	206.1±108.1	0.202±0.234	28	238	82.7±8.6	0.625±0.052	133
109	77.9±20.2	0.869±0.147	60	239	104.1±13.2	0.814±0.071	143
110	66.7±19.5	0.741±0.156	17	240	86.8±11.4	0.666±0.070	196
111	482.1±798.6	0.534±0.399	16	241	92.9±12.0	0.596±0.065	141
112	318.2±603.0	0.610±0.390	38	242	74.4±8.3	0.867±0.066	156
115	45.9±25.6	0.977±0.272	1	243	110.8±22.4	0.383±0.083	177
116	124.2±22.9	1.031±0.102	913	244	70.3±21.2	0.389±0.115	61
117	80.9±4.8	0.744±0.025	1034	256	51.8±35.9	0.665±0.291	7
118	75.1±3.9	0.831±0.023	800	257	333.1±191.7	0.040±0.215	52
119	80.5±4.8	0.687±0.027	826	258	193.2±55.8	0.357±0.115	92
120	73.0±4.1	0.743±0.027	654	259	89.7±13.0	0.652±0.062	106
121	60.0±2.9	0.796±0.024	482	260	80.8±11.7	0.777±0.068	84
122	111.2±10.3	0.503±0.042	358	261	94.1±20.6	0.689±0.100	69
123	62.7±5.3	0.784±0.049	239	262	32.9±5.5	1.216±0.128	12
124	132.3±42.9	0.790±0.184	49	277	29.3±7.0	1.022±0.116	21
125	84.7±22.9	0.449±0.118	30	278	28.0±6.1	0.885±0.061	64
126	48.2±11.2	0.633±0.125	36	279	22.3±3.8	0.777±0.049	36
127	32.3±6.6	0.799±0.130	4	280	741.2±1356.9	0.457±0.397	14

Appendix K. The 275 average Q_{s_n} and a_n values (Eq. [7]) and their corresponding standard errors, σ, computed from the inversion in this study, for the specific *n* cells of **Figure 5** (406 in total). The number of sub-areas starts from the upper left one (**Figure 5**) up to the bottom right one and consecutively counts for the columns of each line.

n, cell-area	Q_{s_n}	$\sigma_{Q_{s_n}}$	a_n	σ_{α_n}	*n, cell-area*	Q_{s_n}	$\sigma_{Q_{s_n}}$	a_n	σ_{α_n}
15	144.9	367.7	0.739	1.171	243	55.8	12.6	0.496	0.105
16	265.3	730.1	0.742	1.252	244	40.1	5.2	0.962	0.082
34	212.9	570.2	0.370	0.624	245	32.7	4.5	0.656	0.076
35	33.9	27.3	0.297	0.271	246	26.3	3.1	0.748	0.067
36	141.2	134.3	0.175	0.269	247	133.0	57.6	0.339	0.204
37	63.2	46.4	0.175	0.245	248	26.3	2.4	0.886	0.058
53	220.1	576.9	0.347	0.580	249	125.2	83.0	0.355	0.276
54	281.9	748.4	0.371	0.621	250	43.9	25.4	0.254	0.182
55	109.8	182.9	0.268	0.406	251	242.2	661.1	0.359	0.612
56	234.9	486.9	0.246	0.395	254	947.6	2364.4	0.312	0.517
57	19.5	10.1	0.697	0.207	255	263.0	96.2	0.061	0.099
58	12.3	6.2	1.242	0.291	256	44.3	5.3	0.843	0.066
71	138.8	360.9	0.307	0.516	257	32.4	2.4	0.923	0.044
72	10.0	3.9	1.468	0.354	258	157.5	34.3	0.092	0.089
73	37.6	55.5	1.384	1.166	259	32.8	3.2	0.806	0.058
74	42.4	74.3	1.206	1.165	260	51.7	8.6	0.647	0.091
75	12.0	4.9	0.818	0.227	261	39.1	6.2	0.708	0.087
76	176.3	344.8	0.236	0.372	262	42.1	6.2	0.758	0.085
77	16.6	9.0	1.172	0.329	263	31.3	3.2	0.859	0.063
78	23.6	18.6	1.240	0.438	264	31.1	3.9	0.841	0.077
79	30.1	39.3	0.619	0.434	265	40.5	7.7	0.643	0.103
89	77.7	29.1	0.072	0.113	266	63.3	16.7	0.567	0.137
90	173.4	198.6	0.379	0.387	267	35.1	5.2	0.842	0.091
91	137.3	281.6	1.116	1.518	268	36.3	4.9	1.046	0.096
92	55.6	32.9	0.172	0.212	269	95.2	36.9	0.342	0.172
93	23.0	10.1	1.438	0.403	270	133.2	95.8	0.674	0.369
94	344.3	786.6	0.309	0.502	271	37.8	15.4	0.604	0.177
95	20.2	11.2	1.611	0.369	272	275.9	754.7	0.374	0.638
96	11.2	2.7	0.577	0.109	274	2.7	1.5	0.126	0.202
97	97.9	115.2	0.248	0.349	275	46.8	21.4	0.961	0.226
98	411.1	907.6	0.414	0.649	276	99.6	54.2	0.928	0.318
99	88.0	104.2	1.284	1.009	277	28.4	2.7	1.026	0.063
100	50.4	51.9	1.282	0.781	278	33.3	3.2	1.069	0.066
101	231.4	626.9	0.269	0.458	279	51.7	9.1	1.401	0.133
102	72.4	78.7	0.121	0.197	280	341.3	207.1	0.232	0.254
103	172.9	482.4	0.387	0.662	281	42.9	6.2	0.835	0.087
110	336.3	351.3	0.127	0.209	282	33.2	4.4	0.863	0.083
111	50.0	13.5	0.904	0.161	283	67.8	18.3	0.723	0.151
112	32.5	5.7	0.850	0.106	284	105.1	32.8	0.513	0.156
113	22.4	3.9	0.666	0.094	285	29.1	3.0	0.815	0.061
114	636.5	1595.3	0.627	1.002	286	66.0	17.1	0.493	0.129
115	374.3	891.5	0.718	1.064	287	93.1	37.2	0.704	0.225

116	74.3	81.4	1.951	0.805	288	57.4	17.7	0.509	0.157
117	17.2	6.2	0.666	0.128	289	60.6	20.0	0.542	0.170
118	18.7	7.4	1.148	0.296	290	47.0	12.6	0.825	0.164
119	145.1	201.6	0.279	0.394	291	62.7	32.9	1.988	0.472
120	159.0	163.5	0.163	0.261	292	93.8	84.6	0.536	0.355
121	126.6	158.9	0.182	0.285	293	237.9	490.0	0.508	0.677
122	17.5	9.5	0.559	0.229	294	249.0	693.0	0.480	0.818
123	31.2	34.6	0.738	0.489	295	327.5	806.9	0.648	0.891
124	314.0	872.8	0.459	0.785	296	24.3	7.9	1.076	0.192
131	11.7	0.9	0.924	0.051	297	108.9	52.6	0.201	0.186
132	23.6	2.1	0.764	0.048	298	66.4	18.0	0.388	0.108
133	24.2	2.7	0.713	0.058	299	47.6	8.3	0.405	0.065
134	32.2	5.7	0.720	0.099	300	23.3	2.5	0.657	0.047
135	51.5	21.2	0.714	0.214	301	23.8	2.5	0.697	0.054
136	188.6	221.9	0.371	0.457	302	24.6	2.2	0.662	0.045
137	25.3	4.8	0.801	0.101	303	25.8	2.8	0.664	0.057
138	60.0	30.3	0.472	0.211	304	29.5	3.4	0.665	0.061
139	19.2	3.6	1.162	0.143	305	30.3	3.0	0.663	0.053
140	27.8	10.5	1.119	0.294	306	35.9	4.0	0.619	0.058
141	50.4	34.7	0.399	0.286	307	401.6	191.6	0.103	0.162
142	381.2	994.9	0.735	1.181	308	66.0	18.9	0.245	0.125
143	41.4	50.1	0.473	0.429	309	51.0	16.0	0.338	0.135
144	207.8	564.2	0.810	1.338	310	140.7	37.5	0.049	0.080
152	124.8	39.6	0.198	0.125	311	164.0	87.1	0.133	0.199
153	80.1	13.5	0.490	0.076	312	103.5	39.3	0.108	0.147
154	60.8	11.9	0.701	0.105	313	242.8	598.9	1.178	1.793
155	68.1	18.0	1.167	0.207	314	168.9	358.0	1.202	1.633
156	333.3	511.9	0.695	0.746	316	90.3	248.5	0.328	0.557
157	49.8	15.9	1.358	0.242	317	37.6	30.7	0.476	0.293
158	114.7	74.1	0.516	0.315	318	177.9	82.4	0.088	0.137
159	47.8	13.1	0.429	0.130	319	46.9	11.2	0.958	0.158
160	1368.8	3536.6	0.706	1.153	320	71.1	21.3	1.990	0.235
161	32.7	9.4	0.662	0.150	321	139.9	86.9	2.172	0.508
162	391.3	958.8	0.729	1.141	322	73.6	22.5	0.875	0.186
163	82.0	96.5	0.328	0.412	323	30.0	2.9	1.212	0.074
164	21.3	15.3	1.390	0.511	324	35.7	5.3	0.829	0.089
165	11.4	4.3	0.583	0.144	325	32.0	4.8	0.766	0.084
172	55.6	59.5	1.814	1.241	326	35.6	4.1	0.776	0.065
173	19.6	0.8	1.001	0.024	327	25.4	2.3	0.758	0.052
174	42.9	4.2	0.732	0.051	328	28.2	2.8	0.970	0.065
175	50.7	7.3	0.706	0.079	329	32.1	5.3	0.887	0.106
176	51.5	8.3	0.652	0.089	330	38.1	9.1	1.413	0.195
177	305.0	130.7	0.079	0.123	331	39.4	10.6	0.934	0.180
178	22.1	1.8	1.003	0.058	332	1503.7	4093.5	0.981	1.649
179	42.4	7.3	0.932	0.111	333	835.0	2139.4	0.546	0.895
180	44.3	8.9	0.415	0.088	334	210.6	520.1	0.691	1.088
181	28.6	2.9	1.192	0.083	338	10.7	3.8	1.245	0.304
182	18.6	1.9	0.982	0.073	339	20.3	3.5	1.088	0.116
183	62.9	33.4	0.674	0.301	340	27.8	4.0	0.729	0.078

184	11.2	2.2	0.821	0.120	341	34.7	4.9	0.833	0.079
185	10.8	3.0	0.776	0.136	342	49.0	9.3	0.805	0.094
186	13.6	5.7	0.934	0.247	343	62.7	16.5	0.965	0.167
193	460.9	407.6	0.251	0.336	344	83.0	24.7	0.848	0.177
194	109.4	19.6	0.417	0.079	345	32.7	6.6	0.839	0.112
195	26.7	1.6	0.825	0.034	346	22.9	3.5	0.665	0.080
196	70.5	13.3	0.828	0.111	347	1450.8	3725.2	0.701	1.138
197	47.9	7.0	1.091	0.107	348	29.4	3.0	0.396	0.047
198	63.7	12.6	0.436	0.085	349	181.7	87.1	0.192	0.210
199	26.5	2.3	1.066	0.057	350	62.0	18.3	0.462	0.143
200	74.8	20.0	0.662	0.142	351	54.8	14.1	0.454	0.123
201	56.5	12.6	0.466	0.105	352	54.5	21.7	0.507	0.194
202	50.7	9.1	1.002	0.123	353	57.5	38.4	0.701	0.328
203	30.9	4.3	0.766	0.083	354	473.7	1075.0	0.268	0.439
204	26.8	3.7	0.889	0.094	359	6.6	1.7	1.227	0.164
205	109.2	43.1	0.101	0.140	360	53.6	34.2	0.620	0.194
206	73.2	51.1	0.669	0.370	361	89.2	40.8	0.325	0.179
207	63.3	51.4	0.980	0.582	362	38.7	5.9	0.619	0.065
208	27.2	30.2	0.262	0.381	363	25.2	2.4	1.033	0.065
213	781.2	2054.9	0.453	0.760	364	23.6	2.9	0.822	0.065
214	55.4	7.4	0.589	0.062	365	38.4	12.7	0.778	0.163
215	77.2	11.9	0.484	0.071	366	71.9	96.3	1.351	0.930
216	38.3	3.2	0.808	0.047	367	15.0	5.0	1.232	0.215
217	38.5	4.0	0.867	0.064	368	320.8	867.0	1.091	1.794
218	59.9	12.3	0.802	0.123	369	32.7	14.1	0.505	0.157
219	33.8	3.9	0.810	0.070	370	75.0	38.0	0.340	0.234
220	43.8	6.8	0.873	0.098	371	149.1	167.6	1.949	1.081
221	42.2	6.3	0.763	0.088	372	107.0	74.0	0.349	0.299
222	43.6	8.3	0.649	0.099	373	31.9	17.4	0.502	0.241
223	51.7	8.9	0.730	0.099	374	12.5	4.1	1.134	0.264
224	24.0	2.2	0.891	0.059	375	78.4	193.4	0.274	0.449
225	22.1	2.1	0.771	0.061	381	9.4	4.3	0.922	0.120
226	245.2	75.1	0.051	0.082	382	931.2	2396.7	0.383	0.639
227	39.9	7.9	1.423	0.167	383	18.1	2.4	0.698	0.062
228	25.6	4.8	0.864	0.102	384	33.9	6.9	0.898	0.112
229	16.0	3.8	0.594	0.074	385	17.1	3.0	0.789	0.092
230	17.8	20.7	1.061	0.574	386	109.0	210.2	1.137	1.334
233	15.3	7.0	0.336	0.201	387	24.9	16.9	1.042	0.355
234	22.7	3.1	1.457	0.129	388	18.5	12.5	1.595	0.388
235	36.6	2.5	0.673	0.034	389	31.6	27.9	1.109	0.556
236	50.1	4.9	0.635	0.049	390	34.8	26.1	0.370	0.294
237	53.3	7.0	0.605	0.067	391	127.4	245.9	0.372	0.585
238	69.8	11.3	0.441	0.078	403	26.1	21.4	0.128	0.204
239	51.8	8.5	0.549	0.083	404	41.5	37.1	0.126	0.207
240	38.3	5.6	0.815	0.086	405	39.1	13.3	0.058	0.096
241	59.5	11.9	0.939	0.130	406	421.3	1131.5	0.599	1.003
242	41.9	5.6	0.748	0.076					

Appendix L. The Horizontal to Vertical Spectral Ratios (HVSR) (grey lines) computed from the western Greece dataset (**Figure 5**) of S-wave Fourier Amplitude Spectra, also used at the corresponding GIT application (*ch*. 3.3.3) of this study. Their geometric mean and the corresponding standard deviation range are depicted (black lines).

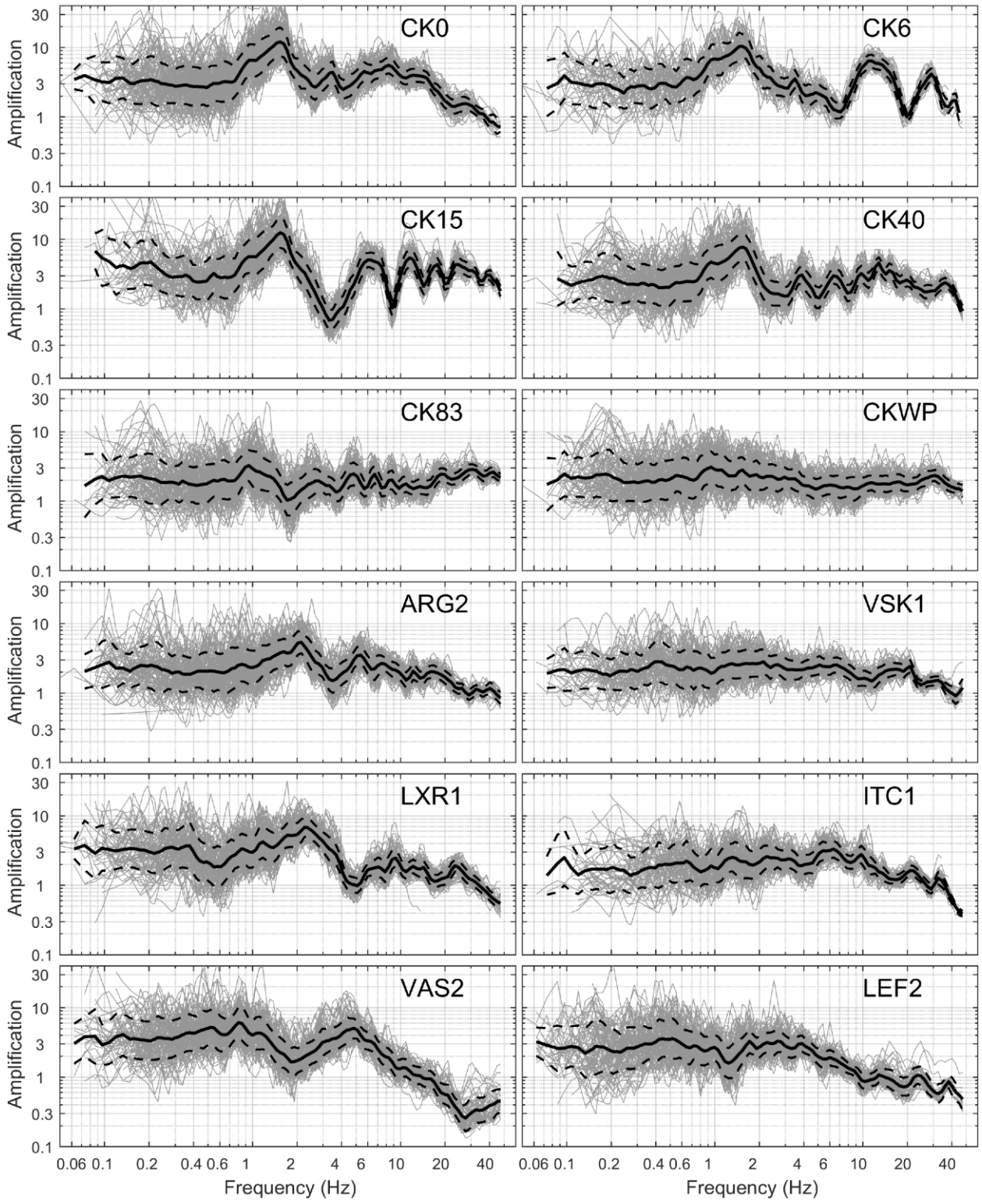

Appendix L. (continue)

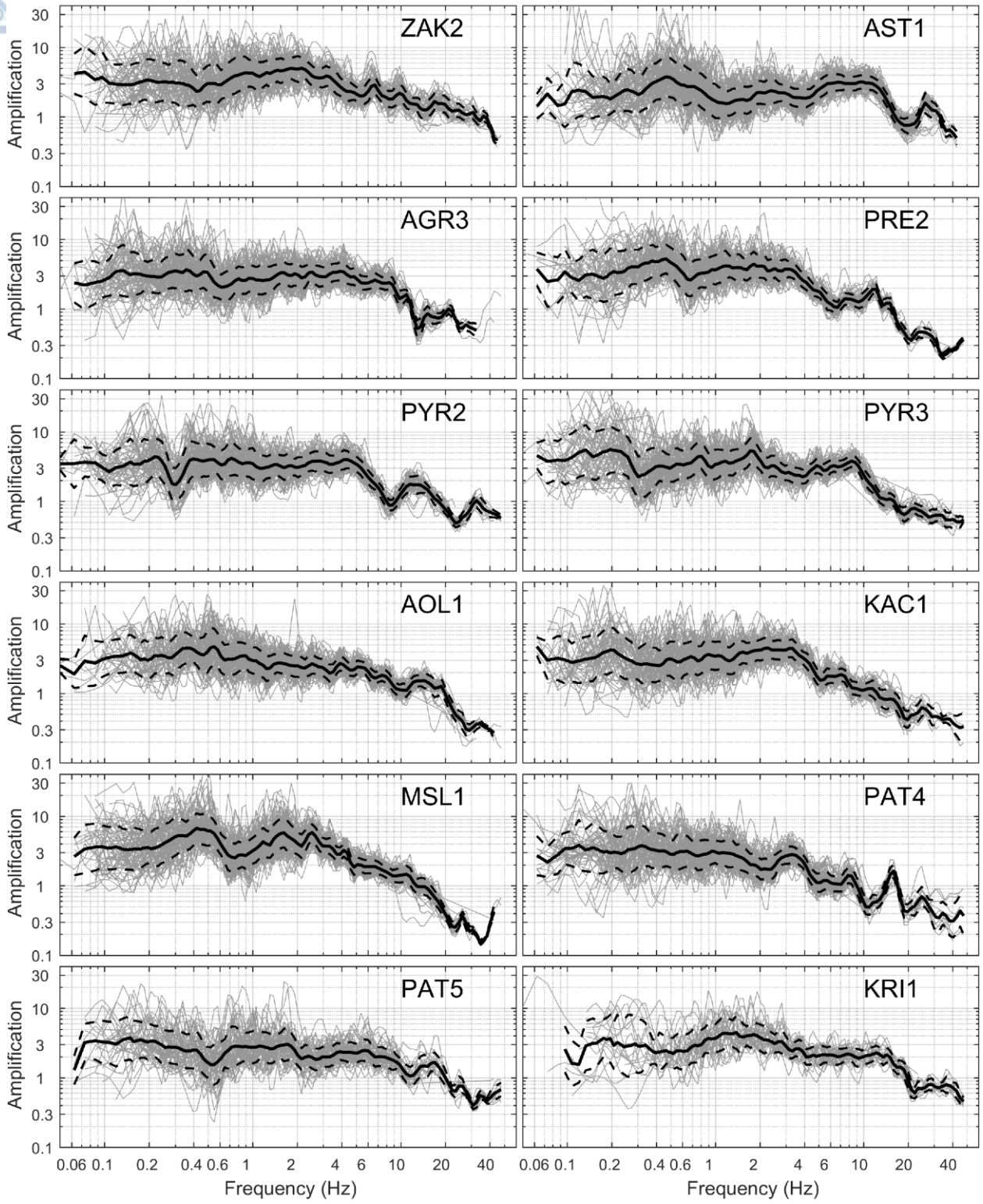

Appendix M. The post-inversion computed (Eq. [7]) non-parametric source spectra (grey lines), for each earthquake of **Appendix B** (details into the text), corresponding to their id (YYYYMMDD_hhmmss). With black lines the average values and their standard deviation are presented, while with red lines the corresponding parametric Brune's (Eq. [7]) source factors computed by the GIT method and the calculated seismic moment, M_w and corner frequency, f_c, are depicted (**Appendix B**).

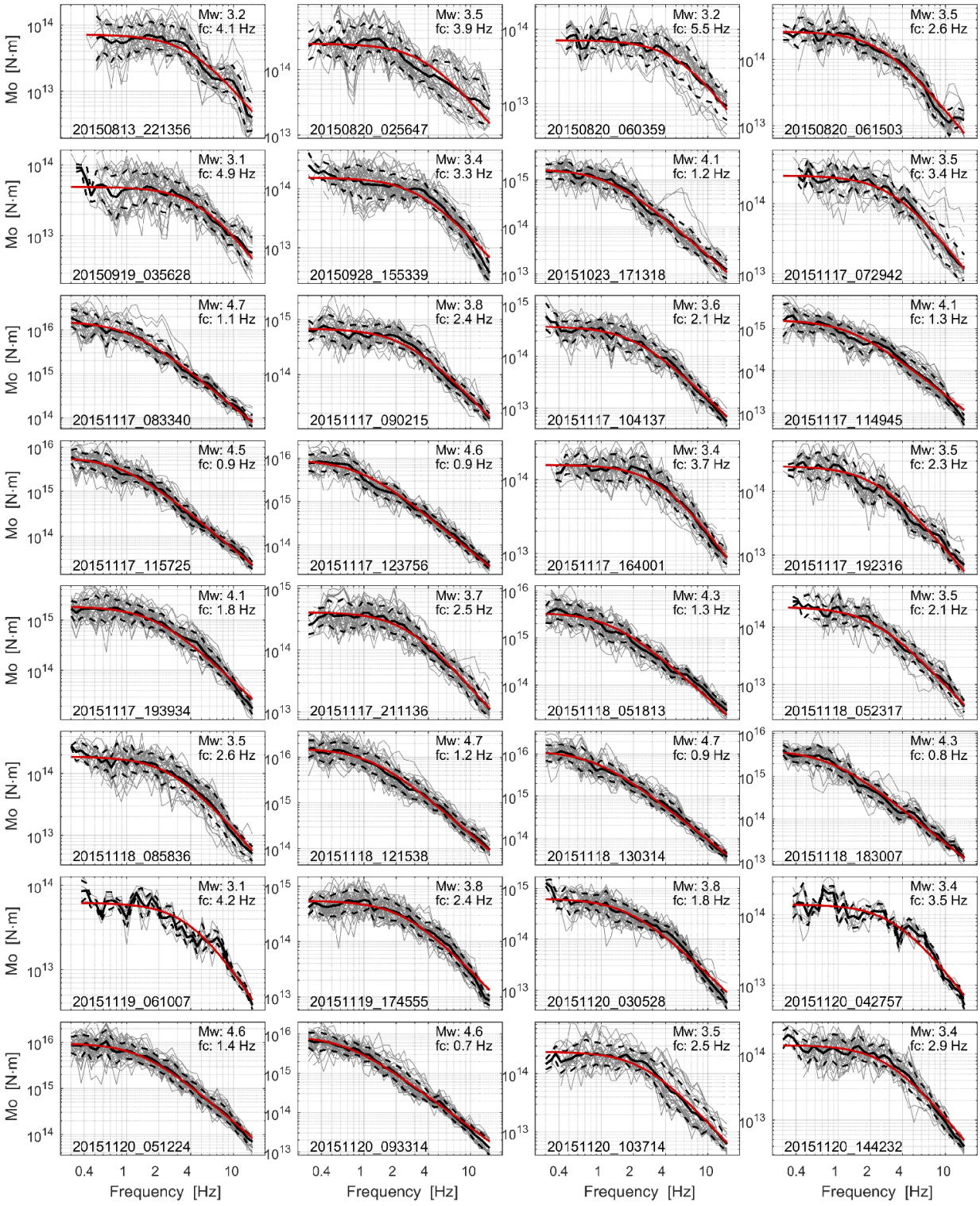

Appendix M. (continued)

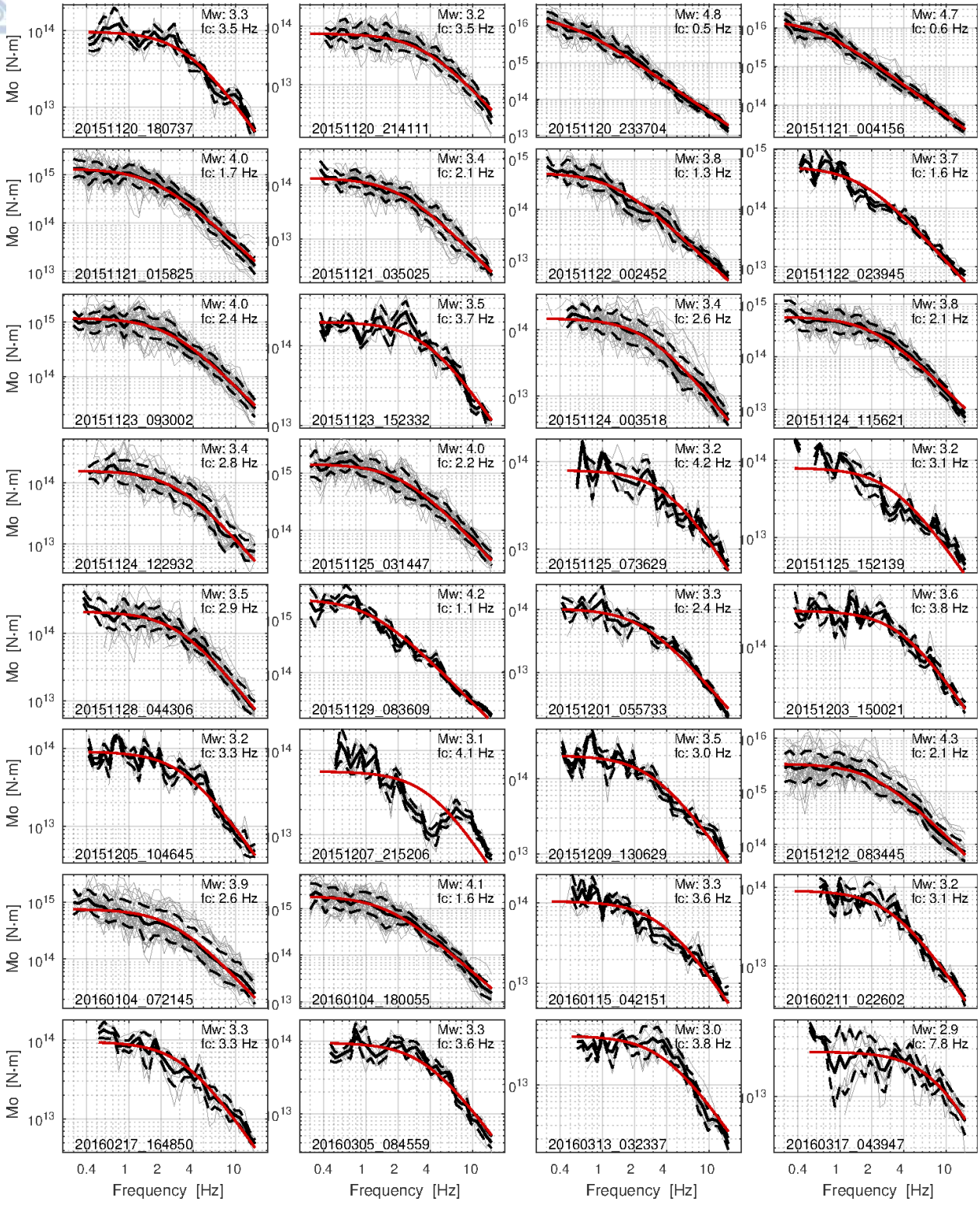

Appendix M. (continued)

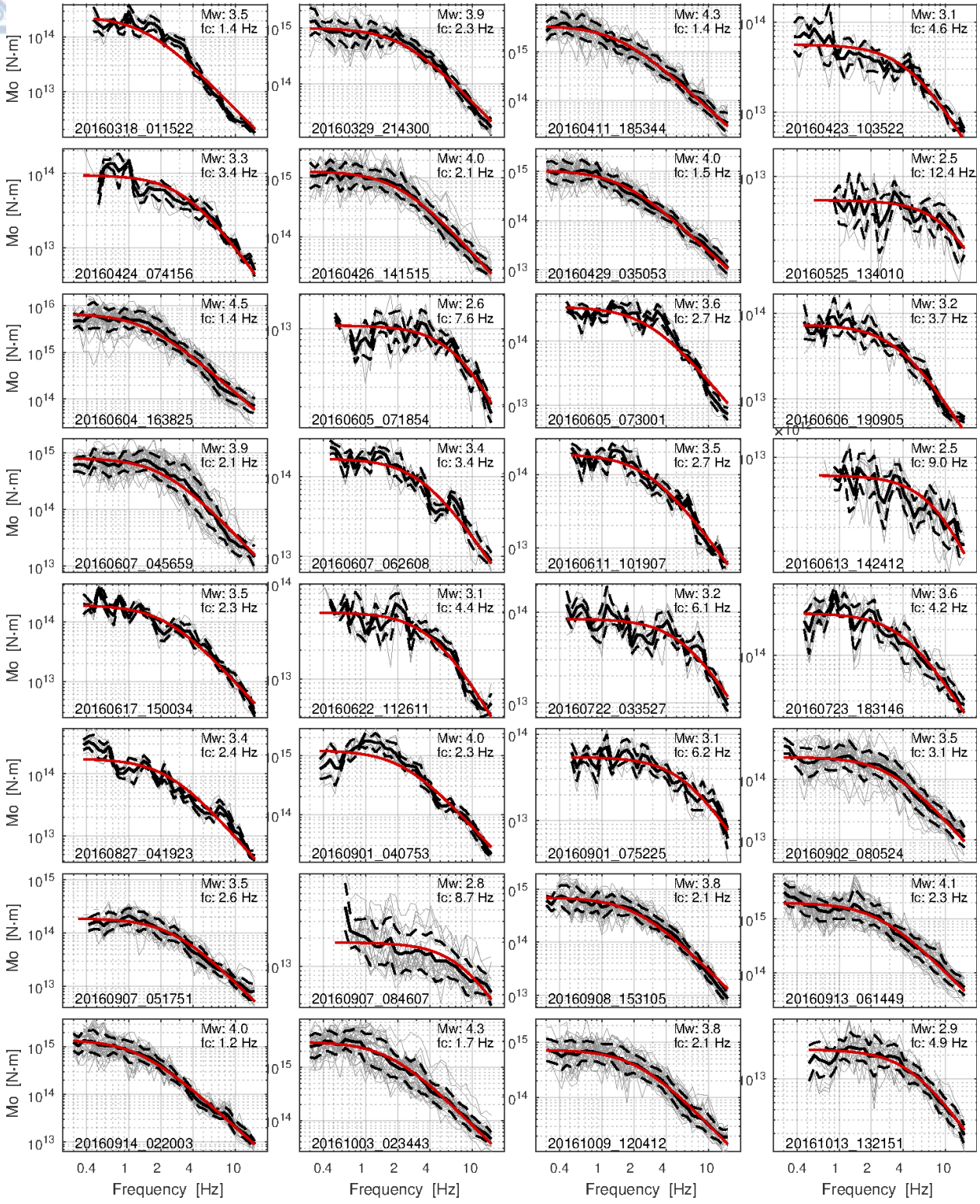

Appendix M. (continued)

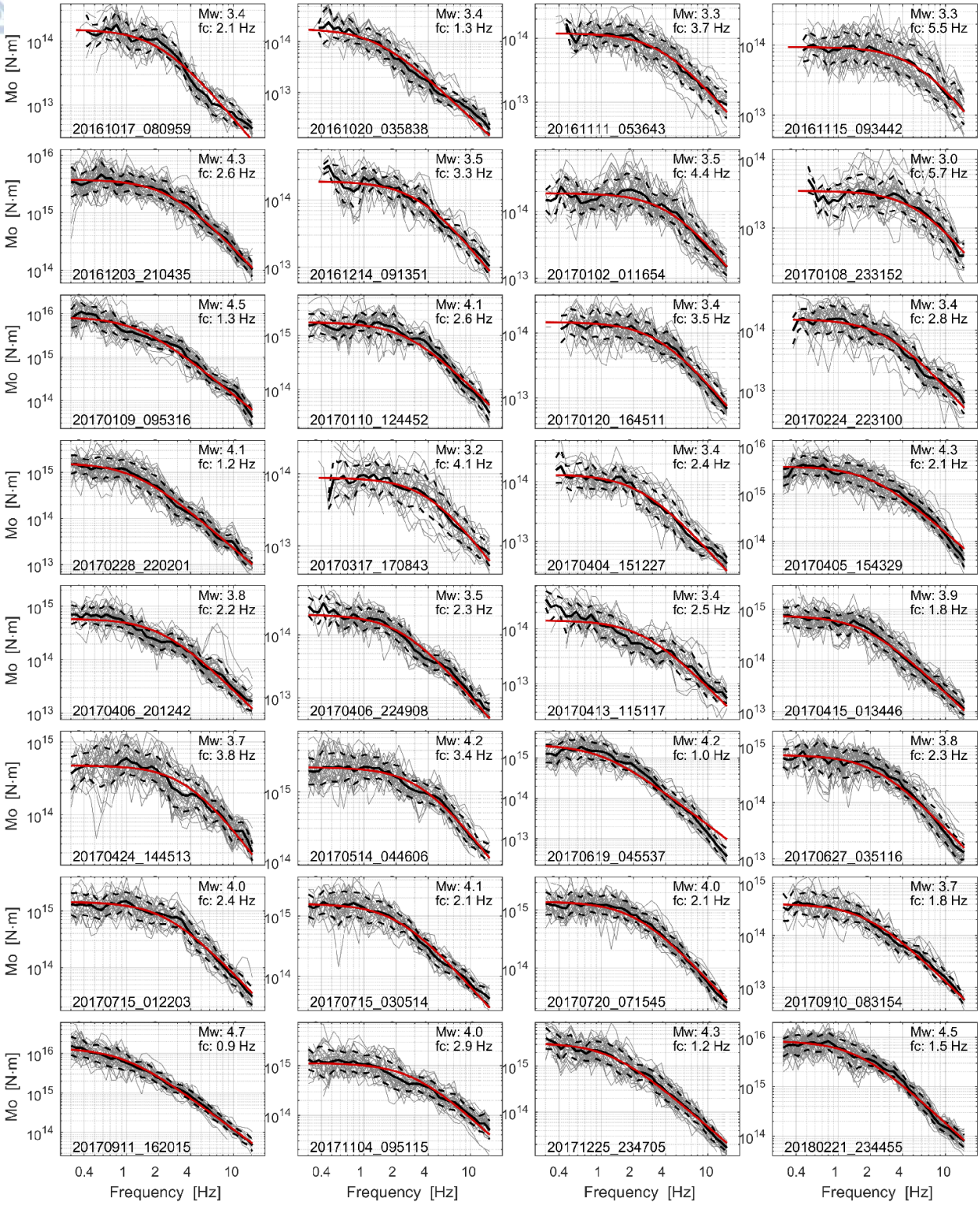

Appendix M. (continued)

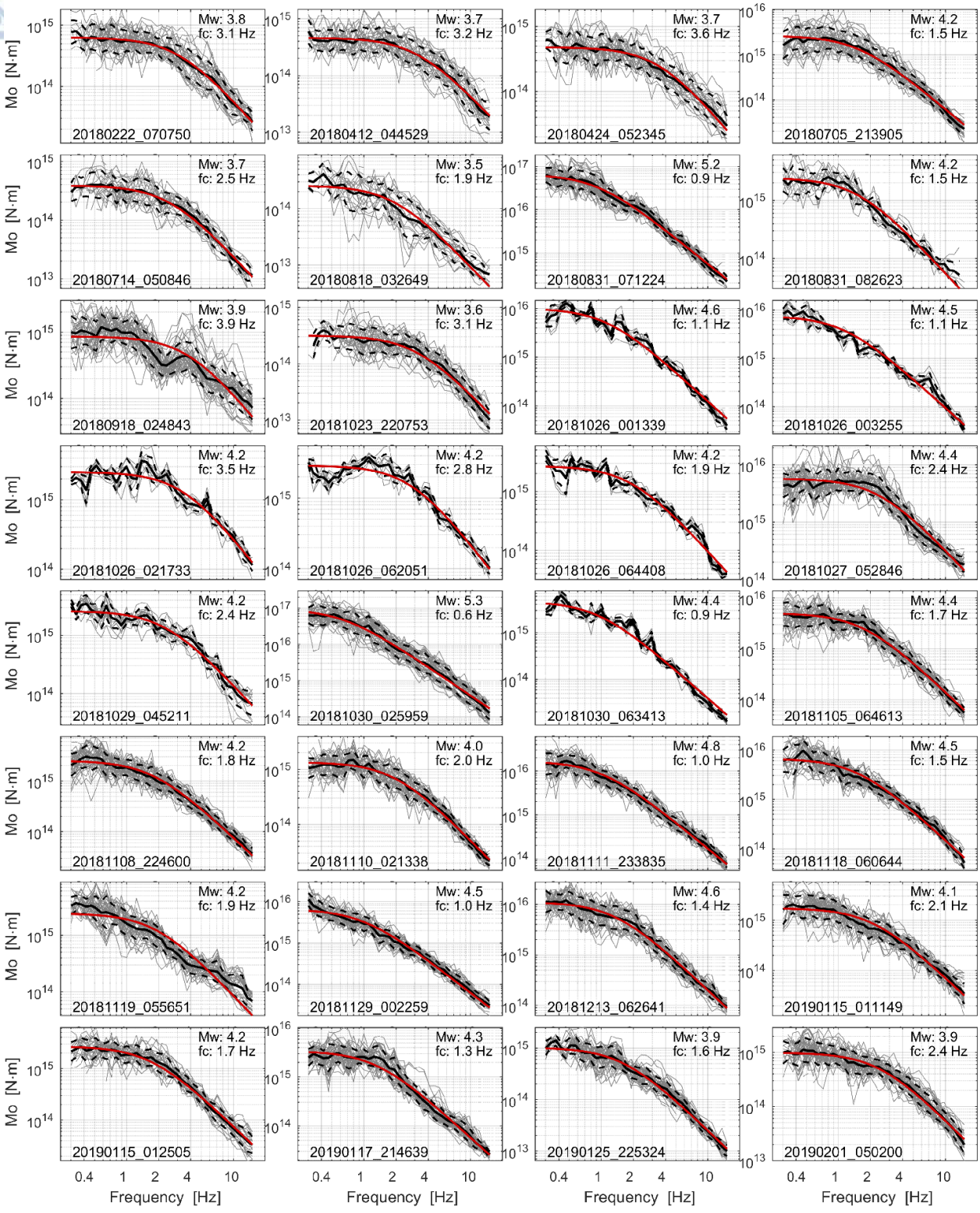

Appendix M. (continued)

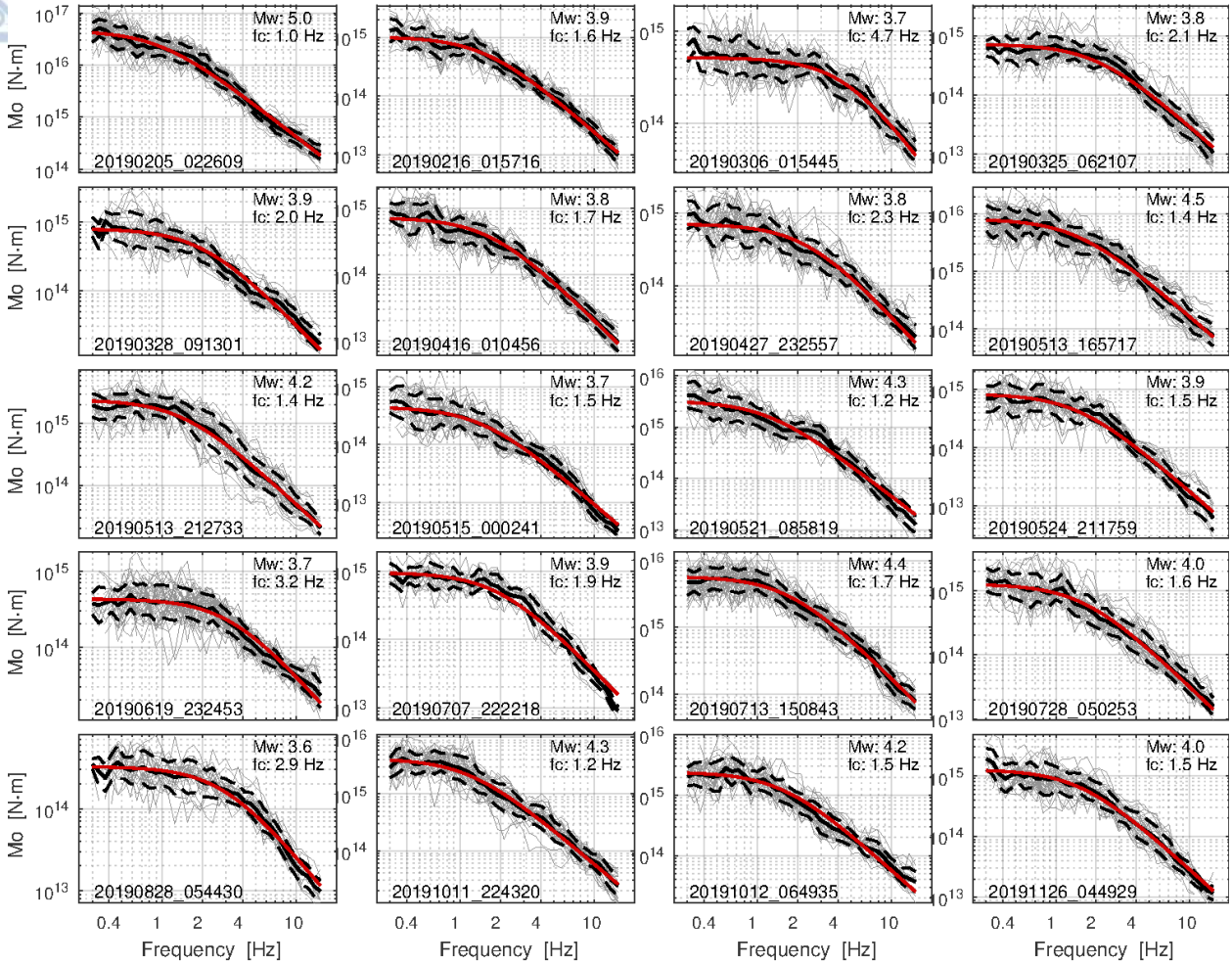

Appendix N. The $Q_c(f)$ models (red lines) and their standard deviation range (red dashed lines) computed from each pair of earthquake-station for all the 24 examined sites and the 89 earthquakes examined (**Figure 5**) (same as all the $Q_c(f)$ of **Figure 39**). The geometric mean curve (Q(f), black lines) of each station (sub-plot), based on **Figure 39**, is also displayed.

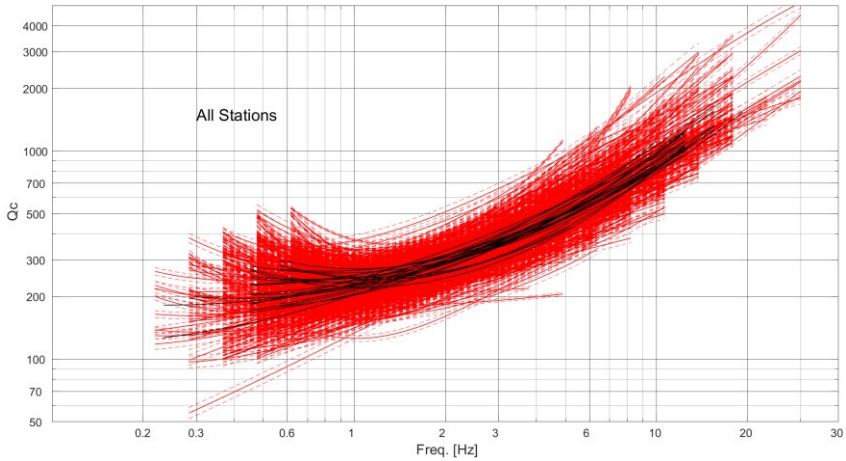

Appendix O. The HVSRs (grey lines), computed based on each estimated $FAS[S\dot{T}F_{comp}^{sc}]$ (Eq. [32], e.g. **Figure 37**), at each one of the 24 sites shown in **Figure 7** and **Appendix C**, for the examined 88 earthquakes (**Figure 7** and **Appendix B**), their geometric mean (black lines) and the corresponding standard deviation range (in logarithmic scale).

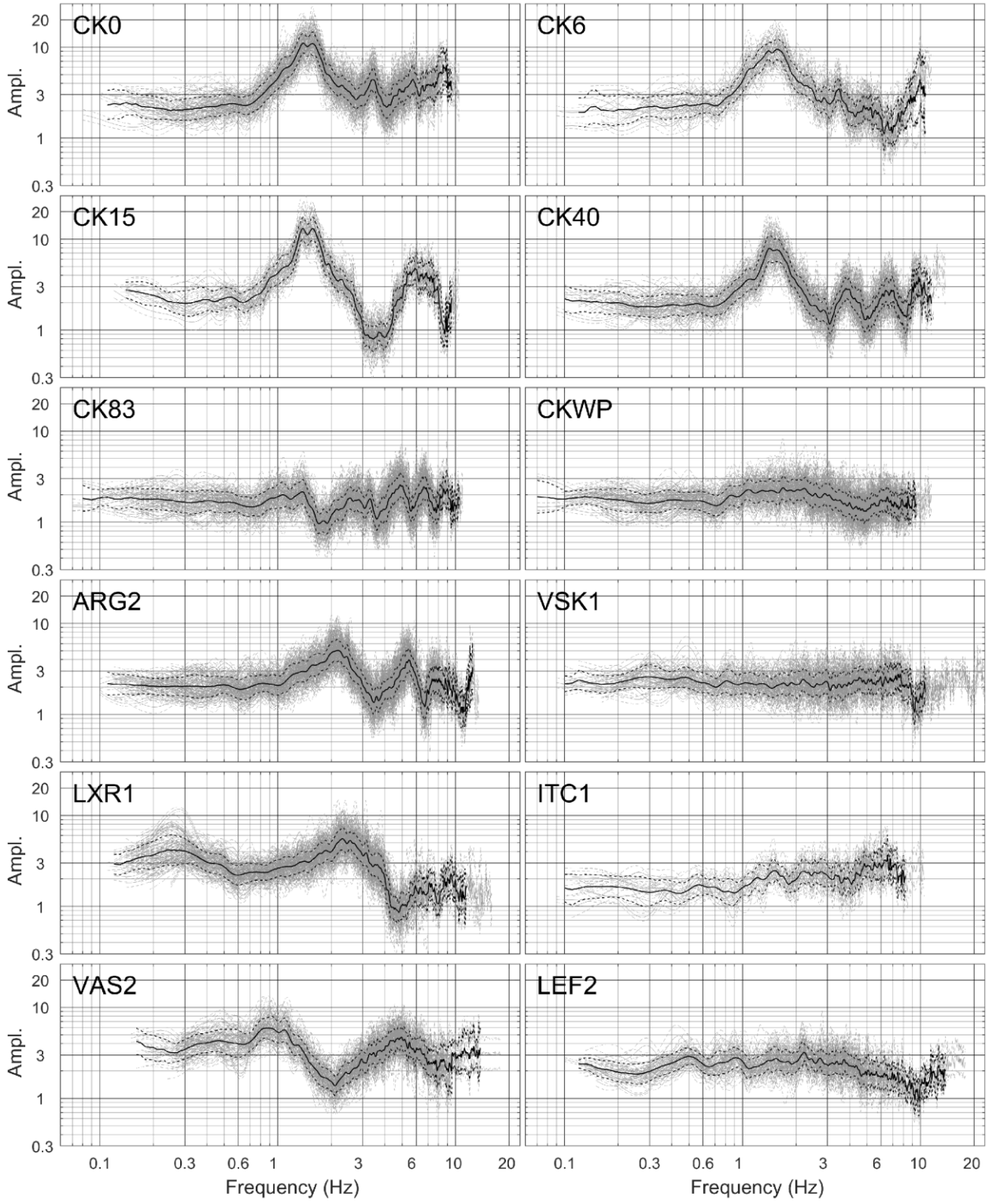

Appendix O. (continued)

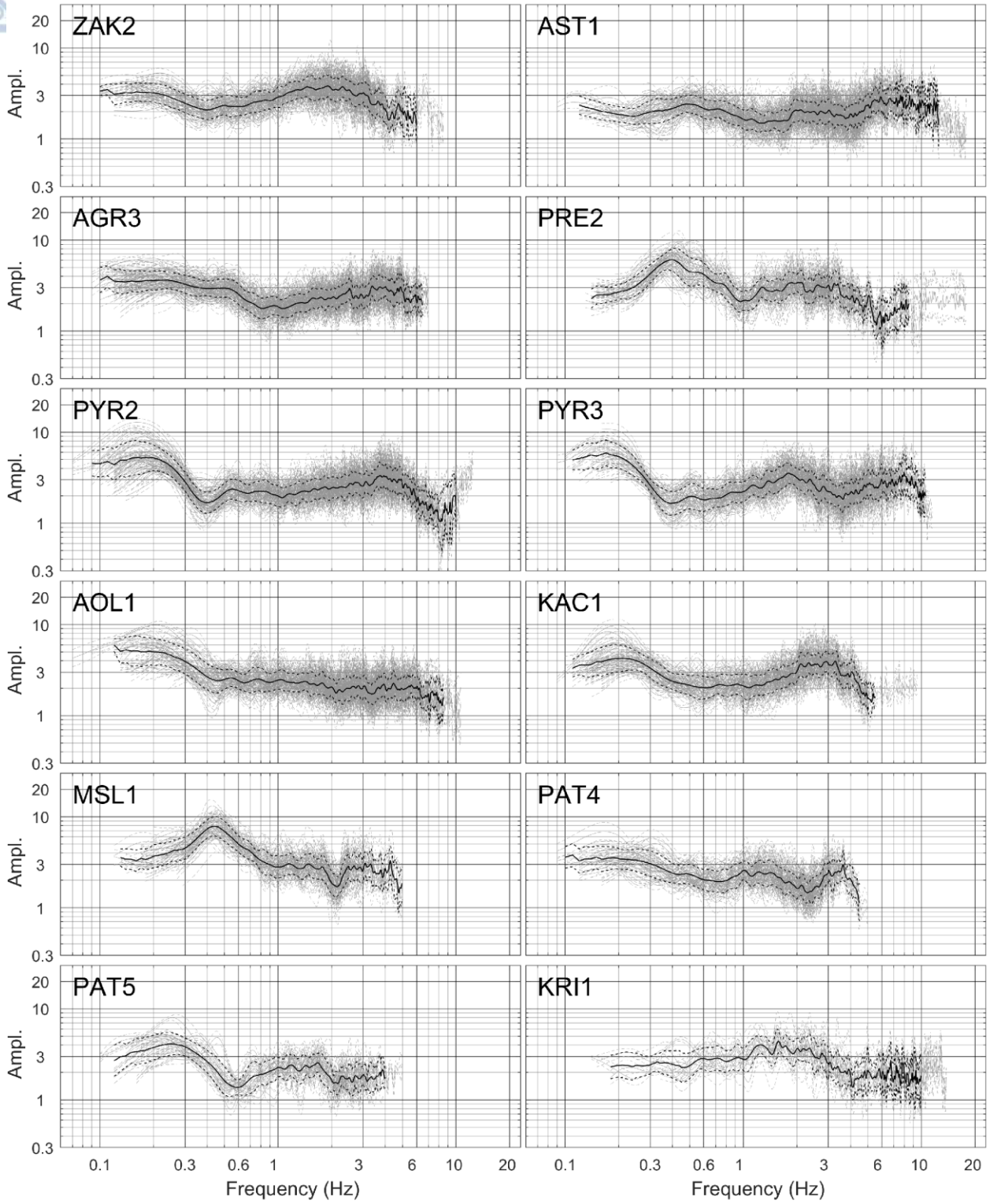

Appendix P. The corresponding to **Figure 43** and **Figure 45**, $SAFs(f)$, using station "AST1" as reference (black lines).

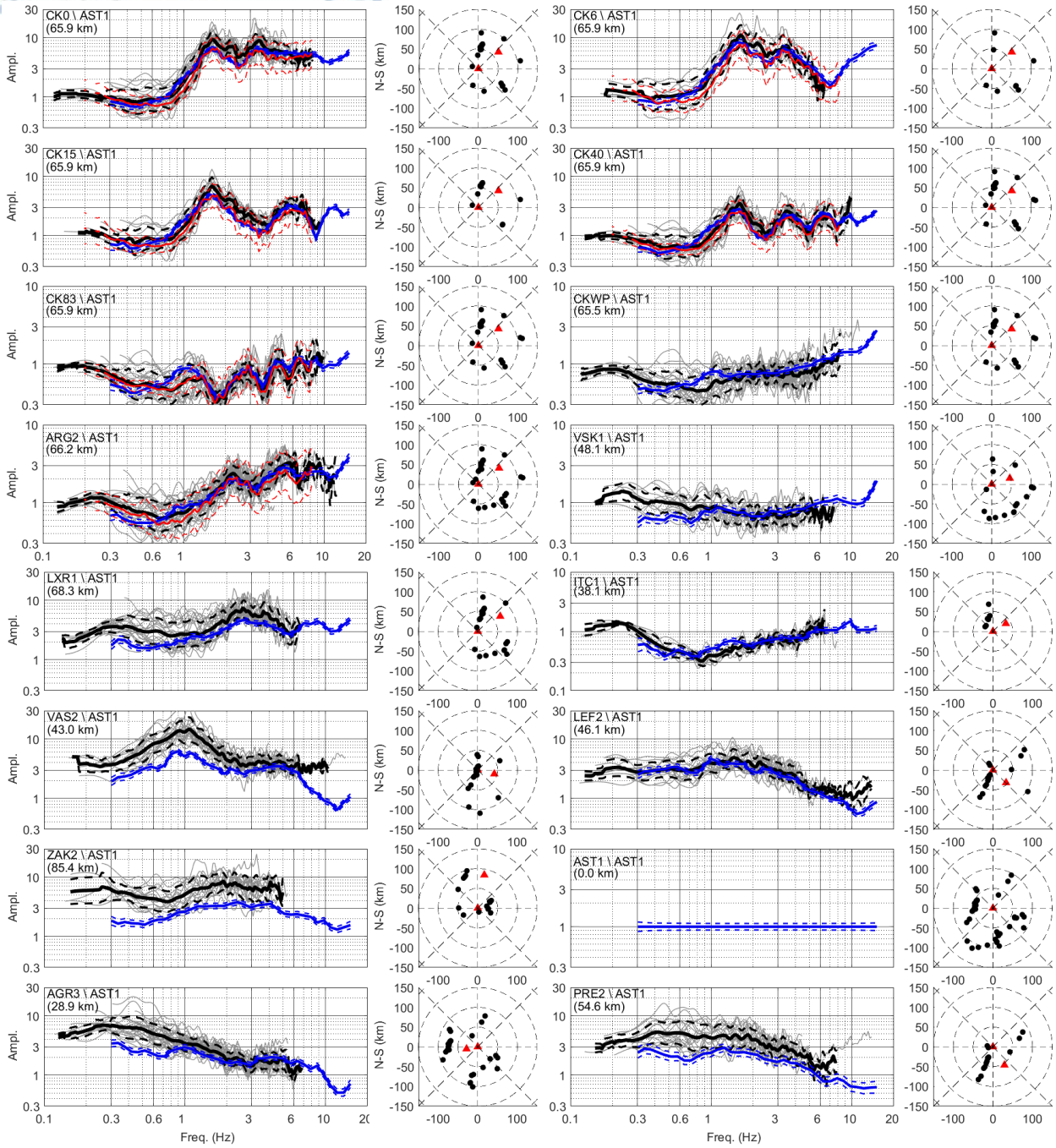

Appendix P. (continued)

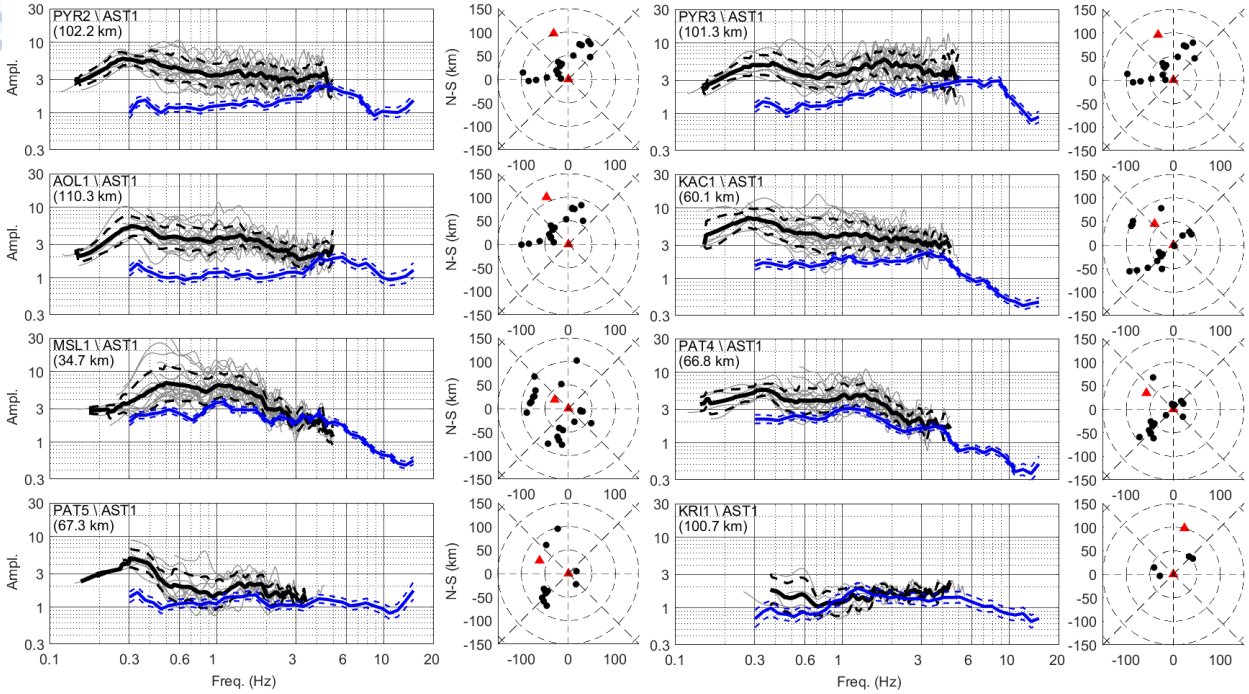

Appendix Q. The corresponding to **Figure 43** and **Figure 45**, $SAFs(f)$ using station "ITC1" as reference (black lines)

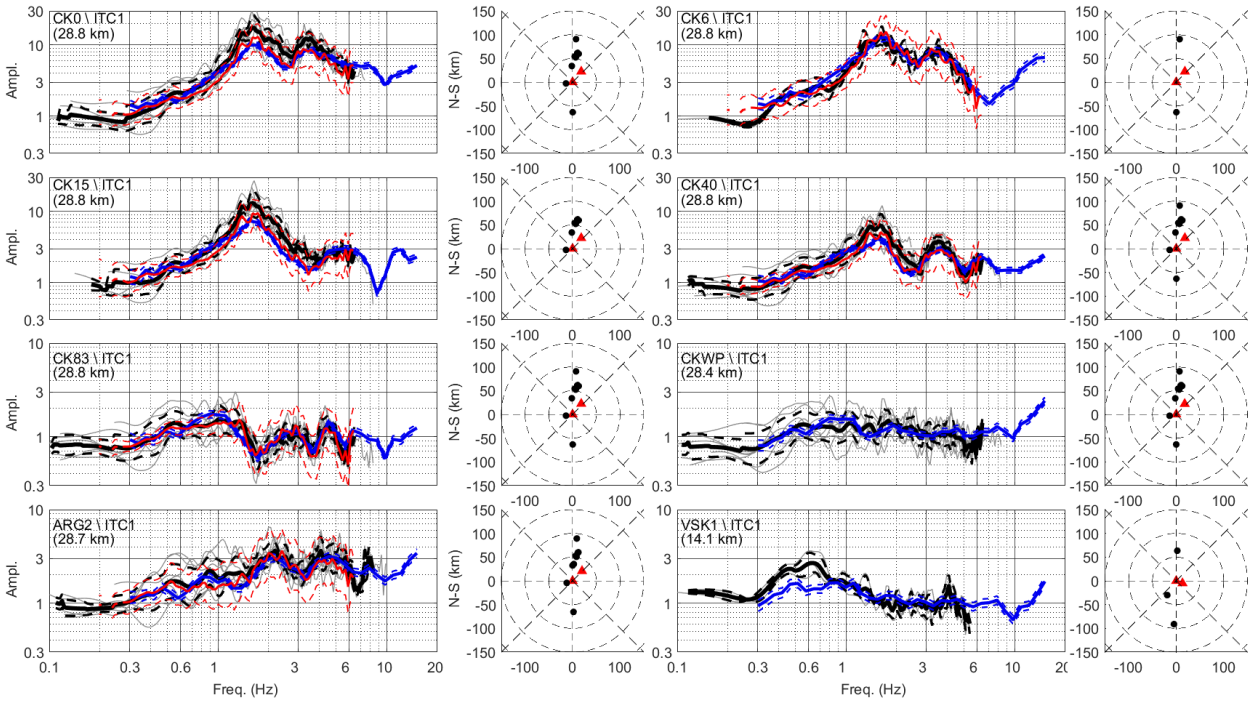

Appendix Q (continued)

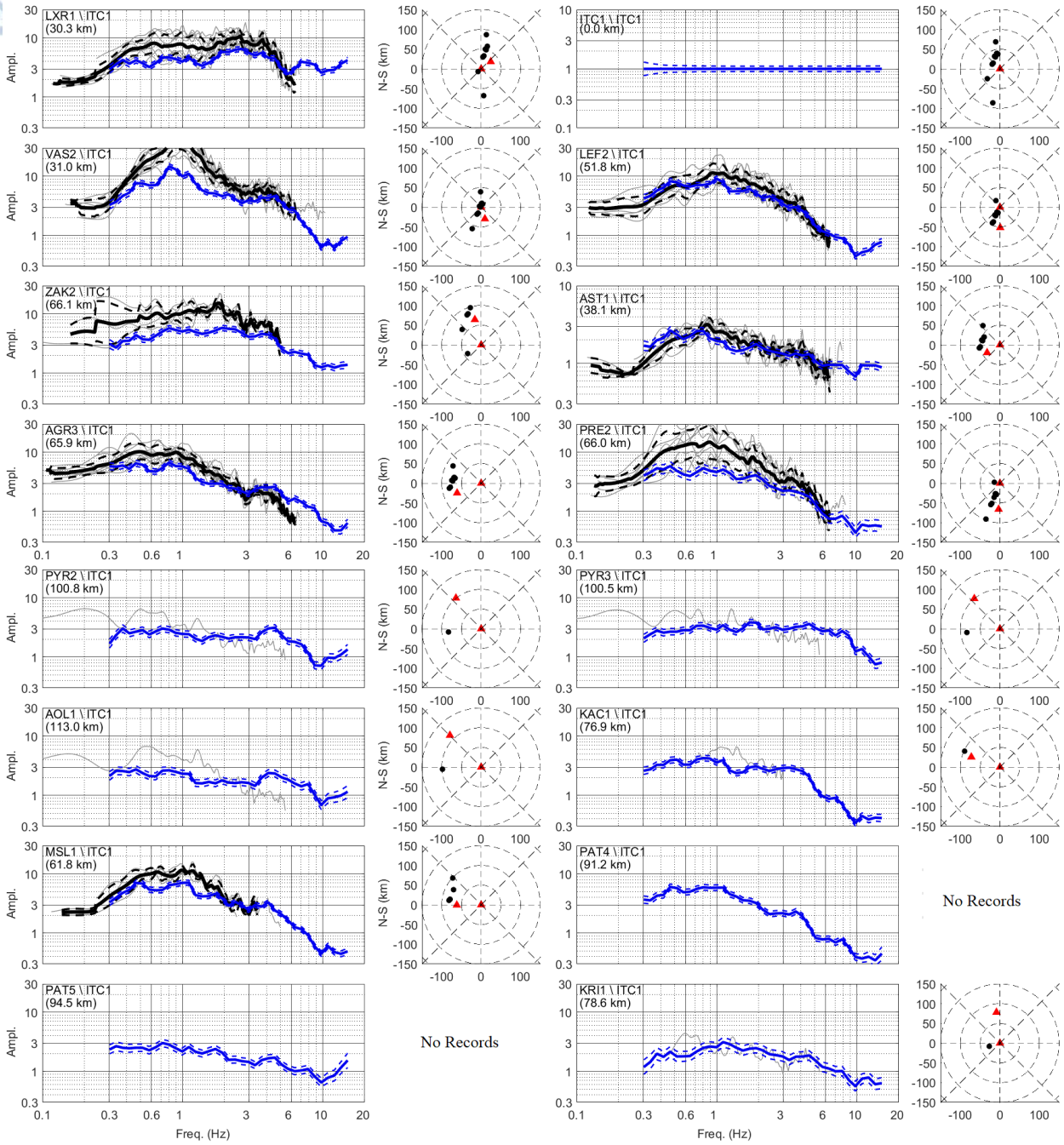

Appendix R. The corrected for the SAF(f) (**Figure 45**), FAS[STF^{sc}], of all the 89 earthquakes (**Appendix B**), corresponding to each coda wave record (common horizontal components), selected at each one of the 24 sites (**Appendix C**), for which the SFC analysis was applied. The FAS[**STF^{sc}**], are scaled for the constant factor, $\sqrt{\boldsymbol{F}}$ (Eq. [28]).

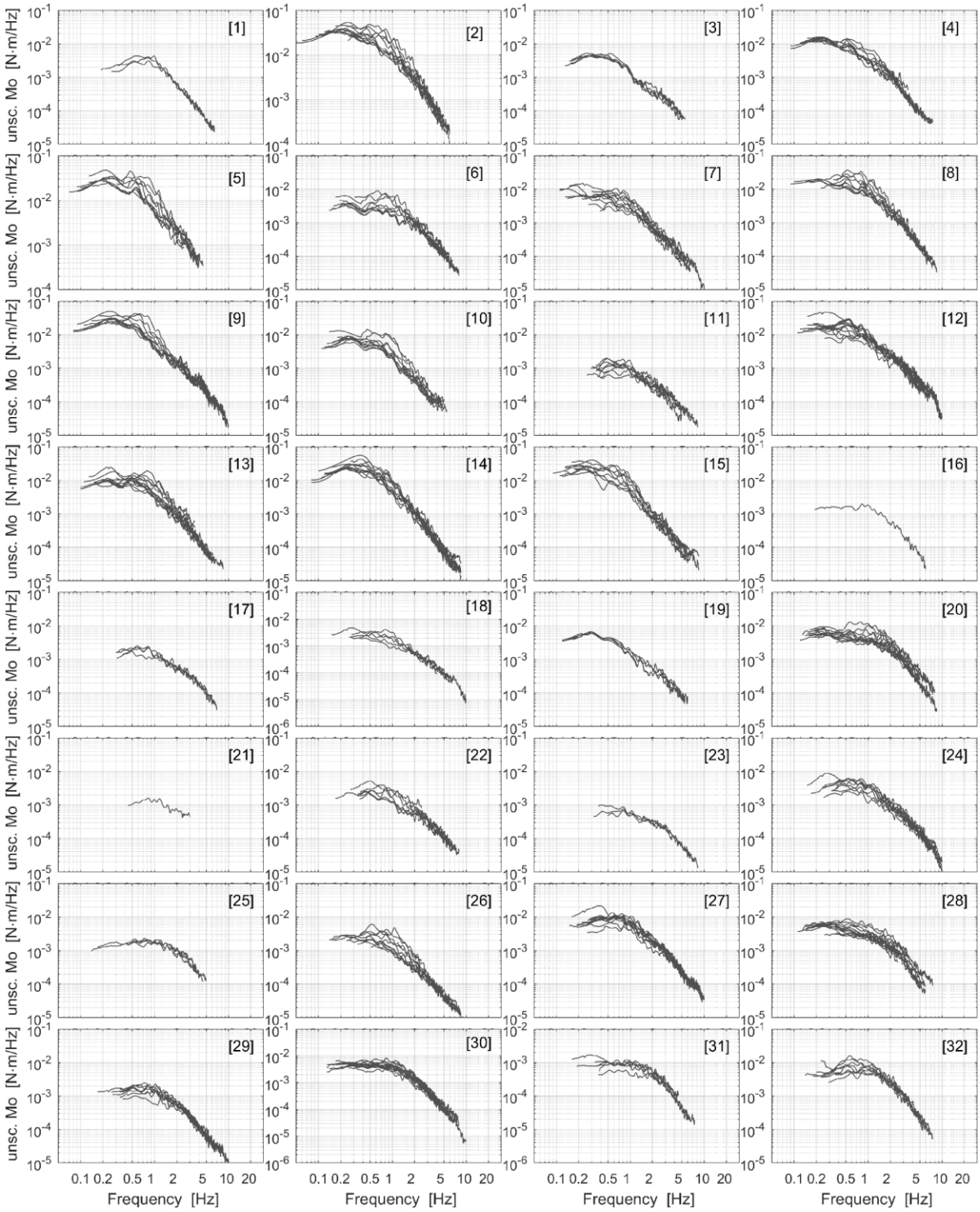

Appendix R. (continued).

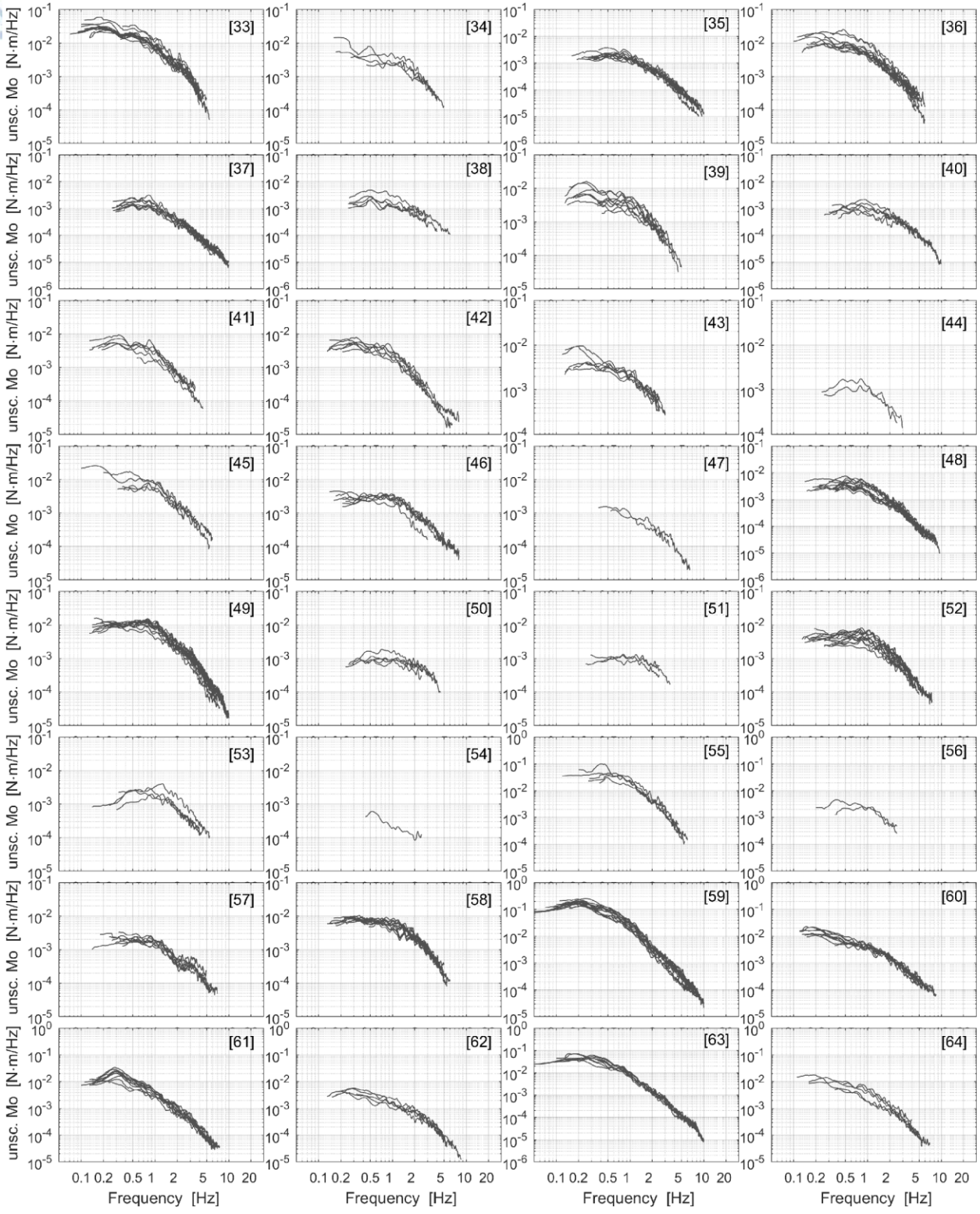

Appendix R. (continued).

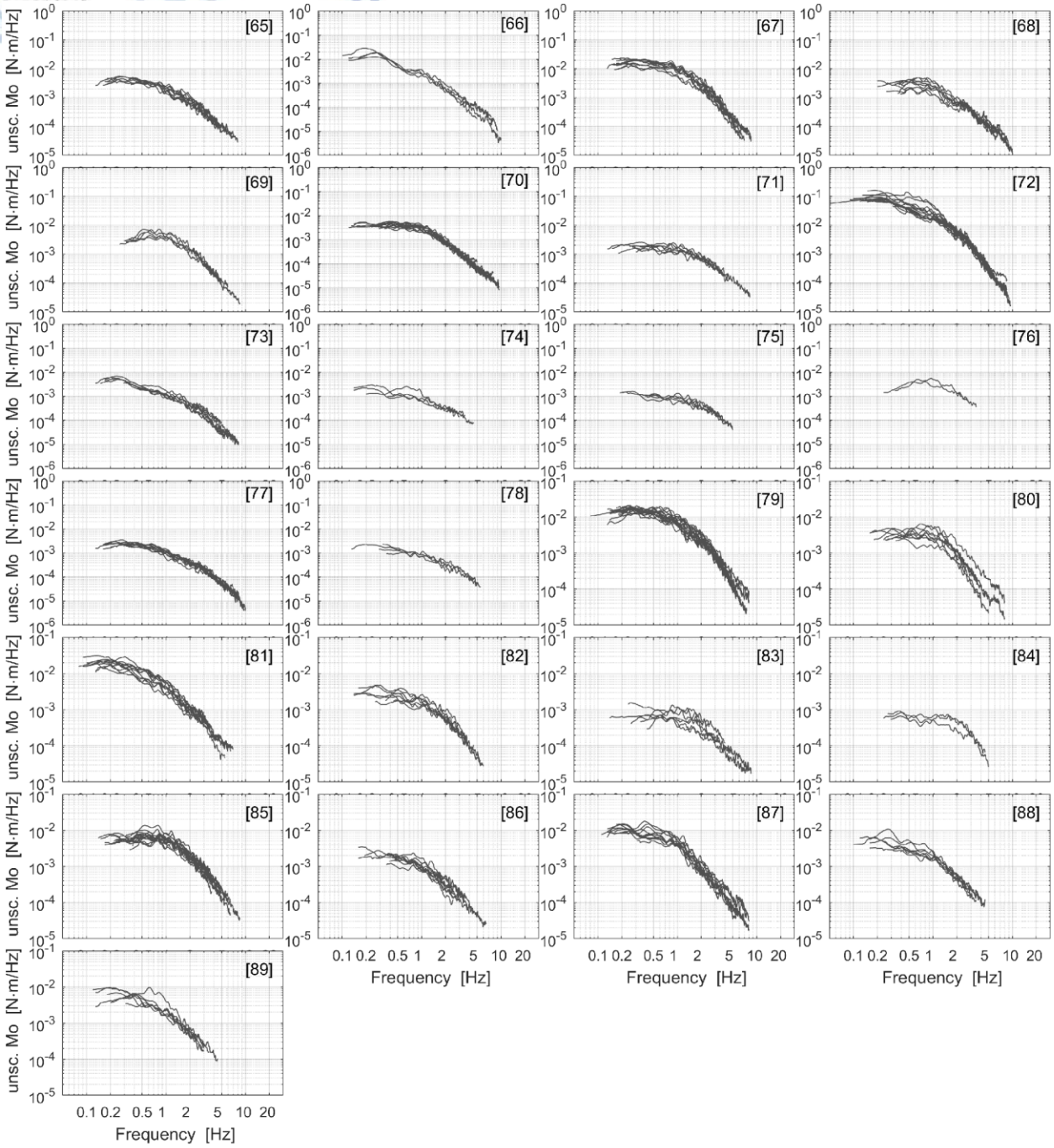

Appendix S. The HVSRs (grey lines), computed based on each estimated $FAS[S\dot{T}F_{comp}^{sc}]$ (Eq. [32], e.g. **Figure 37**), at each one of the 16 sites of **Figure 8** and **Appendix D**), for the examined earthquakes of **Figure 8** and **Appendix F** and their geometric mean (black lines) and the corresponding standard deviation range (in logarithmic scale) .

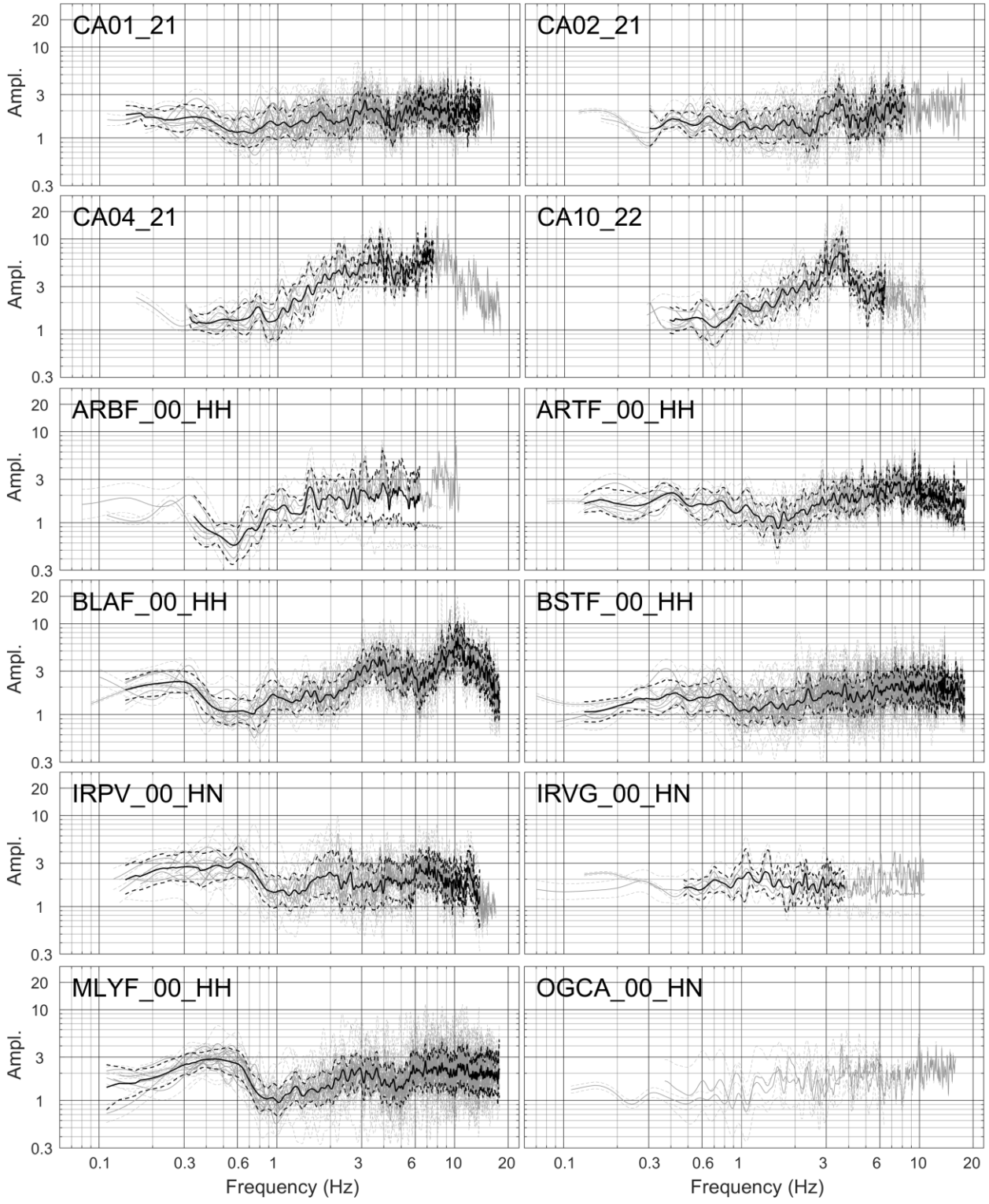

Appendix S. (continued)

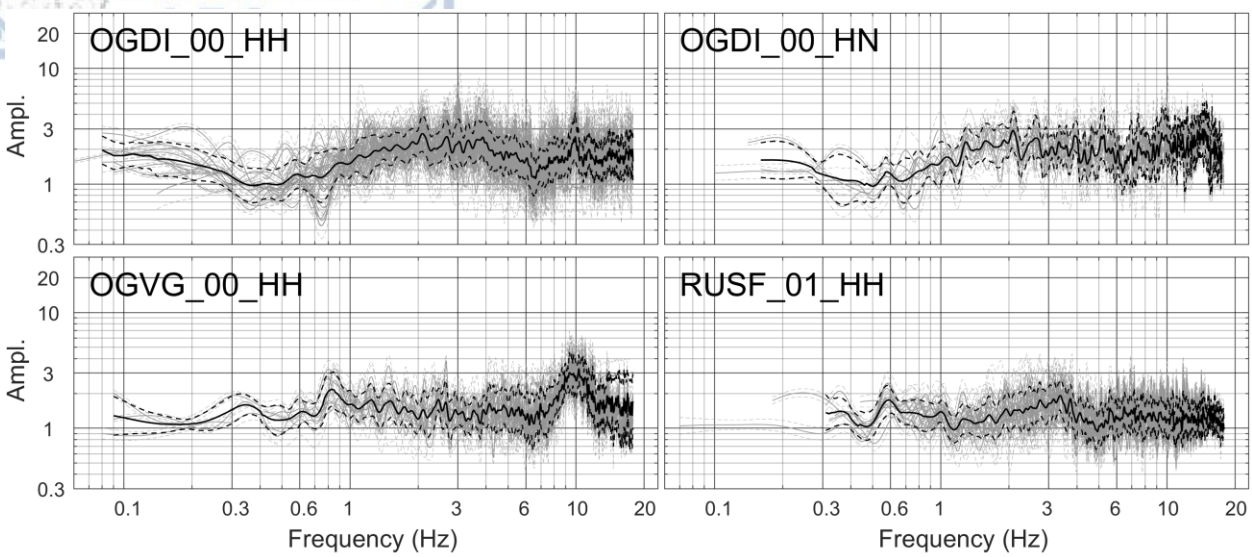

Appendix T. (**left**) The SSR results of the Cadarache examined stations (**Appendix D**), with respect to the CA01_21 station that is considered as "reference". The distance between the target and reference station is also given. (**right**) The epicenters of the earthquakes the records of which were used for the SSR computations. The (0,0) point is the location of the target site, while N-S and E-W represent the North-South and East-West axes (in scale of km).

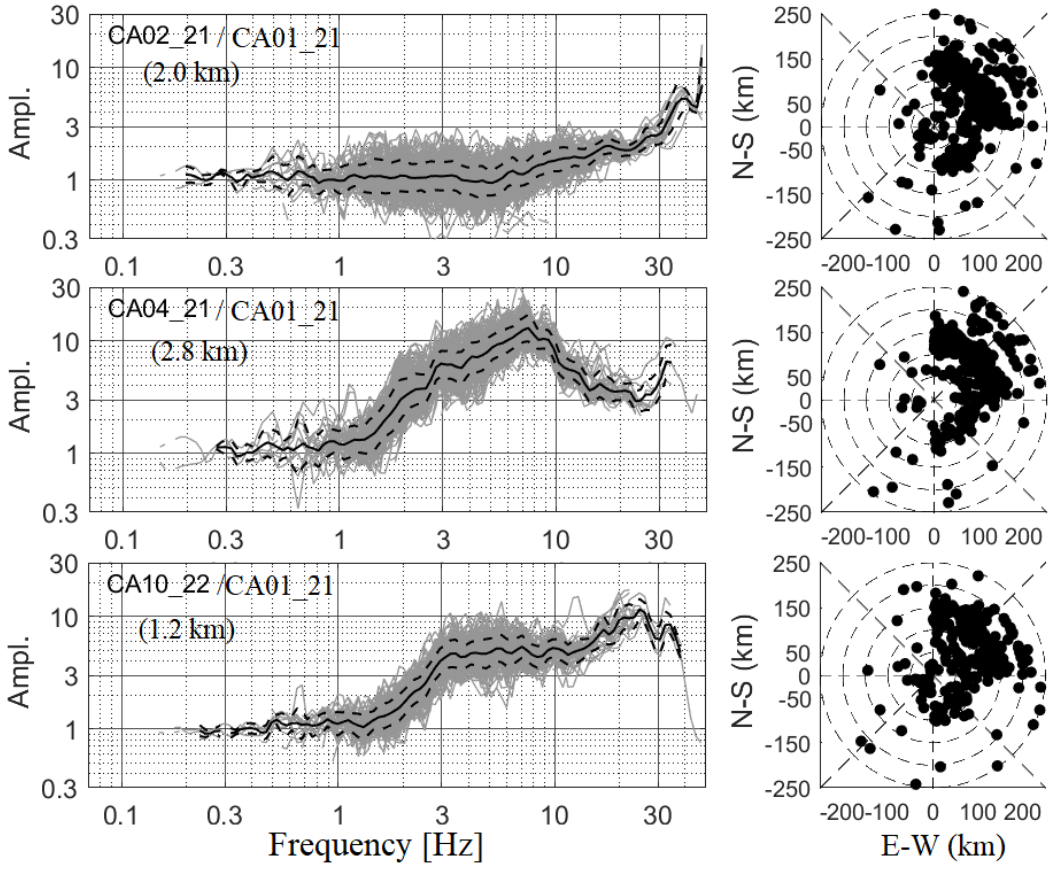

Appendix U. The corresponding figure to **Figure 57**, for the M_w= 4.85 (earthquake id: 2019111_105245). (OM.01, 02 and 03 represent the STFs computed by other methodologies, for the average STF, the minim duration-maximum peak STF and maximum duration-minimum peak, STF, respectively.

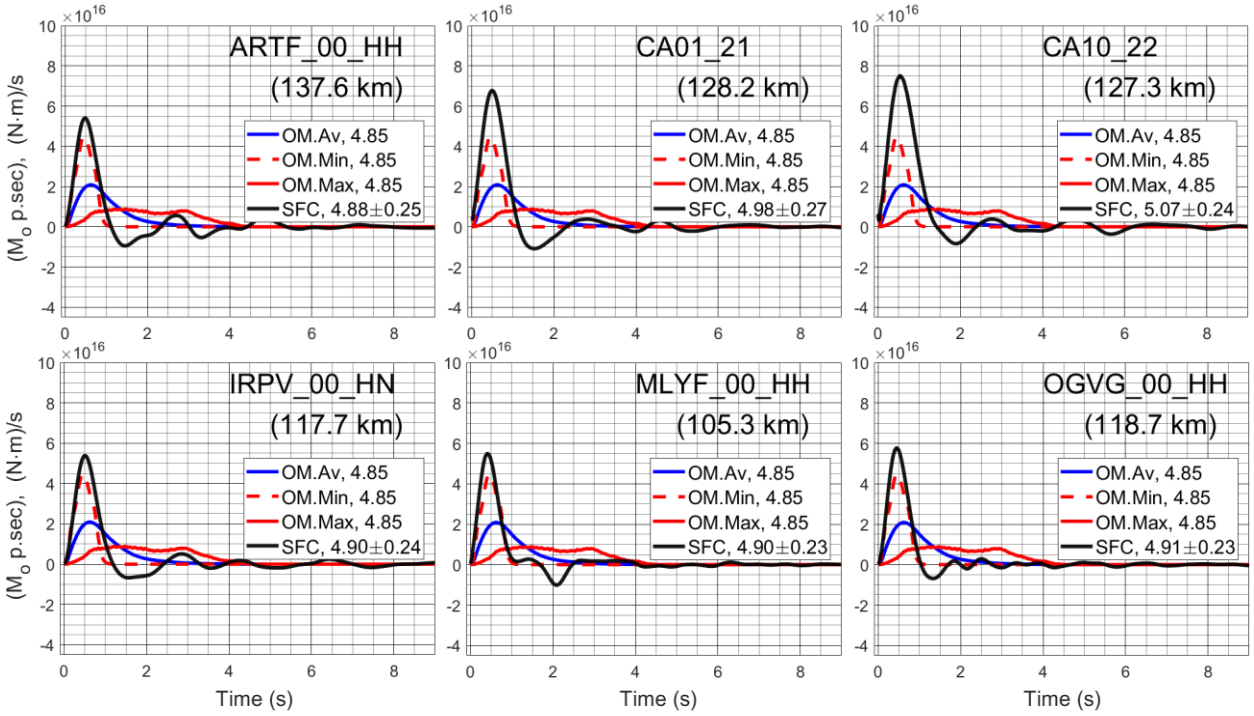

Appendix V. The corresponding FAS of the STF presented in **Appendix U**, for the M_w= 4.85 (earthquake id: 2019111_105245).

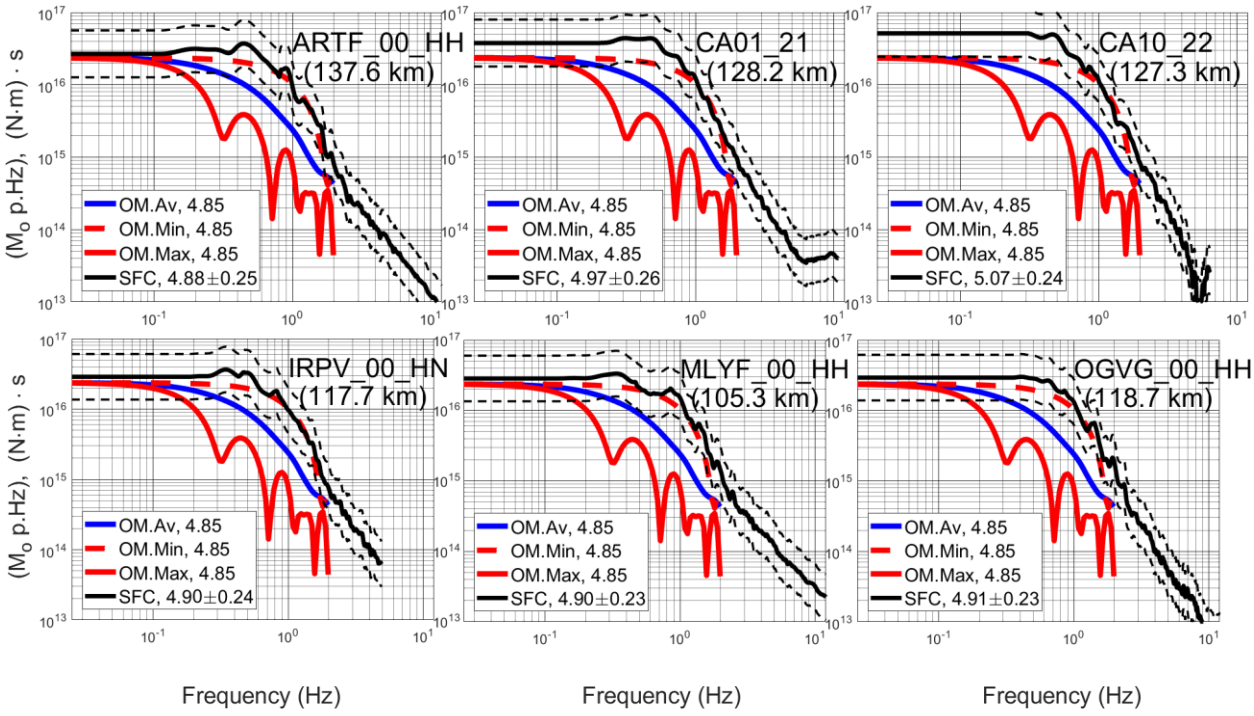

Appendix W. The corresponding figure to **Figure 57**, for the M_w= 6.05 (earthquake id: 20140226_135543). (OM.Av represents the average STF computed by ***Sokos et al., (2015)***.

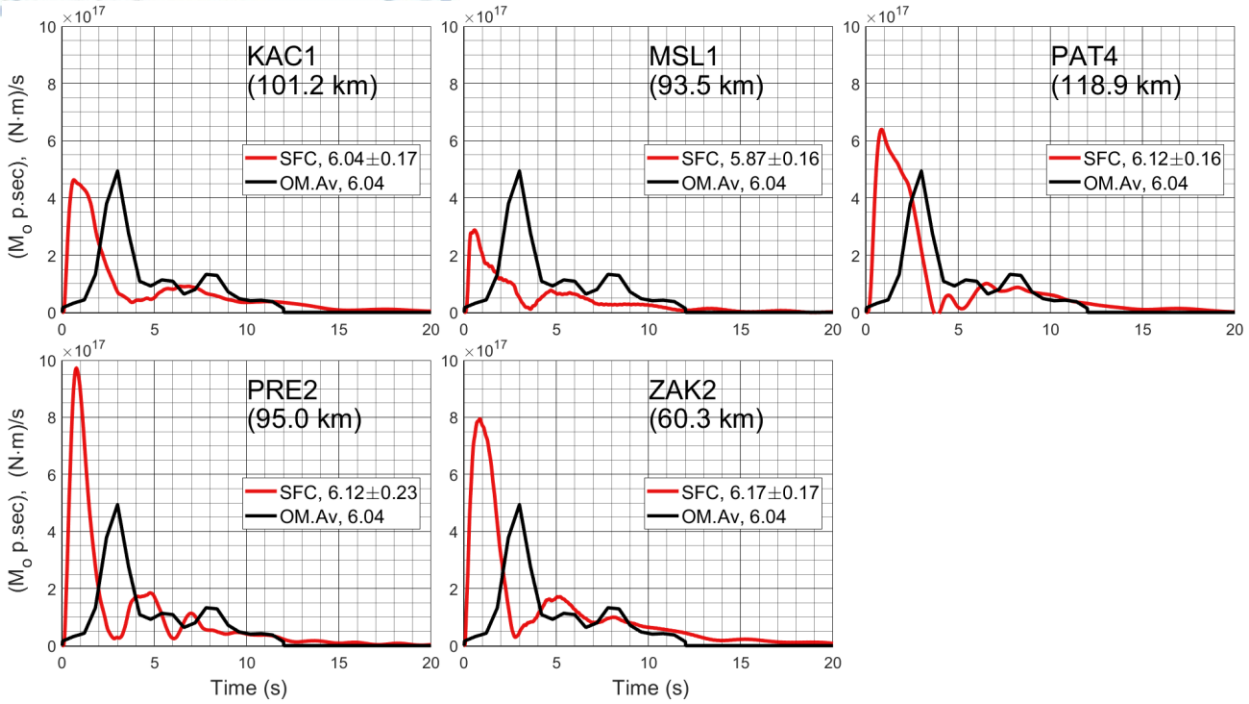

Appendix X. The corresponding FAS of the STF presented in **Appendix W**, for the M_w= 6.05 (earthquake id: 20140226_135543).

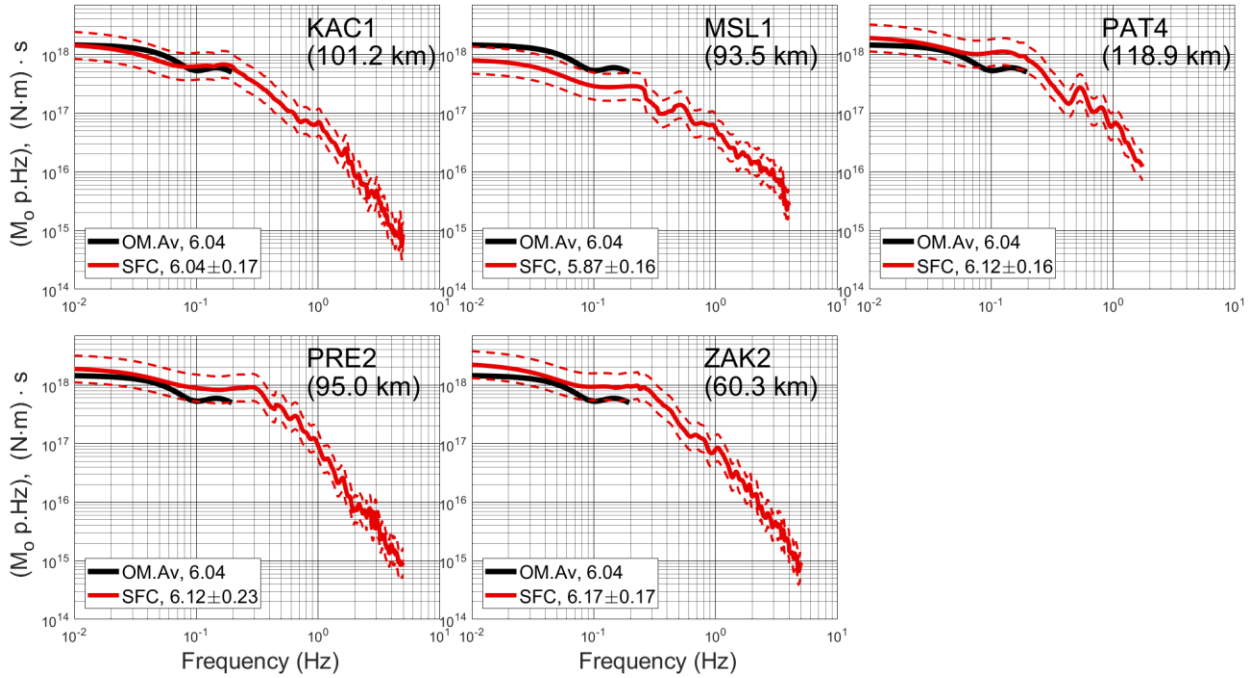

Appendix Y. The corresponding figure to **Figure 57**, for the M_w= 7.0 (earthquake id: 20201030_115125). (OM.01 and OM.02 represents the STF computed by USGS and by ***Lentas et al., (2021)***, respectively

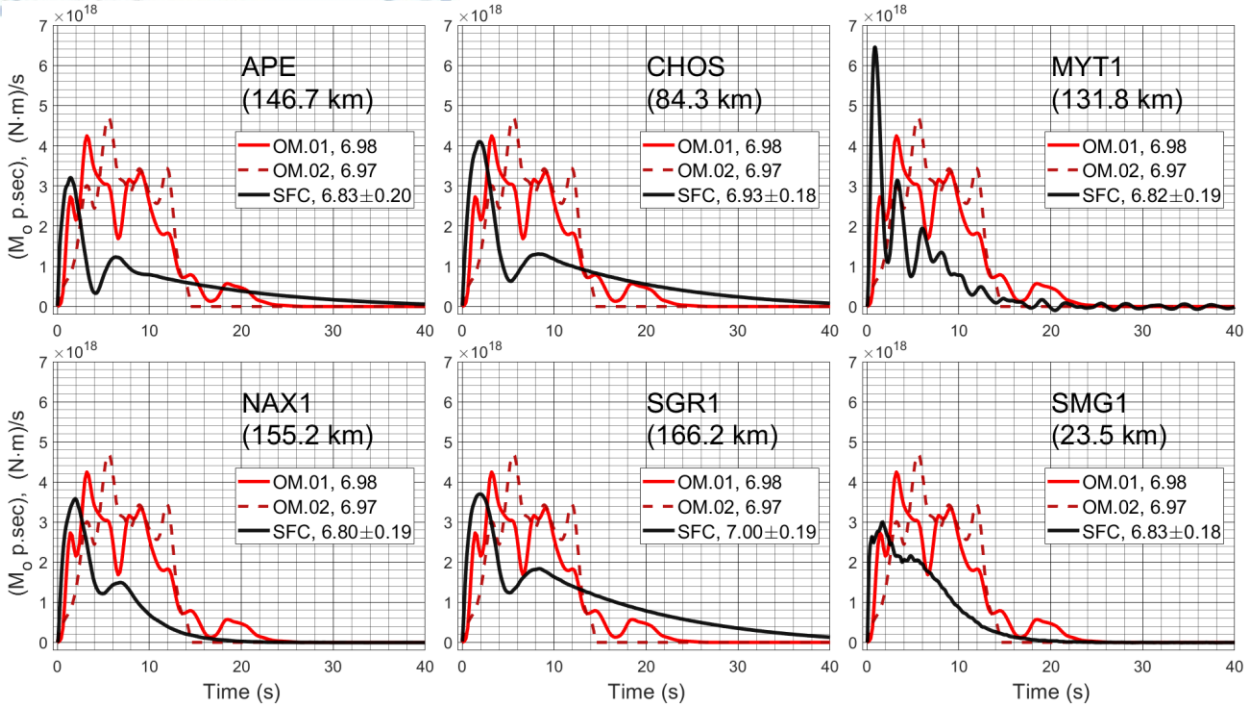

Appendix Z. The corresponding FAS of the STF presented in **Appendix Y**, for the M_w= 7.0 (earthquake id: 20201030_115125).